

Dipartimento di / Department of

Fisica

Dottorato di Ricerca in / PhD program Fisica e Astronomia Ciclo / Cycle XXXV

Curriculum in Fisica dei Plasmi e Biofisica

COLD PLASMAS FOR AIR PURIFICATION AND SANITATION

Cognome / Surname Piferi Nome / Name Cecilia

Matricola / Registration number 834557

Tutore / Tutor: Claudia Riccardi

Coordinatore / Coordinator: Stefano Ragazzi

ANNO ACCADEMICO / ACADEMIC YEAR 2021/2022



UNIVERSITÀ DEGLI STUDI DI MILANO BICOCCA
DIPARTIMENTO DI FISICA
“GIUSEPPE OCCHIALINI”

CORSO DI DOTTORATO IN FISICA E ASTRONOMIA
XXXV CICLO

Curriculum Fisica dei Plasmi e Biofisica
Coordinatore Stefano Ragazzi
Anno Accademico 2021-2022

COLD PLASMAS FOR AIR PURIFICATION AND SANITATION

Dottoranda
Cecilia Piferi
834557

Tutor
Prof. Claudia Riccardi

Abstract

It is generally accepted that the reduction of life quality is largely due to anthropic effects, mainly due to pollutant agents, and possible solutions need to be addressed. An important class pollutants are the so-called Volatile Organic Compounds (VOCs). Many of these compounds are classified as carcinogenic, or possibly carcinogenic, for humans and, in addition, they can cause long term environmental damage. Despite these drawbacks, they are suitable for wall and/or furniture painting, for the textile treatments, and are widely used in a variety of industrial processes. Unfortunately, they are released into the environment as waste products. As of today, it is not possible to replace VOCs with other compounds, but one can attempt to modify them just before they get disseminated in the atmosphere. The easiest way to achieve that goal is by using combustion reactors. However, they are bulky, require a lot of energy and need to reach high temperatures up to 300°C, or more, to be effective. Atmospheric pressure cold plasmas, in particular Surface Dielectric Barrier Discharge (SDBD), can largely improve the abatement process of VOCs. Indeed, SDBD require much less energy than typical combustion reactors, they occupy much smaller volumes (less than a cubic meter) and the global gas temperature gets down to the order of room temperature.

Chemical pollution is not the only problem affecting our living environment, for instance antimicrobial resistance is also becoming an important issue. The antimicrobial and antibacterial drugs have improved our health conditions since they were discovered, but they are becoming less and less effective as a result of their improper use during the last decades. A way to reduce the use of antibiotic can be obtained by eliminating or hindering microbial diffusion in air, such as using particulate filters in ventilation systems. However, the biological agents collected in the filters are not just passive, but get accumulated on the filter surface, thus proliferating during long periods of high relative humidity (> 80%), causing infections at distant places after dissemination. Part of this thesis is devoted to this problem. An innovative use of the SDBD was developed for the abatement of bacteria in air. Its limited volume permits to place the SDBD in contact with the air circulating system of a building, within which one can proceed to the denaturation of the diffusing bacteria by the reactive species produced in the plasma.

Finally, the last part of this thesis is devoted to polymeric surfaces modifications through a capacitive coupled low pressure cold plasma. Surface mod-

ifications of materials by plasma treatments and depositions have attracted a great deal of interest in the last decades. We can create a nanostructurization over the polymeric treated surfaces that can have different applications, from antifouling in water to antibacterial in air.

Contents

I	Introduction	9
1	Aim and motivation	11
2	Cold plasma sources	17
2.1	DBD and SDBD plasma discharge	18
2.2	Capacitive Coupled Plasma	20
3	Air contamination	23
4	Plasma surface treatments	31
II	Volatile Organic Compounds depletion by atmospheric cold plasma and catalyst	35
5	Equipment setups	37
5.1	Sources	37
5.1.1	SDBD plasmas	37
	Teflon and vetronite SDBD	37
	Alumina SDBD	38
5.1.2	Lamps	39
5.2	Experimental configurations	40
5.2.1	Treatment box	40
	Parallelepiped chamber reactor	40
	Cross chamber reactor	40
5.2.2	Photocatalysts	43
5.2.3	VOC injection system	44
	Liquid injection system	44
	Gas injection system	44
5.3	Diagnostics	45
	Rogowski coil	45
	Optical emission spectroscopy device	48
	Radiometric device	48
	Absorption spectroscopy	49
	Temperature	50

Gas chromatography	51
6 Results and analysis	55
6.1 Electric characterization	55
Current analysis	55
Lissajous analysis	56
6.2 Lamps characterization	60
6.3 Measurements of O ₃ and NO ₂ production by SDBD	65
6.4 Depletion with plasma	69
6.4.1 Pentane depletion	69
Treatments in parallelepiped chamber reactor . . .	69
Treatments in cross chamber	70
6.4.2 Propane depletion	72
Treatments in parallelepiped chamber reactor . . .	72
Treatments in cross chamber	72
6.5 Depletion with catalysts	74
7 Conclusions	77
III Bacteria removal by atmospheric cold plasma	81
8 Equipment setup	83
8.1 Plasma sources	83
8.2 Experimental setup and diagnostics	83
Treatment box	83
Bacteria preparation and vaporization	83
Bacteria collection	84
FITC analysis	85
O ₃ and temperature measurements	86
9 Results and analysis	87
9.1 O ₃ production and temperature measurements	87
9.2 Bacteria abatement	89
9.2.1 <i>Escherichia coli</i>	89
Duo Sas bacteria collection	89
Coriolis bacteria collection	91
9.2.2 <i>Staphylococcus epidermidis</i>	96
10 Conclusions	99

IV	Surface treatments by low pressure cold plasma	101
11	Equipment setup	103
12	Results and analysis	105
12.1	Polypropylene	105
12.2	Polytetrafluoroethylene	112
13	Conclusions	115
V	Appendix	117
	Bibliography	119
A	Peer reviewed papers	137
A.1	Current Filaments in Asymmetric Surface Dielectric Barrier Discharge	138
A.2	High concentration propane depletion with photocatalysis	161
A.3	Intensity comparison between UV lamps and plasma emission for air purification studies	171
A.4	Pentane Depletion by a Surface DBD and Catalysis Processing	178
A.5	A study on propane depletion by surface dielectric barrier discharges	194
A.6	Hydrophilicity and Hydrophobicity Control of Plasma-Treated Surfaces via Fractal Parameters	203
A.7	Controlled Deposition of Nanostructured Hierarchical TiO ₂ Thin Films by Low Pressure Supersonic Plasma Jets	218
	Acknowledgments	237

Part I
Introduction



1 Aim and motivation

This thesis can be placed in the context of ‘One Health’ approach. According to the World Health Organization (WHO) [1]

‘One Health’ is an integrated, unifying approach to balance and optimize the health of people, animals and the environment. [...]

The approach mobilizes multiple sectors, disciplines and communities at varying levels of society to work together. This way, new and better ideas are developed that address root causes and create long-term, sustainable solutions.

One Health involves the public health, veterinary, public health and environmental sectors. The One Health approach is particularly relevant for food and water safety, nutrition, the control of zoonoses (diseases that can spread between animals and humans, such as flu, rabies and Rift Valley fever), pollution management, and combating antimicrobial resistance (the emergence of microbes that are resistant to antibiotic therapy) [1].

In this optic, we are trying to develop physical systems able to reduce chemical and biological pollutants, with low energetic request and low environmental impact.

The anthropic origin of climate change is an accepted status that humanity must try to solve. One of the causes is the pollutants that are reducing the human life quality on our only planet. A class of these pollutants is the Volatile Organic Compounds (VOCs) [2]. A lot of these compounds are classified as carcinogenic or possibly carcinogenic for humans, and they can cause long-term environmental damages [3]. Thanks to their chemical-physical properties, they have suitable characteristics for wall or furniture painting, and for textile treatments, they are widely used for industrial processes, and are diffused in the environment as waste products. As of today, it is not possible to replace VOCs with other compounds, but we can try to reduce their diffusion right after their emission. There are different methods tested on pilot plants for

VOC depletion. Some of them are already in use in industries, such as thermal decomposition [4], absorption [5], adsorption [6], bio-filtration [7], membrane separation [8] and catalytic oxidation [9]. However, several economic and efficiency limitations are present in most of these technologies when treating effluents with low VOC concentrations, high airflow rate or with compounds that have low solubility in water [10]. An alternative can be served by plasmas. Non-equilibrium and equilibrium plasma reactors are investigated and their selective efficiencies in VOC abatement are reported in literature reviews [11,12]. Equilibrium plasmas are thermal, since neutrals and charges are produced at high temperatures of the order of 10^4 K. Thermal plasmas (TP), such as arches and torches, are employed for different purposes, e.g. in waste gas decomposition of hard-to-convert components, i.e. Perfluorocarbons PFCs [13], or in the gasification of coal [14]. These plasmas have the advantage of fast and high dissociation rates and rather good efficiency, but most of them are characterized by high energetic consumption, which is required to sustain the discharge itself, and high maintenance and equipment costs [15]. Even if they can be used for the abatement of harmful toxic gases, they are economically unsustainable for the abatement of VOCs at low concentrations. Non-equilibrium plasmas, also known as Non-Thermal Plasmas (NTPs), can be sustained with lower energy than Thermal Plasmas. NTPs are very weakly ionized and are not in thermodynamic equilibrium because electrons absorb most of the electromagnetic energy, reaching temperatures of several eV, while neutral and ionic species kinetic energies remain at room temperature. For this reason, they are also called cold plasmas. NTPs are generated by using different types of devices such as microwave plasma [16], dielectric barrier discharge [11], gliding arc discharge [17] and plasma jets [18,19]. Most of the NTP sources work at atmospheric pressure. They are dominated by kinetic effects, where electrons are the primary source of molecular dissociation and radical formation. The resulting chemical reactions between radicals promote their degradation and oxidation in the presence of oxygen species. Compared to TP, they are characterized by lower dissociation rates, but not by lower efficiency [10]. One of the most employed cold plasma devices is the Dielectric Barrier Discharge (DBD), which has the advantage of requiring very low energy. DBDs have the drawback of processing only small gas volumes. In the DBD configuration, the gas is physically confined to pass between the two electrodes, the plasma state is mostly confined to a volume of a few mL, and gas air flows between a few

mL/min and some L/min [10, 19]. The scale-up factors and operating costs need to be investigated in order to evaluate their real economic sustainability in view of the most interesting applications. One of the ways to overcome this problem could be through the employment of a particular DBD: the surface DBD (SDBD) [20]. In SDBDs, the plasma is produced on a surface without being confined between two electrodes. In this configuration, the gas can move on the surface and rapidly diffuse into larger volumes. Moreover, the waste air remediation applications of these devices has not been investigated as for the DBD configuration. Only a few research papers have been devoted to the application of SDBDs in VOC abatement [21, 22]. Part of this thesis can be inserted in the investigation of VOCs depletion using SDBDs [23–25].

Chemical pollution is not the only problem for good life environment: antimicrobial resistance is an increasingly worrying issue. The antimicrobial and antibacterial drugs improved our health since their discovery, but they are becoming less and less effective due to the improper use in the last decades [26]. A way to reduce the use of antibiotics, is the reduction of microbial diffusion in air, such as using particulate filters in ventilation systems. However, biological agents collected in the filters are not killed but are accumulated on the surface, proliferating during long periods of high relative humidity (>80%) and causing infections at distant places after their dissemination. There is the need of a technology that can inactivate microbes in a very short exposure time. Many technologies are being investigated for this purpose, including electrostatic fields [27], UV radiation [28], carbon nanotubes [29], microwave and heat treatment [30] and afterglow plasma [31]. The use of non-thermal plasma technology for disinfection and sterilization is growing [32–36] since it seems to be a technique that does not cause antimicrobial resistance [37]. In this context is framed a part of this thesis. An innovative use of the SDBD was developed for the abatement of bacteria in air. Its little volume permits to place the SDBD system in the air circulating system and inactivate the bacteria thanks to the reactive species produced by the plasma.

In addition, the last part of this thesis is devoted to the polymeric surfaces nanometric modification through capacitive coupled low pressure cold plasma [38]. Nanotechnology contributes in the development of improved materials with advanced properties for different applications. Nanoparticles embedded in material matrices, nanostructured metamaterials are of great interest in applications, such as energy [39, 40], antibacterial coatings [41, 42], textile

sectors [43], manufacturing [44] environment and catalysis [45]. Synthetic and natural polymer substrates and fibers have been studied for improving surface performances and different functionalities [46] through nanoscale processing, i.e. incorporation of nanoparticles [47], nano-structuring [48], or nanocoatings [49]. Different nanotechnologies are employed, like sol-gel [50], plasma deposition [42], plasma etching [51], grafting of specific chemical groups [52], or wet treatments [53]. Plasma-enabled synthesis, assembly and modification of materials at the nanoscale, due to its strong potential and versatility, is one of the fastest growing fields in basic material science research, in technology and engineering applications. The resulting nanostructured surfaces can be designed to have new characteristic properties unachievable with traditional methods, such as extreme hydrophilic properties [54]. We create a nanostructurization using low pressure cold plasma over the polymeric surfaces that can have different applications. Polymers modified with plasma are suitable for the application as antifouling material, since the nanostructures can slow the growth of the aquatic organism and facilitate their detachment from the hull and so improve the performance and durability vessel. Following a similar principle, these materials can be used for the realization of antibacterial surfaces for hospitals, schools, supermarkets, or more in general places where a lot of people interact each other and with the objects around, limiting the growth of the bacteria and so their transmission in the community.

This thesis is divided in four main parts with different chapters each, divided as following.

Part I is devoted to the introduction and includes Chapters from 1 (this one) to 4. In Chapter 2 we make an introduction of cold plasma sources, and we linger over the sources we used, that are the Surface Dielectric Barrier Discharge and the Capacitive Coupled Plasma. In Chapter 3 we introduce the air pollution issue, focusing on the VOC and bacteria contamination. In Chapter 4 we present the surface plasma treatments application.

Part II, that includes Chapters from 5 to 7, we present the Volatile Organic Compounds experiments. In Chapter 5 we outline the experimental setup, showing which sources, experimental configurations and diagnostics we used for studying the VOC depletion. Chapter 6 is for the presentation of our experimental results and their analysis: electrical characterization, lamps characterization, measurements of O_3 and NO_2 produced by the SDBD, pentane

and propane depletion with plasma, and propane depletion with photocatalysis. The conclusion of this part is in Chapter 7.

Part III is divided in Chapters from 8 to 10 and presents our work on bacteria depletion. In Chapter 8 we describe the equipment setup (plasma sources and experimental configurations) used in this part. In Chapter 9 we present the results and analysis: O₃ production and temperature measurements, and bacteria abatement with the induced contamination system. The bacteria we consider are *Escherichia coli* and *Staphylococcus epidermidis*. Chapter 10 summarizes our results.

The last part, Part IV, is about the plasma surface treatments and includes Chapters from 11 to 13. In Chapter 11 we describe the equipment setup used for the polymeric surface modification. The results and analysis are presented in Chapter 12: polypropylene and polytetrafluoroethylene nanostructurization. Chapter 13 contains the conclusions of this part.

In addition, Part V is the appendix that includes the Bibliography and in Chapter A the peer reviewed papers that I published with my collaborators during the PhD.



2 Cold plasma sources

Plasma is an ionized gas containing electrons and ionized atoms or molecules, which exhibit collective behavior due to the long-range Coulomb forces [55]. Etymologically, the word *plasma* has a Greek origin and means *formed or molded*. Its usage to identify a state of matter was proposed by Irvin Langmuir in 1922 in analogy to blood plasma, which is the fluid medium left after the removal of all the corpuscular material. The word has been accepted in the scientific community even if it has been discovered some time later that there is actually no fluid medium entraining the electrons, ions, and neutrals in an ionized gas [56]. Electrons, positive and negative ions, and neutrals are the species which identify a plasma.

It is difficult to give a unique classification of all natural and laboratory plasmas, because of all the parameters involved in their formation. However, they can be divided in two main groups: Thermal (TPs) and Non-Thermal Plasmas (NTPs). TPs are in local thermal equilibrium state; the temperature of electrons is equal or very similar to the temperature of heavy particles. In contrast, NTPs have different temperatures for neutrals, ions and electrons. The plasmas we use in our experiments are atmospheric or low pressure cold NTPs.

The study of plasma physics starts in the 1920s and 1930s with few isolated researchers willing to investigate the effects of ionospheric plasma on long-distance short-wave radio propagation and gaseous electron tubes used for rectification, switching and voltage regulation in the pre-semiconductor era of electronics. Hannes Alfvén developed in the 1940s a theory of hydromagnetic waves. In the early 1950s, during the Cold War, USA, Britain and Soviet Union started independently to promote researches on large-scale plasma physics, mainly based on magnetic fusion energy. This work was initially classified but in 1958 all three countries declassified their efforts and have co-operated since. Many other countries now participate in fusion research. At the end of the 1960s the empirically developed Russian tokamak configuration began producing plasmas with parameters far better than the lackluster results

of the previous two decades. Fusion break-even had nearly been achieved in tokamaks at the end of twentieth century. In the early twenty-first century, an international agreement was reached to build the International Thermonuclear Experimental Reactor (ITER), a break-even tokamak designed to produce 500 megawatts of fusion output power. Non-tokamak approaches to fusion have also been pursued with varying degrees of success. Simultaneously with the fusion effort, there has been an equally important and extensive study of space plasmas. Space plasmas often behave in a manner qualitatively similar to laboratory plasmas but have larger scale. Since the 1960s significant effort has been directed towards using plasmas for space propulsion. Plasma thrusters are now in use on some spacecraft and could be used for interplanetary missions. Since the late 1980s plasma processing has become crucial for the fabrication of the tiny, complex integrated circuits used in modern electronic devices. In the same years, investigations began on non-neutral plasmas. These mimic the equation of incompressible hydrodynamics and so provide a compelling analog computer for problems in incompressible hydrodynamics. Another application of non-neutral plasmas is the storage of large quantities of positrons. In the 1990s studies began on dusty plasmas. Dust grains immersed in a plasma can become electrically charged and then act as an additional charged particle species. Both non-neutral and dusty plasmas can also form bizarre, strongly coupled collective states where the plasma resembles a solid, e.g. forms quasi-crystalline structures. In addition, there have been continuing investigations of industrially relevant plasmas such as arcs, plasma torches and laser plasmas. Plasma displays are used for flat-panel televisions and there are naturally occurring terrestrial plasmas such as lightnings. Between the late 2000s and the 2010s plasma medicine and environmental plasma application have been developed. Nowadays, plasmas can be used in disinfection, sterilization, cleaning, surgery plasma blades, air pollution control [56].

2.1 DBD and SDBD plasma discharge

Dielectric Barrier Discharge (DBD) and Surface Dielectric Barrier Discharge (SDBD) generate NTP. Both DBD and SDBD generally work in atmospheric pressure condition and have simple design. Some DBD and SDBD configurations are shown respectively in Figure 2.1 and 2.2. They have two metal electrodes, divided by one or more dielectric barriers which obstruct the direct

passage of charge between them. The presence of dielectric barriers precludes DC operation, so one electrode is typically grounded, and the other is feed by a time varying high voltage condition (the simplest is the harmonic alternating voltage) with frequency between 500 Hz and 500 kHz and amplitude ~ 10 kV. In the DBD configuration there is an air gap between electrodes and dielectric that has a typical width ranging from less than 0.1 mm to several cm, depending on the application [57–60]. In the SDBD configuration this gap is zero and so the gas discharge occurs above and close to the surface of the dielectric or electrode material.

It is possible to ignite plasma in dielectric barrier discharge using almost any kind of gas.

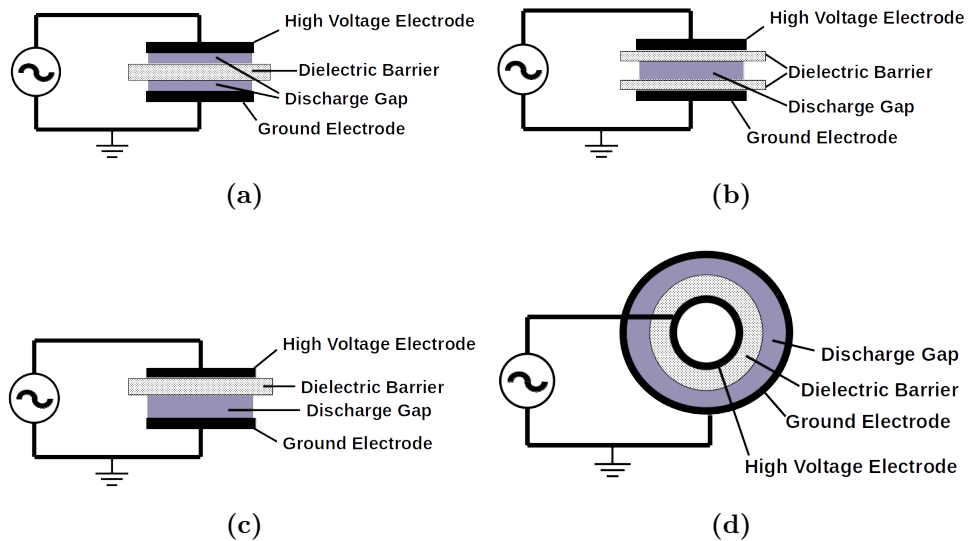


Figure 2.1: Some of the main DBD configuration.

DBDs have been known for more than a century and their first application was ozone generator by Siemens in 1857, who observed a glow between two coaxial glass tubes with external electrodes while generating ozone [58].

In 1937 Klemenc and others made important steps in understanding the physical nature of the DBD. In their work they found that this discharge occurs in a number of individual tiny breakdown channels, now called microdischarges [61]. These microdischarges have temporal scale of about 10 ns and spatial scale of about $100 \mu\text{m}$.

DBDs have different of industrial applications because they operate at strongly non-equilibrium conditions at atmospheric pressure and at reasonably high power levels, without using sophisticated pulsed power supplies. This us-

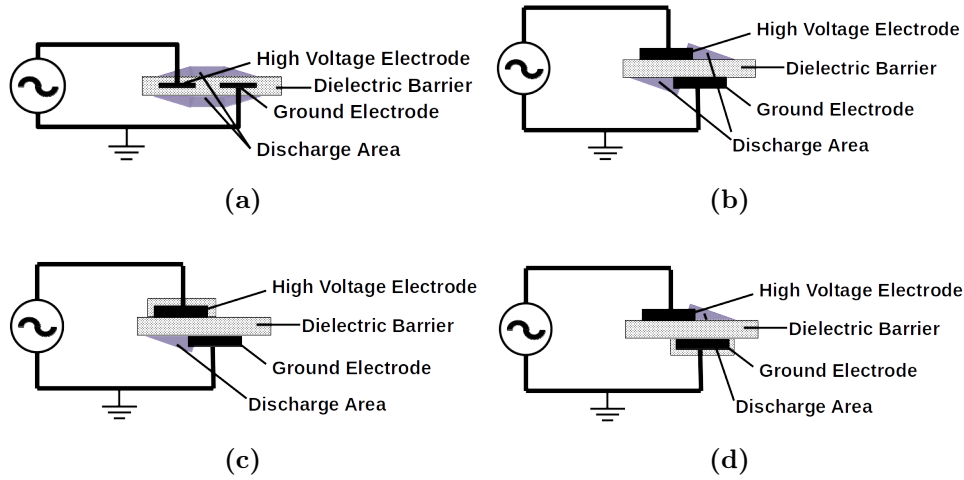


Figure 2.2: Some of the main SDBD configuration.

age goes from ozone generation, CO₂ lasers, UV-sources in excimer lamps, surface treatment in order to promote wettability, printability and adhesion to pollution control, which is the main target of this analysis.

2.2 Capacitive Coupled Plasma

Capacitive Coupled Plasma Radio-Frequency (CCP-RF) is a plasma source that employs an alternated voltage in order to ionize a low-pressure gas between two metal electrodes. The AC voltage has a frequency in the range of the radio waves, typically 13.56 MHz, to ionize the low pressure gas. One of the two electrodes (the antenna) is connected to the phase wire of the power supply. The other electrode, as the vacuum chamber itself, is grounded [38,62].

The system is known as Capacitive Coupled because of a capacitive matching box of variable capacitance is used to adapt the RF wave to the plasma load, to minimize the power of the reflected wave that comes back to the generator. The generator allows setting (manually or automatically) the RF power and the capacitance. A scheme of CCP-RF setup is sketched in Figure 2.3.

The plasma production is due to the free electrons of the gas that are accelerated by the RF field and can ionize other atoms and produce secondary electrons. If the electric field is strong enough, the secondary electrons can ionize again and produce an electron avalanche. This is known as breakdown. After the breakdown, RF signal between the electrodes acquires a negative DC bias caused by ambipolar electric field, due to the different diffusivity of

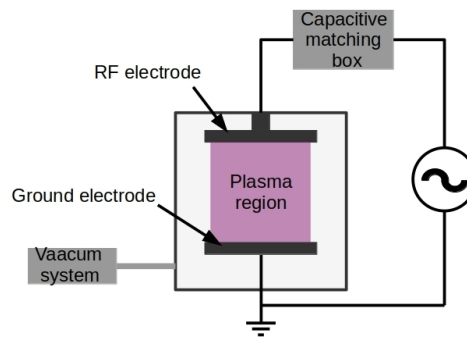


Figure 2.3: Capacitively Coupled Plasma scheme.

negative (light electrons) and positive (heavy ions) charges in the plasma [38].



3 Air contamination

Air pollution is really noxious for the environment and the human healthy. In Europe, the emissions of a lot of the atmospheric pollutant are decreasing in the last decades. However, the pollutants concentrations are still too high, and the problems concerned to air quality are not disappeared. Air pollution is a global issue because the emissions in a place can be moved in the atmosphere and give a bad air quality elsewhere.

NO_x , SO_x , H_2S , particulate matter (PM), ..., and volatile organic compounds are a large and important group of pollutants. They can cause various effect, depending on their chemical structure and concentration. Some of these environment effects are creation of photochemical smog, secondary aerosols, tropospheric ozone, intensification of global warming deterioration of stratospheric ozone layer [3]. In addition, some of these compounds have an impact on human healthy that goes from impairing the respiratory system to premature death caused by their toxicity or carcinogenic effects.

The Italian legislation (Art.268 del DLgs152/2006) defines as VOCs all the organic compounds with a vapor pressure higher than 0.01 kPa at 293.15 K (20° C).

In the words of Hans Bruyninckx, EEA (Europe Environment Agency) Executive Director,

Air pollution is causing damage to human health and ecosystems. Large parts of the population do not live in a healthy environment, according to current standards. To get on to a sustainable path, Europe will have to be ambitious and go beyond current legislation [63].

The EU's air quality directives (2008/50/EC Directive on Ambient Air Quality and Cleaner Air for Europe and 2004/107/EC Directive on heavy metals and polycyclic aromatic hydrocarbons in ambient air) set pollutant concentrations thresholds that shall not be exceeded in a given period of time [2], but this classification doesn't include VOC. In fact the current situation of the legislation in the different Member States of the European Union for what

concerns the VOC emissions is very different and this causes a gap in health, hygiene and environmental protection between the various countries due to the lack of regulations and related controls. To resolve this gap, a process of harmonization was carried out, prescribing the monitoring strategies and methods and the parameters that must be considered for the control of pollutants in the domestic environment. This process led to the publication by the European Collaborative Action - urban air, indoor environment and human exposure of Report n.29 [64] which lists a series of chemical compounds, including VOC and formaldehyde and the relative values of Minimum Concentration of Interest (LCI, Lowest Concentration of Interest) for the evaluation of the emissions produced by building products [65]. The LCI is the lowest concentration above which, according to the best professional judgement, the pollutant may have some effect on people in the indoor environment. EU-LCI values are health-based reference concentrations for inhalation exposure used to assess emissions after 28 days from a single product during a laboratory test chamber procedure. EU-LCI values are applied in product safety assessment with the ultimate goal to avoid health risks from long-term exposure of the general population, and they are usually expressed as $\mu\text{g}/\text{m}^3$ [64].

The 2016/2284 EU Directive on the reduction of national emissions of certain atmospheric pollutants

In order to move towards achieving levels of air quality that do not give rise to significant negative impacts on and risks to human health and the environment, [...] establishes the emission reduction commitments for the Member States' anthropogenic atmospheric emissions of sulphur dioxide (SO_2), nitrogen oxides (NO_x), non-methane volatile organic compounds (NM-VOC), ammonia (NH_3) and fine particulate matter ($\text{PM}_{2.5}$) and requires that national air pollution control programmes be drawn up, adopted and implemented and that emissions of those pollutants and the other pollutants [...] be monitored and reported (Article 1 [66]).

Every member state has different rate of reduction depending on different parameters. Italy decreasing of the non-methane VOC (that are all the VOC except for methane) is set at least at 35% of NM-VOC concentration in the 2005 for any year from 2020 to 2029 in order to reach the 46% for any year from 2030 (Annex II Table A [66]).

For what concerns the indoor total volatile organic compounds (T-VOC) concentration there is not a community or local legislation. The Italian *Direttiva 2004/42/CE - Decreto Legislativo 27 marzo 2006 n.161 su: Limitazione delle emissioni di VOCs dovuti all'uso di solventi organici in alcune vernici e pitture (2006)*, for examples, sets only the maximum concentration of VOC in every selling paintings and in the building coatings, and also obliges the application of a specific label which says the chemical nature of the product and the VOC concentration. On the contrary, the German Federal Environmental Agency gives a guideline in these terms, as explained in Table 3.1, where sets the exposure time limits of T-VOC indoor concentrations [67]. These T-VOCs limits are expressed in ppb, that means parts per billion and indicates how many particles of the substance under examination are in a billion (10^9) of particles of mixture⁽¹⁾.

Level	Hygienic rating	Recommendation	Limits	T-VOC (ppb)
Unhealthy	Situation not acceptable	Use only if unavoidable Intense ventilation	hours	2200-5500
Poor	Major objections	Airing necessary Search for sources	< 1 month	660-2200
Moderate	Some objection	Airing recommended Search for sources	< 12 months	220-660
Good	No relevant objections	Ventilation Airing recommended	no limits	65-220
Excellent	No objections	Target value	no limits	0-65

Table 3.1: T-VOC guidelines issued by the German Federal Environmental Agency [67].

In the last decades there was an increasing of poor indoor air quality illnesses, such as asthma, irritation, allergies or sick building syndrome. This syndrome causes symptoms like general discomfort, headache, irritation of the nose, eyes or mouth, dry cough, dry or itchy skin, dizziness, nausea, difficulty concentrating, fatigue and sensitivity to odors and to feel better you need to change place or ventilate the room [68]. In indoor area constant sources of VOC pollutant are cosmetics products, deodorants, cleaning materials, dry-cleaned dresses, smock, printer and copy machine. Other sources are furniture and walls painting, but their VOC emission is higher in the early stages of the products life and tends to decrease over time. A conspicuous penetration of VOCs from the outside could happen if the air intakes are placed near polluted

(1) Later we will also use the unit ppm (parts per millions) that indicates how many particles of the substance under examination are in a million (10^6) of particles of mixture.

area, such as busy streets or garages.

In our society we have already some methods to control VOC emission, like adsorption, thermal and catalytic oxidation, membrane separation, bioreaction and photocatalysis. However, these methods become cost-inefficient and difficult to operate when low concentration of VOC need to be treated. In this panorama, treatment with non-thermal plasma can help. The non-equilibrium plasma state makes unnecessary to heat the entire treated gas flow. The primary electrons collide with background molecules (N_2 , O_2 , H_2O , ...) producing secondary electrons, photons, ions and radicals. These latter species are responsible for the oxidation of VOC molecules, even if ionic reaction are also possible. This process is highly non-selective, creating chemical reactive environment in which harmful substances are readily decomposed [3, 69–71].

In this thesis we investigated the Volatile Organic Compounds depletion by atmospheric pressure Surface Dielectric Barrier Discharge plasma and catalytic systems in static condition. As a VOC we used pentane and propane.

Pentane [72] is an organic saturated hydrocarbon with formula C_5H_{12} . It has three structural isomers: the n-pentane, the isopentane (or 2-methylbutane) and the neopentane (or 2,2-dimethylpropane). In our work we used n-pentane and from now on we will simply refer to it as pentane.

It is a volatile and colorless liquid. Its molar mass is 72.15 g/mol; at standard conditions its boiling point is $36.1^\circ C$ and its density $0.63 g/cm^3$. It is hydrophobic and flammable. Its vapor pressure is 57.9 kPa at $20^\circ C$.

The combustion of pentane happens according to the following reaction



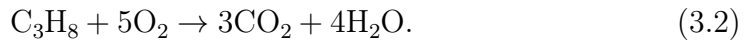
For its properties, according to different classifications it is a volatile organic compound or very volatile organic compound.

We chose pentane as a working VOC because it has a standard alkane behavior with quite a long chain, and it is relatively safe for health with respect to other compounds, even if we reduced the exposure time of the operator to the compound, placing it in a closed bottle.

Propane [73] is an aliphatic hydrocarbon with formula C_3H_8 . At atmospheric standard pressure and room temperature, it is colorless and odorless

gas, that can be liquefied by compression. Its molar mass is 44.097 g/mol and its vapor pressure is 853.16 kPa at 20° C.

The combustion of propane happens according to the following reaction



We selected propane as a working VOC because it is a common gas with an easy availability that does not induce problems to the operators if they work in safe conditions.

Another important component of the air contamination are the biological aerosols, also known as bioaerosols. They are environmental aerosols that contain microorganisms (bacteria, fungi, and viruses), allergens, plant debris, endotoxin, glucans, and skin scales in them. The scientific community is increasing its interest in characterizing the bioaerosol also for their effects over the human health, since they can transmit infections, asthma, allergies and other respiratory diseases. Nowadays, there is not a European legislation about safe limits exposure of the bioaerosol, due to the lack of standardized methods of bioaerosol sampling and the unknown dose-answer [74].

For the Italian legislation the prevention and protection from biological agents are detailed in the X title of the *Decreto Legislativo 81/08 - Testo unico in materia di tutela della salute e della sicurezza nei luoghi di lavoro*⁽²⁾, without set a value for a biological good air quality in works spaces [75]. However, it is reported a classification of the biological agents in four groups according to the infection risks:

- group 1 - biological agent with low probability in causing diseases in humans;
- group 2 - biological agent that can cause diseases in humans and can be a risk for workers; there is low probability in community propagation; generally there are effective prophylactic measures and therapies;
- group 3 - biological agent that can cause serious diseases in humans and can be a risk for workers; it can propagate in community; however generally there are effective prophylactic measures and therapies;

(2) <https://www.ispettorato.gov.it/it-it/strumenti-e-servizi/Documents/TU-81-08-Ed.-Agosto-2022.pdf>

- group 4 - biological agent that can cause serious diseases in humans and can be a risk for workers; it can highly propagate in community; generally there are no effective prophylactic measures and therapies.

The predominant method of controlling microbes in most heating, ventilation and air conditioning systems (HVAC) is through particulate filters. However, the biological agents collected in the filters are not inactivated but are accumulated on the surface, proliferate during long periods of high relative humidity (>80%) and cause infection at distant places after dissemination [76]. There is a need of a technology which can inactivate microbes in a very short exposure time. Many technologies are being investigated for this purpose, including electrostatic fields [27], UV radiation [28], carbon nanotubes [29], microwave and heat treatment [30] and afterglow plasma [31].

Non-thermal plasma technology has been increasing for disinfection and sterilization [32–36] since seems it is a technique that not cause antimicrobial resistance [37]. In fact, antimicrobial resistance (AMR) is a global threat for health and development. It occurs when bacteria, viruses, fungi and parasites change over time and no longer respond to medicines making infections harder to treat and increasing the risk of disease spread, severe illness and death [26].

The number of people for whom treatment is failing or who die of infections will increase due to the lack of effective tools for the prevention and adequate treatment of drug-resistant infections and improved access to existing and new quality-assured antimicrobials. Medical procedures, such as surgery, including cesarean sections or hip replacements, cancer chemotherapy, and organ transplantation, will become more risky [26]. According to WHO [26]

AMR occurs naturally over time, usually through genetic changes. Antimicrobial resistant organisms are found in people, animals, food, plants and the environment (in water, soil and air). They can spread from person to person or between people and animals, including from food of animal origin. The main drivers of antimicrobial resistance include the misuse and overuse of antimicrobials; lack of access to clean water, sanitation and hygiene (WASH) for both humans and animals; poor infection and disease prevention and control in health-care facilities and farms; poor access to quality, affordable medicines, vaccines and diagnostics; lack of awareness and knowledge; and lack of enforcement of legislation [26].

The actual situation of AMR is alarming. For common bacterial infections, such as urinary tract infections, sepsis, sexually transmitted infections, or diarrhea, world-wide high rates of resistance against antibiotics have been observed, indicating that we are running out of effective antibiotics. For example, the rate of resistance to ciprofloxacin, an antibiotic commonly used to treat urinary tract infections, varied from 8.4% to 92.9% for *Escherichia coli* and from 4.1% to 79.4% for *Klebsiella pneumoniae* in countries reporting to the Global Antimicrobial Resistance and Use Surveillance System (GLASS) [26]. Specific antibiotic resistance genes are widespread in *Staphylococcus epidermidis*. Most notably, resistance to methicillin as an antibiotic of first choice against staphylococcal infections is at 75–90% among hospital isolates of *S. epidermidis*, which is even higher than the corresponding rate for *S. aureus* (40–60%) [77].

For these reasons it is important to continue the development of alternative systems in order to prevent humans and animals infection without the use of antibiotic or antimicrobial drugs, such as cold plasmas.

In this thesis, we used atmospheric pressure Surface Dielectric Barrier Discharge plasma for abate *Escherichia coli* (*E. coli*) and *Staphylococcus epidermidis* (*S. epidermidis*) aerosol vapor that flow over the plasma.

E. coli is a Gram-negative bacterium largely used for microbiological studies since most of its strains are harmless and its growth in laboratory is well standardized. According to WHO [78], however, some strains, such as Shiga toxin-producing *E. coli* (STEC), can cause severe foodborne disease. It is transmitted to humans primarily through consumption of contaminated foods, such as raw or undercooked ground meat products, raw milk, and contaminated raw vegetables and sprouts. Symptoms of the diseases caused by STEC include abdominal cramps and diarrhea that may in some cases progress to bloody diarrhea (hemorrhagic colitis). Fever and vomiting may also occur. The incubation period can range from 3 to 8 days, with a median of 3 to 4 days. Most patients recover within 10 days, but in a small proportion of patients (particularly young children and the elderly), the infection may lead to a life-threatening disease, such as hemolytic uremic syndrome (HUS). HUS is characterized by acute renal failure, hemolytic anemia and thrombocytopenia (low blood platelets). It is estimated that up to 10% of patients with STEC infection may develop HUS, with a case-fatality rate ranging from 3 to 5%.

Overall, HUS is the most common cause of acute renal failure in young children. It can cause neurological complications (such as seizure, stroke and coma) in 25% of HUS patients and chronic renal sequela, usually mild, in around 50% of survivors [78].

S. epidermidis is a Gram-positive bacterium in the family of the Staphylococci. It is a colonizer of the skin and mucous membranes of humans and other mammals. It is the most frequently isolated species from human epithelia, and it colonizes predominantly the axillae, head and nares [77]. Even if it is a bacterium that commonly lives on the human skins, hospital-acquired infections associated at *S. epidermidis* are increasingly, such as due to intravascular catheters and other foreign bodies insertion because *S. epidermidis* cells can form biofilms on these materials. Staphylococcal bacteremia is an important cause of morbidity (especially prolongation of hospitalization) and mortality in debilitated patients [79].



4 Plasma surface treatments

Surface modification of materials by plasma treatments and depositions have gained popularity in the last decades [80–83], since can be applied for different purpose, such as controlled release of active agents in drugs [84–86] or creation of hierarchical surface structures [87–89] that can be used for sensors [90–92], photocatalysts [93], bio-electronic interface devices [94], water repelling and self-cleaning materials [95], various nanoelectronics devices [96,97], space technology applications such as photon-active diamond films for space propulsion [98, 99] and nanostructured emitters for plasma propulsion systems [100,101] that are critical for miniaturized space assets [102,103].

The fabrication of the complex hierarchical structures relies on the use of sophisticated processes and complex environments such as, for exemplum, low-temperature plasma [89] and the highly-reactive oxygen plasma [104]. If the fluxes of highly energetic ions and electrons are well-balanced, it is possible to introduce desired physical and/or chemical changes without affecting material bulk [105–109]. These changes can be induced across several length scales, opening up new applications in energy and environmental devices [52,110,111], in antibacterial coatings [41,42], in textiles [112,113], and enabling the creation of nanostructured surfaces that mimic the ones produced by nature for its needs [114,115].

Creation of these surfaces remains a technological challenge, also using plasmas where competitive processes can control the different parameters challenging. At larger length scales the study of the role between macro and micro-metric properties are still important issues both in applied and in basic sciences [116].

Plasma-enabled synthesis, assembly and modification of materials at the nanoscale, due to its strong potential and versatility, is one of the fastest growing fields in basic material science research, in technology and engineering applications. The resulting nanostructured surfaces can be designed to have new characteristic properties not achievable with more traditional methods, such as extreme hydrophilic properties [54]. These nanostructured surface,

despite having very small dimensions, introduce desirable variations in macroscopic functional properties without altering the intrinsic bulk properties of the material. These nanostructures often take form of nanorods, nanowires, and nanotubes, with chemical vapor deposition (CVD) and its more advanced variations, e.g., Plasma Assisted Supersonic Jet Deposition (PA-SJD), frequently used to produce such thin nanostructured films [44, 117–119].

The aim of the work done in this thesis is to study the micro and macroscopic properties of different polymers, such as polypropylene and polytetrafluoroethylene treated for different time in a low pressure Capacitive Coupled Plasma RF system filled with gases, such as oxygen, hydrogen, carbon dioxide and argon. This is a preliminary study, and so we do not tested the antifouling and antibacterial application, yet.

Polypropylene (PP) [120] is a thermoplastic polymer used in different ranges of applications. It is produced via chain-growth polymerization from the monomer propylene. The chemical formula is $(C_3H_6)_n$ (Figure 4.1). It is partially crystalline and non-polar, it has a high chemical resistance and in general it is hydrophilic. Furthermore, it is commonly used in different applications ranging from packaging for consumer products, to plastic parts used in automotive industry, in special devices such as living hinges, and also in textiles.

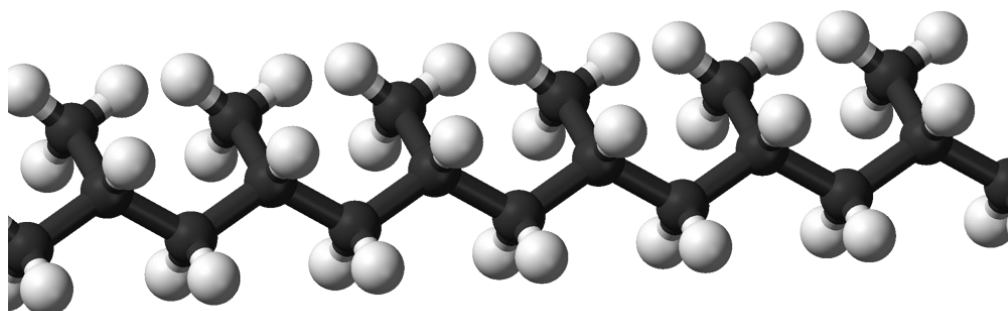


Figure 4.1: Polypropylene structure. Black bullets are the carbon atoms; white bullets are the hydrogen atoms. From Benjah-bmm27 (contributed discussion) - Own work, Public domain, <https://commons.wikimedia.org/w/index.php?curid=1806716>.

Polytetrafluoroethylene (PTFE) [121] is a synthetic fluoropolymer of tetrafluoroethylene. It is also known with its commercial name that is Teflon. PTFE is

a fluorocarbon solid, as it is a high-molecular-weight polymer consisting wholly of carbon and fluorine. The chemical formula is $(C_2F_4)_n$ and its structure is shown in Figure 4.2. It is a hydrophobic material. It is used, for example, as a non-stick coating for pans and other cookware, as a graft material in surgery and as a coating on catheters.

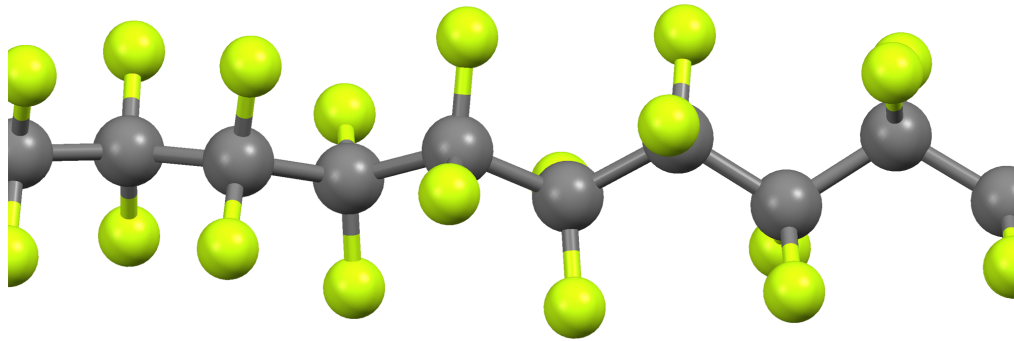


Figure 4.2: Polytetrafluoroethylene structure. Gray bullets are the carbon atoms; yellow bullets are the fluorine atoms. By Ben Mills - Own work, Public Domain, <https://commons.wikimedia.org/w/index.php?curid=17821816>.

Part II

Volatile Organic Compounds
depletion by atmospheric cold
plasma and catalyst

5 Equipment setups

In this Chapter we are going to present all the equipment setup and the instrumentation we used in the experiment for Volatile Organic Compounds depletion. Additional data can be found in our papers in Refs. [20,23,24,122].

5.1 Sources

For the VOC depletion experiments we used different configurations of SDBD plasmas and light sources coupled with catalytic surfaces, in order to compare the different effects and efficiency.

5.1.1 SDBD plasmas

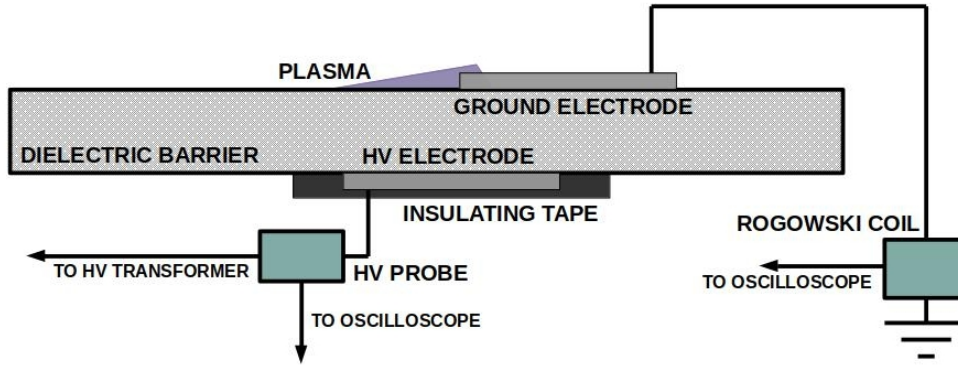
All the plasma we present here are atmospheric pressure Surface Dielectric Barrier Discharge plasmas, but they are realized with different materials and assume different configurations in the different experiments we developed.

Teflon and vetronite SDBD This configuration has been suggested by the simpler version of SDBD used in plasma aerodynamics applications, called plasma actuators [123]. It consists of two conductive electrodes attached to opposite sides of a flat dielectric panel, in the asymmetric arrangement in Figure 5.1a.

The lower electrode is completely coated with an insulating material, while the upper electrode remains completely exposed to air. In this way, the plasma generation region is confined above the dielectric plate. It is a DC voltage supply and a signal generator that feeds the primary windings of an HV transformer whose secondary windings are connected to the electrode. As a dielectric barrier we used a sheet of Teflon or a sheet of vetronite.

The Teflon SDBD (Figure 5.1b) consists of tin clad copper adhesive tapes ($60\ \mu\text{m}$ thick, 4 cm wide and 12 cm long) attached to a Teflon sheet (3 mm thick) and laterally shifted from each other by about 0.5 cm.

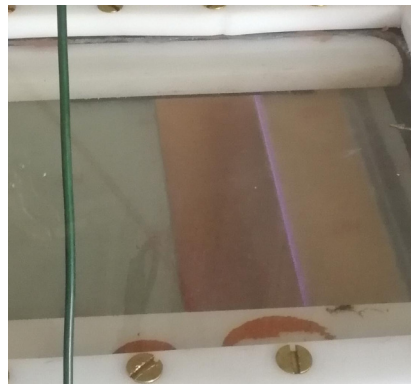
The vetronite SDBD (Figure 5.1c) consists of deposited copper ($35\ \mu\text{m}$ thick, 4 cm wide and 12 cm long) attached to a vetronite sheet (1.5 mm thick) and laterally shifted from each other by about 0.5 cm.



(a)



(b)



(c)

Figure 5.1: Photo of the plasma produced by (a) Teflon SDBD and (b) vetronite SDBD. (c) Plasma device scheme.

In these configurations, the exposed electrode is grounded, while the covered one is powered by a high voltage power supply line. The plasma is lit up by an HV power supply working in a power range of 7-50 W and a frequency in the order of tens of kHz [20, 124–127].

Alumina SDBD This SDBDs consist of two conducting electrodes attached at the opposite sides of a flat dielectric panel, sketched in Figure 5.2a.

The plasma configurations for the exposed electrode:

- bidirectional fingers electrode (Figure 5.2b);
- monodirectional fingers electrode (Figure 5.2c);

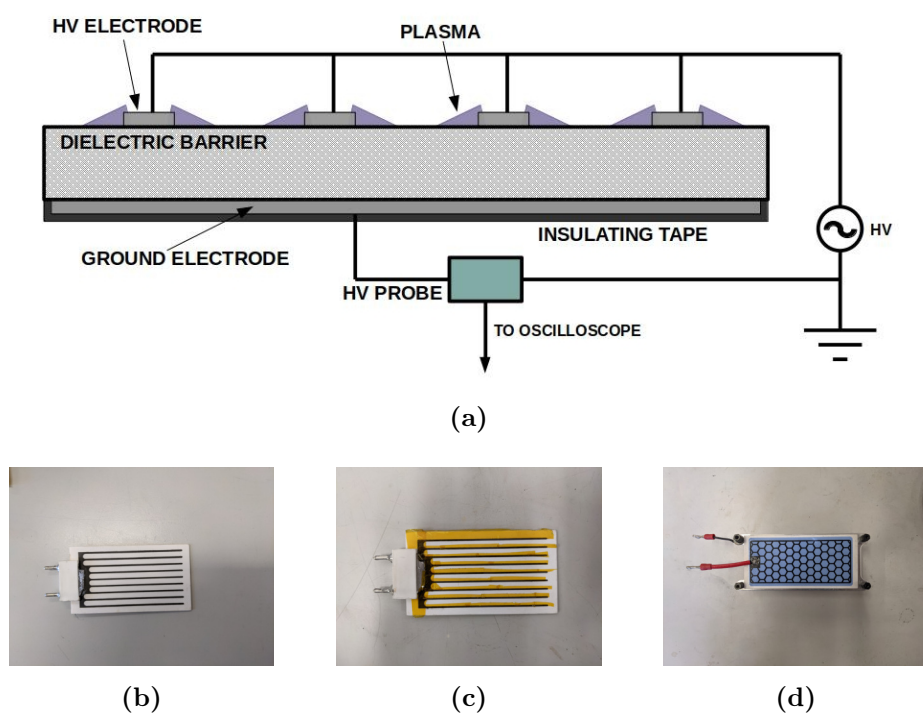


Figure 5.2: (a) Plasma device scheme. Plasma device configuration (b) bidirectional fingers electrode, (c) monodirectional fingers electrode, (d) honeycomb electrode.

- honeycomb electrode (Figure 5.2d).

The buried electrode is a plain plate. The bidirectional and monodirectional SDBD are constituted by $9 \times 5 \text{ cm}^2$ alumina dielectric surface, 1 mm thickness, with 9 metal fingers 7 cm long, 1 mm large and 4 mm apart. The monodirectional configuration is made burying one side of the finger with kapton adhesive tape. The honeycomb SDBD is made by $9.5 \times 4 \text{ cm}^2$ alumina dielectric surface, 1 mm thickness, 70 hexagons with external radius of about 8 mm. The plasma is lit up by an HV power supply working in a power range of 8-120 W and a frequency between 4 and 12 kHz [20, 124].

5.1.2 Lamps

We used different light sources for the catalysis illumination in order to find the best frequency range for its activation. In general, UV lamps are used for the VOC and bacteria abatements. The lamps we used are (these are also the name we are going to use for the identification of the different lamps):

- UV-C lamp (UV Lawtronics centered in 253.7 nm);

- UV-A lamp (UV Philips Lighting centered in 370 nm);
- visible bulb (GLS Osram at 4000 K LED lamp).

All the lamps are powered by 4 W. The UV-A and UV-C lamps shape is a cylinder with a length of about 11 cm (Figure 5.3a), while the visible is the classical spherical LED bulb (Figure 5.3b).



Figure 5.3: (a) UV-A and UV-C lamps shape. (b) Visible bulb shape.

5.2 Experimental configurations

In this Section we present the setup we assembled for our experiments.

5.2.1 Treatment box

In our experiments we mainly used two different treatment box that can be coupled with a contamination system (described in Subsection 5.2.3).

Parallelepiped chamber reactor This reactor (Figure 5.4a) is made by a parallelepiped of size $(1.8 \times 20 \times 18) \text{ cm}^3$, made by Delrin and a cover in Plexiglas, inside which VOC depletion takes place. The volume of the free space used for the air treatment is about 0.5 l. It has two open-close valves to perform static experiments. The SDBD that can be placed inside are the Teflon or the vetronite configuration.

Cross chamber reactor This treatment box (Figure 5.4b) is made using a vacuum cross chamber (20 cm x 20 cm length and 10 cm diameter) with four circular openings that can be closed by glass windows or vacuum enclosure. The volume inside is about 1.5 l. This reactor is used for lamps and plasma optical characterization, for the O_3 and NO_2 detection and for the VOC depletion, making some changes from a configuration and another.

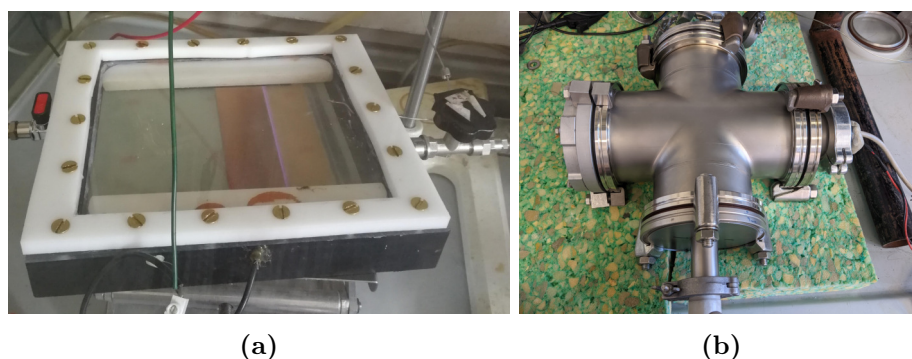


Figure 5.4: Image of (a) the parallelepiped and (b) the cross chamber reactor.

During the intensity light measurements, we placed the radiometric probe (or alternatively during the spectra analysis, the optical fiber) in the middle of a semi-closed box aligned with the light source, as shown in Figure 5.5. To obscure the ambient light, we covered the device with a blanket. The radiometric probes were placed exactly where we will place the photo-catalytic support (see Chapter 6.5). We varied the distance between the lamp and the probe about between 8 and 80 cm.

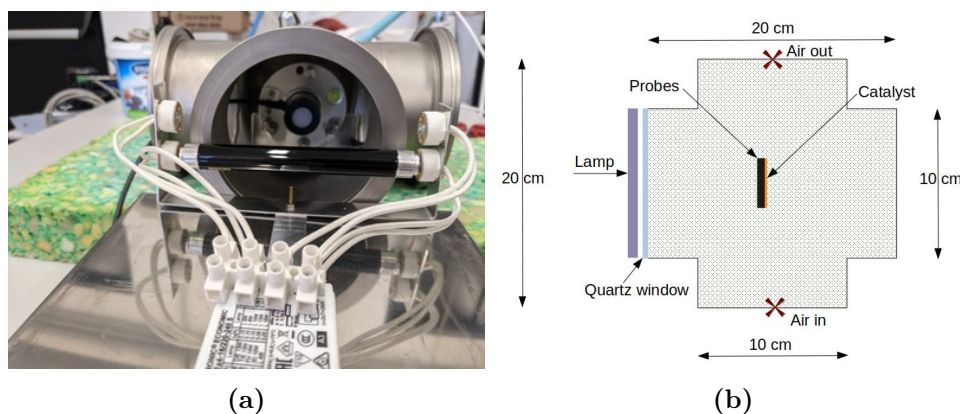


Figure 5.5: Lamps equipment setup (a) photo and (b) scheme.

For the characterization of the plasma emission, we placed the plasma source inside the chamber and the probe in front of it (Figure 5.6) at a proper distance (about 3.5 cm) to avoid electromagnetic interference between the plasma and the probe. As plasma sources, we used the bidirectional alumina SDBD.

For the detection of O_3 and NO_2 , we placed together two cross chambers (Figure 5.7a) in order to have a larger volume, that is about 3l. We placed

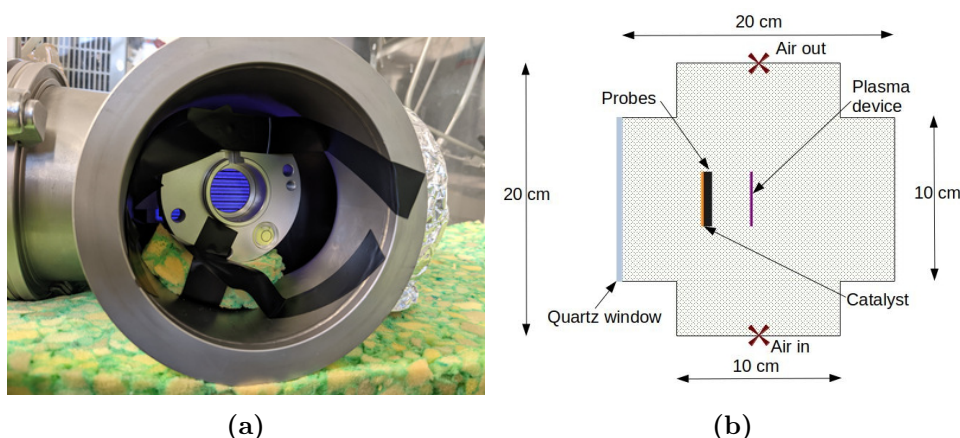


Figure 5.6: Plasma equipment setup (a) photo and (b) scheme.

the SDBD device (bidirectional alumina) inside the box. Two opposite sides are closed by quartz windows and at the other ends by open-close valves or a vacuum closing, as shown in Figure 5.7. In front of one quartz window we placed the lamps, while at the opposite side the radiometric detectors. The lamps and radiometric probes details are in [122]. As we are also interested in measuring the temperature, we placed a temperature probe in contact with the ground side of the SDBD (contact temperature), and a second inside the chamber (gas temperature). Finally, to ensure uniformity of the gas, a vent has been placed inside the chamber. In each experiment, we filled the box with pure air then we close the box before lighting the plasma.

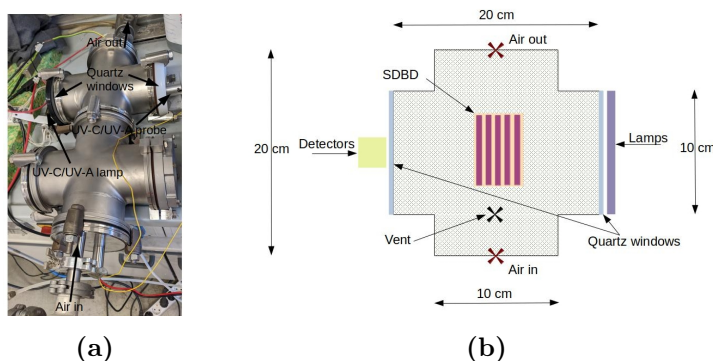


Figure 5.7: (a) Photo and (b) scheme of the equipment setup for the O_3 and NO_2 detection.

For VOC depletion experiments we closed the two opposite enclosures with open-close valves connected with the contamination system, one with a vacuum

enclosure and the last one with a quartz glass windows. We performed both depletion with plasma and photo-catalytic devices. For plasma depletion, we placed inside the box one or two of the alumina SDBD. For the photo-catalytic experiments (Figure 5.8), the catalytic support is placed in the chamber and the lamps are placed facing towards the catalytic support inside the chamber or outside the chamber in front of a quartz window. In the box we also placed a vent to recirculate the air.

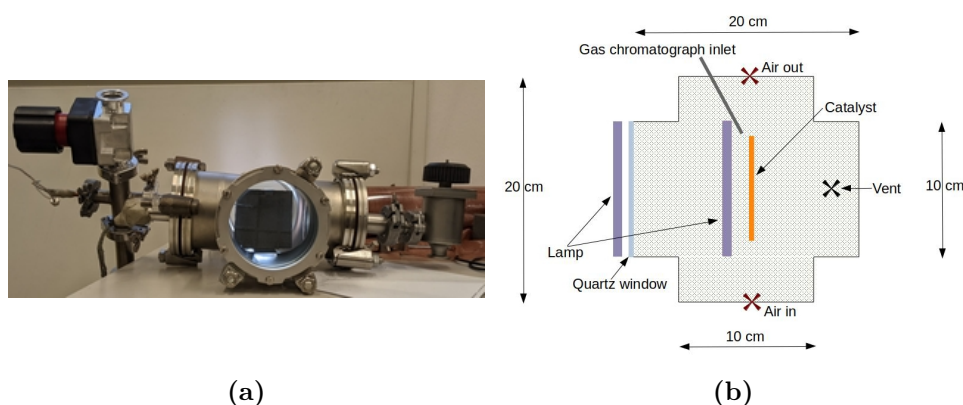


Figure 5.8: (a) Photo and (b) scheme of the reactor setup for VOC depletion by photo-catalytic system.

5.2.2 Photocatalysts

As a catalyst we used a different percentage of TiO_2 and WO_3 supported by CaO , deposited on plane rectangular tile surfaces. The ratio between CaO and the catalyst is about 5 to 2 while the deposited amount of product and the catalyst composition is

- **A:** 34.5 mg/cm² deposited over 7.6x7.3 cm² tile constituted by 100% TiO_2 catalyst;
- **B:** 40.9 mg/cm² deposited over 7.7x7.5 cm² tile constituted by 50% TiO_2 + 50% WO_3 catalysts;
- **C:** 38.2 mg/cm² deposited over 7.4x7.3 cm² tile constituted by 100% WO_3 catalyst.

In the description of the results we are going to identify the catalysts according to that classification.

5.2.3 VOC injection system

To perform the VOC depletion we had to contaminate the treatment box with a known amount of the desired VOC. We used both liquid and gas VOC, so we used to different systems for the contamination.

Liquid injection system The liquid VOC injection setup is shown in Figure 5.9. The black bold lines represent the tube connections through the whole system and the green arrows indicate the direction of the flow. In the diagram, Pure air represents a gas cylinder from Sapio S.R.L. containing 79 % of N_2 and 21 % of O_2 , meaning that the concentrations of CO_2 , CO, hydrocarbons, water and other pollutants are negligible. The red crosses are the symbol the open-close valves. The liquid VOC is placed in a bubbler bottle and let it circulate through the flow meter by the action of the air pressure. We used two gas flow meters and one liquid flow meter, all produced by Bronkhorst factory. The controlled evaporator and mixer (CEM) let the liquid, coming from the liquid flow meter, to evaporate, and mixes it with a line of pure air, coming from the gas flow meter 1, making the first dilution of the VOC. A second dilution is done after the CEM, by adding the pure air coming from the gas flow meter 2. We operated with two different dilution due to the working range of the flow meters. This whole system allows the control of the chamber VOC concentration before the experiments.

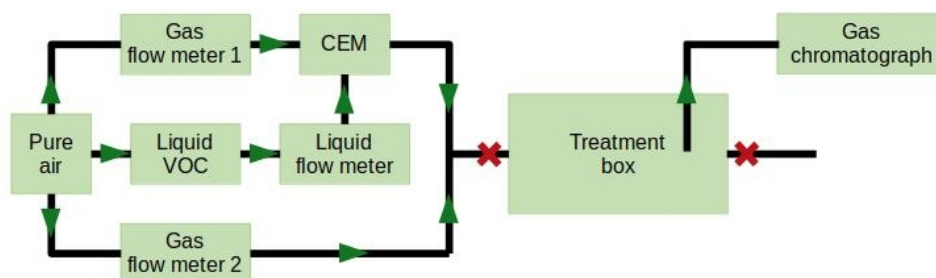


Figure 5.9: Liquid VOC injection setup.

Gas injection system The gas VOC injection setup is shown in Figure 5.10. The black bold lines represent the tube connections through the entire system and the green arrows indicates the direction of the flow. Pure air represents a gas cylinder from Sapio S.R.L. containing 79 % of N_2 and 21 % of O_2 , meaning that the concentrations of CO_2 , CO, hydrocarbons, water and other pollutants

are negligible. The red crosses are the symbol of open-close valves. The VOC is in a cylinder and its flow is regulated by the flow meter 1, while the pure air cylinder flow is regulated by the flow meter 2. As a flow meter we used gas and liquid flow meter produced by Bronkhorst factory.

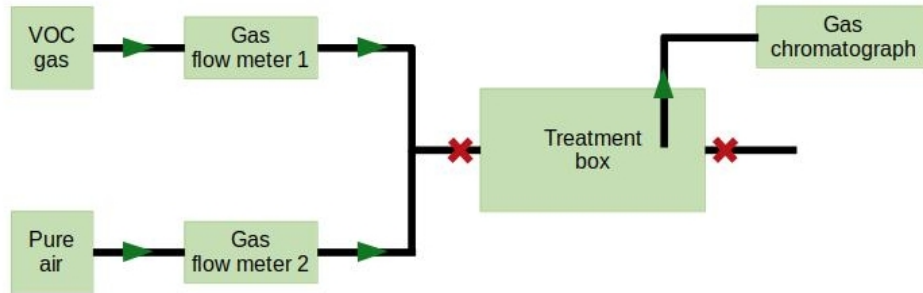


Figure 5.10: Gas VOC injection setup.

5.3 Diagnostics

We used different diagnostics for the sources characterization and for the VOC detection.

Rogowski coil Rogowski coil (Figure 5.11) is a probe that can be used to measure the instantaneous value of the current flowing between the electrodes [126,128]. It consists of a conductor winding around a toroidal support. To use a Rogowski coil as a probe, the current-carrying cable must pass through the toroid. Then the current flowing in the cable generates a voltage change at the output of the coil proportional to the speed of the current change, dI/dt . This voltage signal should be passed through an integration circuit, which could simply be a resistor, to measure $I(t)$. Using a small resistor for the integration system, the probe operates in the so-called self-integration mode in a wide range of frequencies [126].

We used NiZn ferrite N30 with $\mu_i \sim 4300$, with 50Ω integration resistance and 3.5 windings, and a 50 cm long RG-59 BNC coaxial cable with a 50Ω resistance, which have been calibrated with our Rogowski coil. The data was digitized by an Agilent Infinium MSO8104A oscilloscope with a bandwidth of 1 GHz and a maximum acquisition speed of 4 GSamples/s, which was considered suitable for the applications we investigated.



Figure 5.11: Photo of our Rogowski coil.

The sampling of the electric current signal by the Rogowski coil produces two main components: the microdischarges due to the plasma state and the displacement current within the insulated electrode as a result of the HV applied voltage. For a time dependent applied voltage, a displacement current (mainly determined by the capacitance behavior of the electrode system) is always added to the actual discharge current flow. In the case of an oscillating voltage supply, the applied bias of the displacement current has a sinusoidal trend.

The electric field ignites the plasma when it is reached a voltage threshold. This is generally observable as a pulsed current signal, consisting of several fast spikes (bursts), that overlaps the displacement current one, assuming two well separated half cycle patterns within the HV cycle. We are only interested in the plasma contribution, so we have chosen the self-integrating range of the probe, that it suppresses the low frequency capacitive component by itself.

A detailed calibration of this Rogowski coil is in [20].

A typical one-cycle signal acquisition when plasma is light on is plotted in Figure 5.12a, where the black line (left axis) is the applied voltage and the red line (right axis) is the current measured by the Rogowski coil.

When the applied voltage is greater than zero ($V > 0$), the electrons go from the exposed electrode to the dielectric, and the current is defined as negative. The discharges that occur in this case are denoted as a forward stroke (FS). The discharges that occur in the opposite condition ($V < 0$) are denoted as a backward stroke (BS), and the associated current is defined as positive. This is why that if a spike is positive (negative) in a forward (backward) stroke, it is classified as noise. We also consider as noise a peak that both, develops within 25 ns after a burst and its height is lower than 75% of the previous

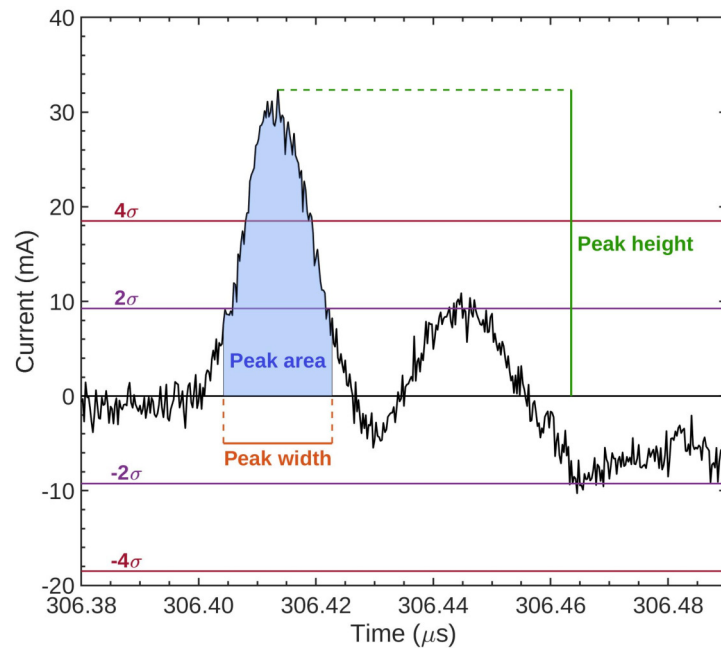
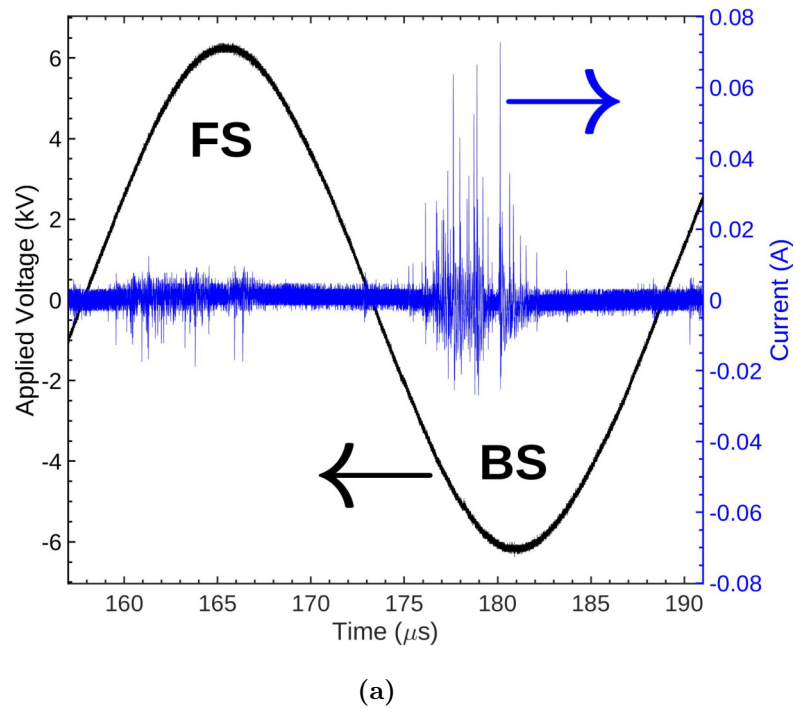


Figure 5.12: (a) Example of a temporal acquisition (FS when $V > 0$, and BS when $V < 0$). The left axis refers to the applied voltage (black line), and the right axis to the current measured by the Rogowski coil (blue line). (b) Definition of the burst (peak) properties: Charge (peak area), maximum current (peak height) and temporal duration (peak width).

burst. These spurious signals are due to the finite system bandwidth.

We performed a fit of the HV signal with a sine function to determine its amplitude, frequency and argument at each point. From the current signal we can notice the presence of a constant baseline and a series of spikes that occur at specific HV phases. These spikes are the current signal caused by the plasma microdischarges. A detail of a microdischarge (called burst) is shown in Figure 5.12b. We characterize a burst by its charge (area of the peak), maximum current intensity (height), time duration (width) and HV phase position.

Since we are interested only in the plasma current, carried by the bursts, we have to determine a background threshold above which a peak can be defined a burst. We choose as background threshold 2σ , that is twice the standard deviation over the whole Rogowski coil data. We identify a peak as a burst if its height overcomes the value of 4σ . The peak duration is given by the peak width at 2σ .

Optical emission spectroscopy device The used spectrometer is Ocean Optic PS2000. The spectrometer is equipped with a diffraction grating dividing the incoming radiation and disperses it to the CCD (Charged Couple Device) pixel matrix. The CCS is a device capable of accumulating electrical charge proportionally to the number of photons from which it is struck. An analog-to-digital converter finally translates the electric charge into discrete values, the counts, which are then associated with each pixel. The spectrometer is designed to acquire a range of wavelengths between about 180 nm and 870 nm with a resolution of about 0.3 nm, it divides the spectrum into 2047 bins and has a maximum number of counts equal to 4096 [125, 129]. The fiber slit is 10 μm . Data are collected by the software SpectraWin. We do not calibrate the spectrometer since we were just interested in knowing the emitted species and not their amount.

Radiometric device As a radiometric device, we used the HD 31 datalogger from DeltaOhm coupled with three radiometric probes (Figure 5.13), that collect the irradiated power per surface unit ($\mu\text{W}/\text{cm}^2$) in specified spectra range. The probes are LP47-RAD for visible spectra (400-1050 nm range), LP471-P-A for UV-A spectra (315-400 nm) and LP471-UVC for UV-C spectra (220-280 nm).

Each probe was employed to collect the intensity per surface unit in the specific spectrum range of the light sources.



Figure 5.13: Photo of the HD 31 datalogger and the radiometric probes.

Absorption spectroscopy Absorption spectroscopy is a spectroscopic technique that measure the intensity of a desired light that passes through a liquid or a gas [130]. Every element has a different absorption rate for different wavelengths. Thanks to these properties, modeled with the Lambert-Beer equation [131], it is possible to estimate the density of some species in the analyzed gases.

We used absorption spectroscopy for the evaluation of the ozone (O_3) and the nitrogen dioxide (NO_2) densities in a closed box when the plasma is on. The absorption coefficients of O_3 and NO_x are shown in Figure 5.14, where we can identify the better region for the species detection: O_3 in yellow [132], NO in blue [133], NO_2 in green [134], NO_3 in red [135]. From that absorption coefficients and our experimental setup we can see that there is no region where it is possible to record the NO concentration, since there is always a predominance of O_3 . Also, NO_3 is difficult to evaluate since between 550 and 600 nm there are two order of magnitude between NO_2 and NO_3 absorption coefficients, but we expect that the concentration of NO_2 produced by the plasma would be two order greater than NO_2 . For these reasons, we can only safely evaluate the concentrations on O_3 and NO_2 .

We used the UV-C lamp for the O_3 detection coupled with the UV-C radiometric probe, while the UV-A lamp and respective probe for the NO_2 . Since we used a radiometer, that gives us an integrated value of the light intensity

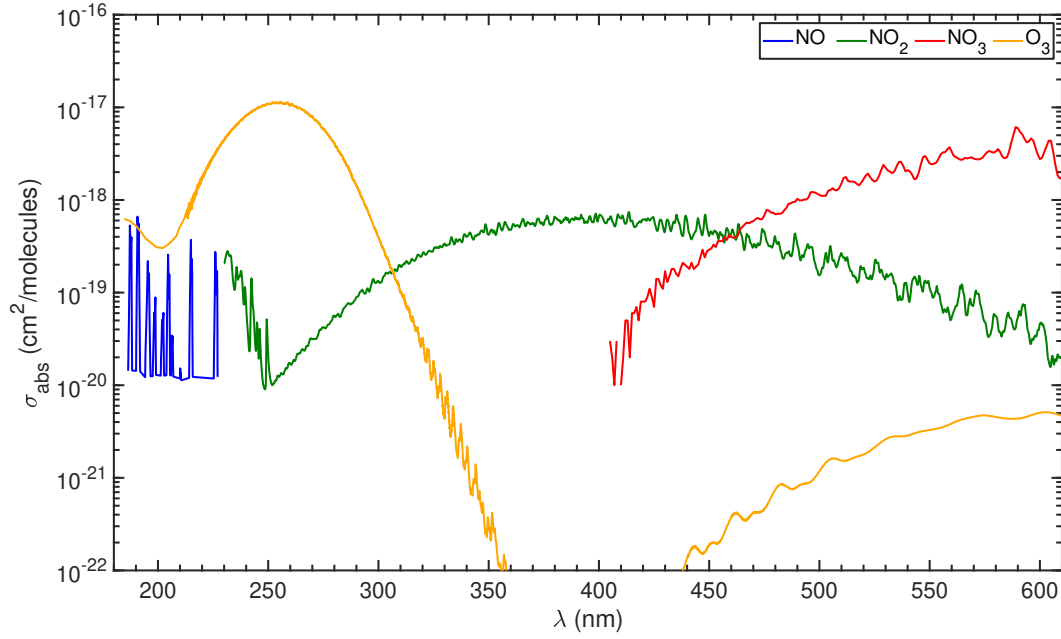


Figure 5.14: Absorption coefficients of O_3 and NO_x [132–135].

within a certain wavelength range, therefore, the absorption coefficients σ_{abs} had to be averaged taking into account the sensitivity of the sensor and the emission shape of the lamp, obtaining $\sigma_{\text{abs},O_3} = 1.127 \times 10^{-17} \text{ cm}^2/\text{molecules}$ for O_3 and $\sigma_{\text{abs},NO_2} = 5.66 \times 10^{-19} \text{ cm}^2/\text{molecules}$.

Using the Lambert-Beer, we can derive the number density n of O_3 and NO_2 as follows

$$n(t) = -\frac{\log\left(\frac{I(t)}{I_{\text{no plasma}}}\right)}{L\sigma_{\text{abs}}} \quad (5.1)$$

where n is the number density expressed in molecules/cm³, $I(t)$ is the intensity at time t , $I_{\text{no plasma}}$ is the intensity before lighting the plasma, L is the distance between the lamps and the probe, and σ_{abs} is the absorption coefficient.

Temperature For temperature recording we used RS PRO 1316 Dual Data-logger Thermometer (Figure 5.15) coupled with two type K (chromel⁽¹⁾–alumel⁽²⁾) thermocouples. The sensitivity is of 0.1°C, and it samples every second.

One thermocouple is placed in contact with the ground side of the SDBD measuring the contact temperature and the other one in the volume measuring

(1) alloy made of approximately 90% nickel and 10% chromium.

(2) alloy consisting of approximately 95% nickel, 2% aluminium, 2% manganese, and 1% silicon.

the gas temperature.



Figure 5.15: Photo of the RS PRO 1316 Dual Datalogger Thermometer.

Gas chromatography Gas chromatography is a term used to describe the group of analytical separation techniques used to analyze volatile substances in the gas phase. In gas chromatography, the components of a sample are dissolved in a solvent and vaporized in order to separate the analytes by distributing the sample between two phases, a stationary phase and a mobile one. The mobile phase is a chemically inert gas that serves to carry the molecules of the analyte through the heated column. The stationary phase is either a solid adsorbant or a liquid on an inert support. Gas chromatography is one of the sole forms of chromatography that does not utilize the mobile phase for interacting with the analyte.

We used the micro gas chromatograph Agilent 3000 (Figure 5.16) coupled with an analysis poraPLOT U column able to detect organic compounds in a range of different specific conditions.

The gas chromatograph (GC) output reports a signal composed of peaks of intensity proportional to the concentration of specific species. The area of each peak is strongly dependent on the setting parameters during the sampling conditions. For a precise evaluation of concentration, it is necessary to perform first a specific calibration. Usually, the calibration is carried out using a cylinder containing a known concentration of the desired gas (one point calibration).

As VOC, we used pentane and propane. Since pentane is liquid, we cannot use a calibrating cylinder, and we adopted a different calibration way (multi-point calibration), that we also used for the propane calibration.



Figure 5.16: Photo of the micro gas chromatograph Agilent 3000.

To let pentane flow in the treatment chamber we used the liquid VOC contamination system (Figure 5.9). The pentane concentration relative to the total input flow, denoted as c , typically expressed in ppm, is given by

$$c = \frac{\Phi_{C_5H_{12}}}{\Phi_1 + \Phi_2 + \Phi_{C_5H_{12}}}, \quad (5.2)$$

where Φ_1 and Φ_2 are the air flows and $\Phi_{C_5H_{12}}$ is the pentane flow, given in liters/sec. The values of air flows are measured by the gas flow meters, and the pentane flow by the liquid flow meter (Figure 5.9). These three values determine the initial conditions of the experiment before plasma treatment. The relative pentane flow, Eq. (5.2), can be used to determine the actual pentane concentration (in ppm), present in the air-pentane mix system, with the help of a GC, connected to the reactor chamber.

A typical pentane chromatogram trace is shown in Figure 5.17a, as a function of retention time. We are interested in the area, denoted as A_{GC} , between the red continuous line (pentane trace) and the blue dashed line (baseline) plotted in Figure 5.17a.

A set of ten measurements of the A_{GC} versus the corresponding relative pentane flow c is displayed in blue in Figure 5.17b. We obtained the interpolation (plotted in red)

$$A_{GC} = 0.72c - 3. \quad (5.3)$$

where A_{GC} is expressed in counts and c in ppm. Inverting the Eq. (5.3), knowing A_{GC} , we can estimate the pentane concentration even if it is not obtained from a known flow. For that reason, we are denoted this quantity as ρ_5 , that is

$$\rho_5(\text{ppm}) = \frac{A_{GC} + 3}{0.72}. \quad (5.4)$$

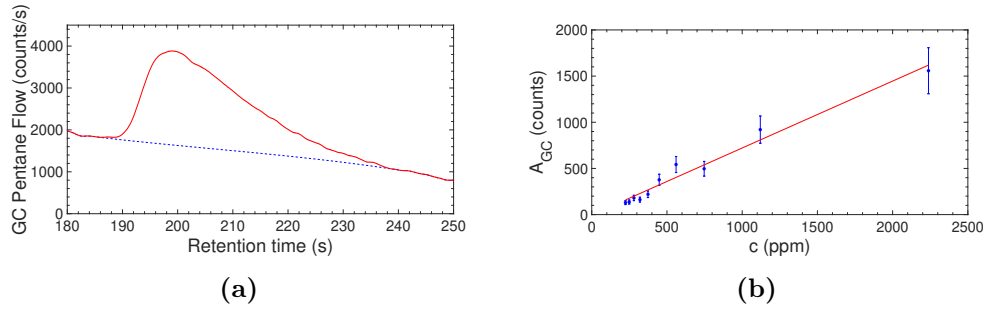


Figure 5.17: (a) Example of a pentane chromatogram peak: GC flow (counts/s) vs retention time (s), obtained from the gas mixture in the reactor chamber. (b) Calibration plot for determining pentane concentration (Eq. 5.2).

This relation is actually used also in the measurements to determine the incoming air and pentane flows in order to have the desired initial pentane concentration. The errors have been estimated as the standard deviation obtained from several preliminary measurements at for the same starting concentration (Figure 5.18a) and after the same treatment condition (Figure 5.18b). Thanks to these measurements, we estimated the error in pentane concentration to be in the order of 10% with respect to the value given in Eq. (5.4). We notice that we are not able to detect concentrations lower than about 15 ppm, due to not detectable pentane peak, so that is our instrumental limit.

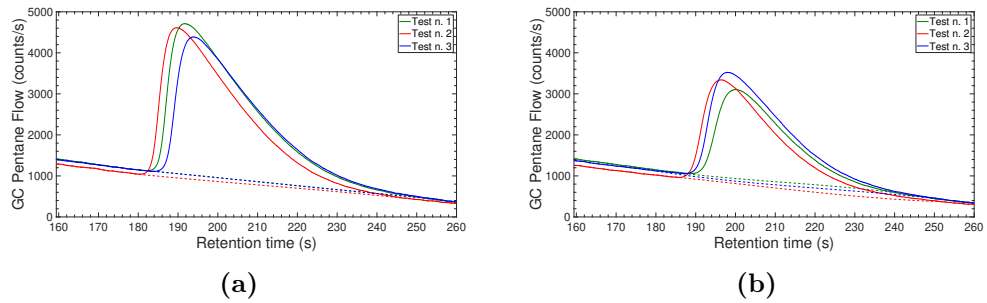


Figure 5.18: Repeated measurements for (a) starting concentration and (b) evaluation of concentration after the same treatment condition.

A similar procedure, considering Figure 5.10 for the contamination system, we adopted for the propane the calibration [25], obtaining

$$\rho_3 \text{ (ppm)} = 12.4(A_{GC} - 8.65). \quad (5.5)$$

We notice that we are not able to detect concentrations lower than about 5 ppm, due to not detectable propane peak, so that is our instrumental limit.

6 Results and analysis

In this Chapter we present the experimental results we obtained about the characterization of the sources and about the depletion of VOCs.

6.1 Electric characterization

In this Section we are going to present the electrical characterization we have done over different SDBD devices.

Current analysis For this analysis we used the Teflon SDBD. Starting from the data collected by the Rogowski coil and the HV probe (Section 5.3), we analyzed the properties the microdischarges produced by a plasma lit on at different voltages. We carried this kind of analysis in order to understand the distribution and the shape of the microdischarges produced by a SDBD. A complete analysis is reported in [20]. In particular, we looked at the current carried by the plasma microdischarges, that is the height of the peaks reported in Figure 5.12, and its statistical distribution. The burst current distributions, $P(I)$, display an exponential shape. For the backward stroke at 5.48 kV HV, the current distribution is shown as an example in Figure 6.1.

To describe the current distributions for BS, we assume an exponential shape for $P(I)$

$$P(I) = \frac{1}{I_0} \exp\left(-\frac{I}{I_0}\right). \quad (6.1)$$

where I_0 is a characteristic current. The values of the characteristic currents I_0 are reported in Figure 6.2a. A plateau above about 5.4 kV is observed for the characteristic current I_0 .

The mean values of the current, $\langle I \rangle$, are displayed in Figure 6.2b, where one can see that for BS (in red) the mean (absolute value) currents are much larger than for FS (in black). For example, at HV=5.5 kV, $\langle I \rangle \sim 35$ mA for BS, while $\langle I \rangle \sim (-)20$ mA for FS.

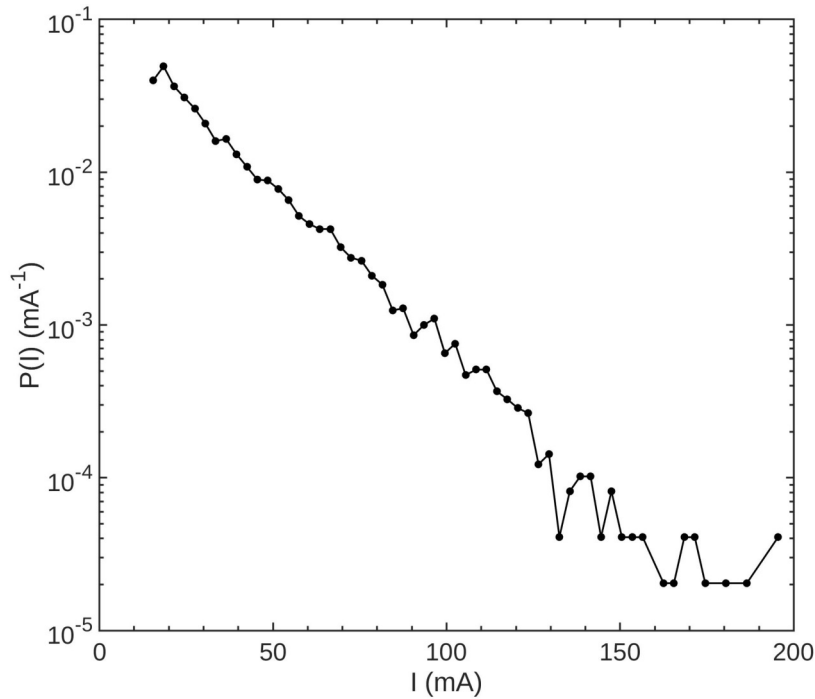


Figure 6.1: The BS current distribution, $P(I)$ vs I , for HV at 5.48 kV.

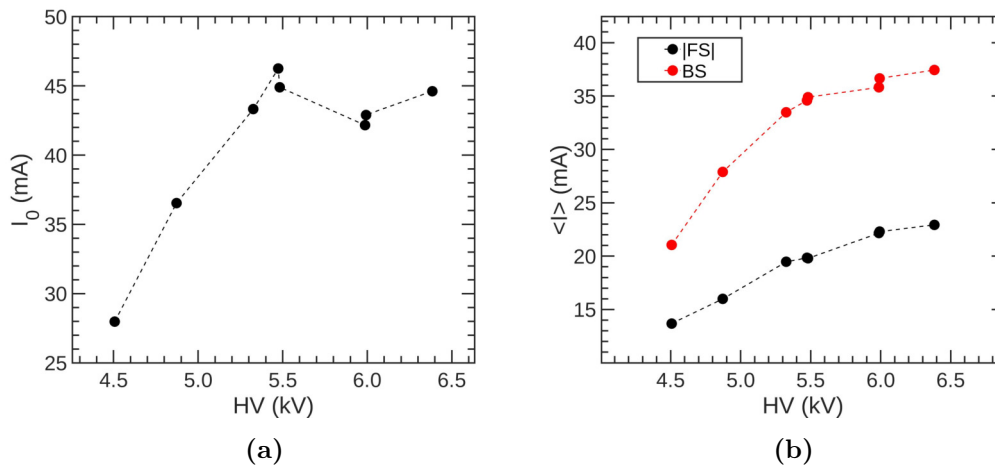


Figure 6.2: (a) I_0 vs HV. (b) Mean current $\langle I \rangle$.

Lissajous analysis Lissajous curves are widely used for the estimation of the power transferred to the plasma [127], and it is obtained by plotting the charge flowing into the circuit Q as a function of the voltage difference HV between the electrodes. The charge is measured through a capacitor in series

with the SDBD (capacitive probe). The area of the current-voltage plot is the power transferred to the plasma. We measured the Lissajous curves of one input power of the vetronite SDBD and for two different input power of the alumina bidirectional finger SDBD.

For the vetronite SDBD measurements we placed a 4.3 nF capacitor in series with the SDBD, and we collected three series of data at about 17 W of input power (Figure 6.3), considering a plasma in air. The area of the Lissajous curves, and so the power transferred at the plasma, is

$$W_{\text{pl}} = (9.6 \pm 0.3) \text{ W},$$

meaning that only the 56% of the power is responsible for the plasma ignition.

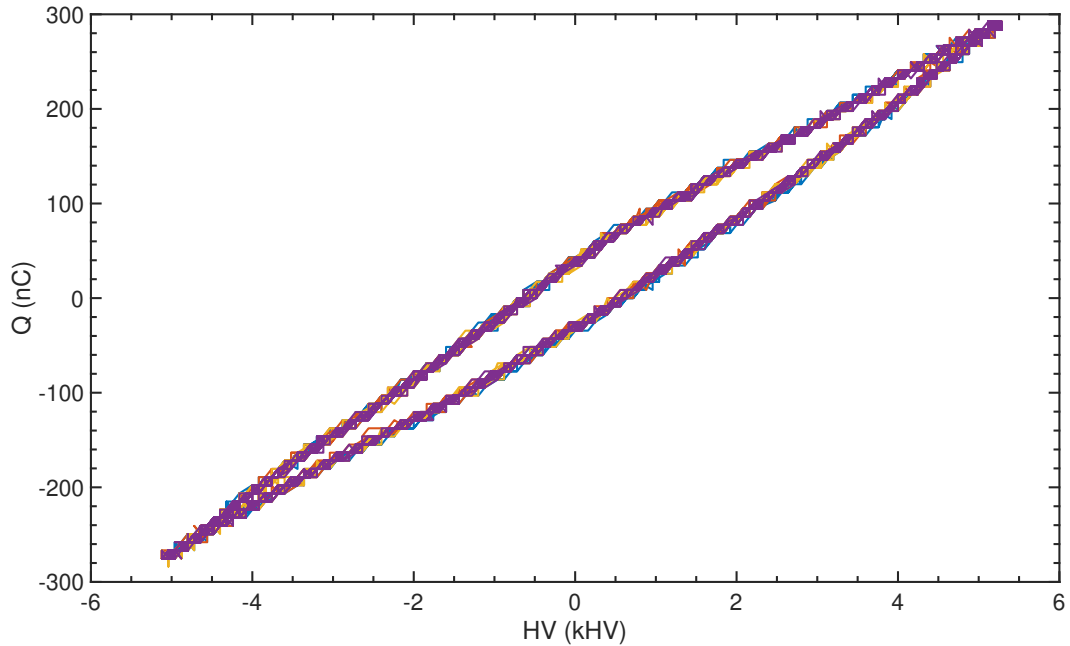


Figure 6.3: Lissajous curves for vetronite SDBD air plasma light on at 17 W input power.

We evaluated if there are differences in power transmission if we ignite plasma in a mixture of air and low amount of pentane and at different time of this ignition. In Figure 6.4 we can notice that there is no difference in the Lissajous curves, so we can assume that there is no difference in the ignition of only air plasma and mixture plasma.

We used 6.5 nF capacitor for the estimation of the transferred power to the plasma generated by the alumina bidirectional finger SDBD. The analyzed input power are 16 W and 35 W, obtaining that the transferred power are,

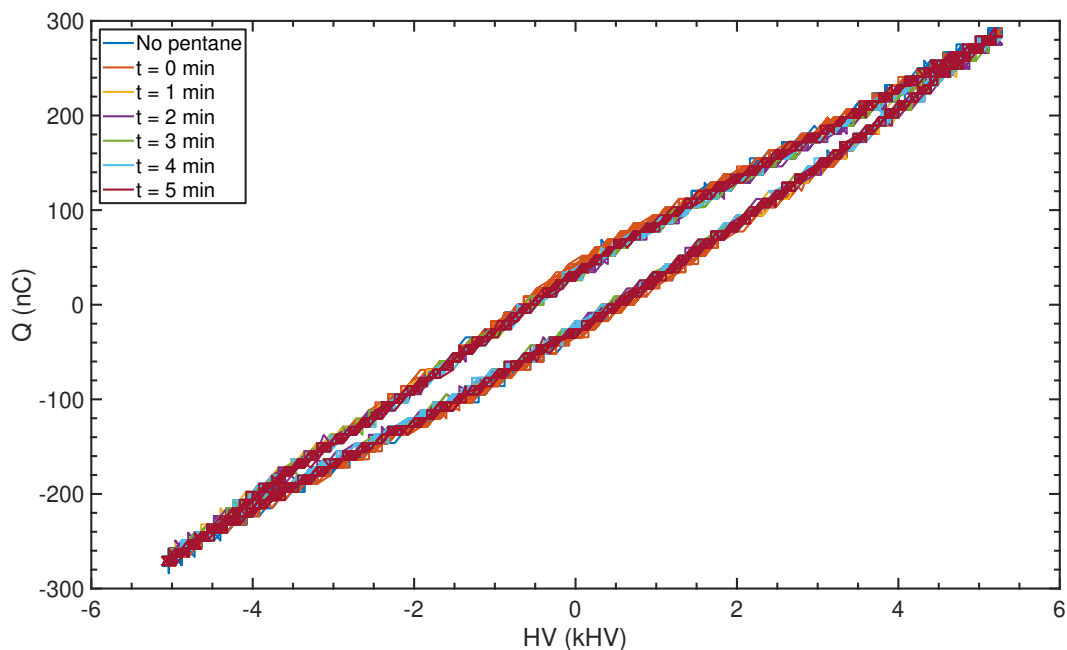


Figure 6.4: Lissajous curves for vetronite SDBD air+pentane plasma light on at 17W input power at different time after ignition.

respectively,

$$W_{p116} = (7.48 \pm 0.01) \text{ W and } W_{p135} = (20.1 \pm 0.2) \text{ W},$$

and so only the 50% and the 57% of the power is transferred to the plasma.

Thanks to this electrical analysis we verified that the SDBD plasma is made by a series of following microdischarges. With the Lissajous curves we figure out that there is not a variation of the transferred power due to the VOCs depletion but also that not all the input power is transferred to the plasma. For simplicity, in the following experiments we are going to classify the plasma with the input power, always remembering that the transferred power is about the (50-55)% respect to the input.

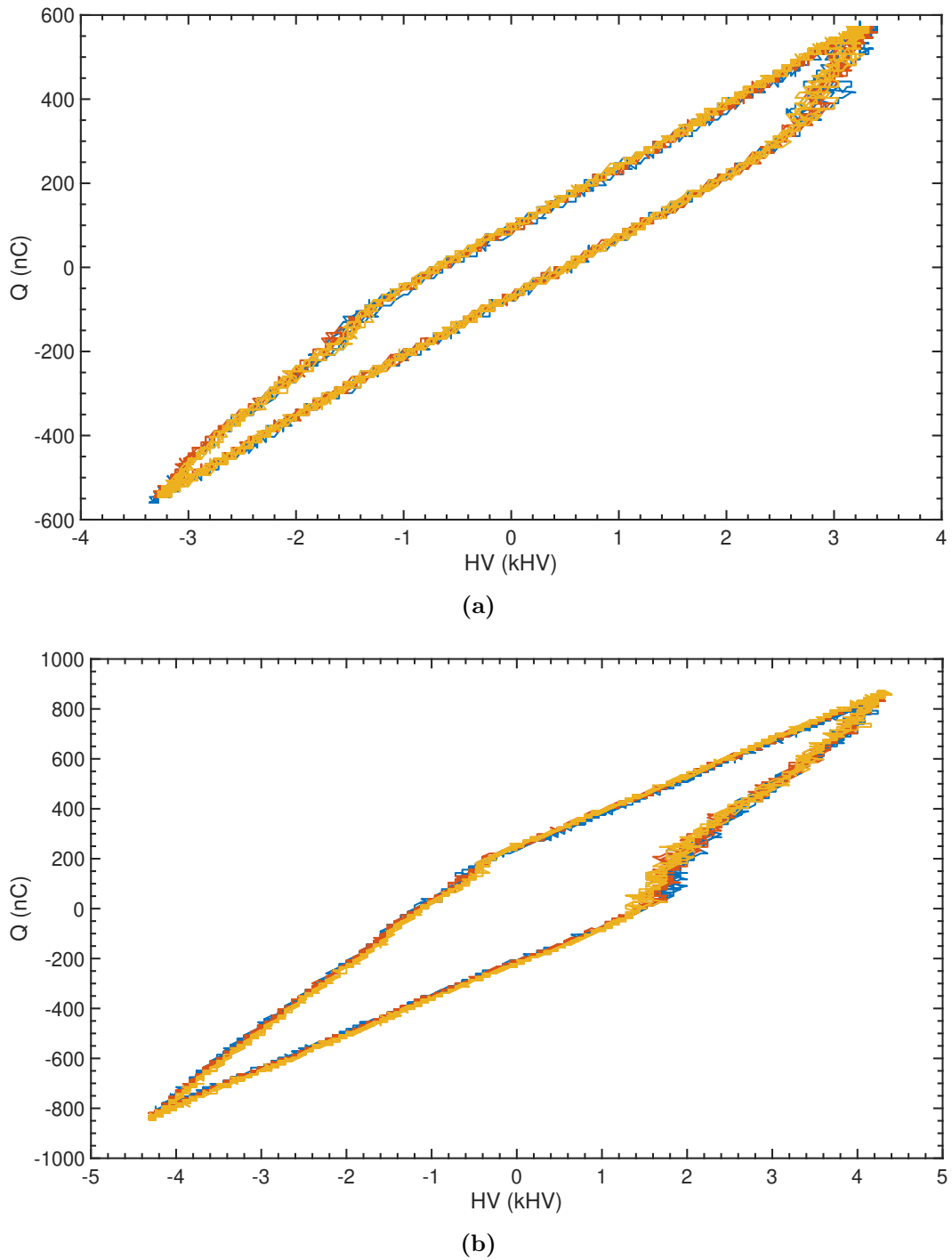


Figure 6.5: Lissajous curves for bidirectional finger alumina SDBD air plasma light on at (a) 16 W and (b) 35 W.

6.2 Lamps characterization

The Section we are going to present the characterization of three lamps that are used for our experiment and its comparison with the plasma. The completed results were published in [122].

The lamps were presented in Subsection 5.1.2 and for the plasma we used the bidirectional alumina SDBD (Subsection 5.1.1 *Alumina SDBD*). The experimental setup used for this analysis was presented in Section 5.2 *Cross chamber reactor*. For every light sources we measured the optical emission spectra and the radiometric intensity by means of the probe.

We used optical emission spectroscopy to characterize the light sources spectra. We show the emission spectra of the lamps in Figure 6.6a, while the plasma one in Figure 6.6b.

The UV-C lamp is characterized by the line spectrum of the low pressure Hg: the main peak is at 253.7 nm in the UV-C region, while there are other minor peaks in the visible, UV-A and IR regions. The UV-A lamp has only a peak at 370 nm produced by the low pressure Hg vapors while all the other lines are suppressed by the lamp glass. The visible bulb has a continuous spectrum in the visible range from about 450 nm to 700 nm, that is exactly in the visible range. The plasma emission is characterized by line spectrum, mainly in the UV-A region but also with a part in visible range, due to the principal, rotational and vibrational emission of N₂ species. The observed N₂ lines are at 315.93 nm, 337.13 nm, 357.69 nm, 380.49 nm and 405.94 nm.

For each light sources we collected the intensities at different distances between the source itself and the probe. We fitted the UV-A and UV-C data considering the emission source as a uniform limited cylinder ($L = 11$ cm), considering d in cm, E in μW , and the result of atan in rad, so its intensity is given by

$$E(d) = 2\frac{A}{d} \left[\text{atan} \left(\frac{L/2}{d} \right) \right] + B, \quad (6.2)$$

while for the visible bulb a spherical symmetry, giving an intensity by

$$E(d) = \frac{A}{d^2} + B, \quad (6.3)$$

where d is the lamp-probe distance.

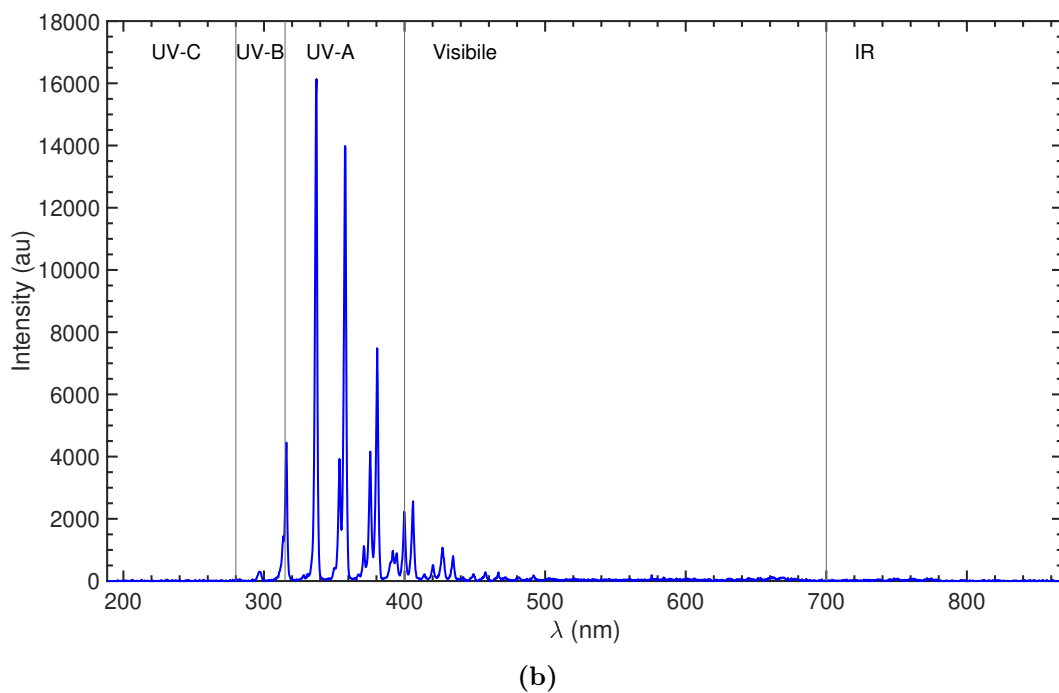
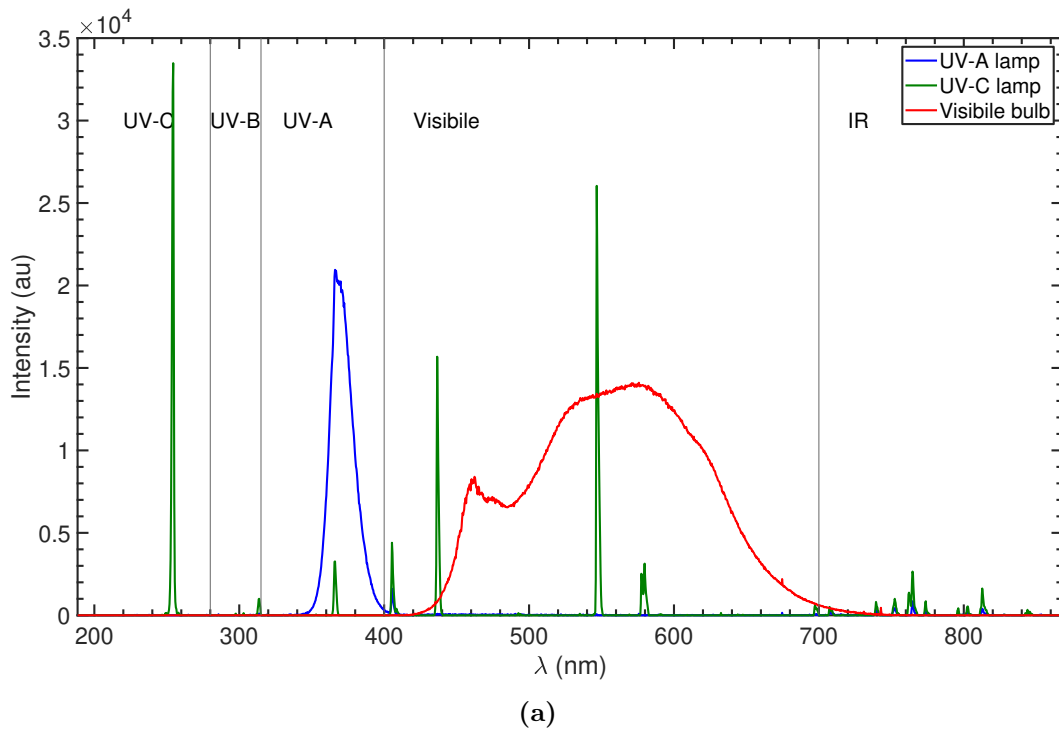


Figure 6.6: Spectra emission (in arbitrary units) of the used light sources: (a) lamps and (b) plasma.

In Eq. (6.2) and Eq. (6.3) the additive parameter B is due to a functional approximation. The errors occurring in the distance measurements are predominant on the intensity ones, to get a better fit we fitted the inverse function

of Eq. (6.2) and Eq. (6.3). However, in Figure 6.7 we plotted the intensity (in $\mu\text{W}/\text{cm}^2$) in function of the distance (in cm). The experimental data are shown in red, while the fitting curve in black. From the fitting we obtained that the UV-C lamps intensity, expressed in μW , in the UV-C region, in function of the distance, expressed in cm, follows the curve

$$E(d) = \frac{26400}{d} \left[\text{atan} \left(\frac{5.5}{d} \right) \right] + 7, \quad (6.4)$$

the UV-A lamps intensity, in the UV-A region, is

$$E(d) = \frac{10800}{d} \left[\text{atan} \left(\frac{5.5}{d} \right) \right] + 3, \quad (6.5)$$

and the visible bulb intensity, in the visible range, is

$$E(d) = \frac{131200}{d^2} + 7. \quad (6.6)$$

The data obtained by the fit are shown in Figure 6.7, denoting a good agreement between experiments and theory.

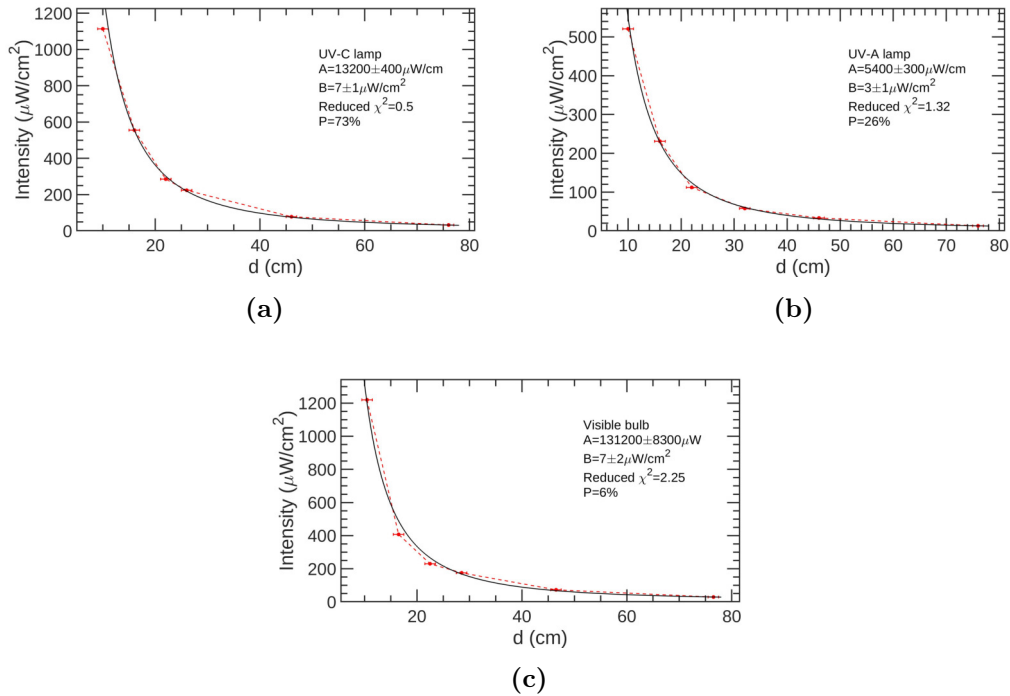


Figure 6.7: Fit and experimental data of intensity vs distance for the three different light sources: (a) UV-C; (b) UV-A; (c) visible.

The intensity of the light sources in the other spectrum regions can be summarized in Table 6.1 (central columns), where we show the relative intensities

of the other components respect to the respectively main light component. With these measurements we confirmed what we found in the emission spectroscopy analysis (Figure 6.6a), so that the UV-C lamp emission is mainly in the UV-C region, with minor components in the visible and UV-A regions; the UV-A lamp emits in the UV-A region with a little amount in the visible; the visible bulb emits only in the visible range.

Since we are interested in using the catalyst support inside the chamber and the lamps can be placed outside in front of a quartz window, we measured the intensity transmission factor due to the quartz window. The results are shown in Table 6.1 (last column). That means that the intensity reduction is the same using UV-A and visible region, while is much higher in UV-C one. However, the main component of each lamp does not change.

Table 6.1: Comparison of the intensity emission of the light sources in the different spectrum region (central columns) and transmission factor due to the quartz window filter (last column).

Source	Probe			Transmission factor
	UV-C	UV-A	Visible	
UV-C lamp	1	0.02	0.14	55%
UV-A lamp	0	1	0.08	80%
Visible bulb	0	0	1	80%

We are also interested in comparing the emission of the lamps with the plasma one. As we showed in Figure 6.6b, the plasma does not emit in the UV-C region, but only in the UV-A and in the visible ones. For that reason, we measured the radiant power per surface unit (simply identified as *Intensity* in this text) at different ignition power at fixed distance (about 3.5 cm), using the UV-A and visible probe (Figure 6.8 in black and in red, respectively). The light emission is strictly dependent of the applied ignition power and the UV-A component is about two times the visible component. The plasma intensity is much lower than the UV-A and visible lamps. In order to have the same UV-A intensity the plasma produced at 3.5 cm, we have to place the UV-A lamp at 200 cm from the target, while for the visible at about 300 cm.

We made these measurements in order to have an overview of the lighting devices we used in the abatement experiments. It figures out that the plasma

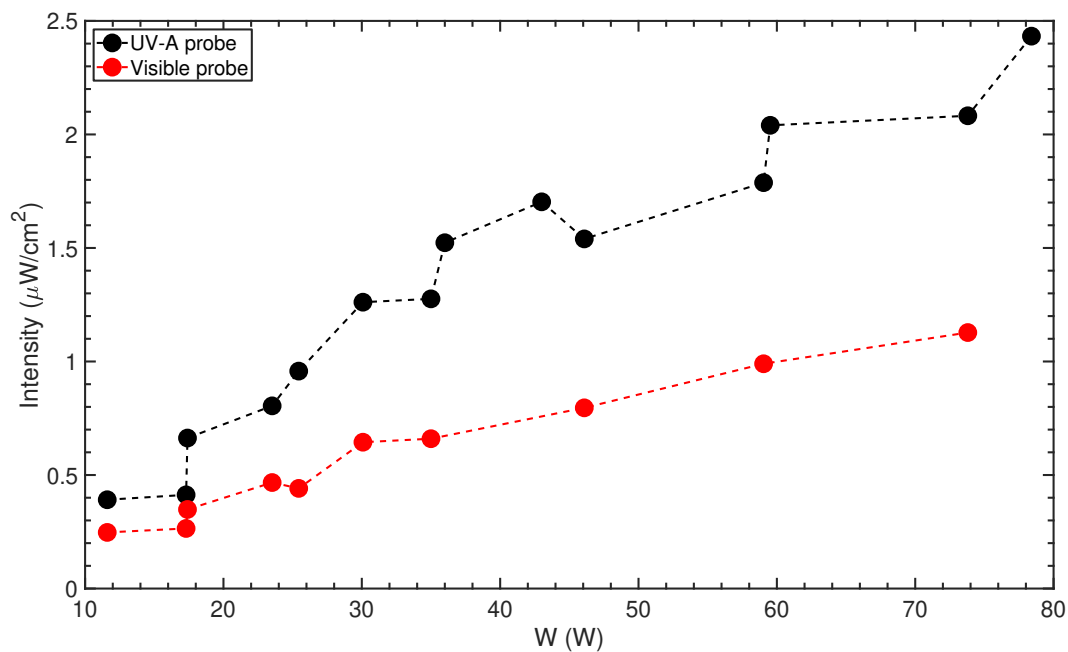


Figure 6.8: Intensity vs plasma ignition power for (black dots) UV-A probe and (red dots) visible probe. The distance between the source and the detector is about 3.5 cm.

light emission is orders of magnitude lower than the lamps, however, for the following experiments, we have to take in account that the plasma activity is not only due to the light emission but also reactive species production, charged particles and electromagnetic fields.

6.3 Measurements of O₃ and NO₂ production by SDBD

In this Chapter we are going to present the results of the measurements by means of the absorption spectroscopy of the O₃ and NO₂ production by the bidirectional alumina SDBD using the setup explained in the Sections 5.1.1 and 5.2.3.

For this experiments we proceeded in the following way:

1. fill the cross chamber box with pure air;
2. close the box;
3. start the acquisition of the (contact and gas) temperature and the UV-A and UV-C light emissions;
4. power on the plasma at a fixed input power;
5. wait for the desired time, i.e. approximately 500 s;
6. switch the plasma off;
7. wait until the contact temperature is lower than 30°C;
8. power on the plasma at a fixed input power again;
9. wait for the desired time;
10. switch the plasma and the sensors off;
11. open the box.

In that way, we can investigate the differences occurring in the O₃ and NO₂ production during the two cycles. Such test is crucial when thinking of a sterilizing device operating in closed systems.

Different O₃ and NO₂ regimes are identified at different input powers. In Figure 6.9 are shown the time traces of the O₃ (blue) and NO₂ (black) on left axis and contact (dashed) and gas (pointed) temperature on right axis. We evaluated increasing power levels from 12 W (a) to 120 W (d). Yellow bands identify time regions when plasma is on, while white ones when plasma is off. The horizontal gray dashed line indicate the upper limit for O₃ detection.

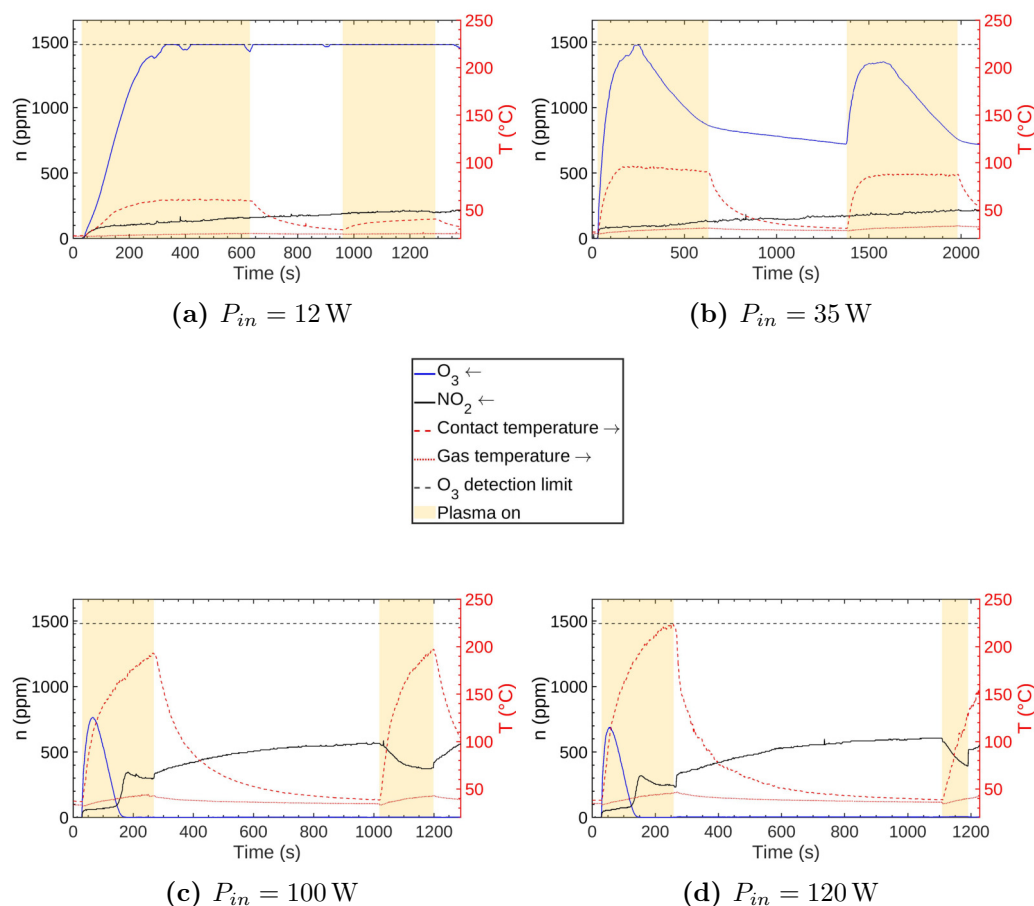
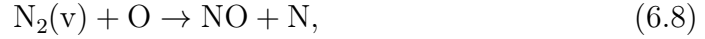


Figure 6.9: (left axis) O_3 (blue) and NO_2 (black) concentrations, (right axis) temperature of the SDBD (dash) and of the gas (pointed) for different input power: (a) 12 W, (b) 35 W, (c) 100 W and (d) 120 W. The yellow background is when plasma is on, while the white one when the plasma is off.

Looking at the first plasma cycle, shown in Figure 6.10, the O_3 slope at the ignition is steeper for increasing power levels. In that figure (Figure 6.10) we plotted the first ignition cycle for the four different input power: in green $P_{in} = 12$ W, in red $P_{in} = 35$ W, in blue $P_{in} = 100$ W and in yellow $P_{in} = 120$ W. The maximum O_3 concentration decreases with the input power. Also, the decrease happens at lower treatment times for higher power levels. This trend is similar to the results obtained by Park et al. [136]. For low input power, we reach an instrumental saturation due to the high O_3 concentration that absorbs all the light emitted by the sources. This saturation corresponds to a bit less than 1500 ppm, meaning that we are not able to detect the maximum O_3 production at 12 W of input power. For higher input powers, numerical simulations supported our trends [137]. In general, the main reaction involved

in the system are (where M is a generic molecule that it is essential for the reaction due to energy conservation, but it does not change its status):



According to those reactions and thanks to related simulations, we can say that the O_3 decreasing followed by the increase of the NO_2 , is due to the reaction between O_3 and NO (that we can not measure from our experiments) that produces NO_2 and O_2 , i.e. Reaction (6.12).

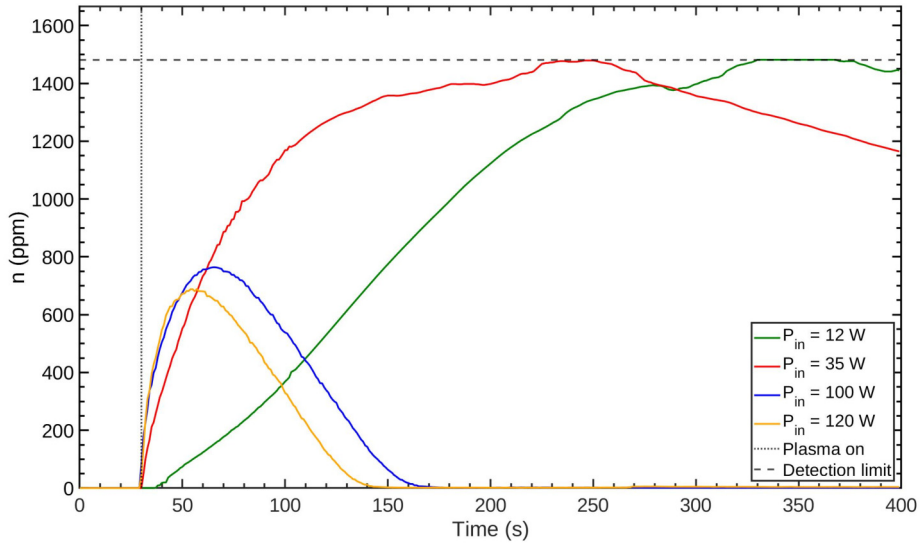


Figure 6.10: O_3 production during the first cycle of plasma powering on for the different input power.

In the second plasma cycle, the O_3 behavior mimics the first cycle for $P_{in} = 35 \text{ W}$, stays over the threshold for $P_{in} = 12 \text{ W}$ for the entire experiments. Instead, for $P_{in} = 100$ and $P_{in} = 120 \text{ W}$, the O_3 concentration remains below the detection threshold due to the dominant presence of NO_2 in the system, where NO_2 concentration is about 500 ppm inhibits the generation of high amount of O_3 , since at that levels of NO_2 Reaction (6.10) has more probability of happening then Reaction (6.9). When plasma is on in the second cycle, the

NO₂ continue to slowly increase if O₃ is high, while it decreases if the O₃ is low. For that reason we have still investigated which processes, that probably include the temperature, induce the NO₂ depletion during the plasma on phase. In particular the maximum contact temperature it is strictly dependent on the power, while the air temperature slightly increases from the initial value and stabilizes in a short time.

These different amounts of the O₃ and NO₂ when the plasma is on in a closed box are important since it means that the air inside the chamber varies during the treatment time, producing transient behaviors that can affect the depletion efficiency.

6.4 Depletion with plasma

In this Chapter we are going to present the VOC depletion obtained using SDBD plasma. In Section 6.4.1 we present analysis we have done using pentane, while in Section 6.4.2 using propane.

6.4.1 Pentane depletion

We performed experiments using both the parallelepiped and the cross chamber reactor. The description of the plasma devices is in Section 5.1.1 and the experimental configuration in Section 5.2.

Treatments in parallelepiped chamber reactor We compared the pentane decomposition that occurs with Teflon and vetronite SDBD in the 0.5 parallelepiped chamber reactor. The starting concentration of pentane is about 300 ppm, while plasma is lit up at about 45 W of input power. We evaluated the normalized concentrations $\rho(t)/\rho(0)$ in function of the treatment time t . In Figure 6.11a we plotted the experimental data in semi-log scale in order to understand if the data are compatible with an exponential decay [138] in the form of

$$\frac{\rho(t)}{\rho(0)} \propto e^{-t/\tau}, \quad (6.13)$$

where $\rho(0)$ is the initial pentane concentration before plasma treatment, $\rho(t)$ the concentration at time t , τ is a parameter representing the characteristic time scale for depletion (for that reason we are going to call it as depletion rate), which is related to the decomposition mean lifetime, $t_{1/2}$, according to $t_{1/2} = \tau \log(2)$.

From Figure 6.11a we can notice that for the Teflon SDBD the complete depletion occurs after 4 min, while for vetronite only after 2 min. The τ are 1.28 and 0.65 min, respectively. Note that the aligned points are due to the gas chromatograph instrumental limit.

Another estimator of the goodness of the depletion is the efficiency, Eff (expressed in g/kWh), evaluated as the ratio of the grams amount of depleted VOC, Δ_g , and the supplied energy in kWh, E_{kWh} , that is

$$\text{Eff [g/kWh]} = \frac{\Delta_g}{E_{kWh}}, \quad (6.14)$$

where

$$\Delta_g = \frac{\Delta_{ppm} * M * 10^{-3}}{24.45} * V, \quad M = 72.15, \quad V = 0.5 \times 10^{-3} \text{ m}^3,$$

$$E_{kWh} = \text{Power}_{kW} \times \frac{t_{min}}{60}.$$

We evaluated the efficiency after 1 min of treatment founding that it is about 0.30 g/kWh for Teflon and about 0.40 for vetronite. Since from this data we obtained that the vetronite SDBD works better than the Teflon one, our following analysis focused on the vetronite SDBD.

We evaluated the depletion rate that occurs when we pulse the plasma, and we compare with the continuous mode (Figure 6.11b). The duty cycle we applied is DC = 15% with a $T_{off} = 100$ ms. The starting concentration is about 300 ppm and the input power is about 45 W. However, since we applied a duty cycle, the effective applied power is 45×0.15 , that is 6.75 W. The depletion rate is clearly higher than the continuous mode, that is 10 min compared to 0.65 min, but the efficiency after 1 min is about 0.60 g/kWh respect to 0.40. This is due to the fact that even if we need more time to have a complete depletion, the applied power is less and the reactive species produced by the plasma can interact with the pentane to continue the depletion.

In Figure 6.11c we also compared the depletion rate and the efficiency for two input power: 17 W and 45 W [23]. We found that τ is 2.48 min respect to 0.65, while the efficiency is about 0.30 respect to 0.40 g/kWh. Additional data and analysis we performed using the vetronite SDBD for pentane depletion were published in [23].

Treatments in cross chamber For these experiments we use two bidirectional alumina SDBD placed inside the cross chamber. The starting concentration is about 300 ppm, and we worked at two different input power: 55 and 30 W (Figure 6.11d). We found that the depletion rate are 0.96 and 2.75 min, respectively, and the efficiency (evaluated considering $V = 1.5 \times 10^{-3} \text{ m}^3$) is 0.70 and 0.80 g/kWh. Even if the effective depletion ratio $\rho(t)/\rho(0)$ of the treatment made by the alumina SDBDs is lower than the treatment made by the vetronite SDBD (Figure 6.11a), we have to consider the volume of the treatment chamber that is three times bigger than the other and so the number of treated particle is higher.

To summarize we found that pentane can be well decomposed in short

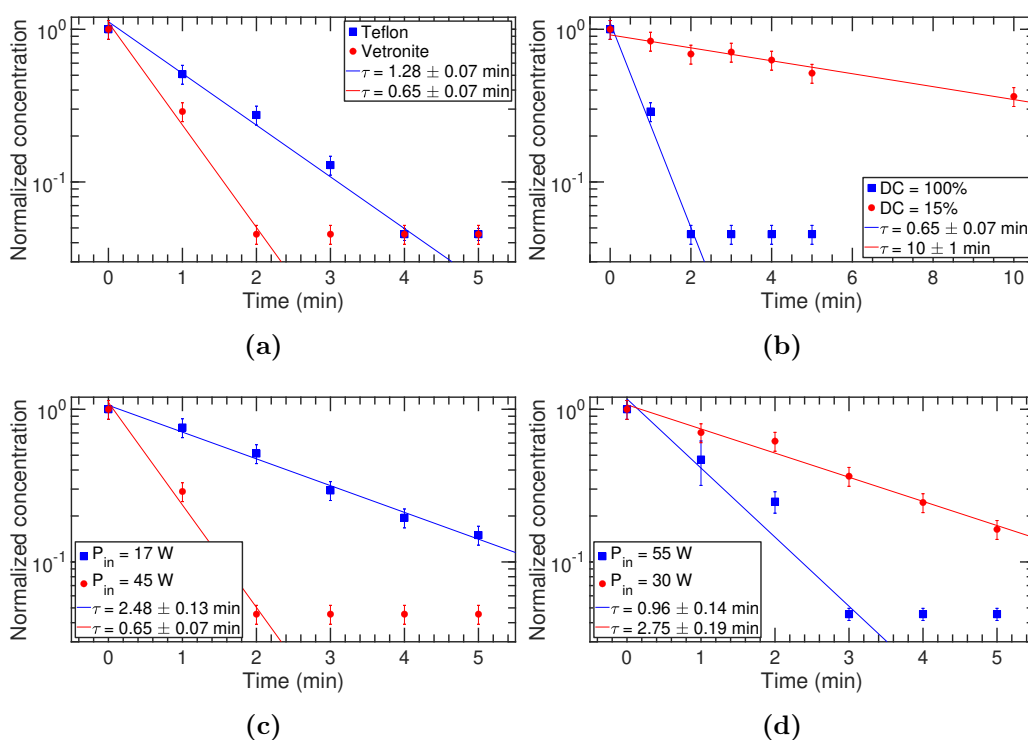


Figure 6.11: Normalized concentration $\rho(t)/\rho(0)$ of pentane vs treatment time for different conditions. (a) For different SDBD: (blue) teflon and (red) vetronite. (b) For vetronite SDBD and different duty cycle: (blue) 100% and (red) 15%. (c) For vetronite SDBD and different input power: (blue) 17 W and (red) 45 W. (d) For bidirectional alumina SDBD and different input power in the cross chamber: (blue) 55 W and (red) 30 W.

time (less than 5 min) by SDBD plasma in closed chamber. The depletion efficiencies in our experiments vary between 0.30 and 0.40 g/kWh.

This is a starting point for the study of the depletion in flow situations. However, we were not able to do that since the injection system cannot produce a sufficiently constant flow, detectable by the gas chromatograph, that we can associate a decreasing to a plasma effect over the injected pentane.

6.4.2 Propane depletion

We performed experiments using both the parallelepiped and the cross chamber reactor. The description of the plasma devices is in Section 5.1.1 and the experimental configuration in Section 5.2. As already discussed in Section 6.4.1, we evaluated the depletion rate and the efficiency after 1 min of treatment also for the propane depletion.

Treatments in parallelepiped chamber reactor The SDBD used in these experiments is the vetronite one. The starting propane concentration is about 5000 ppm, and we worked at two different input power: 17 and 45 W (Figure 6.12a). We have to notice that the starting concentration of propane we used is higher than we used for pentane; this is due to the different injection system that allows us to work in different concentration range.

The depletion rate is about 6.9 min for input power at 17 W and 1.15 min for 45 W. The efficiency (considering the molar mass $M = 44.1$ of the propane) is about 4.0 and 2.4 g/kWh, respectively. Also in this case we notice that having higher depletion rate do not means have a better efficiency.

Treatments in cross chamber For the analysis in the cross chamber we compared all the alumina SDBD, with and without the use of a vent that stir the air (Figure 6.12b and Figure 6.12c). The starting concentration is about 5000 ppm and the input power about 14 W. We found that there is no difference in the use or not of the vent, since the τ is about the same. The depletion rate is almost the same for the bidirectional and the monodirectional fingers ($\tau \sim 13.5$ min), and it is a bit lower ($\tau \sim 11$ min) for the honeycomb one. In the monodirectional and bidirectional conditions the gas flow is parallel to the surface, while in the honeycomb configuration gas flow is perpendicular, favoring a mixing of the gas species in the entire volume and avoiding the adsorption of the molecular species from the surface. This favors the production of reactive oxygen at the SDBD, necessary to oxidize the propane [24]. The efficiency after 1 min of treatment in all of these cases is about 5 g/kWh. A complete discussion of propane treatments is in our paper [24].

The depletion of propane using SDBD plasma has efficiencies that span between 2.4 and 5.0 g/kWh. The higher efficiency respect to the pentane is due to the different properties of the two components and the concentrations

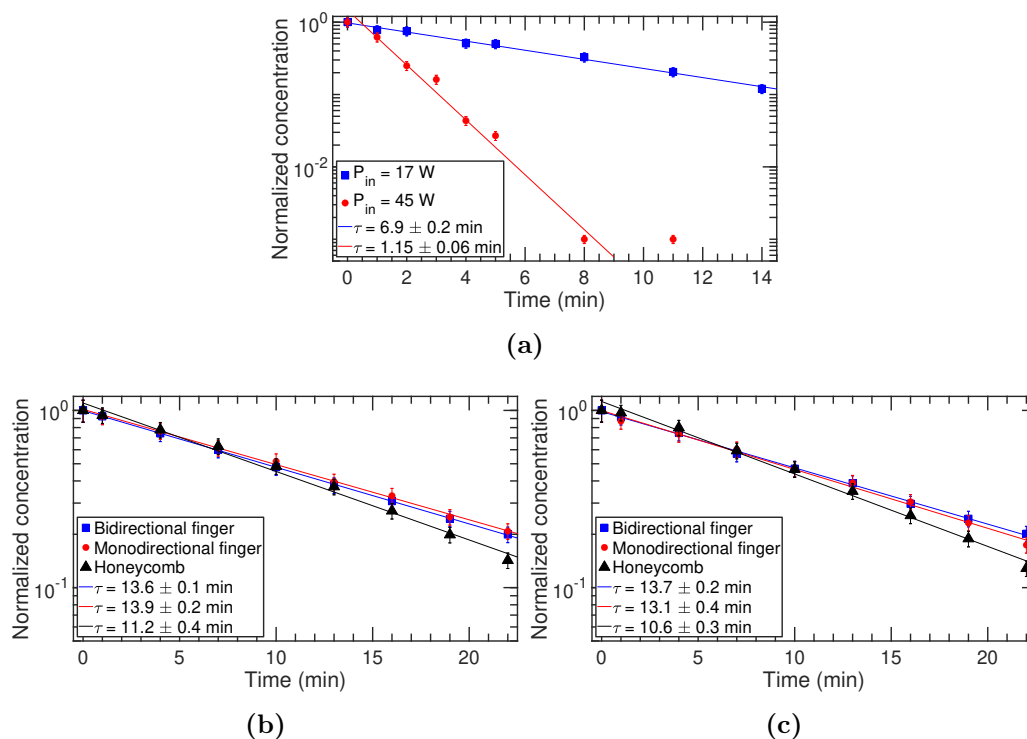


Figure 6.12: Normalized concentration $\rho(t)/\rho(0)$ of propane vs treatment time for different conditions. (a) For vetronite SDBD and different input power: (blue) 17W and (red) 45 W. (b-c) For different SDBD: (blue) bidirectional finger, (red) monodirectional finger and (black) honeycomb; (b) with vent and (c) without vent.

we are treating. However, higher efficiency does not mean quick depletion, in fact the depletion rate τ for propane is greater than the pentane one. Also, the propane flow is not so stable to perform flow measurements, but we think that these results are promising for a good propane, and other VOCs, depletion also in flow situations.

6.5 Depletion with catalysts

In this part we are going to present the depletion of propane using photocatalysts. The treatment box is the cross chamber, the catalysts were presented in Section 5.2.2 and the lamps in Section 5.1.2.

TiO₂ activation occurs when illuminated with wavelength lower than 388 nm, so in the UV-A range [139]. A way to move the activation from UV to visible light is to have a combination of WO₃ and TiO₂ [140]. In this research we are interested in investigate the depletion rate, evaluated from (6.13), of the three catalysts illuminated with UV-A and visible light. In Figures 6.13a, 6.13b and 6.13c are reported the y-log scale normalized concentrations that occur after a treatment with catalyst A, B and C, respectively. We can notice that the depletion rate in that cases are larger than the ones we obtain with plasma depletion. However, the catalysts are a sort of passive methods for depletion, for instance incorporated in wall paints, working with sunlight or in common interior lamps if sufficient visible light is available for activation.

In Table 6.2 we report the depletion rate for the different catalysts and lamps. We can notice that, for catalyst A, the most efficient light, as expected, is the UV-A. In catalyst B, the visible light does not induce any depletion. For catalyst C, on the other hand, the visible is the most effective and the UV-A does not induce depletion. A more exhaustive and complete discussion about depletion with catalyst can be found in Ref. [25].

Table 6.2: Summary of the depletion rate for the different catalysts and lamps.

Catalyst	Source	UV-A	Visible
A		220	1100
B		510	∞
C		∞	630

Since the propane catalyst depletion time scale is much larger than the plasma one, it is not suitable for being used in flow situations, but only in quasi-static ones. This is not a problem because catalysts are passive methods which can be embedded, for example, in wall paintings. For that reason, it is important to study further the issue of visible light catalysts to be used

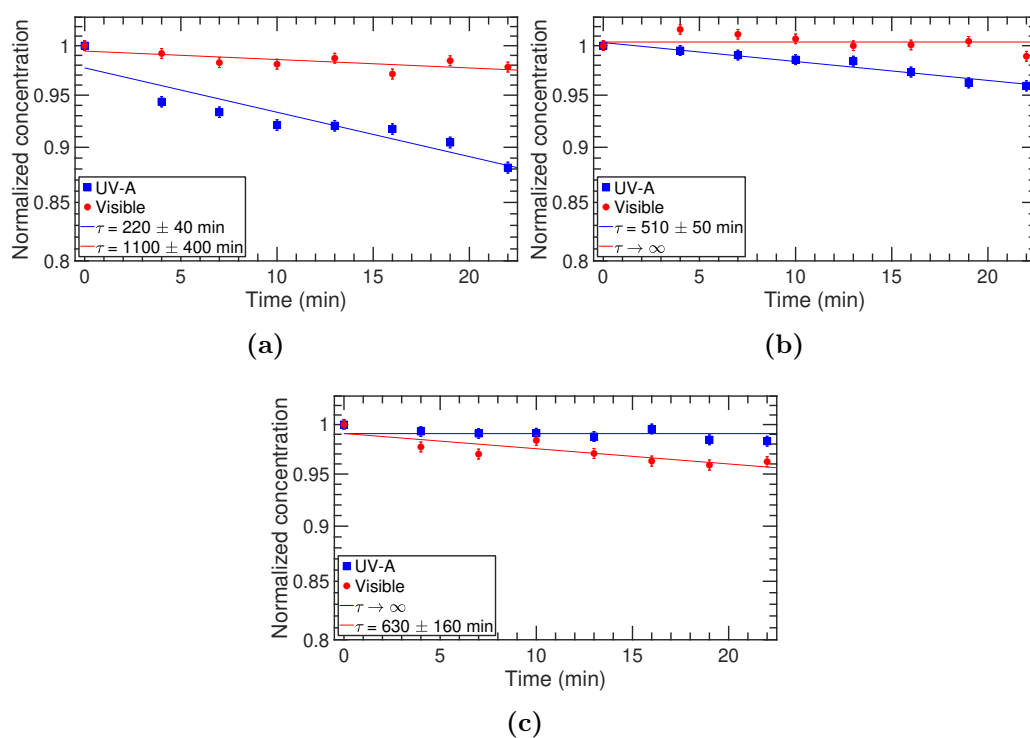


Figure 6.13: Normalized concentration $\rho(t)/\rho(0)$ of propane vs treatment time using different catalysts and lamps. (a) Catalyst A, (b) catalyst B, (c) catalyst C illuminated with different lamps: (blue) UV-A and (red) visible.

indoors. In any case, it would be useful to develop a coupled system of a catalyst and a plasma to exploit the advantages from both systems, that is, the fast depletion action by the plasma combined with the long-time scale behavior of the catalyst.



7 Conclusions

These experimental campaigns were carried out to outline some methods for the VOCs depletion. All the experiments were done in a closed box with high VOC concentrations to have a good sensitivity in the measurements.

The results for the active depletion with plasma, but also the passive one with catalysts, are promising, even if it is necessary to perform some improvement and scale up for the actual application in real open places.

The preliminary measurements outlined the discharges properties such as the carried current or the transferred power from the electrical power supply to the plasma. It figures out that only the (50-55)% of that power is transferred to the plasma.

When we light on the plasma there is a production of O_3 and NO_2 that we measured with absorption spectroscopy. These species are not directly responsible for the VOC depletion, and so its reduction can also improve the depletion efficiency. For what concerns the scalability of the system, we have to consider that our analysis were carried in a closed small box and so the O_3 and NO_2 behavior in a bigger or open room may be different.

In Table 7.1 are summarized the depletion rate, the efficiency after one minute and the depleted percentage after one minute for all the plasma depletion devices mode we tested. The fact that efficiency is power dependent suggests that plasma energy was either not well-distributed in the reactor or that the plasma produced a larger amount of by-products such as ozone, thus limiting other chemical reactions.

A more complete analysis of the depletion processes of propane and pentane with plasma and catalysts were carried out in our papers *Pentane Depletion by a Surface DBD and Catalysis Processing* [23], *A study on propane depletion by Surface Dielectric Barrier Discharges* [24] and *High concentration propane depletion with photocatalysis* [25].

In [23] we compared the differences in the depletion of pentane using both SDBD and TiO_2 catalyst, investigating the pentane depletion and also the by-products formations. The analysis of the temporal evolution of pentane and

Table 7.1: Summary of the depletion rate, the efficiency after one minute and the depleted percentage after one minute for all the plasma depletion devices mode we tested.

VOC	Start. conc. (ppm)	Box vol. (L)	Device	Input power (W)	τ	Eff. @ 1 min (g/kWh)	Depletion @ 1 min (%)
C_5H_{12}	300	0.5	Teflon	45	1.28	0.30	45%
			Vetronite	45	0.65	0.40	70%
				45 DC 15%	10	0.60	25%
				17	2.48	0.30	20%
		1.5	Bidir. alumina	55	0.96	0.70	55%
				30	2.75	0.80	30%
C_3H_8	5000	0.5	Vetronite	45	1.15	2.4	50%
				17	6.9	4.0	35%
		1.5	Bid. al.	14	13.7	5.0	10%
				14	13.1	5.0	10%
				14	10.6	5.0	10%
				14	10.6	5.0	10%

the associated concentrations of the intermediate reaction products allowed us to quantitatively describe the kinetics of VOC depletion in the plasma hybrid system. In an SDBD–catalyst reactor, the plasma primarily acts to decompose pentane, while the catalyst mostly concerns the intermediate reaction products. During the first minutes of treatment in a single experiment, gas processing is dominated by plasma decomposition of pentane, followed by the generation of the intermediate products, which are progressively depleted by the catalytic processes acting on longer time scales. The plasma dynamics depends on both the pentane concentration and applied power. It is faster at higher power and lower concentrations, where pentane is abated in less than 1 min. The typical time scale varies between 0.7 and 1.7 min for 300 ppm and 1200 ppm initial pentane concentrations, respectively.

In [24] we analyzed the temporal evolution of propane provided in a wide range of VOC concentrations, between about 1000 and 10000 ppm, permitted to evaluate depletion time rates decreasing as a function of plasma power and concentration. The efficiency evaluated as quantity of propane per unit of energy takes values between 2 and 7.5 g/kWh and depends strongly on the propane concentration.

In [25] we demonstrated the ability of TiO_2 catalysts to deplete high propane concentrations using UV-A lamp. The abatement rate for the initial propane concentration between 1200 and 5000 ppm is of the order of 10% after 22 min, and the time scale of depletion is of the order of hours. We found that the TiO_2 photo-catalytic activity slowly depends on the initial concentration. The TiO_2 catalyst suffers from aging effects since after two months, its depletion action is greatly reduced.

Part III

Bacteria removal by atmospheric cold plasma

8 Equipment setup

In this Chapter we are going to present all the equipment setup we used for the air purification from biological pollutants. These experiments are done in collaboration with a group from Department of Pharmacological and Biomolecular Sciences at University of Milano and a group from Department of Medicine and Surgery, experimental neurology unit at University of Milano-Bicocca.

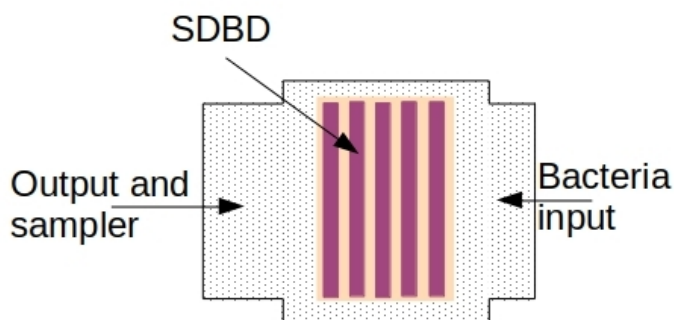
8.1 Plasma sources

To perform the abatement we used the bidirectional alumina SDBD, detailed in Subsection 5.1.1. The input powers we worked with are about 16 and 35 W, that corresponds at about 7.5 and 20 W of transferred power to the plasma, respectively, as shown in Section 6.1.

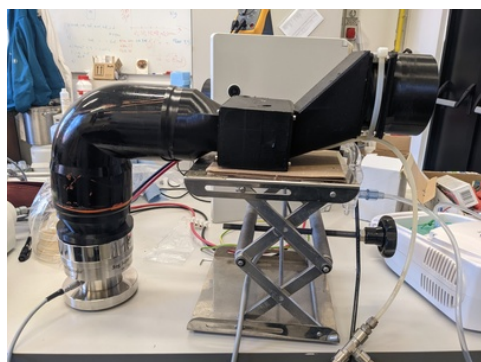
8.2 Experimental setup and diagnostics

Treatment box The treatment box is a homemade 3D printed case with the SDBD place at the bottom (Figure 8.1a). At about the same level of the SDBD, bacteria are vaporized using an aerosol machine and collected by two different sampling methods that are going to be presented below: DUO SAS air sampler (Figure 8.1b) and Coriolis liquid sampler (Figure 8.1c). The input opening has also a fan that can be switch on or not during the experiments.

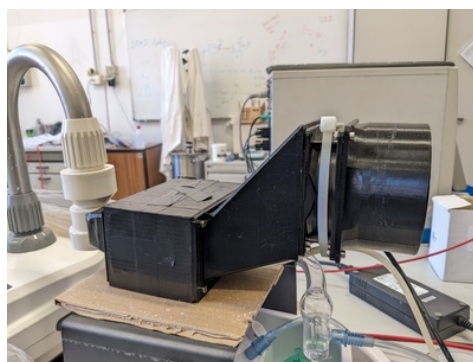
Bacteria preparation and vaporization Bacterial cells were cultivated in LB broth (supplied from DIFCO) at 37°C. Stationary phase bacterial cultures were diluted in LB broth to an OD600 (Optical Density) of 0.05 and growth was monitored by measuring OD600 over time. At OD600 = 0.5 bacteria were collected by centrifugation (5000 rpm for 15 min) and re-suspended in an equal volume of 0.9% NaCl or 0.1M phosphate buffer solution at pH 7.00. Bacteria were then appropriately concentrated or diluted to obtain the desired concentration CFU/ml (Colony Forming Unit/ml) to be vaporized. The bacteria we



(a)



(b)



(c)

Figure 8.1: (a) Sketch of the setup. Photo of the experimental setup using (b) Duo SAS air sampler and (c) Coriolis liquid sampler.

used are the non-pathogenic Gram-negative *Escherichia coli* and the Gram-positive *Staphylococcus epidermidis* species. For the bacteria vaporization we used (Figure 8.2) Master Aid Dynamic aerosol coupled with Med+s Medical Solution aerosol ampule. The medium vaporization flow is 0.2 ml/min.

The bacteria growth and the evaluation of the abatement was done at University of Milano - Department of Pharmacological and Biomolecular Sciences (microbiology laboratory).

Bacteria collection Sampling of the bacteria was carried out using the Duo SAS and Coriolis systems.

The air sampler SAS Super 180 Duo (Figure 8.3a) has a speed of 180 L/min and the sampled air is directly conveyed to a Petri dish with Difco Nutrient Broth agar medium (NA). Petri dishes are incubated for 18-24 h at 30°C and then colonies enumerated to calculate bacterial concentration expressed as CFU/m³.

The liquid sampler is Coriolis (Figure 8.3b). It has a maximum speed of



Figure 8.2: Photo of the Master Aid Dynamic aerosol coupled with Med+s Mediacal Solution aerosol ampoule.

300 L/min and a maximum sampling time of 10 min. For the experiments we set the speed at 200 L/min and the time at 10 min. The sampling is done in a 0.1 M phosphate buffer solution at pH 7.00. Bacterial concentration is calculated by plating appropriate dilution of the liquid on a Petri dish. Petri dishes are incubated for 18-24 h at 30°C and then colonies enumerated to calculate bacterial concentration expressed as CFU/ml. Note that the minimum concentration we can detect with this setup is 1×10^1 CFU/ml. In the histograms concentrations below 1×10^1 CFU/ml are plotted as 1×10^1 CFU/ml without error since we cannot have a better esteem, meaning that the abatement estimation is below the detection limit in that cases.

FITC analysis Fluorescein isothiocyanate (FITC) [141] is a fluorescent molecule that is unable to cross membranes and bacterial walls when they are intact. However, if membranes and walls are damaged, FITC enters the bacteria and therefore these bacteria are defined as FITC positive. The percentage of the FITC positive bacteria respect to the total number of bacteria is an esteem of the amount of the damaged bacteria.

For this analysis, it is necessary to add the FITC (Merk) at the bacteria solution and after an opportune preparation the bacteria are deposited over a Petri dish. Using a fluorescence microscope (Cell Observer from Zeiss) and a 60x immersion lens, a series of images are acquired. The total number of bacteria and the FITC positive ones are manually estimated with the support of ImageJ software. This analysis were done in collaboration with the Department of Medicine and Surgery, experimental neurology unit at University of

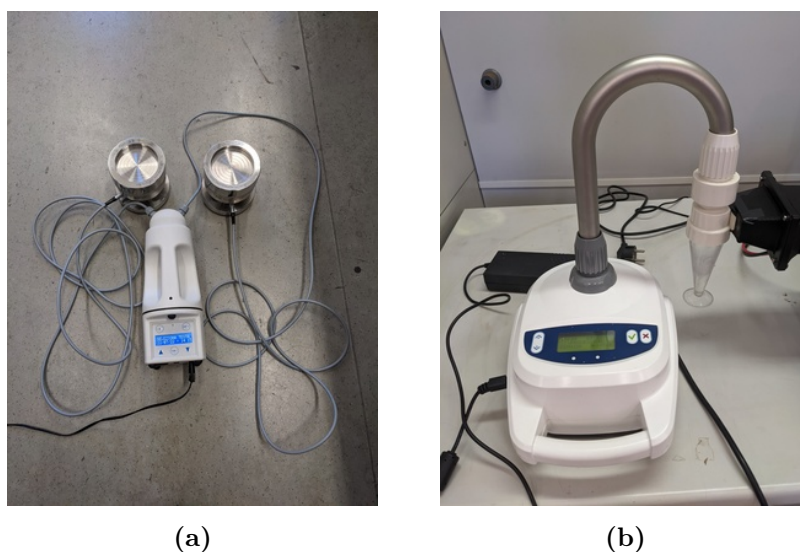


Figure 8.3: Photo of (a) the air sampler SAS Super 180 Duo and (b) the liquid sampler is Coriolis.

Milano-Bicocca.

O₃ and temperature measurements We measured the O₃ produced by the plasma with the absorption spectroscopy as described in 5.3 - *Absorption spectroscopy* section. The temperature collection is described in 5.3 - *Temperature*. For these measurements we cannot use the treatment box we used for the bacteria, since we need quartz windows for the absorption spectroscopy recording. We placed the SDBD inside one cross chamber reactor with two opposite enclosure with quartz window, one with the connection for the Coriolis and the last one for the air and vaporizer incoming. The data collection consists in recording the lamp light intensity and the temperature for the desired time (about 30 s), switching on the plasma and let the Coriolis and vaporizer start after about 20s. When the Coriolis treatment ends (about after 10 min) we switch off the vaporizer and the plasma.

9 Results and analysis

In this Chapter we present the results of the characterization of the source and the abatement of the bacteria.

9.1 O₃ production and temperature measurements

In this Section we are going to present the O₃ and temperature trends while Coriolis moves the air.

In Figure 9.1 we show the O₃ produced by the plasma at two different input power: about 16 (in red) and about 35 W (in blue). The yellow bar represents the time when only plasma is on, while the green one is when both plasma and Coriolis are on. The box inside is a zoom of the O₃ between 100 and 645 s. We operated similarly as we do for the bacteria treatments, we light on plasma and when is well powered, that is about 20 s later, we switch on the Coriolis and simultaneously the vaporizer. The Coriolis treatment is for about 10 min with automatic stop. After that we switch off the vaporizer and the plasma. From Figure 9.1 we can see two separated regimes for the two different input power. Higher is the power, higher is the O₃ production. The O₃ concentration is quite stable when the Coriolis is on at about 10 ppm for 16 W input power and about 23 ppm for 35 W.

In Figure 9.2 we show the contact temperature (dashed line) of the SDBD and the gas temperature (dotted line) that there is around the plasma. The latter is the temperature the majority of bacteria feel when they flow over the treatment box. We can see that the contact temperature reaches about 70°C for 35 W input plasma power and 45° for 16 W. These are not safe temperatures for bacteria, however the gas temperatures are lower than 30°, thus we can exclude that the bacteria abatement is due to temperature effects during the treatment, as shown in the next paragraphs.

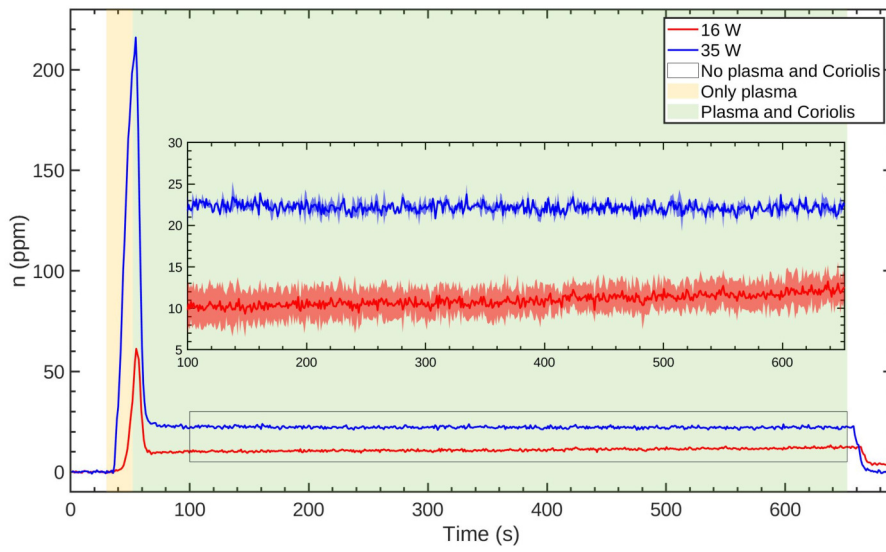


Figure 9.1: O₃ production while Coriolis moves the air.

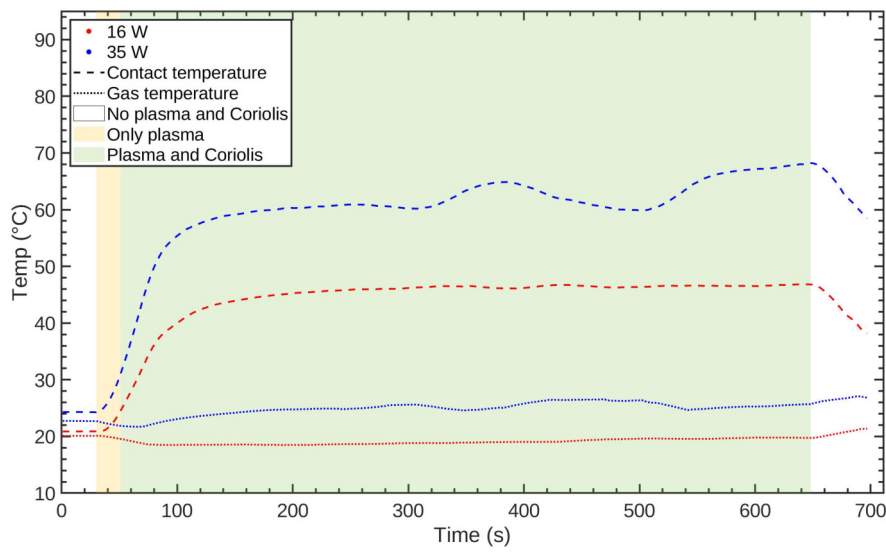


Figure 9.2: Gas and contact temperature of the SDBD while Coriolis moves the air.

9.2 Bacteria abatement

In this Section we are going to present the results of bacteria abatement by plasma treatment. The bacteria we chose for these experiments are the Gram-negative *Escherichia coli* (*E. coli*) and Gram-positive *Staphylococcus epidermidis* (*S. epidermidis*).

To analyze that data, for every couple x_u and x_t (untreated and treated mean concentrations), we evaluated the Log reduction

$$\Delta_{10} = \log_{10}(x_u) - \log_{10}(x_t), \quad (9.1)$$

in order to know how good the abatement is. The Δ_{10} is linked to the abatement percentage by the relation

$$\% \text{ abatement} = 100 \times (1 - 10^{-\Delta_{10}}), \quad (9.2)$$

meaning that highest Δ_{10} corresponds to a better abatement.

To compare the two samples, we made the compatibility test

$$t = \frac{|x_u - x_t|}{\sqrt{\sigma_u^2 + \sigma_t^2}}, \quad (9.3)$$

where σ_i is the mean standard deviation of the variable x_i . We can assume, with a confidence level of 5%, that the two values x_u and x_t are compatibles if $t \leq 2$ and incompatible if $t > 2$. For that reason we can say that a treatment is effective (there is a real reduction of the bacterial concentration) if $t > 2$, otherwise the treated and the untreated samples are statistically compatible and there is no abatement.

9.2.1 *Escherichia coli*

To evaluate *Escherichia coli* abatement we used both bacteria collection systems, Duo Sas and Coriolis.

Duo Sas bacteria collection For this experimental campaign we compared the *E. coli* abatement that occurs when the bacteria are suspended in NaCl 0.9% or in phosphate buffer solution 0.1 M at pH 7.00. The plasma works at about 16 W of input power.

In Figure 9.3 we report the bacterial concentration expressed as CFU/m³ under different conditions:

1. without plasma: vaporized bacteria are collected in 2 minutes over a Petri dish (NA) without generating plasma (condition blue in figure),
2. bacteria aerosol after having plasma treated the Petri dish: vaporized bacteria are collected in 2 minutes over the Petri dish (NA) after having plasma treated the Petri dish for 2 minutes (condition orange in figure), in order to investigate if plasma could be responsible for a Petri dish poisoning, affecting the bacteria growth,
3. plasma treatment of bacteria aerosol: vaporized bacteria are collected in 2 minutes over a Petri dish (NA) while plasma is on (condition yellow in figure).

The concentration expressed as CFU/m³ is evaluated dividing the number of CFU counted over the Petri dish by the amount of air sampled by Duo Sas in 2 min, that is 0.360 m³.

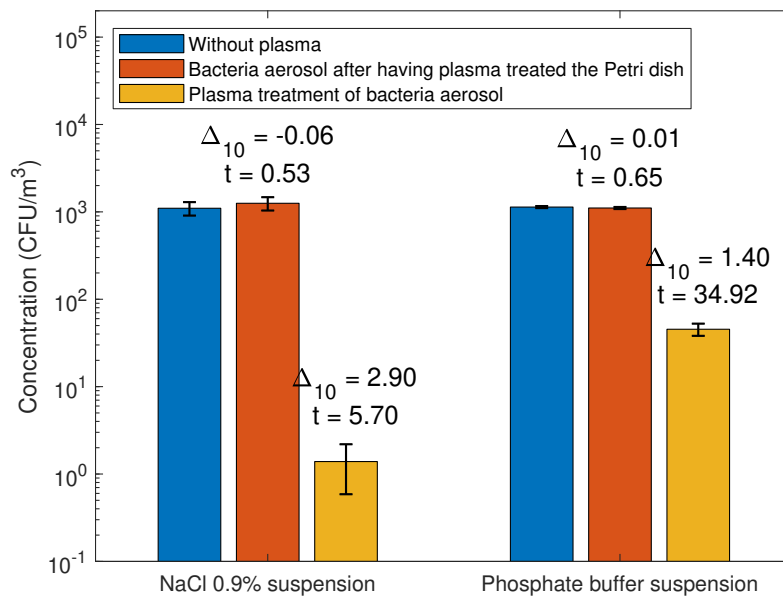


Figure 9.3: Concentration of bacteria collected over a Petri dish with bacteria vaporization without plasma (condition blue), with plasma and following bacteria vaporization (condition orange), with bacteria vaporization and with simultaneously plasma (condition yellow), using bacteria in NaCl 0.9% (left) and in phosphate buffer (right) solution.

Data exploit the bacteria abatement during the bacteria vaporization and plasma treatment. The abatement is therefore not generated by an eventual Petri dish poisoning by plasma as we can see that the concentration of bacteria vaporized after having plasma treated the Petri dish is the same of the

concentration of the bacteria vaporized without plasma ($t = 0.53$ and 0.65 and Δ_{10} close to zero). This means that the abatement occurs during the very low time that the bacteria flow over the plasma and interact with the treated air while reaching the Petri dish.

The suspension medium plays a role in the abatement: bacteria suspended in phosphate buffer solution before vaporization are less vulnerable. We found that Δ_{10} is 1.40 ± 0.07 for the bacteria suspended in buffer and 2.90 ± 0.30 for the ones suspended in NaCl 0.9%; both t values are greater than 2. However, the bacteria in the environment are in a condition that is much more similar to the NaCl 0.9% than the phosphate buffer solution with a stable pH, meaning that this system is effective for the reduction of bacteria in the order of $10^3 \text{ CFU/m}^3 = 10^{-3} \text{ CFU/ml}$ that flow over the plasma with a 180 L/min speed.

Coriolis bacteria collection The bacteria cells in this experimental campaign are always suspended in NaCl 0.9%, while the liquid medium for the collection after treatment is phosphate buffer solution at pH 7.00. We chose that liquid medium in order to reduce the possibility of the bacteria abatement occurs in the liquid instead of in the air.

The concentration range for the starting concentration that we can exploit with this collection sampling is about between 10^3 and 10^9 CFU/ml (that correspond to 10^9 and 10^{15} CFU/m³), so it is larger and higher than the one we explored during the Duo Sas collection.

We evaluated the abatement of the *E. coli* starting from vaporized solutions at different concentrations using plasma at 16 W of input power (Figure 9.4). The Log reduction and the compatibility factor are shown in Table 9.1.

Table 9.1: Log reduction and the compatibility factor of the *E. coli* treatment at 16 W of plasma input power.

Starting concentration (CFU/ml)	Δ_{10}	t	Abatement
3.5×10^7	0.51 ± 0.40	0.92	No
5.5×10^5	0.61 ± 0.15	2.40	75%
3.5×10^4	1.08 ± 0.12	4.96	92%
1.5×10^3	> 2.23	> 2.98	$> 99.4\%$

A Log reduction plot in function of the starting concentration is reported in Figure 9.5. Red dot means that Δ_{10} is greater than the reported value.

From Figure 9.4 and Figure 9.5, we can notice that the Log reduction, and so the order of abatement, is dependent of the starting bacteria concentration and goes from 0.5 for about 10^7 CFU/ml, where we cannot see that there is abatement ($\Delta_{10} = 0.51 \pm 0.40$ and $t = 0.92$) to more than 2 order for 10^3 CFU/ml ($\Delta_{10} > 2.23$ and $t > 2.98$) where the abatement is more than 99.4%.

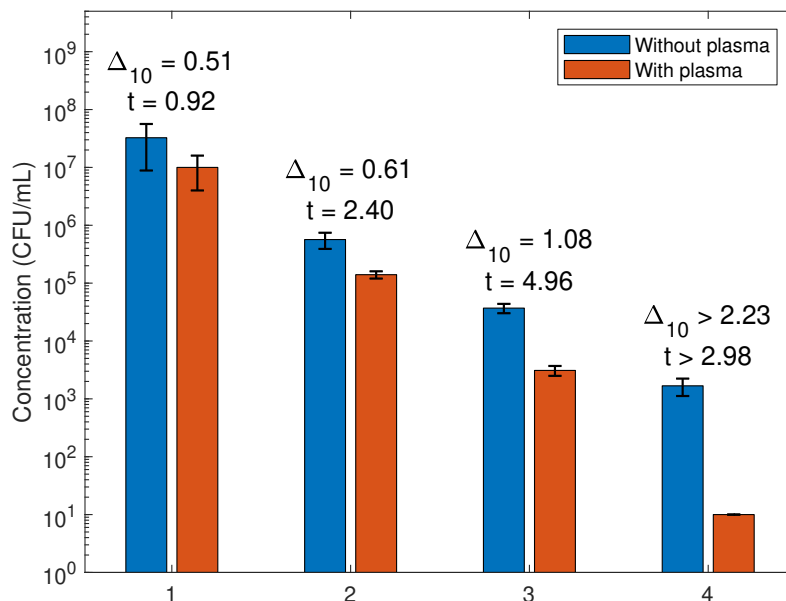


Figure 9.4: Abatement of *E. coli* cells at different starting concentrations at 16 W input power of plasma. (blue bars) Not treated samples, (orange bars) plasma treated samples.

Working with the highest concentration, where there is not the abatement for 16 W input plasma, we evaluated what happens if we increase the plasma at about 35 W (Figure 9.6). We notice that the plasma power plays a role, since higher plasma power made a quite good abatement, obtaining $\Delta_{10} = 0.91 \pm 0.10$, $t = 10.18$ and abatement of 87%, compared to the no abatement of the low power situation. We are also interested to verify that the abatement happens while the bacteria flow over the plasma and interact with air and not in the collecting liquid medium. From Figure 9.6 right columns we show that there is no abatement in the liquid medium since the concentration of the bacteria added after a coriolis treatment with plasma is the same of without plasma ($\Delta_{10} = 0.04 \pm 0.10$ and $t = 0.37$). Note that there is a difference in the bacteria concentration of the vaporized bacteria and in the added after

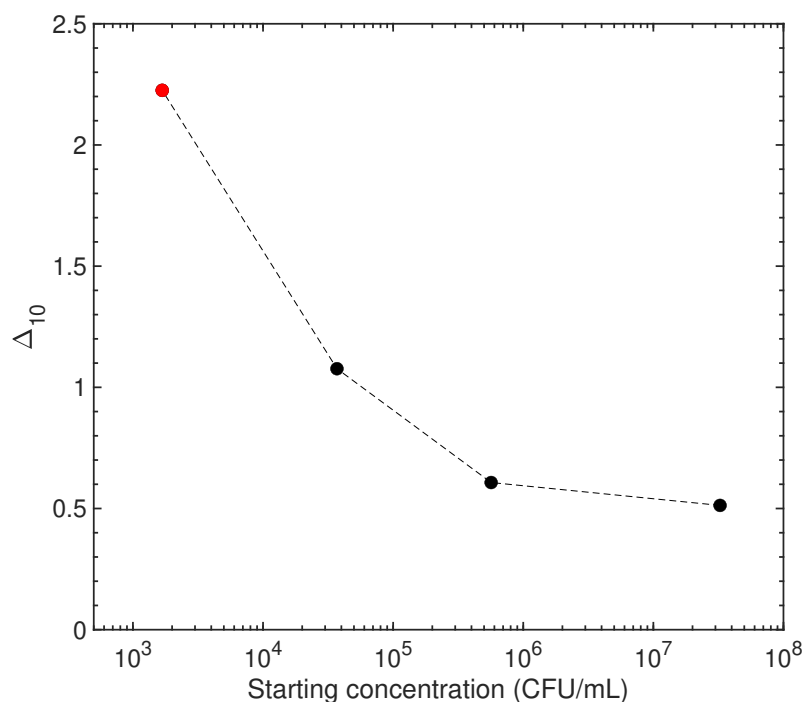


Figure 9.5: Log reduction in function of starting concentration. Red dot means that Δ_{10} is greater than the reported value.

the treatment ones since during the vaporization there is a loosing of bacteria along the path that do not happen when we added 2 mL of bacteria directly in the treated liquid.

These last two studied conditions (center and right columns in Figure 9.6) were also tested by FITC test, figuring out, as can be seen in Figure 9.7 and Table 9.2, that there is a significant increasing of the positivity in the vaporized bacteria 35 W treated respect to the untreated, while there is not in the bacteria added after the treatment. The amount of FITC positive bacteria in the untreated vaporized condition are significantly ($t = 5.8$) higher than the ones are added after the Coriolis treatment, meaning that there is damage while the bacteria are vaporized, pass through the system and are collected by the Coriolis. However, the higher damaging is due to the plasma, since the FITC positive bacteria go from about 23% in the untreated to about 70% in the treated condition. The bacteria damaging induces bacteria killing or a reduction in their reproduction, confirmed by the reduction of concentration (Figure 9.6 central columns).

We are interested in knowing if the reactive species produced by the plasma play a role in the bacteria abatement. We placed the whole device (vaporizer,

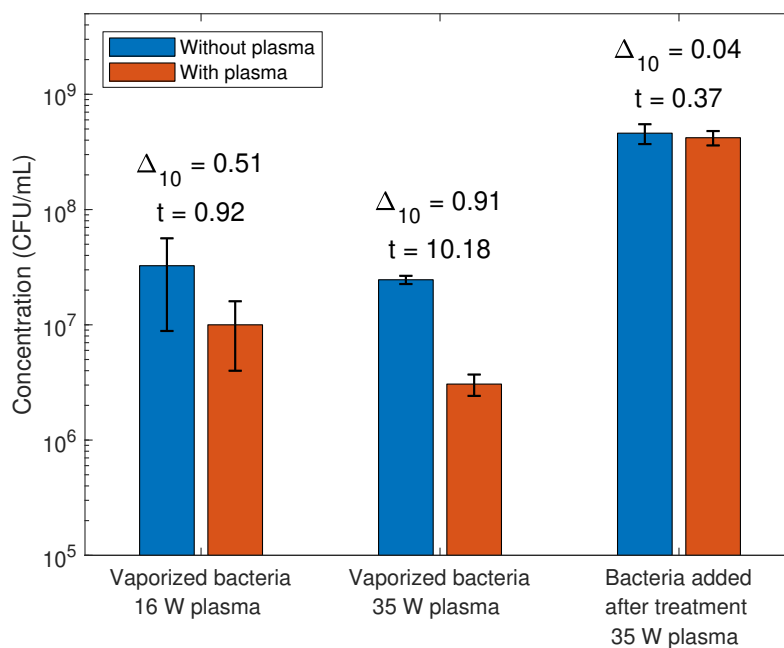


Figure 9.6: Abatement of *E. coli* cells at different plasma conditions: (left columns) 16 W input power of plasma and (center columns) 35 W input power of plasma. (right columns) Bacteria added after coriolis treatment with plasma at 35 W input power and without plasma. (blue bars) Not treated samples, (orange bars) plasma treated samples.

Table 9.2: Percentage of FITC positivity bacteria over total number of counted bacteria. The percentage is evaluated over at least 5 images for each condition.

Bacteria		Positivity (%)	t
Vaporized	Not treated	23 ± 3	8
	35 W plasma treated	70 ± 5	
Added after	Not treated	2.5 ± 1.8	0.5
	35 W plasma treated	1.4 ± 1.3	

plasma box, Coriolis) in a glow box filled with argon, we collected with the Coriolis the bacteria sampled without and with the argon plasma, and we compared with the same concentration abatement in air (Figure 9.8). The plasma input power is about 16 W in both cases. We found that there is no abatement when the plasma is lit up argon ($\Delta_{10} = -0.07 \pm 0.15$ and $t = 0.44$). That means that the reactive species produced by the air plasma play a direct role in the bacteria abatement.

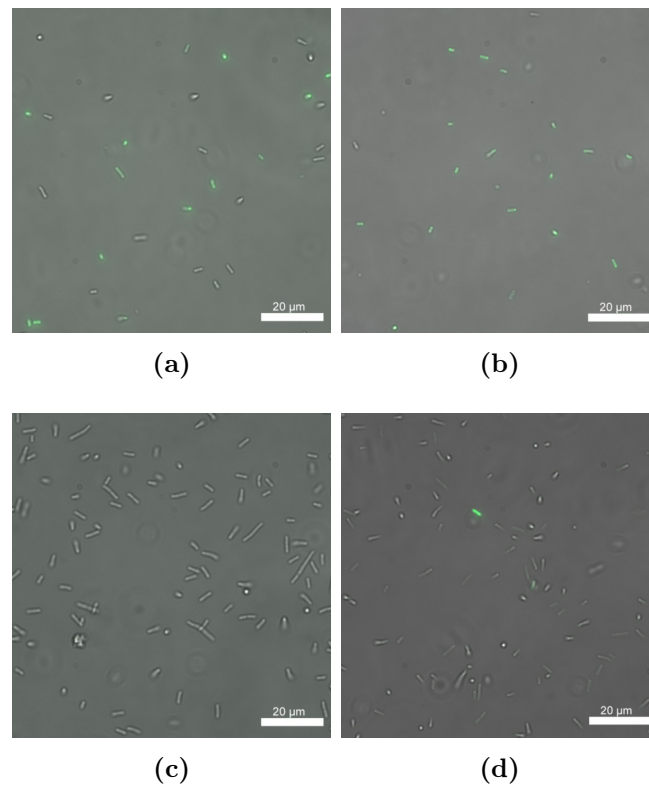


Figure 9.7: *E. coli* FITC images for vaporized (a) untreated and (b) 35 W plasma treated bacteria; bacteria added after (c) only coriolis treatment and (d) coriolis and 35 W plasma treatment.

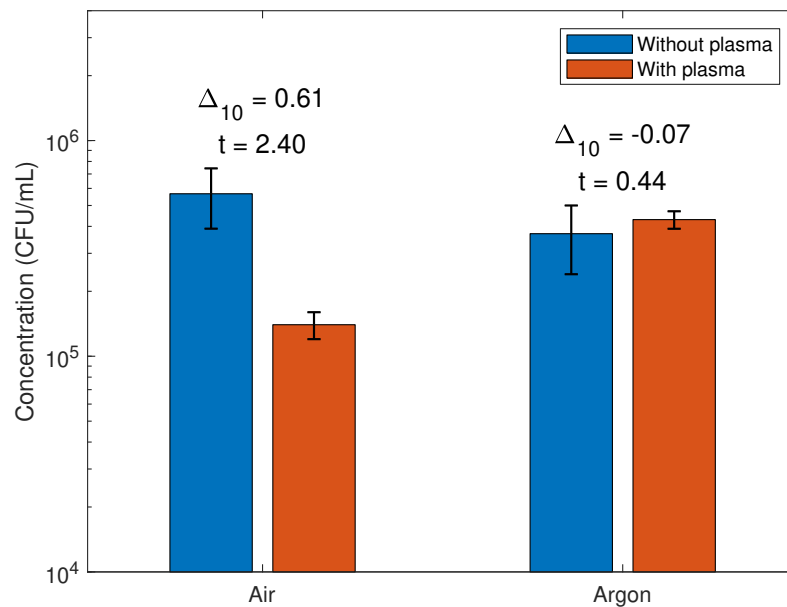


Figure 9.8: Abatement of *E. coli* cells in different atmosphere: (left columns) air and (right columns) argon. (blue bars) Not treated samples, (orange bars) plasma treated samples.

9.2.2 *Staphylococcus epidermidis*

We investigated the *Staphylococcus epidermidis* abatement using only Coriolis collection system.

As we have done for *E. coli*, the bacteria in this experimental campaign are always suspended in NaCl 0.9% and the liquid medium for the collection after treatment is phosphate buffer solution at pH 7.00.

We analyzed the conditions with about 5×10^6 CFU/ml starting concentration and plasma input power at about 16 W; about 1×10^8 CFU/ml starting concentration for plasma input power at about 35 W. The results are shown in Figure 9.9. We can see that in both cases there is an abatement higher than 90% (Table 9.3). The last condition was also tested at FITC. The results are shown in Table 9.4 and Figure 9.10, where we can see that also in the *S. epidermidis* bacteria have a significant increasing of FITC test positivity after plasma treatment.

Comparing the abatement of *S. epidermidis* with the corresponding situation of *E. coli* (Figure 9.4 first two columns block for 16 W plasma power that is less the 75% and Figure 9.6 central block for 35 W plasma power that is 88%) we can notice that the effectiveness of abatement is higher for *S. epidermidis*.

Table 9.3: Log reduction and the compatibility factor of the *S. epidermidis* treatment.

Starting concentration (CFU/ml)	Plasma power (W)	Δ_{10}	t	Abatement
5×10^6	16	1.15 ± 0.11	8.0	92.9%
1×10^8	35	1.20 ± 0.17	4.4	93.6%

Table 9.4: Percentage of FITC positivity bacteria over total number of counted bacteria. The percentage is evaluated over at least 5 images for each condition.

Bacteria		Positivity (%)	t
Vaporized	Not treated	30 ± 3	17
	35 W plasma treated	83 ± 1	

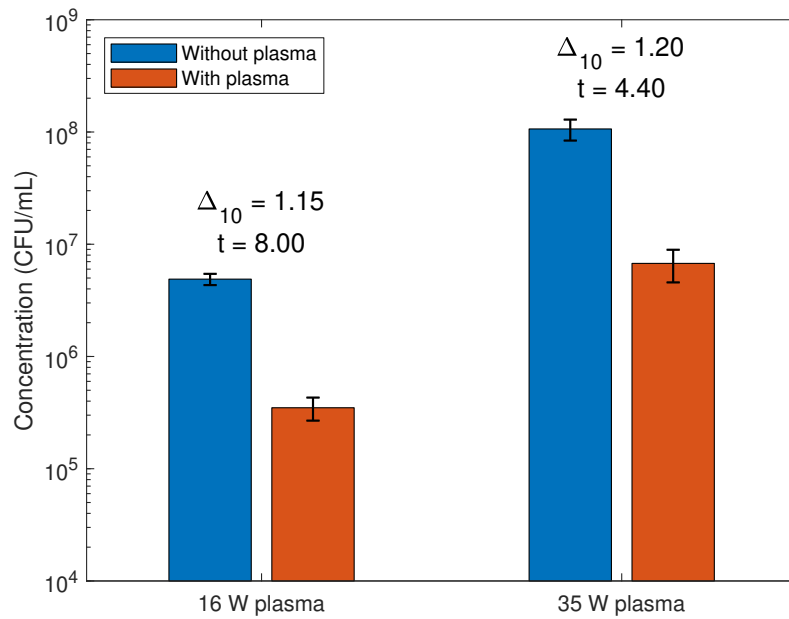


Figure 9.9: Abatement of *S. epidermidis* cells at different plasma conditions and starting concentration: (left columns) 16 W input power of plasma and 5×10^6 CFU/ml (right columns) 35 W input power of plasma and 1×10^8 CFU/ml. (blue bars) Not treated samples, (orange bars) plasma treated samples.

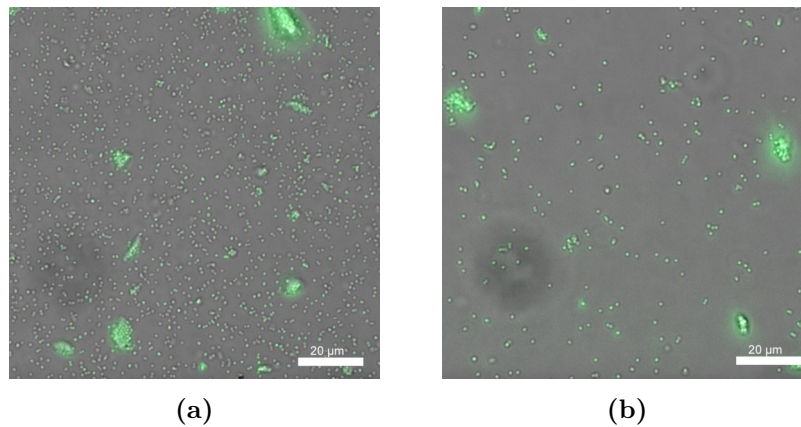


Figure 9.10: *S. epidermidis* FITC images for vaporized (a) untreated and (b) 35 W plasma treated bacteria.

10 Conclusions

We investigated how SDBD (bidirectional alumina) abate bacteria that are vaporized over there. The bacteria we used are *Escherichia coli* and *Staphylococcus epidermidis*, since the first one is Gram-negative and the latter Gram-positive. We used the non-pathogenic strain of both the bacteria species. This system was designed in order to simulate a very contaminated air volume. In general, the room contamination (considering our work office) is in the order of 10^{-5} CFU/ml. We increased the contamination to have a bigger range of investigation and well identify if there is an abatement or not.

The *E. coli* experimental campaign reaches an abatement close to 99.9% starting from the low concentration of about 10^{-3} CFU/ml (of sampled air) collected by the Duo Sas.

The results of the Coriolis sampling of *E. coli* and *S. epidermidis* investigated conditions are summarized in Table 10.1, where the bacteria concentration is expressed in CFU/ml (of liquid).

Table 10.1: Summary of the effectiveness of the *E. coli* and *S. epidermidis* air treatments.

Bacteria	Plasma power (W)	Starting conc. (CFU/ml)	Δ_{10}	t	Abatement
<i>E. coli</i>	16	3.5×10^7	0.51 ± 0.40	0.92	No
		5.5×10^5	0.61 ± 0.15	2.40	75%
		3.5×10^4	1.08 ± 0.12	4.96	92%
		1.5×10^3	> 2.23	> 2.98	$> 99.4\%$
	35	3.5×10^7	0.91 ± 0.10	10.18	88%
<i>S. epidermidis</i>	16	5×10^6	1.15 ± 0.11	8.0	92.9%
	35	1×10^8	1.20 ± 0.17	4.4	93.6%

We can notice that the *E. coli* abatement increase with the decreasing of the starting concentration or with the increasing of the plasma power. The *S. epidermidis* abatement is more effective compared with the respective condition of *E. coli*, meaning that *S. epidermidis* is less resistant to the plasma treatment. Using *E. coli* we also investigate when the abatement happens,

obtaining that it is while the bacteria flow over the plasma and not for a liquid contamination with the reactive species produced by the plasma. The reactive species in the air are responsible for the bacteria abatement since in argon gas plasma we do not see any abatement. In addition, FITC test confirmed that there are bacteria damaging that induces bacteria killing or a reduction in their reproduction.

Thanks to the preliminary measurements we have done registering the contact and gas temperature, we can exclude that the abatement is caused by the temperature increasing, since the air temperature is always between 18 and 25°C.

Part IV

Surface treatments by low pressure cold plasma

11 Equipment setup

In this Chapter we present the equipment setup we used for surface treatments.

The vacuum chamber (Figure 11.1) was designed at the University of Milano-Bicocca by the Plasma Prometeo Center and commissioned to a MORI MECCANICA mechanical workshop (Parma Italy).

The system is made by a vacuum cylinder and two closures, equipped with vacuum feed-throughs for RF power supply, vacuum sensors, gas dispenser, opening for pumping systems, and inspection window made of quartz.

The capacitive antenna was designed and built by the mechanical workshop at the University of Milano-Bicocca. It is made up of two parallel aluminum plates of diameter 190 mm. The distance between the plates can be varied between 3 and 20 cm. The working gas was uniformly distributed in the reactor by the upper shower-head electrode with pinholes of 2 mm diameter (Figure 11.1c). This electrode was connected to a 13.56 MHz RF power supplier (Advanced Energy RFX-600) which provided an RF voltage to the grounded chamber. On the second plate, connected to ground we placed the samples. The maximum working power is 500 W, that correspond to a maximum power density of about 1.8 W/cm^2 .

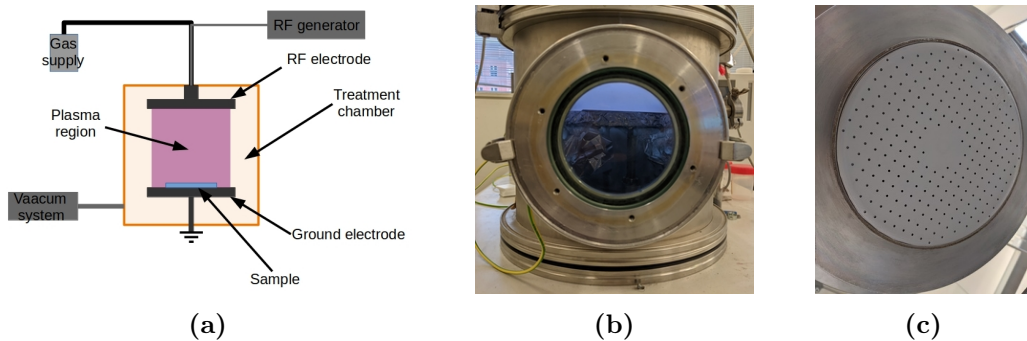


Figure 11.1: (a) Scheme and (b) photo of the experimental setup. (c) Photo of upper shower-head electrode of the capacitive antenna.

The chamber is connected to the pumping system, which allowed to evacuate the reactor up to a residual pressure lower than 10^{-6} mbar. After evacu-

ation, the vacuum chamber is filled with the working gas and the pressure is kept constant inside the reactor.

As a diagnostic we used contact angle, SEM (Scanning Electron Microscopy) and AFM (Atomic Force Microscopy) imaging. The contact angle θ (Figure 11.2) is the angle between a fluid and a solid interface, in the presence of a surrounding gas or different liquid. In our experiments we used water as a fluid and the surrounding gas was air. If θ is greater than 90° (Figure 11.2a) the surface is hydrophobic, if it is smaller (Figure 11.2b) the surface is hydrophilic. For that measurement we used DataPhysics OCA 20 instrument, that allow us to place a defined volume ($3\ \mu\text{L}$) of water over the desired surface and automatically compute the contact angle with the device software SCA20.

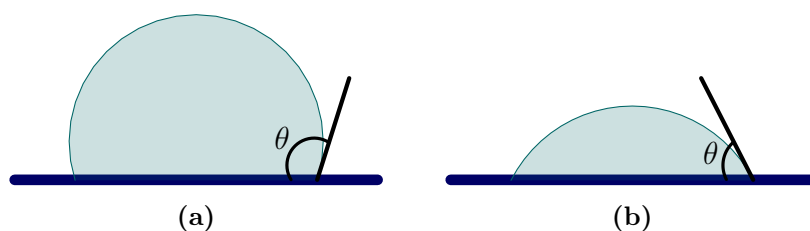


Figure 11.2: Contact angle scheme in case of (a) hydrophobic and (b) hydrophilic surface.

For the SEM analysis we used the FEG microscopy (SEM-FEG) Gemini 500 Zeiss [142]. This microscopy can work with acceleration power in the range of 0.5 and 30 kV, beam currents of 3 pA-20 nA, and it has a nominal resolution of 0.6 nm at 15 kV. As in-camera detectors it has the secondary electrons (SE) and the back-scattered electrons (BSE), but also it has the in-lens (BSE/SE) detector for high resolution images and the STEM detector for the transmission observations for the thick and the biological samples.

For AFM, we used the Nanosurf CoreAFM [143]. It has electronics with 24-bit ADC and DAC that ensure high-resolution XYZ and allow the low-noise force detection limited only by the cantilever. Thirty-two standard and optional modes with fully compatible add-ons make the CoreAFM the tool of choice for applications ranging from materials research to life science and electrochemistry.

In this work we used polypropylene polymers that we treated with oxygen, argon, carbon dioxide and hydrogen for different times, and polytetrafluoroethylene that we treated with oxygen for different times. The description of the used polymers is in Chapter 4.

12 Results and analysis

In this Chapter we are going to present the results of the treatments made using different substrate, gases, and time.

12.1 Polypropylene

We treated $5 \times 5 \text{ cm}^2$ and $20 \mu\text{m}$ thick PP film using different gases and treatment time. The power used for these treatments is about 75 W for O_2 , CO_2 and Ar gases, while 115 W for H_2 . These power were chosen as a compromise of a well diffused switch on plasma and not overheating the sample. The well diffused switch on plasma allowed us to increase the power for the H_2 treatments. In addition, we made an O_2 treatment increasing the power at about 115 W for 5 min. For the different studied condition we evaluated the water contact angle in air, and we watched the SEM images of the sample.

The untreated sample has a contact angle of $(87.0 \pm 0.4)^\circ$, the SEM image reveals a plain surface (Figure 12.1a), with a maximum height, reveled by the AFM (Figure 12.1b), lower than 40 nm.

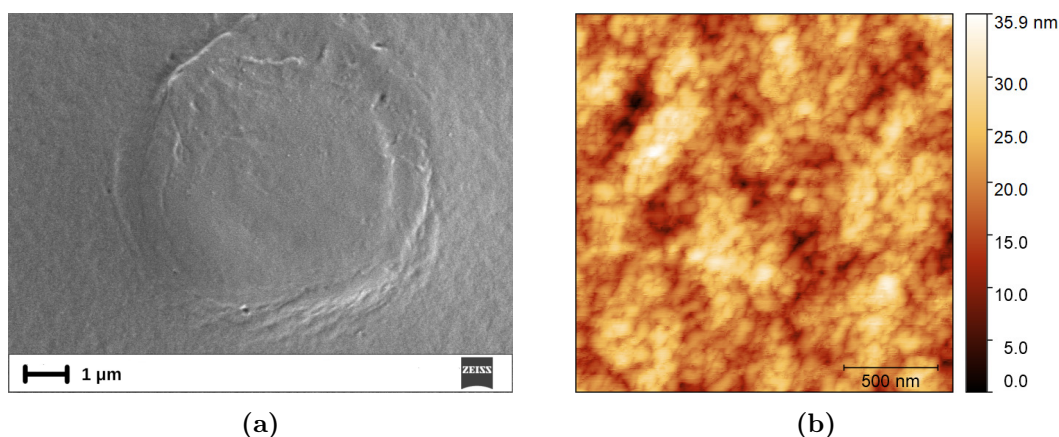


Figure 12.1: (a) SEM image of the untreated PP sample. Images correspond to a 24k magnitude. (b) AFM image of the untreated PP sample. Sample dimension $2 \times 2 \mu\text{m}^2$.

In Figure 12.2 we report the SEM images of the different sample treated

with oxygen. In the SEM images we can identify pillars that with the increasing of the treatment times seems to clustering. That process is due to the chemical etching of the surface by oxygen. The PP treatment seems to be different from what we observed in the PET (polyethylene terephthalate) samples discussed in our previous work *Hydrophilicity and Hydrophobicity Control of Plasma-Treated Surfaces via Fractal Parameters* [144], where we can identify two competitive processes that produce the nanostructurization: polymer chemical etching by oxygen, that produces hollow of the order of 200 nm, and low weight molecular polymer clusters deposition with size of 10-100 nm. These different behaviors are mainly due to the different chemistry of the polymers, in fact PP is composed of an aliphatic chain of carbon and hydrogen, while PET has both aromatic and linear components made by carbon, hydrogen and oxygen.

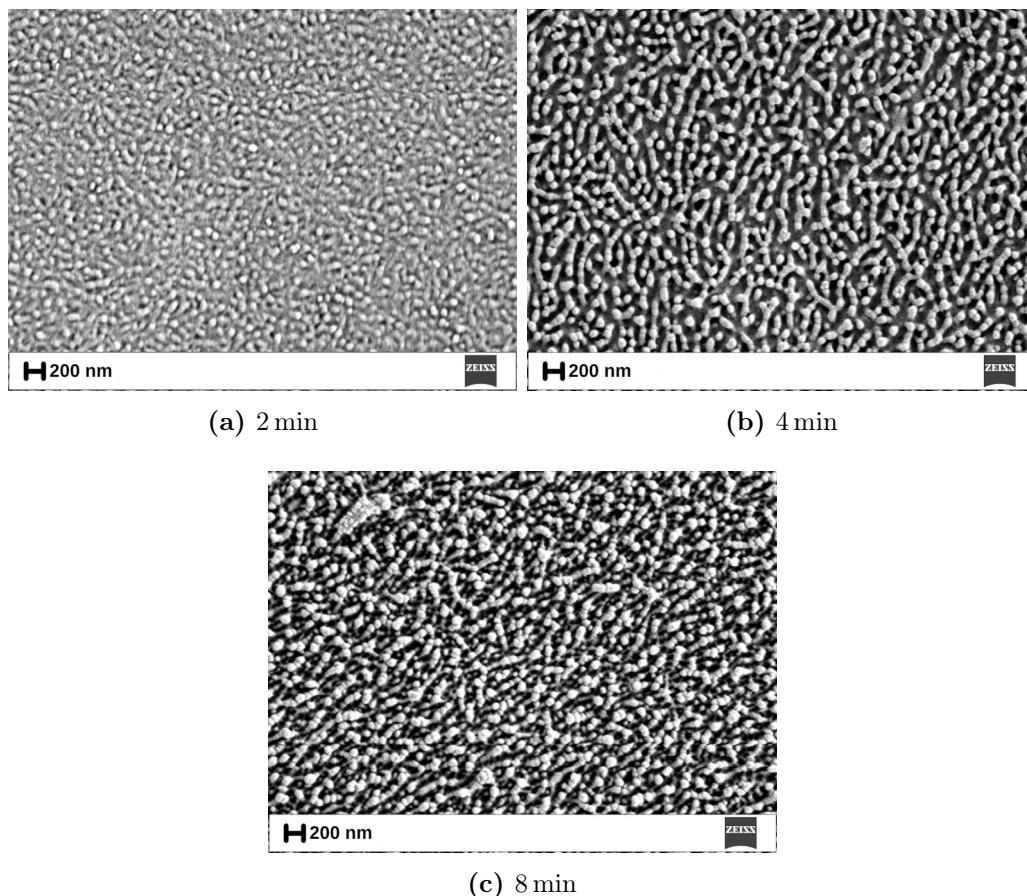


Figure 12.2: SEM images of the O_2 75 W treated sample for different treatment times. Images correspond to a 50k magnitude.

The increase of the power (Figure 12.3) produces the formation of the

pillars arranged in a cauliflower like structure. Over this sample we made also the AFM, and we studied its fractality. From Figure 12.3b we can see that the maximum height of the pillars is about five times higher than the untreated one. For the study of the fractality we used a similar method as the described in [20]. The AFM image has 512×512 pixels and can be visualized as a matrix of indices (i, k) , where each element (i, k) has an associated height z .

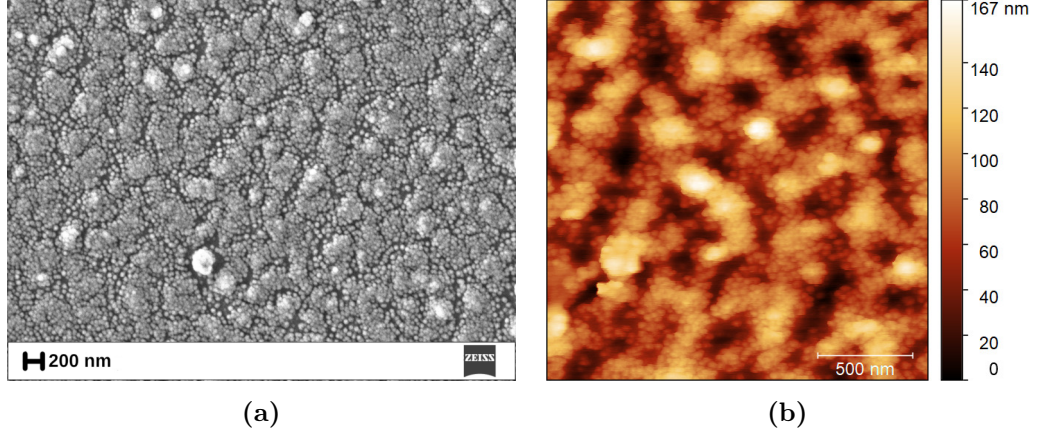


Figure 12.3: O₂ treatment at 115 W for 5 min. (a) SEM images at magnitude 50k. (b) AFM images with sample dimension $2 \times 2 \mu\text{m}^2$.

To study the profile we can fix the column k (in Figure 12.4a is shown an example for both untreated and treated sample) and define the signal as

$$\mathcal{S}(i) = z_k(i), \quad \text{at fixed } k, \quad (12.1)$$

or we can fix the row i (Figure 12.4b) and define the signal as

$$\mathcal{S}(k) = z_i(k), \quad \text{at fixed } i, \quad (12.2)$$

where $1 \leq i, k \leq N$ and $N = 512$ is the number of pixels. The mean roughness of the samples are (20 ± 5) nm for the untreated and (70 ± 30) nm for the treated one.

In order to determine the degree of auto-correlation in the signal, we rely on the calculation of the Hurst exponent [145–147]. At ‘distance scale’ $1 \leq \ell \leq N$, we evaluate the m th ($1 \leq m \leq \lfloor N/\ell \rfloor$) mean random walk profile given by,

$$\mathcal{B}_m(\ell) = \frac{1}{\ell} \sum_{n=1}^{\ell} \mathcal{S}[(m-1)\ell + n], \quad (12.3)$$

and we studied the fluctuation between neighboring boxes according to

$$\mathcal{F}(\ell) = \langle [\mathcal{B}_{m+1}(\ell) - \mathcal{B}_m(\ell)]^2 \rangle^{1/2}, \quad (12.4)$$

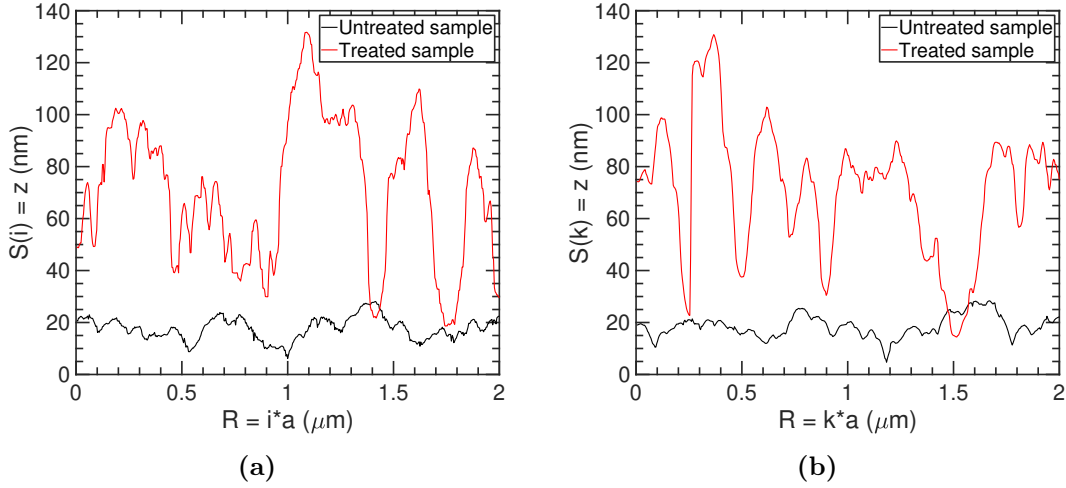


Figure 12.4: Examples of untreated and treated profiles for: (a) fixed column, and (b) fixed row. Here, a is the pixel size.

which is expected to display a power-law behavior

$$\mathcal{F}(\ell) \sim \ell^H, \quad (12.5)$$

where $0 \leq H \leq 1$. This relation can be expressed in terms of real distances considering that $\ell = R/a$ (R is the distance and a is the pixel dimension in nm),

$$\mathcal{F}(R) \sim \left(\frac{R}{a}\right)^H. \quad (12.6)$$

It is convenient to average $\mathcal{F}(\ell)$ over all the columns and rows to reduce the statistical errors. We found that, for both the analyzed length scales, the Hurst exponent for the treated sample is $H = 0.75$ (Figure 12.5). This suggests the presence of persistent (positive) correlations of height-height fluctuations up to $R \simeq 40$ nm for $L = 2 \mu\text{m}$. This fractal regime extends further for $L = 1 \mu\text{m}$, reaching $R \simeq 70$ nm. The thus obtained values of H provide an estimate of the actual surface fractal dimension (within the same length scales) of $d_s = 3 - H \simeq 2.25 > 2$. A similar fractal dimension ($d_s \simeq 2.2$) was found in [144] over PET treatments.

The CO_2 treatment (Figure 12.6) does not seem to induce any nanostructurization of the PP samples, apart for the creation of little holes from the chemical etching due to CO_2 .

Argon treatments (Figure 12.7) induced a low nanostructurization and a deposition of about 200 nm or less diameter carbon sphere that are due to the

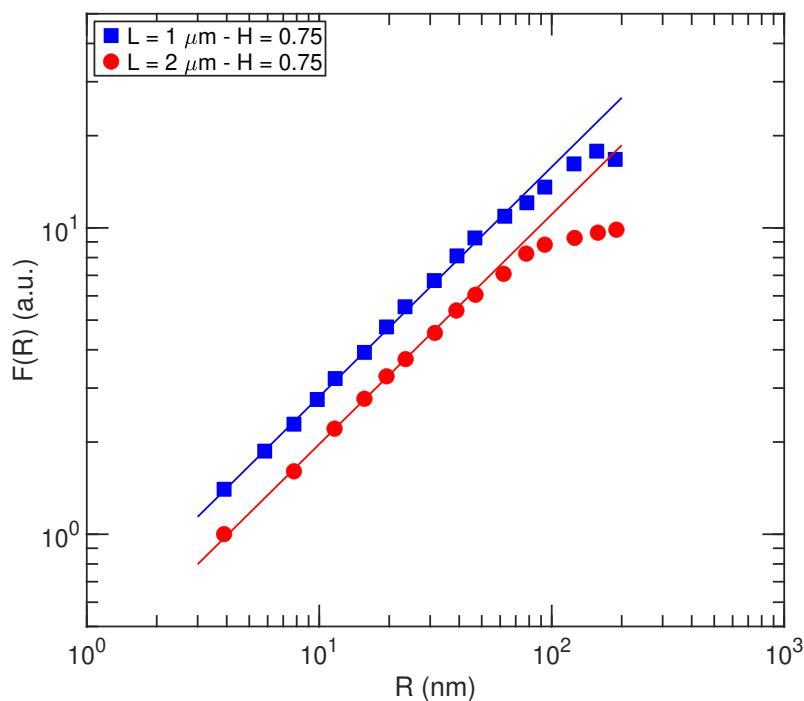


Figure 12.5: Fluctuation analysis of surface height variations vs length scale R (nm). The curves have been vertically shifted for clarity and $F(R)$ is expressed in arbitrary unit.

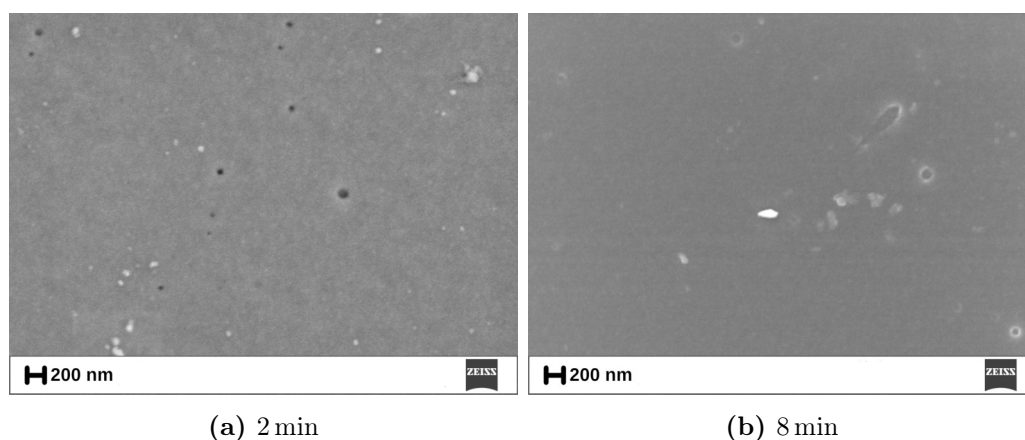


Figure 12.6: SEM images of the CO_2 treated sample for different treatment times. Images correspond to a 50k magnitude.

argon plasma carbonization. This behavior is typical of Ar plasmas over the surfaces since argon can not oxidize the evaporated broken carbon chain, as it happens with oxygen plasma.

The H_2 treatments (Figure 12.8) induced a very dense nanostructurization with different deepness according to the film region. Similar behavior was observed with the atmospheric pressure plasma treatment over PP [49].

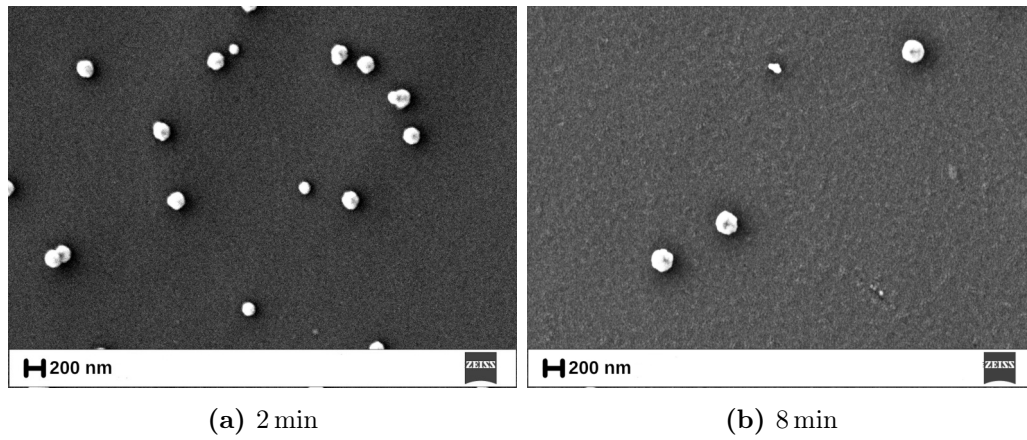


Figure 12.7: SEM images of the Ar treated sample for different treatment times. Images correspond to a 50k magnitude.

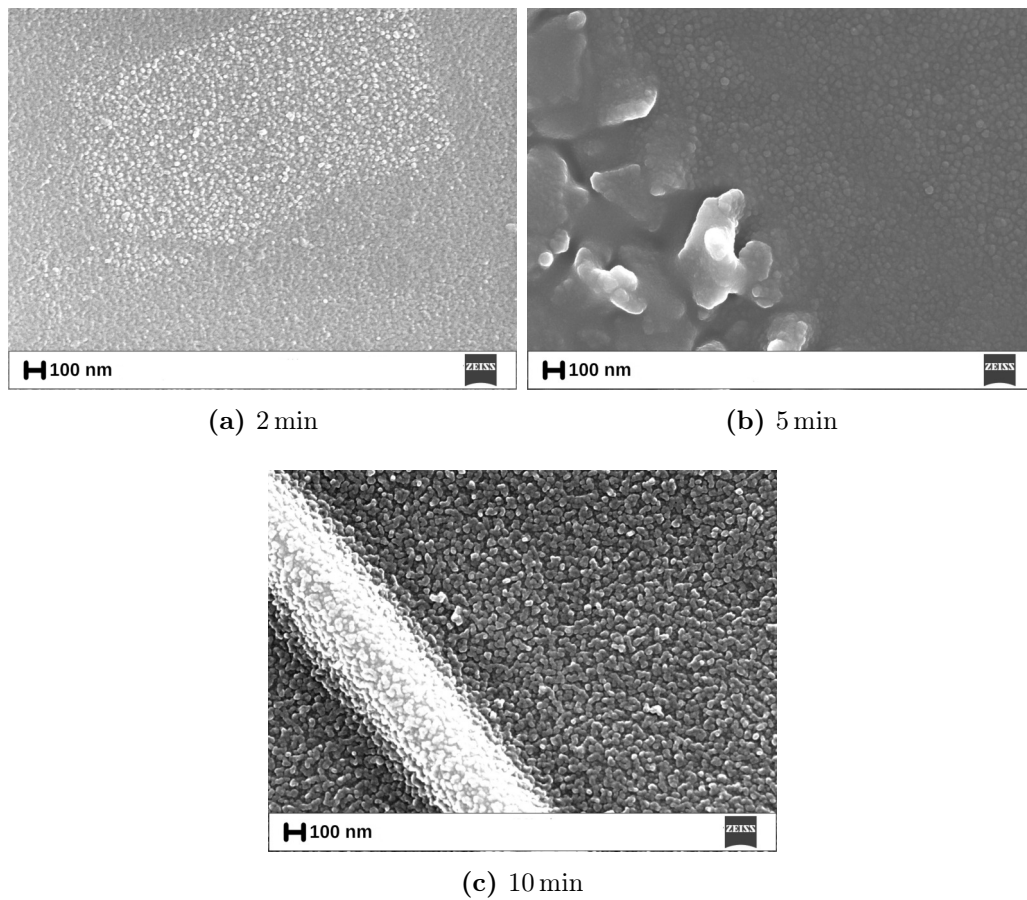


Figure 12.8: SEM images of the H₂ treated sample for different treatment times. Images correspond to a 100k magnitude.

The contact angle θ trends for the different gases are shown in Figure 12.9. For O_2 , CO_2 and Ar treatments, we found a decreasing of the contact angle which depends on the type of gas used, while for O_2 there is a saturation after 4 min of treatment. On the other hand, the H_2 treatment induces an increasing of the contact angle, meaning that the modified surface becomes hydrophobic. The O_2 results confirm the data in [148], where they attribute the reduction in contact angle values by the formation of oxygen functional groups on the polypropylene surfaces.

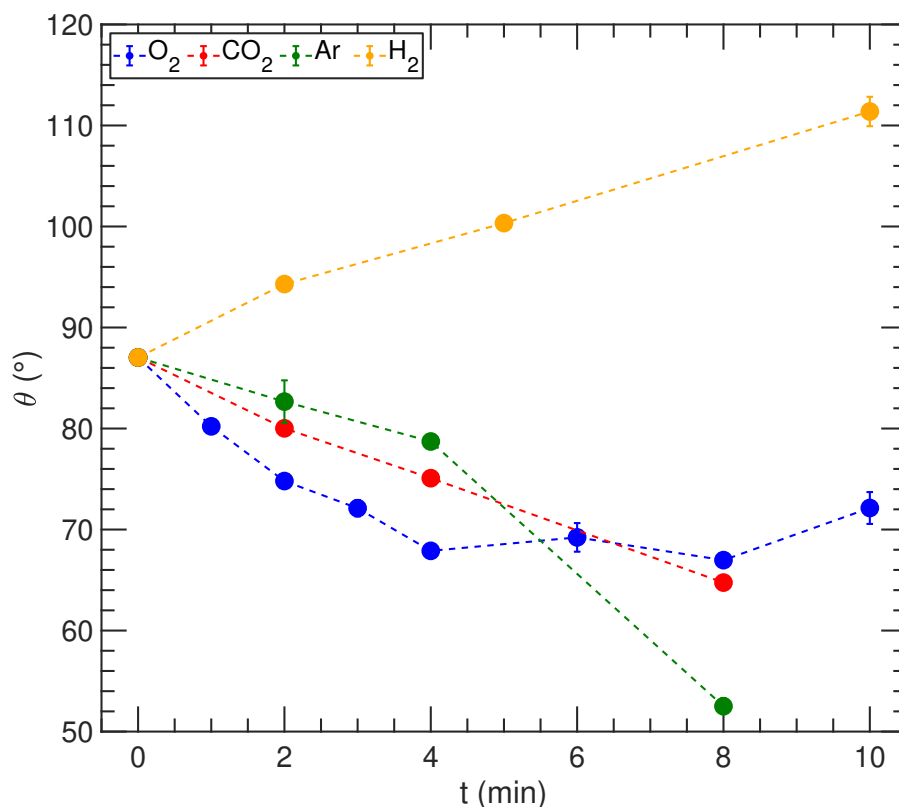


Figure 12.9: Contact angle as a function of time for the different treatment gases.

12.2 Polytetrafluoroethylene

We treated $5 \times 5 \text{ cm}^2$ and 4 mm thick PTFE samples using different treatment times. The power used for these treatments is about 150 W and the used gas is O_2 . We chose a higher power than for PP, since PTFE is much more resistant and requires more power for its modification.

By looking at the SEM images in Figure 12.10 the nanometrical structure of the treated polymers compared with the untreated one, we can identify two competitive processes: etching and low weight molecular polymer clusters deposition, similar to what happens in PET treatments [20].

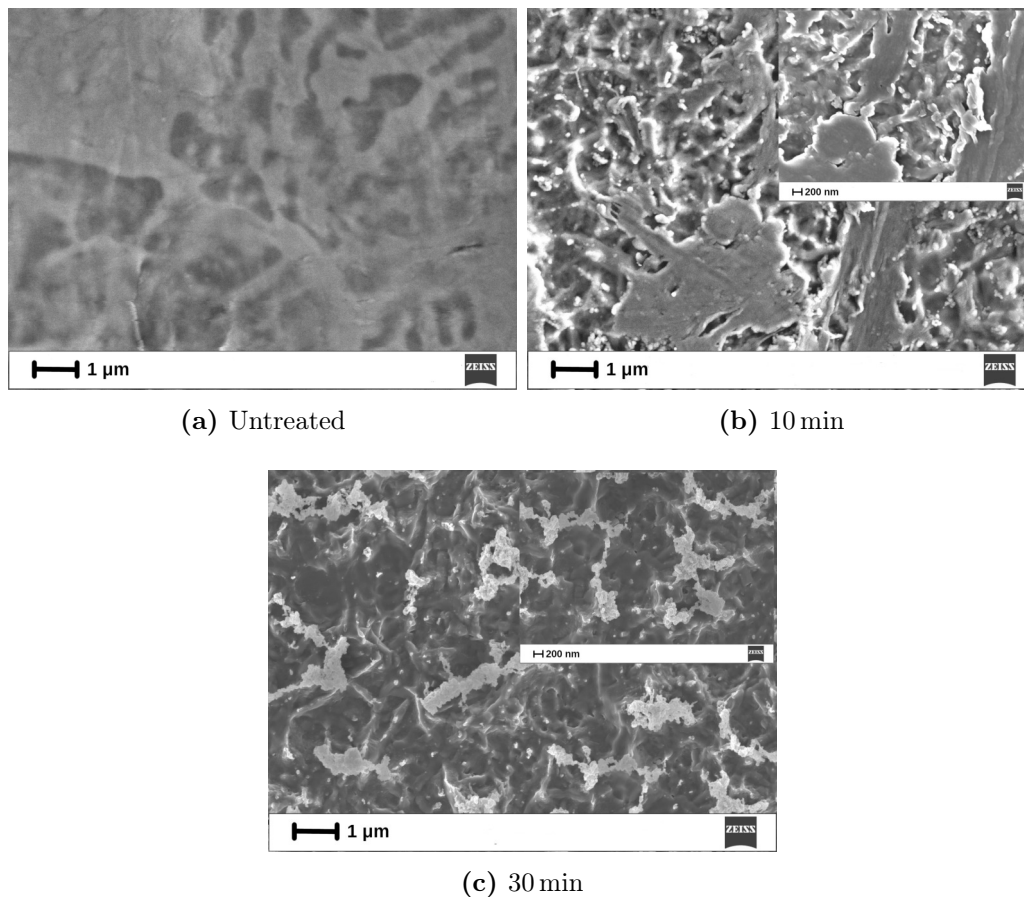


Figure 12.10: SEM images of the untreated and O_2 treated PTFE sample for different treatment times. Images correspond to 24k and 50k magnitude.

In Figure 12.11 we can see that the O_2 plasma treatment induces an increasing of the contact angle, obtaining a condition of super-hydrophobicity, from about $\theta = 105^\circ$ for the untreated sample to about $\theta = 140^\circ$ for the 30 min treated one. This is the opposite behavior to the PET samples [144], where

starting from $\theta = 90^\circ$ of the untreated sample, it reaches a super-hydrophilic condition after 30 min of treatment with $\theta < 10^\circ$. These results confirm that low pressure oxygen plasma over PTFE is able to sculpture nano-features on its surface and producing a super-hydrophobic material, as previously found in Ref. [51].

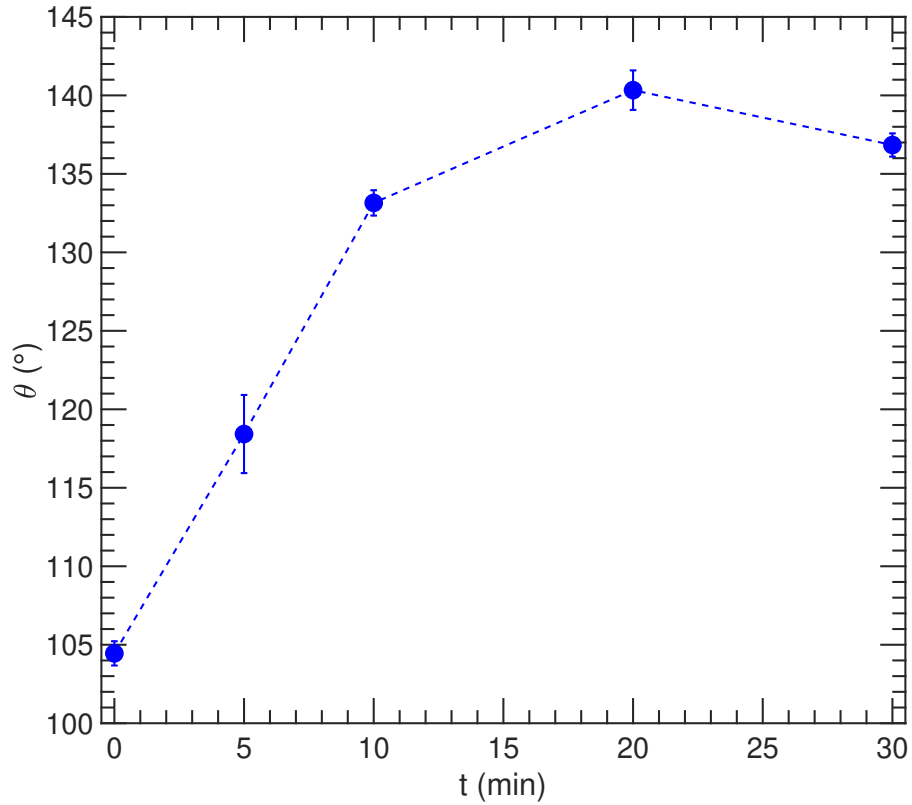


Figure 12.11: Contact angle of the PTFE surfaces in function of time.

13 Conclusions

Nanostructured surfaces are a growing research field for their variety of applications, as we detailed in the Chapter 4. The present experiments were focused on the nanostructurization of materials, which can be useful for creating antibacterial surfaces or materials displaying antifouling properties.

For the polypropylene samples we found out different nanostructurization depending on the used gas. O_2 treatment induces the creation of pillars that with the increasing of the treatment times seems to clustering; CO_2 does not produce a nanostructurization but generates nanometrical holes; Ar causes a dense base nanostructurization with the deposition of carbon spheres; H_2 formed a nanostructurization over different length scales, but further work is necessary in order to elucidate possible fractal properties. As a consequence, also different contact angle trends are identified: a decreasing angle for O_2 , CO_2 and Ar treatment, and an increasing one for H_2 . For the O_2 treatments we also made AFM analysis finding that the treated surfaces have a fractal dimension $d_s \simeq 2.25$. These microscopical and macroscopical modifications are interesting since we can modify a polymeric surface according to the specific application, without interfering with the chemical-physical properties of the polymer, such as strength, color or composition.

The polytetrafluoroethylene samples are more resistant, and so we used higher power for the plasma treatments respect to the one we used for PP. For this experimental campaign we used only O_2 as plasma working gas. Looking at the SEM images we can identify the growth of nanostructures over the different treatment times of PTFE samples, due to the chemical etching and the low weight polymer clusters deposition. These nanostructures are visible at different length scales, showing a sort of fractal structure. These features, such as e.g. the fractal dimension, remain to be investigated using AFM imaging and statistical analysis.

Part V

Appendix

Bibliography

- [1] WHO, “One health.” <https://www.who.int/news-room/questions-and-answers/item/one-health>.
- [2] EEA, “Air quality standards,” *European Environment Agency*, 2017.
- [3] A. M. Vandenbroucke, R. Morent, N. De Geyter, and C. Leys, “Non-thermal plasmas for non-catalytic and catalytic VOC abatement,” *Journal of Hazardous Materials*, vol. 195, pp. 30 – 54, 2011.
- [4] E. Donley and D. Lewandowski, “Optimized design and operating m911 parameters for minimizing emissions 24& 7 during voc thermal oxidation,” *Metal finishing*, 1996.
- [5] W. Wang, X. Ma, S. Grimes, H. Cai, and M. Zhang, “Study on the adsorbability, regeneration characteristics and thermal stability of ionic liquids for vocs removal,” *Chemical Engineering Journal*, vol. 328, pp. 353–359, 2017.
- [6] I. Aguayo-Villarreal, M. Montes-Morán, V. Hernández-Montoya, A. Bonilla-Petriciolet, A. Concheso, C. Rojas-Mayorga, and J. González, “Importance of iron oxides on the carbons surface vs the specific surface for voc’s adsorption,” *Ecological engineering*, vol. 106, pp. 400–408, 2017.
- [7] A. Vergara-Fernández, S. Revah, P. Moreno-Casas, and F. Scott, “Biofiltration of volatile organic compounds using fungi and its conceptual and mathematical modeling,” *Biotechnology advances*, vol. 36, no. 4, pp. 1079–1093, 2018.
- [8] B. Belaisaoui, Y. Le Moullec, and E. Favre, “Energy efficiency of a hybrid membrane/condensation process for voc (volatile organic compounds) recovery from air: A generic approach,” *Energy*, vol. 95, pp. 291–302, 2016.
- [9] X. Chen, S. Carabineiro, S. Bastos, P. B. Tavares, J. Órfão, M. Pereira, and J. L. Figueiredo, “Catalytic oxidation of ethyl acetate on cerium-

- containing mixed oxides,” *Applied Catalysis A: General*, vol. 472, pp. 101–112, 2014.
- [10] M. Schiavon, V. Torretta, A. Casazza, and M. Ragazzi, “Non-thermal plasma as an innovative option for the abatement of volatile organic compounds: a review,” *Water, Air, & Soil Pollution*, vol. 228, no. 10, pp. 1–20, 2017.
- [11] S. Li, X. Dang, X. Yu, G. Abbas, Q. Zhang, and L. Cao, “The application of dielectric barrier discharge non-thermal plasma in VOCs abatement: A review,” *Chemical Engineering Journal*, vol. 388, p. 124275, 2020.
- [12] C. Dobslaw and B. Glocker, “Plasma technology and its relevance in waste air and waste gas treatment,” *Sustainability*, vol. 12, no. 21, p. 8981, 2020.
- [13] S. Choi, S. H. Hong, H. S. Lee, and T. Watanabe, “A comparative study of air and nitrogen thermal plasmas for pfc’s decomposition,” *Chemical Engineering Journal*, vol. 185, pp. 193–200, 2012.
- [14] D. H. Shin, Y. C. Hong, S. J. Lee, Y. J. Kim, C. H. Cho, S. H. Ma, S. M. Chun, B. J. Lee, and H. S. Uhm, “A pure steam microwave plasma torch: gasification of powdered coal in the plasma,” *Surface and Coatings Technology*, vol. 228, pp. S520–S523, 2013.
- [15] A. Suris, “Investigation of high-temperature steam–air reagents for plasma waste treatment processes,” *Theoretical Foundations of Chemical Engineering*, vol. 51, no. 3, pp. 348–351, 2017.
- [16] L. Pietanza, G. Colonna, and M. Capitelli, “Kinetics versus thermodynamics on co₂ dissociation in high temperature microwave discharges,” *Plasma Sources Science and Technology*, vol. 29, no. 3, p. 035022, 2020.
- [17] A. George, B. Shen, M. Craven, Y. Wang, D. Kang, C. Wu, and X. Tu, “A review of non-thermal plasma technology: A novel solution for co₂ conversion and utilization,” *Renewable and Sustainable Energy Reviews*, vol. 135, p. 109702, 2021.
- [18] R. Barni, R. Benocci, N. Spinicchia, H. E. Roman, and C. Riccardi, “An experimental study of plasma cracking of methane using dbds aimed

- at hydrogen production,” *Plasma Chemistry and Plasma Processing*, vol. 39, no. 1, pp. 241–258, 2019.
- [19] D. Dobslaw, O. Ortlinghaus, and C. Dobslaw, “A combined process of non-thermal plasma and a low-cost mineral adsorber for voc removal and odor abatement in emissions of organic waste treatment plants,” *Journal of Environmental Chemical Engineering*, vol. 6, no. 2, pp. 2281–2289, 2018.
- [20] C. Piferi, R. Barni, H. E. Roman, and C. Riccardi, “Current Filaments in Asymmetric Surface Dielectric Barrier Discharge,” *Applied Sciences*, vol. 11, no. 5, p. 2079, 2021.
- [21] A. A. Abdelaziz, T. Seto, M. Abdel-Salam, and Y. Otani, “Performance of a surface dielectric barrier discharge based reactor for destruction of naphthalene in an air stream,” *Journal of Physics D: Applied Physics*, vol. 45, no. 11, p. 115201, 2012.
- [22] A. A. Assadi, A. Bouzaza, and D. Wolbert, “Comparative study between laboratory and large pilot scales for voc’s removal from gas streams in continuous flow surface discharge plasma,” *Chemical Engineering Research and Design*, vol. 106, pp. 308–314, 2016.
- [23] C. Piferi, M. Daghetta, M. Schiavon, H. E. Roman, and C. Riccardi, “Pentane Depletion by a Surface DBD and Catalysis Processing,” *Applied Sciences*, vol. 12, no. 9, p. 4253, 2022.
- [24] C. Piferi and C. Riccardi, “A study on propane depletion by Surface Dielectric Barrier Discharges,” *Cleaner Engineering and Technology*, vol. 8, p. 100486, 2022.
- [25] C. Piferi and C. Riccardi, “High concentration propane depletion with photocatalysis,” *AIP Advances*, vol. 11, no. 12, p. 125008, 2021.
- [26] WHO, “Antimicrobial resistance.” <https://www.who.int/news-room/fact-sheets/detail/antimicrobial-resistance>.
- [27] M. Yao, G. Mainelis, and H. R. An, “Inactivation of microorganisms using electrostatic fields,” *Environmental science & technology*, vol. 39, no. 9, pp. 3338–3344, 2005.

- [28] K. F. McDonald, R. D. Curry, and P. J. Hancock, "Comparison of pulsed and CW ultraviolet light sources to inactivate bacterial spores on surfaces," *IEEE transactions on plasma science*, vol. 30, no. 5, pp. 1986–1989, 2002.
- [29] T. Guan and M. Yao, "Use of carbon nanotube filter in removing bioaerosols," *Journal of Aerosol Science*, vol. 41, no. 6, pp. 611–620, 2010.
- [30] Q. Zhang, B. Damit, J. Welch, H. Park, C.-Y. Wu, and W. Sigmund, "Microwave assisted nanofibrous air filtration for disinfection of bioaerosols," *Journal of Aerosol Science*, vol. 41, no. 9, pp. 880–888, 2010.
- [31] H. Zerrouki, V. Rizzati, C. Bernis, A. Nègre-Salvayre, J. P. Sarrette, and S. Cousty, "Escherichia coli morphological changes and lipid: A removal induced by reduced pressure nitrogen afterglow exposure," *PLoS One*, vol. 10, no. 4, p. e0116083, 2015.
- [32] M. Moreau, N. Orange, and M. Feuilleley, "Non-thermal plasma technologies: new tools for bio-decontamination," *Biotechnology advances*, vol. 26, no. 6, pp. 610–617, 2008.
- [33] M. Cooper, G. Fridman, A. Fridman, and S. Joshi, "Biological responses of bacillus stratosphericus to floating electrode-dielectric barrier discharge plasma treatment," *Journal of applied microbiology*, vol. 109, no. 6, pp. 2039–2048, 2010.
- [34] S. G. Joshi, M. Paff, G. Friedman, G. Fridman, A. Fridman, and A. D. Brooks, "Control of methicillin-resistant staphylococcus aureus in planktonic form and biofilms: a biocidal efficacy study of nonthermal dielectric-barrier discharge plasma," *American journal of infection control*, vol. 38, no. 4, pp. 293–301, 2010.
- [35] N. D. Vaze, S. Park, A. D. Brooks, A. Fridman, and S. G. Joshi, "Involvement of multiple stressors induced by non-thermal plasma-charged aerosols during inactivation of airborne bacteria," *PLOS ONE*, vol. 12, no. 2, p. e0171434, 2017.
- [36] Y. Liang, Y. Wu, K. Sun, Q. Chen, F. Shen, J. Zhang, M. Yao, T. Zhu, and J. Fang, "Rapid Inactivation of Biological Species in the Air using

-
- Atmospheric Pressure Nonthermal Plasma,” *Environmental Science & Technology*, vol. 46, no. 6, pp. 3360–3368, 2012.
- [37] P. Brun, V. Russo, E. Tarricone, S. Corrao, V. Deligianni, A. Leonardi, R. Cavazzana, M. Zuin, and E. Martines, “Using helium-generated cold plasma to control infection and healing,” *Plasma Medicine*, vol. 5, no. 2-4, 2015.
- [38] Y. P. Raizer, *Gas discharge physics*. Springer-Verlag, 1991.
- [39] L. Liu, S. Wang, H. Huang, Y. Zhang, and T. Ma, “Surface sites engineering on semiconductors to boost photocatalytic co2 reduction,” *Nano Energy*, vol. 75, p. 104959, 2020.
- [40] V. Trifiletti, R. Ruffo, C. Turrini, D. Tassetti, R. Brescia, F. Di Fonzo, C. Riccardi, and A. Abbotto, “Dye-sensitized solar cells containing plasma jet deposited hierarchically nanostructured tio 2 thin photoanodes,” *Journal of Materials Chemistry A*, vol. 1, no. 38, pp. 11665–11673, 2013.
- [41] S. Zanini, A. Polissi, E. A. Maccagni, E. C. Dell’Orto, C. Liberatore, and C. Riccardi, “Development of antibacterial quaternary ammonium silane coatings on polyurethane catheters,” *Journal of colloid and interface science*, vol. 451, pp. 78–84, 2015.
- [42] S. Zanini, L. Zoia, R. Della Pergola, and C. Riccardi, “Pulsed plasma-polymerized 2-isopropenyl-2-oxazoline coatings: Chemical characterization and reactivity studies,” *Surface and Coatings Technology*, vol. 334, pp. 173–181, 2018.
- [43] T. Zhao, J. Li, H. Zeng, Y. Fu, H. He, L. Xing, Y. Zhang, and X. Xue, “Self-powered wearable sensing-textiles for real-time detecting environmental atmosphere and body motion based on surface-triboelectric coupling effect,” *Nanotechnology*, vol. 29, no. 40, p. 405504, 2018.
- [44] E. Dell’Orto, S. Caldirola, A. Sassella, V. Morandi, and C. Riccardi, “Growth and properties of nanostructured titanium dioxide deposited by supersonic plasma jet deposition,” *Applied Surface Science*, vol. 425, pp. 407–415, 2017.
-

- [45] X. Wang, L. Zhuang, Y. Jia, H. Liu, X. Yan, L. Zhang, D. Yang, Z. Zhu, and X. Yao, "Plasma-triggered synergy of exfoliation, phase transformation, and surface engineering in cobalt diselenide for enhanced water oxidation," *Angewandte Chemie International Edition*, vol. 57, no. 50, pp. 16421–16425, 2018.
- [46] T. Heinzl and R. Stewart, "Introduction: Textile intersections-textile discipline at cross-roads," 2021.
- [47] M. Radetić and D. Marković, "Nano-finishing of cellulose textile materials with copper and copper oxide nanoparticles," *Cellulose*, vol. 26, no. 17, pp. 8971–8991, 2019.
- [48] H. Saleem and S. J. Zaidi, "Sustainable use of nanomaterials in textiles and their environmental impact," *Materials*, vol. 13, no. 22, p. 5134, 2020.
- [49] E. Dell'Orto, A. Vaccaro, and C. Riccardi, "Morphological and chemical analysis of pp film treated by dielectric barrier discharge," in *Journal of Physics: Conference Series*, vol. 550, p. 012032, IOP Publishing, 2014.
- [50] A. V. Abramova, V. O. Abramov, V. M. Bayazitov, Y. Voitov, E. A. Straumal, S. A. Lermontov, T. A. Cherdyntseva, P. Braeutigam, M. Weiße, and K. Günther, "A sol-gel method for applying nanosized antibacterial particles to the surface of textile materials in an ultrasonic field," *Ultrasonics sonochemistry*, vol. 60, p. 104788, 2020.
- [51] C. L. Porto, R. Di Mundo, V. Veronico, I. Trizio, G. Barucca, and F. Palumbo, "Easy plasma nano-texturing of ptfе surface: From pyramid to unusual spherules-on-pyramid features," *Applied Surface Science*, vol. 483, pp. 60–68, 2019.
- [52] S. Zanini, L. Zoia, E. C. Dell'Orto, A. Natalello, A. M. Villa, R. Della Pergola, and C. Riccardi, "Plasma polymerized 2-ethyl-2-oxazoline: Chemical characterization and study of the reactivity towards different chemical groups," *Materials & Design*, vol. 108, pp. 791–800, 2016.

- [53] P. D. Venkatraman, U. Sayed, S. Parte, and S. Korgaonkar, "Development of advanced textile finishes using nano-emulsions from herbal extracts for organic cotton fabrics," *Coatings*, vol. 11, no. 8, p. 939, 2021.
- [54] Y. Lv, X. Xi, L. Dai, S. Tong, and Z. Chen, "Hydrogel as a superwetting surface design material for oil/water separation: a review," *Advanced Materials Interfaces*, vol. 8, no. 7, p. 2002030, 2021.
- [55] J. Bittencourt, *Fundamentals of Plasma Physics*. Springer Science+Business Media New York, 2004.
- [56] P. M. Bellan, *Fundamentals of Plasma Physics*. Cambridge University Press, 2006.
- [57] U. Kogelschatz, B. Eliasson, and W. Egli, "Dielectric-Barrier Discharges. Principle and Applications," vol. 07, 10 1997.
- [58] U. Kogelschatz, "Dielectric-Barrier Discharges: Their History, Discharge Physics, and Industrial Applications," *Plasma Chemistry and Plasma Processing*, vol. 23, pp. 1–46, 03 2003.
- [59] U. Kogelschatz, "Filamentary, Patterned, and Diffuse Barrier Discharges," *Plasma Science, IEEE Transactions on*, vol. 30, pp. 1400 – 1408, 09 2002.
- [60] B. Eliasson and U. Kogelschatz, "Modeling and applications of silent discharge plasmas," *IEEE Transactions on Plasma Science*, vol. 19, pp. 309–323, April 1991.
- [61] A. Fridman, A. Chirokov, and A. Gutsol, "Non-thermal atmospheric pressure discharges," *Journal of Physics D: Applied Physics*, vol. 38, pp. R1–R24, jan 2005.
- [62] M. A. Lieberman and A. J. Lichtenberg, *Principles of Plasma Discharges and Materials Processing, Second Edition*. John Wiley & Sons, Inc, 2005.
- [63] EEA, "Air pollution," *European Environment Agency*, 2017.
- [64] European Commission, "Harmonisation framework for health based evaluation of indoor emissions from construction products in the European Union using the EU-LCI concept Report n.29," *European Commission*

Institute for Health and Consumer Protection Chemical Assessment and Testing Unit, 2013.

- [65] M. Fellin, M. Negri, and M. Marra, “Legislazione e normativa nazionale ed europea inerente le emissioni di composti organici volatili e di formaldeide dei prodotti a base legno in ambiente domestico,” *Foroeuropa*, 2018.
- [66] European Parliament, “Directive EU 2016/2284 on the reduction of national emissions of certain atmospheric pollutants,” *Official Journal of the European Union*, 2016.
- [67] Umweltbundesamt, “Beurteilung von Innenraumluftkontaminationen mittels Referenz und Richtwerten,” *Bundesgesundheitsblatt Gesundheitsforschung Gesundheitsschutz*, vol. 50, pp. 990–1005, 07 2007.
- [68] United States Environmental Protection Agency, “Sick Building Syndrome, Indoor Air Facts No. 4 (revised),” *United States Environmental Protection Agency*, 1991.
- [69] F. Thevenet, L. Sivachandiran, O. Guaitella, C. Barakat, and A. Rousseau, “Plasma-catalyst coupling for volatile organic compound removal and indoor air treatment: A review,” *Journal of Physics D: Applied Physics*, vol. 47, p. 224011, 05 2014.
- [70] M. Schiavon, M. Scapinello, P. Tosi, M. Ragazzi, V. Torretta, and E. Rada, “Potential of non-thermal plasmas for helping the biodegradation of volatile organic compounds (VOCs) released by waste management plants,” *Journal of Cleaner Production*, vol. 104, 05 2015.
- [71] A. Abdelaziz, T. Seto, M. Abdel-Salam, and Y. Otani, “Performance of a surface dielectric barrier discharge based reactor for destruction of naphthalene in an air stream,” *Journal of Physics D-applied Physics - J PHYS-D-APPL PHYS*, vol. 45, 03 2012.
- [72] GESTIS-Stoffdatenbank, “n-pentane.” <https://gestis.dguv.de/data?name=010040&lang=en>.
- [73] GESTIS-Stoffdatenbank, “Propane.” <https://gestis.dguv.de/data?name=010020&lang=en>.

- [74] J. Douwes, P. Thorne, N. Pearce, and D. Heederik, “Bioaerosol health effects and exposure assessment: progress and prospects,” *The Annals of occupational hygiene*, vol. 47, no. 3, pp. 187–200, 2003.
- [75] D. Pomata, P. Di Filippo, C. Riccardi, F. Buiarelli, G. Simonetti, and F. Castellani, “Procedura sperimentale per la determinazione della componente batterica del materiale particolato.” https://www.inail.it/cs/internet/docs/alg-pubbl-procedura-sperim-per-detterm-comp-batterica_6443144134235.pdf.
- [76] M. Möritz, H. Peters, B. Nipko, and H. Rüden, “Capability of air filters to retain airborne bacteria and molds in heating, ventilating and air-conditioning (HVAC) systems,” *International journal of hygiene and environmental health*, vol. 203, no. 5-6, pp. 401–409, 2001.
- [77] M. Otto, “Staphylococcus epidermidis—the ‘accidental’ pathogen,” *Nature reviews microbiology*, vol. 7, no. 8, pp. 555–567, 2009.
- [78] WHO, “E. coli.” <https://www.who.int/news-room/fact-sheets/detail/e-coli>.
- [79] L. M. Bush and M. T. Vazquez-Pertejo, “Staphylococcal infections.” <https://www.msmanuals.com/professional/infectious-diseases/gram-positive-cocci/staphylococcal-infections>.
- [80] S. Zanini, M. Orlandi, C. Colombo, E. Grimoldi, and C. Riccardi, “Plasma-induced graft-polymerization of polyethylene glycol acrylate on polypropylene substrates,” *The European Physical Journal D*, vol. 54, no. 2, pp. 159–164, 2009.
- [81] S. Zanini, C. Riccardi, E. Grimoldi, C. Colombo, A. M. Villa, A. Nattalello, P. Gatti-Lafranconi, M. Lotti, and S. M. Doglia, “Plasma-induced graft-polymerization of polyethylene glycol acrylate on polypropylene films: chemical characterization and evaluation of the protein adsorption,” *Journal of colloid and interface science*, vol. 341, no. 1, pp. 53–58, 2010.

- [82] C. Riccardi, H. Roman, and R. Ziano, “Attachment of polymer chains on plasma-treated surfaces: experiments and modeling,” *New Journal of Physics*, vol. 12, no. 7, p. 073008, 2010.
- [83] L. Russo, S. Zanini, C. Riccardi, F. Nicotra, and L. Cipolla, “Diazo transfer for azido-functional surfaces,” *Materials Today*, vol. 14, no. 4, pp. 164–169, 2011.
- [84] H. Yasuda and M. Gazicki, “Biomedical applications of plasma polymerization and plasma treatment of polymer surfaces,” *Biomaterials*, vol. 3, no. 2, pp. 68–77, 1982.
- [85] K. Vasilev, N. Poulter, P. Martinek, and H. J. Griesser, “Controlled release of levofloxacin sandwiched between two plasma polymerized layers on a solid carrier,” *ACS applied materials & interfaces*, vol. 3, no. 12, pp. 4831–4836, 2011.
- [86] A. Shahravan and T. Matsoukas, “Encapsulation and controlled release from core–shell nanoparticles fabricated by plasma polymerization,” *Journal of Nanoparticle Research*, vol. 14, no. 1, pp. 1–11, 2012.
- [87] S. Alancherry, M. Jacob, K. Prasad, J. Joseph, O. Bazaka, R. Neupane, O. Varghese, O. Baranov, S. Xu, I. Levchenko, *et al.*, “Tuning and fine morphology control of natural resource-derived vertical graphene,” *Carbon*, vol. 159, pp. 668–685, 2020.
- [88] O. Baranov, I. Levchenko, J. Bell, J. Lim, S. Huang, L. Xu, B. Wang, D. Aussems, S. Xu, and K. Bazaka, “From nanometre to millimetre: a range of capabilities for plasma-enabled surface functionalization and nanostructuring,” *Materials Horizons*, vol. 5, no. 5, pp. 765–798, 2018.
- [89] I. Levchenko, K. Bazaka, M. Keidar, S. Xu, and J. Fang, “Hierarchical multicomponent inorganic metamaterials: intrinsically driven self-assembly at the nanoscale,” *Advanced Materials*, vol. 30, no. 2, p. 1702226, 2018.
- [90] S. Alancherry, K. Bazaka, I. Levchenko, A. Al-Jumaili, B. Kandel, A. Alex, F. C. Robles Hernandez, O. K. Varghese, and M. V. Jacob,

- “Fabrication of nano-onion-structured graphene films from citrus sinensis extract and their wetting and sensing characteristics,” *ACS applied materials & interfaces*, vol. 12, no. 26, pp. 29594–29604, 2020.
- [91] Z. Wang, T. Liu, L. Jiang, M. Asif, X. Qiu, Y. Yu, F. Xiao, and H. Liu, “Assembling metal–organic frameworks into the fractal scale for sweat sensing,” *ACS applied materials & interfaces*, vol. 11, no. 35, pp. 32310–32319, 2019.
- [92] Z. Fusco, M. Rahmani, T. Tran-Phu, C. Ricci, A. Kiy, P. Kluth, E. Della Gaspera, N. Motta, D. Neshev, and A. Tricoli, “Photonic fractal metamaterials: a metal–semiconductor platform with enhanced volatile-compound sensing performance,” *Advanced Materials*, vol. 32, no. 50, p. 2002471, 2020.
- [93] Y. de Mimérand, K. Li, C. Zhou, X. Jin, X. Hu, Y. Chen, and J. Guo, “Functional supported ZnO/Bi₂MoO₆ heterojunction photocatalysts with 3D-Printed fractal polymer substrates and produced by innovative plasma-based immobilization methods,” *ACS Applied Materials & Interfaces*, vol. 12, no. 38, pp. 43138–43151, 2020.
- [94] H. Li, H. Liu, M. Sun, Y. Huang, and L. Xu, “3D interfacing between soft electronic tools and complex biological tissues,” *Advanced Materials*, vol. 33, no. 3, p. 2004425, 2021.
- [95] M. Konar, B. Roy, and T. Govindaraju, “Molecular Architectonics-Guided Fabrication of Superhydrophobic and Self-Cleaning Materials,” *Advanced Materials Interfaces*, vol. 7, no. 11, p. 2000246, 2020.
- [96] F. Shahzad, A. Iqbal, H. Kim, and C. M. Koo, “2D transition metal carbides (MXenes): applications as an electrically conducting material,” *Advanced Materials*, vol. 32, no. 51, p. 2002159, 2020.
- [97] Z. Chen, A. Narita, and K. Müllen, “Graphene nanoribbons: on-surface synthesis and integration into electronic devices,” *Advanced Materials*, vol. 32, no. 45, p. 2001893, 2020.
- [98] I. Levchenko, K. Bazaka, S. Mazouffre, and S. Xu, “Prospects and physical mechanisms for photonic space propulsion,” *Nature Photonics*, vol. 12, no. 11, pp. 649–657, 2018.

- [99] I. Levchenko, S. Xu, Y.-L. Wu, and K. Bazaka, “Hopes and concerns for astronomy of satellite constellations,” *Nature Astronomy*, vol. 4, no. 11, pp. 1012–1014, 2020.
- [100] I. Levchenko, S. Xu, G. Teel, D. Mariotti, M. Walker, and M. Keidar, “Recent progress and perspectives of space electric propulsion systems based on smart nanomaterials,” *Nature communications*, vol. 9, no. 1, pp. 1–19, 2018.
- [101] I. Levchenko, K. Bazaka, T. Belmonte, M. Keidar, and S. Xu, “Advanced Materials for Next-Generation Spacecraft,” *Advanced Materials*, vol. 30, no. 50, p. 1802201, 2018.
- [102] I. Levchenko, M. Keidar, J. Cantrell, Y.-L. Wu, H. Kuninaka, K. Bazaka, and S. Xu, “Explore space using swarms of tiny satellites,” 2018.
- [103] I. Levchenko, S. Xu, S. Mazouffre, D. Lev, D. Pedrini, D. Goebel, L. Garrigues, F. Taccogna, and K. Bazaka, “Perspectives, frontiers, and new horizons for plasma-based space electric propulsion,” *Physics of Plasmas*, vol. 27, no. 2, p. 020601, 2020.
- [104] K. Bazaka, O. Baranov, U. Cvelbar, B. Podgornik, Y. Wang, S. Huang, L. Xu, J. Lim, I. Levchenko, and S. Xu, “Oxygen plasmas: a sharp chisel and handy trowel for nanofabrication,” *Nanoscale*, vol. 10, no. 37, pp. 17494–17511, 2018.
- [105] S. Zanini, A. Citterio, G. Leonardi, and C. Riccardi, “Characterization of atmospheric pressure plasma treated wool/cashmere textiles: Treatment in nitrogen,” *Applied Surface Science*, vol. 427, pp. 90–96, 2018.
- [106] R. A. Siliprandi, S. Zanini, E. Grimoldi, F. S. Fumagalli, R. Barni, and C. Riccardi, “Atmospheric pressure plasma discharge for polysiloxane thin films deposition and comparison with low pressure process,” *Plasma Chemistry and Plasma Processing*, vol. 31, no. 2, pp. 353–372, 2011.
- [107] S. Zanini, E. Grimoldi, and C. Riccardi, “Development of controlled releasing surfaces by plasma deposited multilayers,” *Materials Chemistry and Physics*, vol. 138, no. 2-3, pp. 850–855, 2013.
- [108] I. Adamovich, S. Baalrud, A. Bogaerts, P. Bruggeman, M. Cappelli, V. Colombo, U. Czarnetzki, U. Ebert, J. Eden, P. Favia, *et al.*, “The 2017

-
- Plasma Roadmap: Low temperature plasma science and technology,” *Journal of Physics D: Applied Physics*, vol. 50, no. 32, p. 323001, 2017.
- [109] S. Zanini, M. Lehocky, J. Lopez-Garcia, and C. Riccardi, “Plasma polymerization of 2-isopropenyl-2-oxazoline: Improvement of the coating stability by co-polymerization with 1-octene,” *Thin Solid Films*, vol. 677, pp. 55–61, 2019.
- [110] R. Barni, C. Riccardi, E. Selli, M. R. Massafra, B. Marcandalli, F. Orsini, G. Poletti, and L. Meda, “Wettability and dyeability modulation of poly (ethylene terephthalate) fibers through cold SF₆ plasma treatment,” *Plasma Processes and Polymers*, vol. 2, no. 1, pp. 64–72, 2005.
- [111] S. Asadollahi, M. Farzaneh, and L. Stafford, “On the icephobic behavior of organosilicon-based surface structures developed through atmospheric pressure plasma deposition in nitrogen plasma,” *Coatings*, vol. 9, no. 10, p. 679, 2019.
- [112] S. Zanini, P. Massini, M. Mietta, E. Grimoldi, and C. Riccardi, “Plasma treatments of PET meshes for fuel–water separation applications,” *Journal of colloid and interface science*, vol. 322, no. 2, pp. 566–571, 2008.
- [113] E. Grimoldi, S. Zanini, R. Siliprandi, and C. Riccardi, “AFM and contact angle investigation of growth and structure of pp-HMDSO thin films,” *The European Physical Journal D*, vol. 54, no. 2, pp. 165–172, 2009.
- [114] G. D. Bixler and B. Bhushan, “Fluid drag reduction and efficient self-cleaning with rice leaf and butterfly wing bioinspired surfaces,” *Nanoscale*, vol. 5, no. 17, pp. 7685–7710, 2013.
- [115] A. Tripathy, P. Sen, B. Su, and W. H. Briscoe, “Advances in colloid and interface science,” *Adv Colloid Interface Sci*, vol. 248, pp. 85–104, 2017.
- [116] D. P. Linklater, V. A. Baulin, S. Juodkazis, R. J. Crawford, P. Stoodley, and E. P. Ivanova, “Mechano-bactericidal actions of nanostructured surfaces,” *Nature Reviews Microbiology*, vol. 19, no. 1, pp. 8–22, 2021.
- [117] I. Biganzoli, F. Fumagalli, F. Di Fonzo, R. Barni, C. Riccardi, *et al.*, “A supersonic plasma jet source for controlled and efficient thin film deposition,” *Journal of Modern Physics*, vol. 3, no. 10, p. 1626, 2012.
-

- [118] C. Carra, E. Dell’Orto, V. Morandi, and C. Riccardi, “ZnO nanostructured thin films via supersonic plasma jet deposition,” *Coatings*, vol. 10, no. 8, p. 788, 2020.
- [119] C. Piferi, C. Carra, K. Bazaka, H. E. Roman, E. C. Dell’Orto, V. Morandi, I. Levchenko, and C. Riccardi, “Controlled deposition of nanostructured hierarchical TiO₂ thin films by low pressure supersonic plasma jets,” *Nanomaterials*, vol. 12, no. 3, p. 533, 2022.
- [120] M. Gahleitner and C. Paulik, *Polypropylene*, pp. 1–44. John Wiley & Sons, Ltd, 2014.
- [121] The Chemours Company, “The History of Teflon™ Fluoropolymers.” <https://www.teflon.com/en/news-events/history>.
- [122] C. Piferi, A. Brescia, and C. Riccardi, “Intensity comparison between UV lamps and plasma emission for air purification studies,” *AIP Advances*, vol. 11, no. 8, p. 085209, 2021.
- [123] T. C. Corke, M. L. Post, and D. M. Orlov, “SDBD plasma enhanced aerodynamics: concepts, optimization and applications,” *Progress in Aerospace Sciences*, vol. 43, no. 7-8, pp. 193–217, 2007.
- [124] P. Esena, S. Zanini, and C. Riccardi, “Plasma processing for surface optical modifications of PET films,” *Vacuum*, vol. 82, no. 2, pp. 232–235, 2007.
- [125] I. Biganzoli, R. Barni, C. Riccardi, A. Gurioli, and R. Pertile, “Optical and electrical characterization of a surface dielectric barrier discharge plasma actuator,” *Plasma Sources Science and Technology*, vol. 22, no. 2, p. 025009, 2013.
- [126] I. Biganzoli, R. Barni, and C. Riccardi, “Note: On the use of Rogowski coils as current probes for atmospheric pressure dielectric barrier discharges,” *Review of Scientific Instruments*, vol. 84, no. 1, p. 016101, 2013.
- [127] I. Biganzoli, R. Barni, A. Gurioli, R. Pertile, and C. Riccardi, “Experimental investigation of lissajous figure shapes in planar and surface dielectric barrier discharges,” in *Journal of Physics: Conference Series*, vol. 550, p. 012039, IOP Publishing, 2014.

- [128] M. Argüeso, G. Robles, and J. Sanz, "Implementation of a Rogowski coil for the measurement of partial discharges," *Review of scientific instruments*, vol. 76, no. 6, p. 065107, 2005.
- [129] I. Biganzoli, R. Barni, and C. Riccardi, "Temporal evolution of a surface dielectric barrier discharge for different groups of plasma microdischarges," *Journal of Physics D: Applied Physics*, vol. 46, no. 2, p. 025201, 2012.
- [130] J. Hollas, *Modern Spectroscopy*. Wiley, 2004.
- [131] Beer, "Bestimmung der absorption des rothen lichts in farbigen flüssigkeiten," *Annalen der Physik*, vol. 162, no. 5, pp. 78–88, 1852.
- [132] A. Serdyuchenko, V. Gorshlev, M. Weber, W. Chehade, and J. Burrows, "High spectral resolution ozone absorption cross-sections—Part 2: Temperature dependence," *Atmospheric Measurement Techniques*, vol. 7, no. 2, pp. 625–636, 2014.
- [133] B. Thompson, P. Harteck, and R. Reeves Jr, "Ultraviolet absorption coefficients of CO₂, CO, O₂, H₂O, N₂O, NH₃, NO, SO₂, and CH₄ between 1850 and 4000 a," *Journal of Geophysical Research*, vol. 68, no. 24, pp. 6431–6436, 1963.
- [134] K. Bogumil, J. Orphal, T. Homann, S. Voigt, P. Spietz, O. Fleischmann, A. Vogel, M. Hartmann, H. Kromminga, H. Bovensmann, *et al.*, "Measurements of molecular absorption spectra with the SCIAMACHY pre-flight model: instrument characterization and reference data for atmospheric remote-sensing in the 230–2380 nm region," *Journal of Photochemistry and Photobiology A: Chemistry*, vol. 157, no. 2-3, pp. 167–184, 2003.
- [135] R. Atkinson, D. L. Baulch, R. A. Cox, J. N. Crowley, R. F. Hampson, R. G. Hynes, M. E. Jenkin, M. J. Rossi, and J. Troe, "Evaluated kinetic and photochemical data for atmospheric chemistry: Volume I - gas phase reactions of O_x, HO_x, NO_x and SO_x species," *Atmospheric Chemistry and Physics*, vol. 4, no. 6, pp. 1461–1738, 2004.

- [136] S. Park, W. Choe, and C. Jo, “Interplay among ozone and nitrogen oxides in air plasmas: Rapid change in plasma chemistry,” *Chemical Engineering Journal*, vol. 352, pp. 1014–1021, 2018.
- [137] C. Piferi, G. Pierotti, M. Cavedon, A. Popoli, E. Martines, A. Cristofolini, and C. Riccardi, “Investigation on O₃ and NO_x Production in a Surface DBD.” Conference proceeding - 48th EPS Conference on Plasma Physics https://indico.fusenet.eu/event/28/contributions/486/attachments/500/1002/EPS2022_Ozono_paper.pdf, 2022.
- [138] H. Kim, “Nonthermal plasma processing for air-pollution control: a historical review, current issues, and future prospects,” *Plasma Processes and Polymers*, vol. 1, no. 2, pp. 91–110, 2004.
- [139] Z. Shayegan, C. Lee, and F. Haghghat, “TiO₂ photocatalyst for removal of volatile organic compounds in gas phase—A review,” *Chemical Engineering Journal*, vol. 334, pp. 2408–2439, 2018.
- [140] D. Hu, R. Li, M. Li, J. Pei, F. Guo, and S. Zhang, “Photocatalytic efficiencies of WO₃/TiO₂ nanoparticles for exhaust decomposition under UV and visible light irradiation,” *Materials Research Express*, vol. 5, no. 9, p. 095029, 2018.
- [141] G. Herrera, A. Martinez, M. Blanco, and J.-E. O’Connor, “Assessment of escherichia coli b with enhanced permeability to fluorochromes for flow cytometric assays of bacterial cell function,” *Cytometry: The Journal of the International Society for Analytical Cytology*, vol. 49, no. 2, pp. 62–69, 2002.
- [142] Piattaforma Microscopia Unimib, “Microscopio Elettronico Zeiss FEG Gemini 500.” <https://piattaformadimicroscopia.unimib.it/strumenti/microscopio-elettronico-zeiss-feg-gemini-500/>.
- [143] Nanosurf, “Coreafm.” <https://www.nanosurf.com/en/products/coreafm-the-essence-of-atomic-force-microscopy>.
- [144] C. Piferi, K. Bazaka, D. L. D’Aversa, R. Di Girolamo, C. De Rosa, H. E. Roman, C. Riccardi, and I. Levchenko, “Hydrophilicity and Hydrophobicity Control of Plasma-Treated Surfaces via Fractal Parameters,” *Advanced Materials Interfaces*, vol. 8, no. 19, p. 2100724, 2021.

- [145] J. W. Kantelhardt, H. E. Roman, and M. Greiner, “Discrete wavelet approach to multifractality,” *Physica A: Statistical Mechanics and its Applications*, vol. 220, no. 3-4, pp. 219–238, 1995.
- [146] E. Koscielny-Bunde, A. Bunde, S. Havlin, H. E. Roman, Y. Goldreich, and H.-J. Schellnhuber, “Indication of a universal persistence law governing atmospheric variability,” *Physical Review Letters*, vol. 81, no. 3, p. 729, 1998.
- [147] R. Siliprandi, H. Roman, R. Barni, and C. Riccardi, “Characterization of the streamer regime in dielectric barrier discharges,” *Journal of applied physics*, vol. 104, no. 6, p. 063309, 2008.
- [148] C. Mandolino, E. Lertora, C. Gambaro, and M. Pizzorni, “Functionalization of neutral polypropylene by using low pressure plasma treatment: Effects on surface characteristics and adhesion properties,” *Polymers*, vol. 11, no. 2, p. 202, 2019.



A Peer reviewed papers


In this Chapter, I append all the peer reviewed papers I wrote with my collaborators during the PhD.

A.1 Current Filaments in Asymmetric Surface Dielectric Barrier Discharge

Reproduced from Piferi, C.; Barni, R.; Roman, H. E.; Riccardi, C. Current Filaments in Asymmetric Surface Dielectric Barrier Discharge. *Applied Sciences* 2021, 11 (5), 2079, <https://doi.org/10.3390/app11052079>.

Article

Current Filaments in Asymmetric Surface Dielectric Barrier Discharge

 Cecilia Piferi , Ruggero Barni , H. Eduardo Roman  and Claudia Riccardi *

Dipartimento di Fisica, Università degli Studi di Milano-Bicocca, Piazza della Scienza 3, 20126 Milano, Italy; c.piferi@campus.unimib.it (C.P.); ruggero.barni@mib.infn.it (R.B.); eduardo.roman@mib.infn.it (H.E.R.)

* Correspondence: claudia.riccardi@unimib.it

Abstract: In this study, we examine the statistical properties of asymmetric surface dielectric barrier discharges (SDBD) produced by applying a periodic high voltage between two conducting displaced electrodes, located at the opposite sides of a flat dielectric panel. Here, the asymmetry refers to the fact that the lower electrode is fully covered with an insulating material, while the upper one, glued onto the dielectric surface, is otherwise left exposed to the air. Such a configuration allows the formation of a thin layer of plasma above the insulating surface. A single cycle signal consists of two well-separated half-cycle patterns, denoted as forward and backward strokes, corresponding to positive and negative voltages, respectively. They display a quite complex discharge pattern constituted by a sequence of individual peaks (bursts) of varying current and time duration. Specifically, we find that backward stroke bursts carry a positive mean charge $\langle Q \rangle \simeq 0.3$ nC and mean current $\langle I \rangle \simeq 35$ mA, with a mean duration $\langle \tau \rangle \simeq 15$ ns, while forward stroke bursts have a negative mean charge $\langle Q \rangle \simeq -0.1$ nC, a mean current $\langle I \rangle \simeq -20$ mA, and a mean duration $\langle \tau \rangle \simeq 11$ ns. The statistical analysis suggests that power injection can be tailored to produce the active agents in the plasma needed for a particular application. We also determined discharge spatial correlation patterns from measurements of the associated stimulated optical emission. The optical excitations occur as a result of the ionizing effect of the electromagnetic waves which ignite the discharge, followed by the electric current flow. In particular, we point out that one of the phases of the discharge is compatible with a cathode directed streamer phenomenon (backward stroke), while the mechanism acting for a forward stroke has a different structure.

Keywords: surface dielectric barrier discharge; atmospheric pressure non thermal plasma; streamer discharge



Citation: Piferi, C.; Barni, R.; Roman, H.E.; Riccardi, C. Current Filaments in Asymmetric Surface Dielectric Barrier Discharges. *Appl. Sci.* **2021**, *11*, 2079. <https://doi.org/10.3390/app11052079>

Received: 15 January 2021

Accepted: 20 February 2021

Published: 26 February 2021

Publisher's Note: MDPI stays neutral with regard to jurisdictional claims in published maps and institutional affiliations.



Copyright: © 2021 by the authors. Licensee MDPI, Basel, Switzerland. This article is an open access article distributed under the terms and conditions of the Creative Commons Attribution (CC BY) license (<https://creativecommons.org/licenses/by/4.0/>).

1. Introduction

Dielectric barrier discharges (DBD) have found many industrial applications as ozone generators, plasma discharge panels, excimer lamps and in different types of surface modifications [1–5]. DBD are characterized by the presence of an insulating material between the electrodes to prevent the occurrence of high electrical current arcs between them (arcing). They produce a non-thermal plasma at (or near) atmospheric pressure in the discharge gap region between electrodes (Figure 1a) [6,7].

The DBD geometry results in a quite uniform plasma distributed between electrodes, providing a large flow of activated or reactive compounds for the treatment of materials [8–10]. This technique enables the application of plasma processes at atmospheric pressure without a damaging heat load [11–15].

DBD have been used, for instance, to increase the wettability of polymers, to grow silicon oxide thin films, to perform sterilization by UV irradiation, and for air purification [16,17]. Variants of DBD are surface dielectric barrier discharges (SDBD) (Figure 1b), obtained by using a particular configuration of electrodes in direct contact with the dielectric material. To extend SDBD applications, asymmetrical electrode layouts (one isolated

and the other exposed to the air) were developed, in particular in the context of aerodynamics [18–21]. In the latter, the main purpose was the production of an ionic wind, flowing along the wing surface [22,23]. The resulting enhanced mixing of air flow and ionic wind was found to be beneficial for an active boundary layer control, pursuing drag reduction [24], lift enhancement [21], and stall prevention [25].

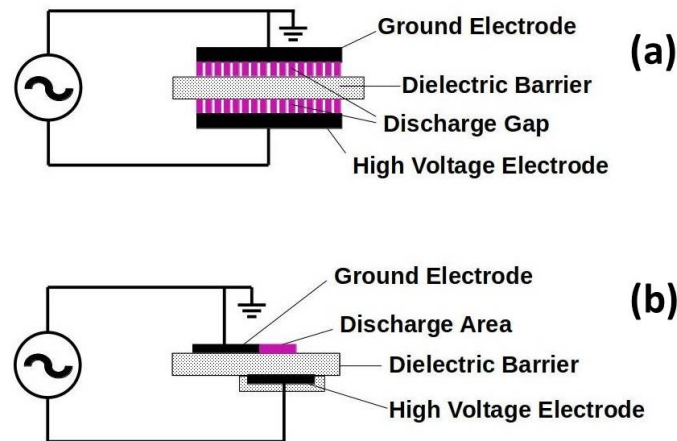


Figure 1. Schematic representations of: (a) dielectric barrier discharges (DBD), and (b) surface dielectric barrier discharges (SDBD). Discharges within the plasma are indicated in magenta colour.

In this work, we perform extensive statistical analysis of SDBD, complementing the study on DBD performed in [26], using an asymmetric device with an exposed (grounded) metal electrode, glued onto the dielectric surface, and a lower electrode covered by an insulating material (see Figure 1b). The purpose of our work is the characterization and the analysis of the mechanisms taking place during the discharge formation in SDBD, and its robustness when operating under steady state conditions. This is a basic requirement that a working plasma device should fulfil in order to be used in large-scale industrial applications. The study of SDBD properties are also interesting from a fundamental physics point of view, since they have not been thoroughly investigated, while DBD have not been thoroughly investigated either [6,26].

In the presence of high-voltage oscillating signals, SDBD display a complex pattern of electric discharges in the form of short bursts of activity, concentrated within each half-cycle of the wave signal period. They are often referred to as forward discharge or forward stroke (FS), and backward discharge or backward stroke (BS), depending on the sign of the applied voltage [27]. The two strokes are composed of a relatively large number of individual events, carrying electrical currents in the discharge area, for which the expression microdischarge was coined [6]. It is still not clear yet what the role played by FS and BS microdischarges is in the production of the induced airflow around the plasma [22,28,29].

At atmospheric pressure in air, SDBD operate in the so-called microdischarge regime, characterized by narrow current filaments with very short lifetimes (few tens of ns) [6,30]. Microdischarge filaments, or streamers, extend from the exposed electrode towards the dielectric surface above the covered electrode, more or less perpendicularly to the electrodes [30]. This spatial region roughly corresponds to the region where the electric field strength is at its maximum.

At a more fundamental level, it is not even clear if the discharge mechanism is the same during the two AC semi-cycles [30,31]. The origin of the differences between the two strokes may be due to the different asymmetries that, as a matter of fact, can be present in typical SDBD setups. The second, more general, source of asymmetry resides in the electrodes and

dielectric surface geometry, which induces electric field spatial non-uniformities, that can lead to differences between the two voltage polarities [22]. The alternating nature of the power supply, however, induces a subtle correlation between the two strokes, which are at work when the steady state operation regime is reached. Such correlations have been studied in DBD [26] by calculating the Hurst exponent of the corresponding random walk profiles [32,33], and we extend a similar study to SDBD.

In particular, further investigations are necessary by dealing with the mechanisms of microdischarge initiation at the restart of each one of the two strokes, and to the role played by the charges left on the active areas of the dielectric surface or in the gas gap above it [34]. Several models have been proposed in the literature for simulating microdischarge generation, evolution and quenching, even in non uniform electric field configurations. Unfortunately, they are limited, due to numerical constraints, to single-microdischarge events [35–40]. Thus, more experimental and analytical studies are needed for their general assessment and validation.

The paper is organized as follows. In Section 2, we briefly review the state of the art on SDBD. In Section 3, we describe the experimental set up, and in Section 4, we present the plasma diagnostics employed, the latter consisting of a Rogowski coil (Section 4.1) and a photomultiplier (Section 4.2). The experimental results are discussed in Section 5, and the conclusions are summarized in Section 6.

2. Recent Works on SDBD Microdischarges

The study of the SDBD microdischarges is an active field of research which has drawn a great deal of interest in recent years, both in applied and basic plasma physics communities. We briefly review some of the works relevant for our present study.

In [41], the authors studied an extension of SDBD to a volume-surface dielectric barrier discharge for the ozone production and benzene degradation. Concerning the discharge characterization, they found that both SDBD and V-SDBD configurations worked in a filamentary discharge mode, which produced current pulses superimposed to the capacitive current, resulting in an increasing number and amplitude of current pulses with the applied voltage. In a typical SDBD configuration, the charges are transferred along a thin layer on the dielectric surface, and the accumulation of charges on the dielectric surface finally leads to a reduction in the transfer, and therefore to the extinction of the electric discharge. Compared to conventional SDBD, the hybrid volume-surface DBD (V-SDBD) apparently enhances the discharge current, widening the spatial distribution of discharge plasma, which can be explained by the enhanced spatial electric field due to the added ground electrode over SDBD configuration.

In [42], the inactivation of *Bacillus subtilis* spores using coplanar surface dielectric barrier discharge (CSDBD) is studied. As in any other plasma-chemical application, the efficacy of the treatment depends on various discharge operating conditions, such as discharge electrode geometry, mean dissipated power, and feed gas flow and composition, all of which influence the chemical and physical processes of the discharge. For that reason, the authors studied the plasma properties using a photomultiplier and ICCD camera to record the optical emission waveforms and the spectra collected from the whole surface of the CSDBD electrode. The production of micro-discharges occurs with a certain distribution along the rising slope of a positive half-period with a typical pulse-to-pulse separation of a few microseconds. A similar trend can be observed during any negative half-cycle. The characteristic distribution of micro-discharges during both the positive and negative half-cycles captured by the photomultiplier tube (PMT) waveforms for a (peak-to-peak) HV amplitude of 22 kV, has been acquired by averaging over 1024 samples. The highest probability of micro-discharge onset occurs for positive AC voltages between 6.6 and 7 kV, while for negative AC voltages, the best conditions occur between -8.5 and -9.5 kV. Further insight can be obtained by analysing the voltage, current and PMT waveforms for micro-discharges onset at a defined HV amplitude.

In [43], the effects of optical characteristics, electrical performances and mechanical properties of SDBD carrying a composite dielectric glass/polyimide film were investigated. The current, discharge plasma morphology, electrical power consumption, and induced airflow velocity were analyzed at an applied voltage of 17–23 kV with a working frequency of 9.15 kHz. The SDBD physical process of discharge is complicated, of which discharge characteristics are influenced by many factors, including the applied power, electrode parameters, dielectric properties, environmental conditions and so on. The discharge intensity at the positive half cycle is higher than the negative one, corresponding to a large number of intense pulses with noticeable amplitude difference, and the maximum pulse current peak is about 17 mA. The changes in current are relatively low, having an average value of about 4 mA during the negative half cycle.

3. Plasma Device Setup

The configuration adopted in our experiments was suggested by the simplest version of SDBD used in plasma aerodynamics applications, named a plasma actuator [18]. It consists of two conducting electrodes attached at the opposite sides of a flat dielectric panel, in the asymmetrical arrangement sketched in Figure 2.

The lower electrode is fully covered with an insulating material, whereas the upper one remains fully exposed to the air. In this way, the plasma generation region is confined above the dielectric plate. As a dielectric barrier, we used a teflon sheet with a thickness of about 3 mm.

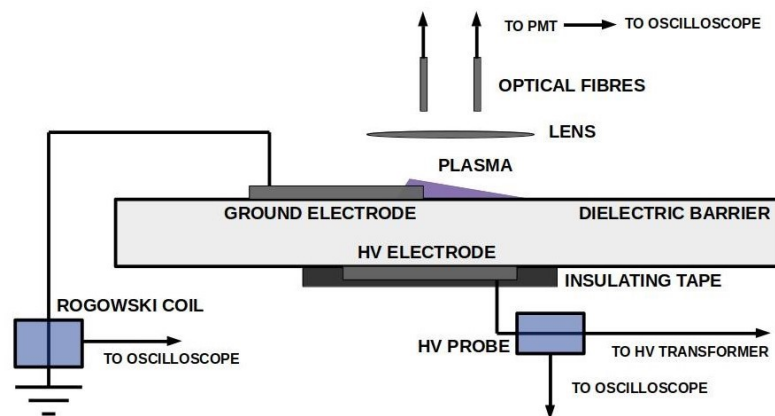


Figure 2. Plasma device scheme: the two electrodes, consisting of tin clad copper adhesive tapes (60 μm thick, 4 cm wide and 12 cm long), are attached to a dielectric material and are laterally shifted from each other by about 0.5 cm (typical asymmetry in SDBD). The lower electrode, fed by the high-voltage (HV) supply, is covered with an insulating material, whereas the upper one, fed to ground, is exposed to air (second type of asymmetry). The Rogowski coil is placed around the ground cable and it is linked to an oscilloscope. The optical fibres are placed over the plasma region (violet colour) and are connected to the photomultiplier, the latter linked to an oscilloscope. The HV probe is net to the oscilloscope from the HV cable. In this work, unless otherwise specified, an asymmetric SDBD refers to the second type of asymmetry.

Upon the application of a sufficiently high-voltage (HV), the air portion in proximity of the device gets weakly ionized, thus creating a thin plasma layer above the insulating plate, as illustrated in Figure 2. The SDBD plasma actuator generates a non-thermal self-limiting plasma in which the accumulation of charged particles onto the dielectric surface opposes the applied electric field [20]. Consequently, AC or pulsed high-voltages are required to have a temporally prolonged discharge operation, otherwise only a transient air ionization occurs at the voltage ignition [6].

In the present configuration, the exposed electrode is grounded, whereas the covered one is fed by a high-voltage power supply line. This consists of a DC-voltage supply and a signal generator feeding the primary windings of a HV transformer whose secondary windings are connected to the electrode. We set the reference DC-supply voltage, V_{DC} , in the small range, $V_{DC} = (7\text{--}14)$ V. The whole system behaves like a resonant circuit, so the sinusoidal voltage frequency slightly depends on the DC-supply voltage. In Figure 3a, we report the coupling of the applied DC voltage and the resulting amplified HV. In Figure 3b, a typical high-voltage response signal used in the experiments is reported.

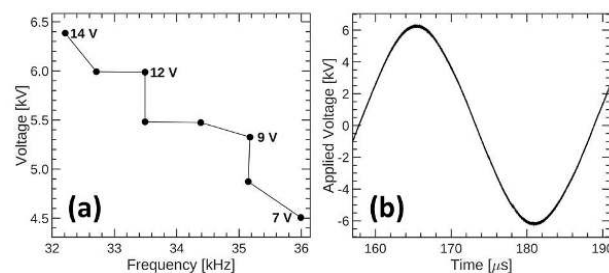


Figure 3. (a) Amplitude of the amplified voltage V_{HV} , resulting from the applied reference DC voltage, V_{DC} (of which few values are indicated), as a function of the corresponding optimal frequency. The latter is chosen to maximize the output voltage V_{HV} , for each reference value V_{DC} . (b) Typical applied signal $V_{HV}(t)$ vs. time, employed in our experiments.

4. Plasma Diagnostics

The experimental setup consists of a Rogowski coil to investigate the electrical parameters of the discharges, and an optical emission spectroscopy and photomultiplier tube to investigate the electromagnetic radiation of the plasma emission.

4.1. Rogowski Coil

The electrical parameters involved in the discharge events are clearly the most relevant to be measured. This includes the sampling of the instantaneous value of the voltage, as close as possible to the exposed electrode. Since a direct measure of the electric field or potential in the discharge region is generally not feasible, because of the perturbations it induces, the second leg of this diagnostics system is a measurement of the instantaneous value of the current flowing between the electrodes. In our experiments, this was done by means of Rogowski coil sensors [44,45].

A Rogowski coil usually consists of a conductor winding wrapped around a toroidal support of a non-ferromagnetic material, such as an air core. This ensures excellent linearity to the response of the coil due to the absence of saturation and fast timing sensitivity. To use a Rogowski coil as a probe, the cable transporting the current has to pass through the toroid. Then, the current flowing in the cable generates a voltage variation at the output of the coil proportional to the rate of the current variation, dI/dt . This voltage signal should be passed through an integrating circuit, that could simply be a resistance, for measuring $I(t)$. Using a small resistance for the integrating system, the probe operates in the so called self-integrating mode in a large frequency range.

Within this range, the voltage signal produced by the coil is directly proportional to the instantaneous current value. Outside this range, however, the probe response displays a frequency-dependent attenuation and phase-shift. Thus, in order to recover the actual value of the current, an accurate calibration and a FFT decomposition of the signal is required [45]. There are some difficulties related to air core Rogowski coils, such as the variation of the coil parameters with temperature and the sensitivity to the exact location and orientation of the circuit section passing through the torus. However, the main drawbacks in our application are due to the fact that Rogowski coils with air core have small sensitivity to

weak currents. This cannot be overlooked, since our aim is to identify the signal produced by single microdischarges.

To overcome this problem, a ferromagnetic coil can be employed for the Rogowski coil core. Here, we use NiZn ferrite N30 with $\mu_i \sim 4300$, with 50Ω integration resistance and 3.5 windings, and a 50 cm-long RG-59 BNC coaxial cable with a 50Ω resistance, which were calibrated with our Rogowski coil. Data were digitized by an Agilent Infinium MSO8104A oscilloscope with 1 GHz bandwidth and maximum acquisition rate of 4 GSamples/sec, which was found to be suitable for the applications we envisaged.

The electric current signal sampled by the Rogowski coil has two main components: the first one consists of the microdischarges producing the plasma state, and the second one is due to the displacement current within the insulated electrode as a result of the HV applied voltage. Thus, for a time-dependent applied voltage, a displacement current is always added to the actual discharge current flow, that is mainly determined by the capacitance behavior of the electrode system. In the case of an oscillating voltage supply, the displacement current has a sinusoidal trend with the same frequency as the applied bias.

Above a voltage threshold, the electric field ignites the plasma. This is generally observable as a pulsed current signal that overlaps the displacement current signal, consisting of several fast spikes (bursts), yielding two well-separated half-cycle patterns within the HV cycle. Since we are only interested in the plasma contribution, we chose the self-integrating range of the probe so that it suppresses the low frequency capacitive component by itself.

The calibration of the circuit was performed by using frequency waveform generators, depending on the frequency range to be analyzed. We used an NF-1940 Synthesizer, with bandwidth (0–20) MHz, and a Kenwood SG-7130 Synthesizer, with bandwidth (0.1–1300) MHz. The Rogowski coil was inserted using two BNC breakouts, as close as possible to a high-power 50Ω resistor R (Bird Electronic Co. 8135, maximum power 150 W) in order to avoid the external cable stray capacitances. We collected input HV probe signal and Rogowski output signal through an oscilloscope. Using the amplitude attenuation and phase-shift information, we obtained the calibration parameters shown in Figure 4. Unless otherwise stated, we referred to the phase during the oscillation cycle as the argument of a sine function expressed in radians, such as

$$V_{\text{Rog}}(t) = V_{\text{Rog}} \sin(\omega t + \phi_{\text{Rog}}). \quad (1)$$

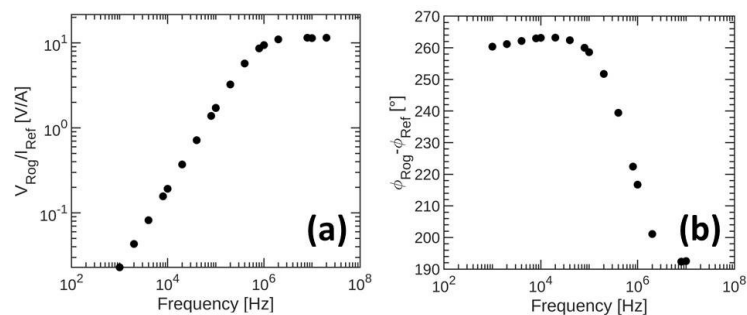


Figure 4. Calibration of the Rogowski coil vs. frequency [Hz]. (a) Voltage response. (b) Phase shift.

After the amplitude calibration, we obtained the attenuation factor to correct our Rogowski response in the bandwidth (10^6 – 10^8) Hz, which is fit to measure the characteristics of current pulses corresponding to single individual microdischarges, i.e.,

$$\frac{V_{\text{Rog}}}{I_{\text{Ref}}} \sim 10 \text{ V/A}, \quad (2)$$

where I_{Ref} is the reference current in the frequency range (10^6 – 10^8) Hz. This is the self-integrating bandwidth that we extrapolate up to 10^9 Hz. Using this optimised design of the coil, a phase calibration correction [45] is no longer needed.

4.2. Photomultiplier Tube

As is well known, during the development of an electrical discharge, part of the energy is lost into the excitation of internal states of atoms and molecules. From their de-excitation, plasma emissions of electromagnetic radiation are produced, and part of this radiation lies in the optical range. This could be exploited for diagnostics purposes by using optical emission spectroscopy (OES) [46]. In addition to providing information on the emitting species, the time of emission could give some hints about the mechanisms of the discharge itself. This is all the more true for SDBD, where the region of emission is concentrated and discharge happens mainly through quick, independent events of ionization and subsequent electric current flow, when most of the excitations happens [6,23]. The spreading and development of the discharge in the air gap can then be traced by registering the delays in the emissions.

Here, we use a multi-anode PMT (Hamamatsu H8711), built upon 16 channels arranged in a 4×4 matrix form. Each channel can collect electrons coming from a 4.3 mm square photocathode. The rise time of the PMT signal, 0.83 ns, is short enough to retain the relevant information of the emitting times. Their high sensitivity is optimal to obtain light even from single discharge events. In our experiments, we kept the gain of the PMT constant, by supplying it with a regulated high-voltage generator (Matsusada AU-5R20-LCl), biased to -850 V.

Besides having suitable rise time and multichannels, the choice of the PMT was motivated also by the radiant sensitivity of the photocathode, a bialkali one, in order to match with the plasma emission spectrum. The model we use has a maximum sensitivity in the 300–500 nm range. This fits well the reported average discharge emission spectra, measured in the range 200–850 nm by means of a wide-band and low-resolution spectrometer (PS2000 by Ocean Optics), similar to those already discussed in [23]. They are consistent with typical spectra of dielectric barrier discharges in air at atmospheric pressure, with the brightest feature being the second positive system of molecular nitrogen N_2 , approximately lying in the interval 300–500 nm, and showing minor evidence of the first negative system of the nitrogen molecular ion N_2^+ , extending to the 380–480 nm range. One such spectrum is shown in Figure 5, together with the sensitivity curve of the PMT.

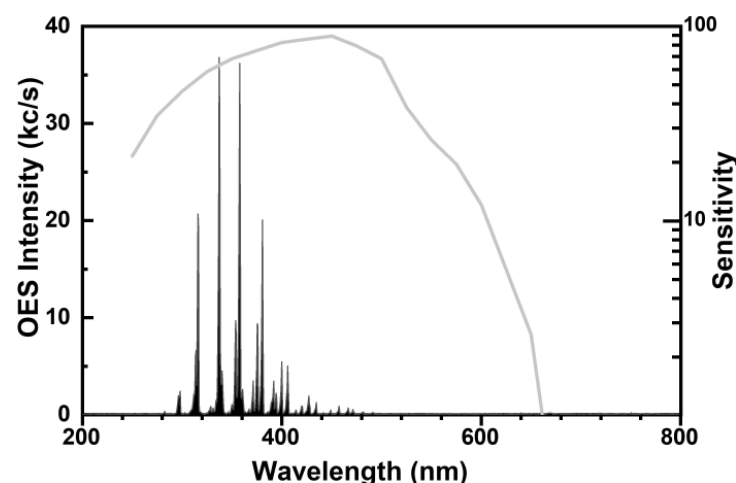


Figure 5. Light emission spectra of a typical discharge recorded by a low resolution spectrometer, compared to the sensitivity range of the photomultiplier tube (PMT) (continuous line).

The radiative lifetime of the excited levels involved in the emission of the second positive system is around 40 ns. However, quenching in atmospheric air, enhanced also by impurities and excited states produced in the plasma gas-phase, reduces the lifetime of such excited levels to below 1 ns. Thus, the sensitivity of the excitation timing is retained and OES could be used to measure the spatio-temporal development of the discharges [47]. This was the main goal of our OES measurements.

The outputs of the PMT were registered on the low impedance input ($50\ \Omega$) of a fast digital scope (Agilent MSO-8104A1). This retains the timing information of the emission, while producing pulses which could easily be recorded and separated from the noise. Usually, the light emitted from each microdischarge appears in the recorded temporal series as a (3 ± 1) ns negative voltage pulse, which is due to the temporal response of our PMT. Indeed, the signals were absolutely similar to those detected when collecting light emitted by a lamp. The shape of the signal could also be used to safely remove electromagnetic disturbances occasionally coming from the discharge.

The light emitted from plasma microdischarges was collected by UV-enhanced optical fibres by Avantes (FCB-UV800-2). In order to increase light collection, instead of placing the optical fibres directly above the discharge region, we imaged the discharge onto their inlets by means of a commercial objective lens ($1:2.8/F = 50\ \text{mm}$ by Durst). In the simplest OES setup, we chose to look first at two spatially separated spots. By back-illuminating the optical fibres, we could check the actual size and location of the discharge region imaged by each of the channels of the PMT. Since we are primarily interested in the correlations and delays between plasma emission from different discharge regions, we should exclude any spurious signal arising from cross-talk between the different channels of the PMT. This was indeed one of main factors in the choice of the PMT.

As an example, we show in Figure 6 a portion of the time series recorded by the digital scope, where a couple of light pulses associated to plasma microdischarges are detected by a channel of the multianode PMT. Besides the shape of the pulses, it appears that no signal was associated to the second channel (in this case, we chose two pins at the opposite corners of the square PMT matrix), where the optical fiber input was plugged in. We also tested that all channels are similar in sensitivity and time response, and switched the viewlines several times in order to exclude any interference from the choice of the PMT channels.

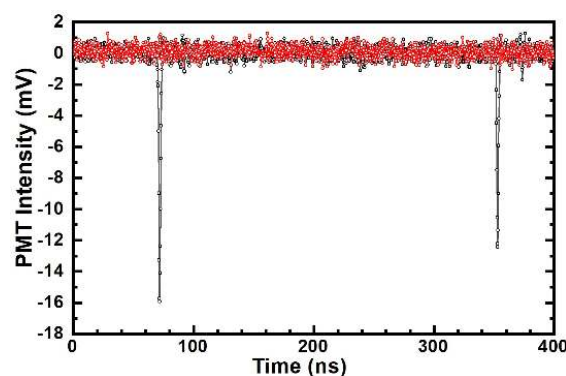


Figure 6. PMT output recorded by two different channels, the black one looking at the discharge and the red one blinded, showing the shape of the signals (vertical lines) coming from the plasma and the absence of cross-talk.

5. Experimental Results

In the following, we discuss the experimental results for the Rogowski coil measurements in Section 5.1, and for the PMT measurements in Section 5.2.

5.1. Rogowski Coil

Every oscilloscope channel acquisition has 41×10^6 points, sampled every 0.25 ns. That means that every acquisition length is 1.025 ms. To increase the statistics, we analyzed 30 realizations for each voltage, yielding a total time span of 30.75 ms. A typical one-cycle signal acquisition is plotted in Figure 7a, where the left axis refers to the applied voltage (black line) and the right axis refers to the current measured by the Rogowski coil (red line).

When the applied voltage $V > 0$, the electrons go from the exposed electrode to the dielectric, and the current is defined as negative. The discharges that occur in this case are denoted as a forward stroke (FS). The discharges that occur in the opposite condition, $V < 0$, are denoted as a backward stroke (BS), and have an associated current defined as positive. For this reason, if a spike is positive (negative) in a forward (backward) stroke, it is classified as noise. We also consider as noise a peak that both develops within 25 ns after a burst and has a height lower than 75% of the previous burst. These spurious signals are due to the finite system bandwidth.

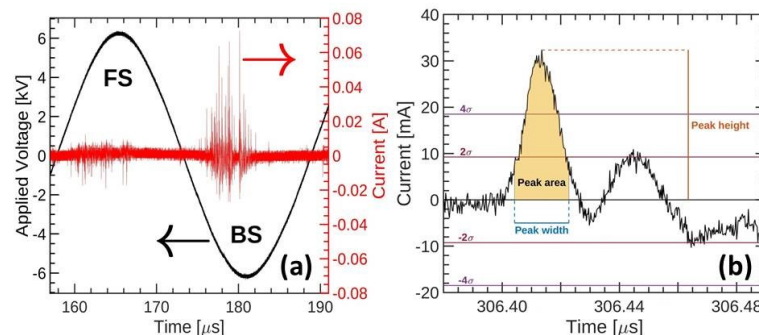


Figure 7. (a) Example of a temporal acquisition (forward stroke (FS) when $V > 0$, and backward stroke (BS) when $V < 0$). The left axis refers to the applied voltage (black line), while the right axis refers to the Rogowski coil current (red line). (b) Burst (peak) properties: charge (peak area), maximum current (peak height), and temporal duration (peak width).

We performed a fit of the HV signal with a sine function to determine its amplitude, frequency, and argument at each point. From the current signal, we can notice the presence of a constant baseline and a series of spikes that occur at specific HV phases. These spikes are the current signal caused by the plasma microdischarges. Detail of a microdischarge (called burst) is shown in Figure 7b. We characterize a burst by its charge (area of the peak), maximum current intensity (height), time duration (width), and HV phase position. Since we are interested only in the plasma current, carried by the bursts, we have to determine a background threshold above which a peak can be defined as a burst. We choose as background threshold, $\epsilon_B = 2\sigma$, i.e., twice the standard deviation over the whole Rogowski coil data. We identify a peak as a burst if its height is greater than the value of 4σ . The peak duration is given by the peak width at ϵ_B .

5.1.1. Phase Analysis

We determine first the normalized burst count distribution as a function of phase within a single HV cycle (Figure 8). One can notice two well-separated phase zones. The FS occurs at lower phases $0 \leq \phi \leq \pi$, and the BS when $\pi \leq \phi \leq 2\pi$. The number of events within FS is much smaller than within BS. It can be noted that for BS, the number of bursts increases with increasing HV, and a double peak structure emerges at high HV. The origin of this structure remains to be understood.

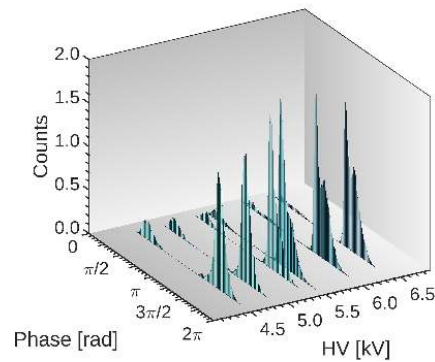


Figure 8. Distribution of bursts counts vs. HV phase. The FS occurs for phases $0 \leq \phi \leq \pi$, and the BS for $\pi \leq \phi \leq 2\pi$. Note the conspicuous difference in the counts between the FS and BS phases.

5.1.2. Charge Analysis

Next, we consider the charge Q (peak area) associated to bursts. The distributions of charge, $P(Q)$, are shown in Figure 9a for FS, and in Figure 9b for BS, respectively. The distributions are plotted in semi-logarithmic scale for clarity of presentation.

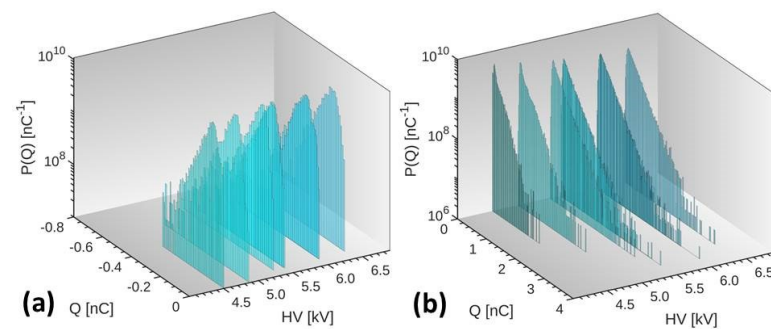


Figure 9. Burst charge distribution $P(Q)$ vs. charge Q for different HV. (a) Forward stroke (negative charge). (b) Backward stroke (positive charge).

For a more quantitative analysis, we consider the charge distribution $P(Q)$ for a single HV, in the illustrative case $HV = 5.48$ kV, shown in Figure 10. The two half-cycle responses, the FS and BS, are plotted for comparison. Both distributions display a maximum near $Q = 0$, while for BS, the decay is approximately exponential at large Q .

Thus, for BS we use the exponential form to fit the charge distributions,

$$P(Q) = \frac{1}{Q_0} \exp\left(-\frac{Q}{Q_0}\right), \quad (3)$$

where Q_0 is a characteristic charge. The values of Q_0 are shown in Figure 11a, as a function of the applied HV. As one can see, the characteristic charge Q_0 first increases with HV, reaching a plateau for HV larger than ≈ 5.4 kV. The latter can be seen as the separation voltage between two different regimes, similar to that found for DBD [26]. The plateau value $Q_0 \approx 0.7$ nC suggests that BS bursts reach a maximum saturation charge at high voltages.

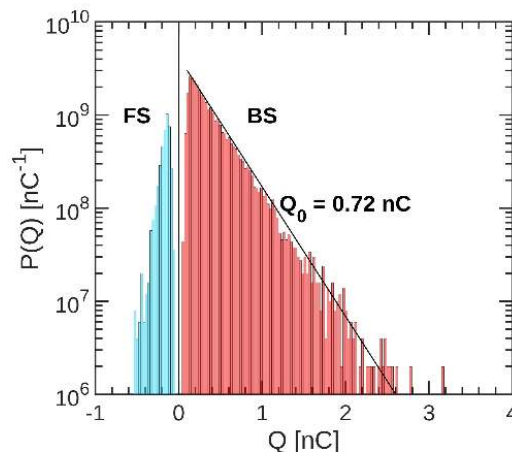


Figure 10. Distribution $P(Q)$ vs. Q for both FS ($Q < 0$) and BS ($Q > 0$) at HV = 5.48 kV. For BS, we find the exponential decay $P(Q) \approx \exp(-Q/Q_0)$, for $Q > 0$, with $Q_0 \approx 0.72$ nC.

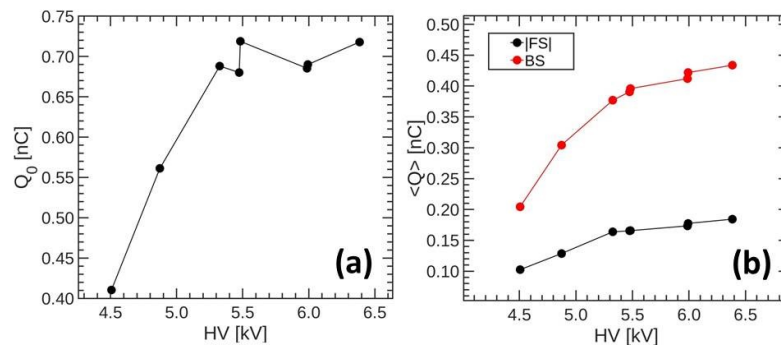


Figure 11. (a) Characteristic charge Q_0 vs. HV for BS. (b) Mean charge $\langle |Q| \rangle$ for both FS and BS.

The corresponding mean charges, $\langle |Q| \rangle$, are shown in Figure 11b. The mean charge (absolute) values are very different, ~ 0.35 nC for BS and $\sim (-)0.15$ nC for FS. This asymmetry, both in the number and charge of bursts, is consistent with the existence of different discharge mechanisms due to the setup asymmetry.

5.1.3. Burst Time Duration Analysis

Let us consider next the distribution of burst time duration (see Figure 12).

As is apparent from Figure 12, the distributions $P(\tau)$ are asymmetric and their shapes are non-Gaussian. Indeed, there occur a large number of events of long duration, as the skewness and the flatness (also known as kurtosis) testify. The skewness is a measure of the asymmetry of the distribution around its mean value ($S_\tau = 0$ for a normal distribution), and the flatness is a measure of the relative importance of the values at the tails ($F_\tau = 3$ for the normal distribution). The corresponding moments, S and F , for the actual burst distribution strongly differ from their Gaussian counterparts, as one can see in Figure 13. Furthermore, for BS, the mean duration of bursts increases with the applied voltage and is about $\langle \tau \rangle \approx 15$ ns for HV=5.5 kV; for FS, $\langle \tau \rangle \approx 11$ ns, and it is weakly dependent on HV.

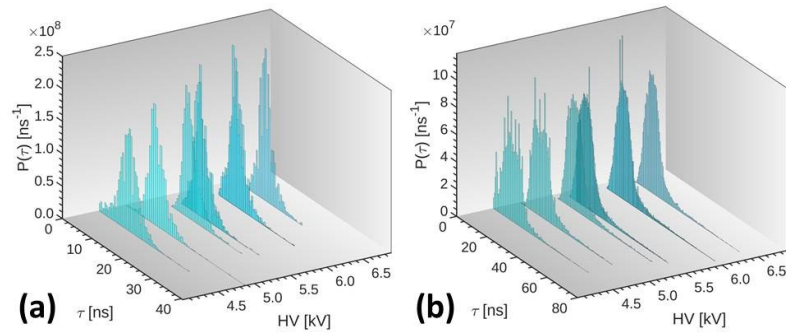


Figure 12. Burst time duration distribution, $P(\tau)$ vs. τ , for different HV. (a) Forward stroke. (b) Backward stroke. Note the different time scales in (a,b).

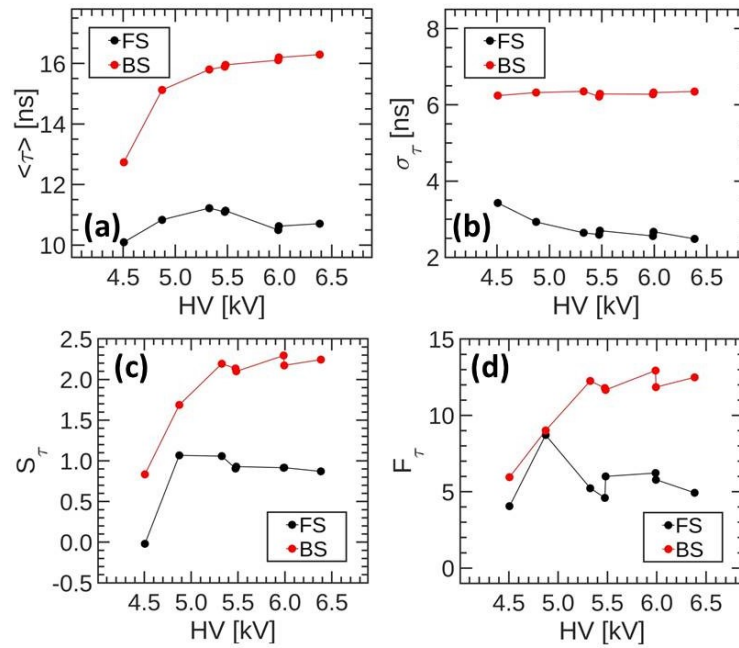


Figure 13. Moments of burst time duration vs. HV. (a) Mean value $\langle \tau \rangle$. (b) Standard deviation σ_τ . (c) Skewness (S_τ). (d) Flatness (F_τ).

5.1.4. Current Analysis

The burst current distributions, $P(I)$, display an exponential shape similar to $P(Q)$. For BS, the current distributions are shown in Figure 14. To describe the current distributions for BS, we assume an exponential shape for $P(I)$, as we did for $P(Q)$, Equation (3), $P(I) = (1/I_0) \exp(-I/I_0)$.

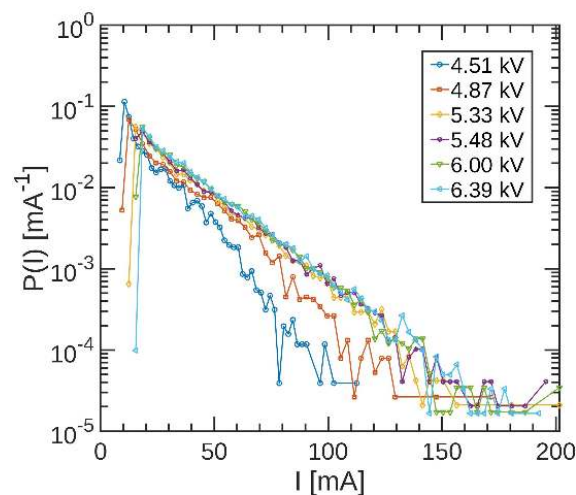


Figure 14. The BS current distribution, $P(I)$ [mA^{-1}] I [mA], for different HV, displaying a shape which is approximately exponential at the tails.

The values of the characteristic currents I_0 are reported in Figure 15a. This behaviour can be compared with a similar HV dependence found for Q_0 in Figure 11. A plateau above about 5.4 kV is also observed here for the characteristic current I_0 . Finally, the mean values of the current, $\langle I \rangle$, are displayed in Figure 15b, where one can see that for BS, the mean currents are much larger than for FS. For example, at HV = 5.5 kV, $\langle I \rangle \sim 35$ mA for BS, while $\langle I \rangle \sim (-)20$ mA for FS.

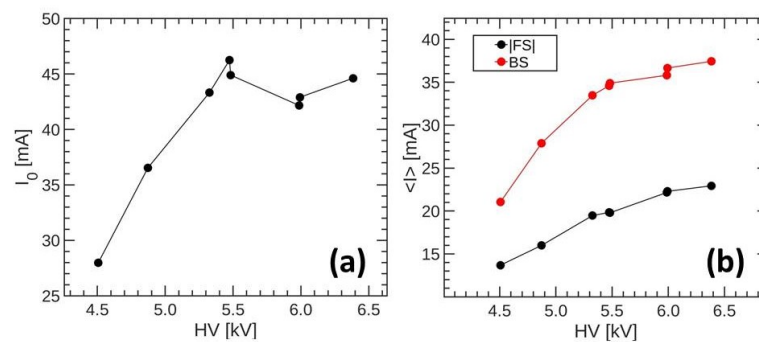


Figure 15. (a) Characteristic current I_0 [mA] and (b) mean current $\langle I \rangle$ [mA] vs. HV [kV].

Analogously to the moments shown in Figure 13, we report in Figure 16 the corresponding ones for the burst current. They definitively show that the associated distributions are also non-Gaussian.

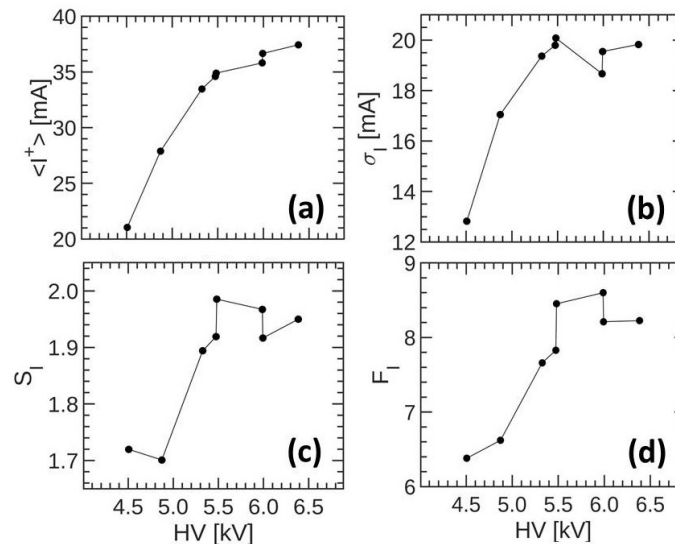


Figure 16. Same as in Figure 13 for the BS currents. Note that the value $HV \simeq 5.5$ kV seems to play the role of a separation voltage between two regimes, as found for the charge.

5.1.5. Correlations between BS

A question that often arises in DBD is whether bumps (here called strokes) are correlated to each other [26]. The same quest applies to our SDBD results. We therefore calculated, for our records, the cross-correlations, $C_{BS,BS}^{(i,j)}$, between BS separated by a time lag $\Delta t = |i - j|T$, where T is the applied signal period, according to the standard definition,

$$C_{BS,BS}^{(i,j)} = \frac{\langle [I_{BS}^{(i)}(t) - \langle I_{BS}^{(i)} \rangle][I_{BS}^{(j)}(t) - \langle I_{BS}^{(j)} \rangle] \rangle_{\Delta t}}{\sigma_{BS}^{(i)} \sigma_{BS}^{(j)}}, \quad (4)$$

where $I_{BS}^{(i)}(t) (> 0)$ is the value of the burst current within the i th BS at time t , $\langle I_{BS}^{(i)} \rangle$ the mean current value, and $\sigma_{BS}^{(i)}$ the corresponding standard deviation.

A typical cross-correlation analysis is illustrated in Figure 17, for $HV = 5.48$ kV. Similar results (not shown here) are obtained for the other applied voltages. As one can see from this analysis, there is a residual or almost no apparent temporal correlations between BS.

Therefore, in order to uncover a possible hidden structure of BS, we compared two consecutive BS with each other (i.e., 1–2, 3–4, etc.), by building their burst current intensity differences as a function of time,

$$\Delta I_{BS,BS}^{(i+1,i)}(t) = I_{BS}^{(i+1)}(t) - I_{BS}^{(i)}(t), \quad (5)$$

for $i = 1, 3, 5, \dots, 2N_p - 1$, where N_p is the total number of consecutive BS pairs in the record. An example is shown in Figure 18a, for $i = 1$ and $HV = 5.48$ kV. As one can see, bursts do not occur at the same time (note that the time origin, the start of the BS half-cycle, is the same for all strokes). We found that the time delay between bursts follows a uniform random distribution (results not shown).

Next, to find the mean behaviour of BS, we average the differences in Equation (5), determined at fixed times $t = n\Delta$, with $1 \leq n \leq N$ and $\Delta t = 0.25$ ns, over all pairs N_p ,

$$\langle \Delta I_{BS,BS}^{(i+1,i)}(t) \rangle_i = \frac{1}{N_p} \sum_{j=1}^{N_p} \Delta I_{BS,BS}^{(2j,2j-1)}(t). \quad (6)$$

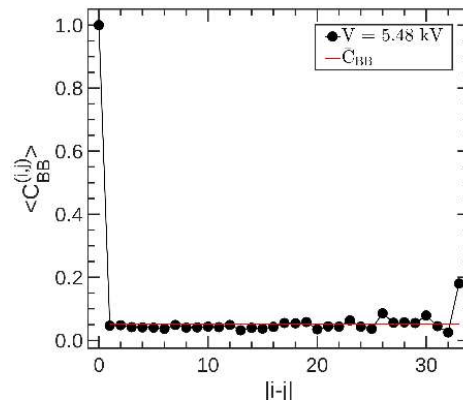


Figure 17. Mean cross-correlations between bumps as time lag for $V = 5.48 \text{ kV}$.

The mean differences are plotted in Figure 18b, where one can see that they do not average out to zero. To better visualize the evolution of differences, it is convenient to add them sequentially, as follows

$$S(n) = \sum_{j=1}^n \langle \Delta I_{BS,BS}^{(i+1,i)}(j\Delta t) \rangle_i. \quad (7)$$

Their time behavior can be conveniently visualized by adding the differences sequentially as for random walks (red line in the figure). The corresponding random walk (RW) profiles, for selected applied HV, are displayed in Figure 19a.

In order to determine the degree of auto-correlation in the signal, in this case referred to a sequence of two consecutive BS, we rely on the calculation of the Hurst exponent (see e.g., [26,32,33]). To this end, we evaluate the m th ($1 \leq m \leq N/\ell$) mean RW profile at 'time scale' ℓ ($\ell \equiv t/\Delta t$), with $1 \leq \ell \leq N$, given by

$$B_m(\ell) = \frac{1}{\ell} \sum_{n=1}^{\ell} S[(m-1)\ell + n]. \quad (8)$$

Next, we study the fluctuations between neighboring boxes according to,

$$F(\ell) = \langle [B_{m+1}(\ell) - B_m(\ell)]^2 \rangle^{1/2}, \quad (9)$$

which is expected to display a power-law behaviour,

$$F(\ell) \simeq \ell^H, \quad (10)$$

where $0 \leq H \leq 1$. It should be noted that fully uncorrelated RW has $H = 1/2$, and $H = 1$ for fully correlated ones. The results shown in Figure 19b suggest that initially, within about 6 ns, the neighboring BS remain strongly correlated. A second regime develops at intermediate times, $6 < t < 200 \text{ ns}$, suggesting that weaker correlations persist and are well described by an exponent $H \simeq 2/3$. This behaviour is consistent with a temporal fractal-like regime in which discharge fluctuations show self-similar properties. Finally, above about 200 ns, fluctuations tend to remain constant due to the finite duration of the signal, and fluctuations cannot develop further.

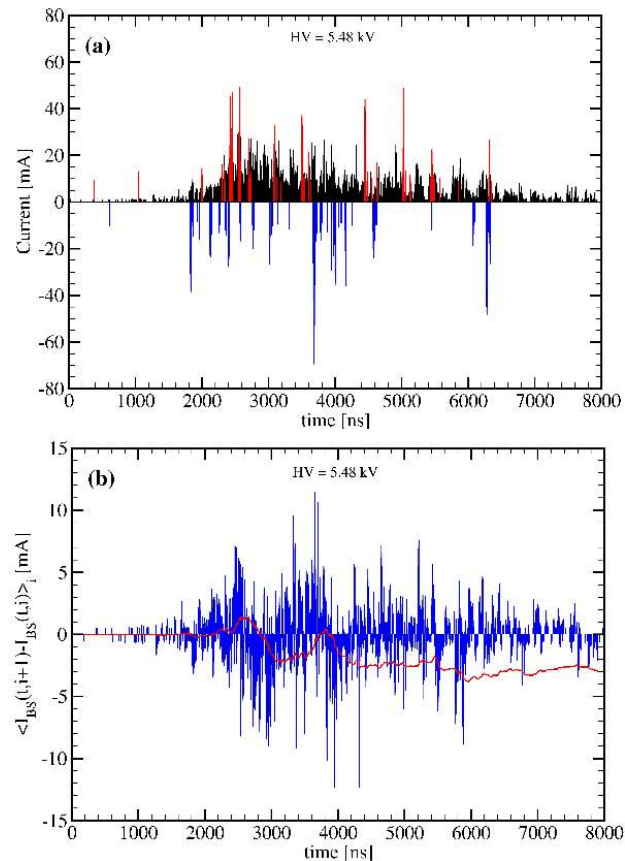


Figure 18. Internal structure of BS. (a) The second BS (red vertical lines), compared with the first one ($i = 1$) (blue vertical lines), the latter multiplied by -1 in order to directly visualize their differences, for the applied voltage $HV = 5.48$ kV. The black vertical lines represent the mean backward stroke (shown as a reference), obtained by averaging BS over the whole record (in this case 34 half-cycles). The time origin coincides with the start of the BS half-cycle, and therefore it is the same for all strokes. (b) Mean current differences, Equation (6), between consecutive BS (blue vertical lines). The accumulated mean differences, $S(n)$, with $n = t/\Delta t$ Equation (7), behave as a random walk time profile (red line).

5.2. Photomultiplier Results

The fast time response of PMT allows us to employ optical diagnostics to study the temporal evolution of the discharge pattern and evaluating the differences between FS and BS. In particular, the use of a multi-anode PMT allows us to measure the correlations and the delays in the plasma light emission between different regions above the active dielectric surface.

In the following, we report results from the analysis of the emitting times of light measured with photomultiplier tubes (PMT) [48]. In particular, we focus on the measurements of the direction and velocity of propagation of light emission along the insulating barrier surface. This was achieved by simultaneously collecting light coming from different points of the discharge air gap.

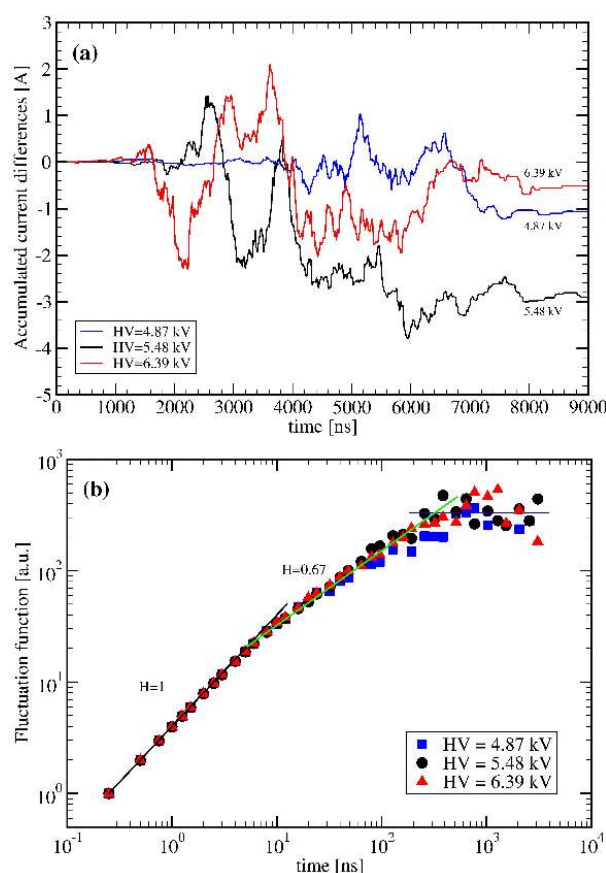


Figure 19. Analysis of time correlations between BS. (a) Accumulated mean current differences (random walk profiles) between successive BS for different HV. (b) Hurst exponent analysis of fluctuations for the profiles shown in (a). The values $H = 1$, for times $t < 6$ ns, and $H = 0.67$, for intermediate times $6 \text{ ns} < t < 200$ ns, represent the slopes of the black and green straight lines, respectively.

First, we locate the position of the bulk of the plasma emission. The discharges are well confined within a thin air sheet of one–two millimeters above the dielectric surface, next to the exposed electrode edge (see Figure 20). Discharges occur where the electric field, determined by the applied external high voltage signal, is maximal. Plasma emissivity is concentrated on such edge and expands for a few millimeters above the dielectric surface, whereas its extension above the exposed electrode is much more limited [23]. The actual size of the active optical region does depend, although not strongly, on the applied high voltage, also increasing in the late phases of the strokes. This is of use to look for correlations and delays in the light emission along the dielectric surface.

It should be noted that the plasma emissivity is quite uniform, on average, in the direction parallel to the exposed electrode edge, until the lateral edges (see Figure 20). Indeed, we did not observe significant differences between different portions of the exposed electrode edge. Moreover, we did not observe any significant correlation in the light emission times from regions even a few millimeters apart along the electrode edge direction. This implies that each discharge event develops mainly in the direction perpendicular to the electrode edge and its lateral extension is limited, as well as its height on the dielectric surface. This

confirms also that each discharge event, identified by current bursts, evolves independently from the others, even when partial overlapping in time happens.

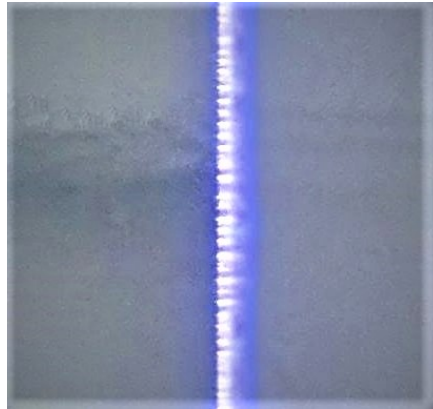


Figure 20. Plasma discharges observed in our SDBD for $V = 5.48$ kV.

The most interesting findings were, however, observed when the PMT channels collected light from regions aligned along a direction perpendicular to the exposed electrode edge. Here, correlation in light emission could be observed, and also delays between the light emission timing could be measured. When light is detected by the PMT on one of its channels, we observe a burst in the corresponding time series, as in Figure 6. Occasionally, we detect several bursts, sometimes partially overlapping, with a global duration which generally never exceeds 10 ns. These events, although interesting, were excluded from the analysis. Light detected in the first channel arrives from a region just across the edge of the exposed electrode, whereas the second channel samples a spot (each about 800 μm in diameter) 2.5 mm away on the dielectric surface.

We find that the detected bursts appear to be very similar in the two channels, with average amplitudes, respectively, of 22.9 ± 0.9 and 21.8 ± 0.9 mV and durations, respectively, of 3.71 ± 0.08 and 3.62 ± 0.09 ns. Their average numbers are different, unveiling the lower emissivity of the regions above the dielectric surface as one moves away from the electrode edge. Over a sample of about one thousand oscillations, the counting rate of bursts is, for the two channels, 130 ± 11 and 74 ± 8 kHz, of which about 65% was within the BS. Another interesting behaviour was found by looking at the times, and the HV phases, when light emission occurred. Although emissivity is somewhat stable over different oscillations, it shows a detectable and characteristic distribution during each HV cycle [48]. In both space regions, emissivity in the BS phase concentrates around the breakdown time and shows a second maximum later on.

On the contrary, emission within a FS is more uniformly distributed with the different phases of the HV oscillation. Another interesting feature of the optical emission pattern is linked to its persistency. Although about half of the events are accompanied by at least another during the same half-cycle, but only a slight minority (less than 10%); this second one is nearer than 250 ns, and in the other case the next one happens in the following half-cycle (about 40%) or in the subsequent cycle. In only 0.5% or 3% of the events, respectively, above the electrode edge and on the dielectric surface, no light was detected in the two subsequent half-cycles. This means that the spatial pattern of the discharges stays more or less stable over a relevant number of subsequent strokes and that the discharges belonging to each half-cycle are spatially related. Moreover, as a path of discharge is established, this repeats over the same spatial location, even if the timing (and so the external electric field strength) could be quite different from one event to the subsequent one. This memory effect is probably related to the dynamics of ions after the microdischarge quenching and

in particular to the charging of the dielectric surface, which could explain the persistence of the discharge pattern between subsequent HV cycles.

Finally, we compare the results of the emitting times between the two PMT channels. Now, all PMT bursts are ordered in time and the minimum delay between bursts belonging to a couple of different channels are calculated. A histogram of estimated delays can thus be obtained, and it is shown in Figure 21 [48].

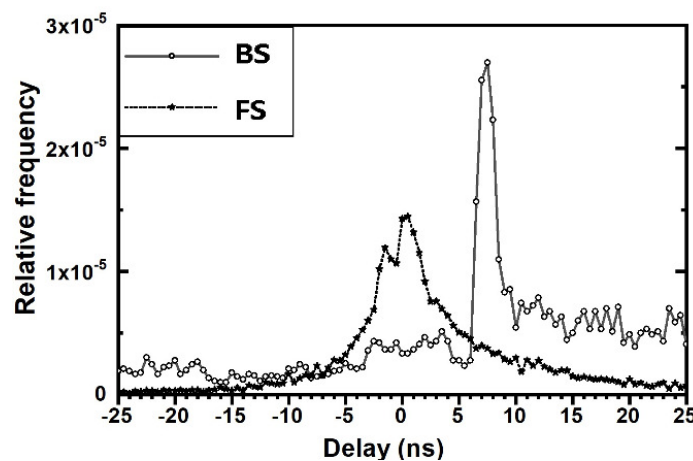


Figure 21. Distribution of delays between bursts in the forward (stars) and backward (o) strokes.

A quite evident maximum appears in BS, corresponding to an average delay of 8.4 ± 1.6 ns. This implies a propagation of the ionizing wave from the electrode edge to the dielectric surface, with an average rate of about 300 km/s. Such propagation occurs in the direction opposite to that of the electron drift, dictated by the external electrode voltage and compatible with a cathode directed streamer mechanism of discharge [2,48].

Nothing comparable could be revealed by the analysis of the FS delays. In this case, the distribution is quite symmetrical, with a slight prevalence of the positive delays. It is also significantly larger and peaking at almost zero delay. It looks like as if propagation happens on a faster time scale, that cannot be revealed by the emission timing alone and with a significant spread. Because of the small sample and uniformity of distribution with the HV phase, FS events do not show any significant dependence of the delay either on the applied HV nor on its instantaneous value.

In the case of BS, it is easy to separate bursts belonging to the near breakdown phase from the group happening towards the maximum HV amplitude. However, the distribution of delays continues to show a single defined burst, with almost the same delay, with only slight differences in the relative height and its tails. This implies that the ionizing wave propagation is not strongly dependent on the actual phase or the absolute value of the external electric field, being somewhat controlled by the local conditions developing with the microdischarge itself. This is in broad agreement with the properties reported for the microdischarges themselves, as discussed previously.

6. Conclusions

We have reported results on the statistical properties of asymmetric surface dielectric barrier discharges with an exposed metal electrode, and the other fully isolated from air, both glued onto a dielectric surface. We study the charge, current, and duration of the individual discharge events composing the two active phases of the SDBD, denoted as forward and backward strokes (FS and BS), respectively. A strong asymmetry between the two strokes has been found. For the BS, the mean charge carried by a burst is about 0.3 nC, the mean current

is 35 mA and the duration is 15 ns, while for the FS, the corresponding values are smaller in magnitude—that is, -0.1 nC, -20 mA and 11 ns, respectively.

We have studied temporal correlations between two successive backward strokes, by building the random walk profiles resulting from differences in current discharges evaluated at the same time within the BS cycle. We applied a fluctuation analysis to extract the scaling behavior of the profiles at different times scales. We found a well defined power-law of fluctuations, for 6 ns $< t < 200$ ns, characterized by a Hurst exponent $H \sim 2/3$, suggesting the presence of persistent (positive) correlations between consecutive BS. At times $t < 6$ ns, the correlation is maximal, leading to $H = 1$. The correlations found at intermediate times are a result of non-trivial phenomena related to the interaction between discharges and plasma. These findings should be useful for better assessing the models attempting to describe this complex behaviour.

We have also measured the optical emission of discharges using a photomultiplier to further study spatial correlation patterns. The optical emission is produced by electron impact excitations due to the ionizing wave propagation igniting the discharge. In particular, we have measured the spreading rate of the ionizing wave associated to microdischarges for BS. The wave moves, mostly perpendicularly, away from the edge of the exposed electrode towards the dielectric surface, roughly corresponding to the direction of the electric field determined by the instantaneous voltage level applied to the insulated electrode, but opposite to the electron drift motion. This is also the direction of the produced ionic wind. Both the order of magnitude and the direction of the ionizing wave velocity are compatible with a cathode directed streamer mechanism. However, the absence of a corresponding propagation for the microdischarges for FS points towards the presence of a different mechanism acting in this opposite phase.

Author Contributions: Conceptualization, C.R. and C.P.; methodology, C.R., R.B., C.P.; software, R.B.; validation, C.P., R.B.; formal analysis, C.P., R.B., H.E.R.; investigation, C.P.; resources, C.R.; data curation, C.P.; writing—original draft preparation, C.P., R.B., H.E.R.; writing—review and editing, C.P., H.E.R.; visualization, C.P.; supervision, C.R.; project administration, C.R.; funding acquisition, C.R. All authors have read and agreed to the published version of the manuscript.

Funding: This research received no external funding.

Acknowledgments: We gratefully acknowledge the technical support of Alessandro Mietner in the device development and experiment execution.

Conflicts of Interest: The authors declare no conflict of interest.

Abbreviations

The following abbreviations are used in this manuscript:

DBD	Dielectric barrier discharge
SDBD	Surface dielectric barrier discharge
UV	Ultraviolet
FS	Forward stroke
BS	Backward stroke
AC	Alternating current
HV	High voltage
DC	Direct current
FFT	Fast Fourier transform
OES	Optical emission spectroscopy
PMT	Photomultiplier tube
RW	Random walk

References

1. Eliasson, B.; Kogelschatz, U. Modeling and applications of silent discharge plasmas. *IEEE Trans. Plasma Sci.* **1991**, *19*, 309–323. [[CrossRef](#)]
2. Raizer, Y.P. *Gas Discharge Physics*; Springer: Berlin/Heidelberg, Germany, 1991.

3. Kogelschatz, U. Filamentary, patterned, and diffuse barrier discharges. *IEEE Trans. Plasma Sci.* **2002**, *30*, 1400–1408. [[CrossRef](#)]
4. Becker, K.H.; Kogelschatz, U.; Schoenbach, K.H.; Barker, R. *Non-Equilibrium Air Plasmas at Atmospheric Pressure*; CRC Press: Boca Raton, FL, USA, 2004.
5. Fridman, A.; Kennedy, L.A. *Plasma Physics and Engineering*; CRC Press: Boca Raton, FL, USA, 2004.
6. Kogelschatz, U. Dielectric-barrier discharges: Their history, discharge physics, and industrial applications. *Plasma Chem. Plasma Process.* **2003**, *23*, 1–46. [[CrossRef](#)]
7. Brandenburg, R. Dielectric barrier discharges: Progress on plasma sources and on the understanding of regimes and single filaments. *Plasma Sources Sci. Technol.* **2017**, *26*, 053001. [[CrossRef](#)]
8. Fridman, A.; Chirokov, A.; Gutsol, A. Non-thermal atmospheric pressure discharges. *J. Phys. Appl. Phys.* **2005**, *38*, R1. [[CrossRef](#)]
9. Esena, P.; Zanini, S.; Riccardi, C. Plasma processing for surface optical modifications of PET films. *Vacuum* **2007**, *82*, 232. [[CrossRef](#)]
10. Zanini, S.; Grimoldi, E.; Citterio, A.; Riccardi, C. Characterization of atmospheric pressure plasma treated pure cashmere and wool/cashmere textiles: Treatment in air/water vapor mixture. *Appl. Surf. Sci.* **2015**, *349*, 235. [[CrossRef](#)]
11. Napartovich, A.P. Overview of atmospheric pressure discharges producing nonthermal plasma. *Plasmas Polym.* **2001**, *6*, 1–14. [[CrossRef](#)]
12. Siliprandi, R.; Zanini, S.; Grimoldi, E.; Fumagalli, F.; Barni, R.; Riccardi, C. Atmospheric pressure plasma discharge for polysiloxane thin films deposition and comparison with low pressure process. *Plasma Chem. Plasma Process.* **2011**, *31*, 353–372. [[CrossRef](#)]
13. Massines, F.; Gherardi, N.; Sommer, F. Silane-based coatings on polypropylene, deposited by atmospheric pressure glow discharge plasmas. *Plasmas Polym.* **2000**, *5*, 151–172. [[CrossRef](#)]
14. Zanini, S.; Citterio, A.; Leonardi, G.; Riccardi, C. Characterization of atmospheric pressure plasma treated wool/cashmere textiles: Treatment in nitrogen. *Appl. Surf. Sci.* **2018**, *427*, 90. [[CrossRef](#)]
15. Zanini, S.; Freti, S.; Citterio, A.; Riccardi, C. Characterization of hydro- and oleo-repellent pure cashmere and wool/nylon textiles obtained by atmospheric pressure plasma pre-treatment and coating with a fluorocarbon resin. *Surf. Coat. Technol.* **2016**, *292*, 155. [[CrossRef](#)]
16. Dell’Orto, E.C.; Vaccaro, A.; Riccardi, C. Morphological and chemical analysis of PP film treated by Dielectric Barrier Discharge (Conference Paper). *J. Phys. Conf. Ser.* **2014**, *550*, 012032.
17. Barni, R.; Riccardi, C. Perspective of NO_x removal from numerical simulation of non-thermal atmospheric pressure plasma chemical kinetics. *High Temp. Mater. Process.* **2010**, *14*, 205.
18. Corke, T.C.; Post, M.C.; Orlov, D.M. SDBD plasma enhanced aerodynamics: Concepts, optimization and applications. *Prog. Aerosp. Sci.* **2007**, *43*, 193–217. [[CrossRef](#)]
19. Enloe, C.L.; McLaughlin, T.E.; VanDyken, R.D.; Kachner, K.D.; Jumper, E.J.; Corke, T.C. Mechanisms and responses of a single dielectric barrier plasma actuator: Plasma morphology. *AIAA J.* **2004**, *42*, 589–594. [[CrossRef](#)]
20. Pons, J.; Moreau, E.; Touchard, G. Asymmetric surface dielectric barrier discharge in air at atmospheric pressure: Electrical properties and induced airflow characteristics. *J. Phys. Appl. Phys.* **2005**, *38*, 3635. [[CrossRef](#)]
21. Caruana, D. Plasmas for aerodynamic control. *Plasma Phys. Control. Fusion* **2010**, *52*, 124045. [[CrossRef](#)]
22. Corke, T.C.; Enloe, C.L.; Wilkinson, S.P. Dielectric barrier discharge plasma actuators for flow control. *Annu. Rev. Fluid Mech.* **2010**, *42*, 505–529. [[CrossRef](#)]
23. Biganzoli, I.; Barni, R.; Riccardi, C.; Gurioli, A.; Pertile, R. Optical and electrical characterization of a surface dielectric barrier discharge plasma actuator. *Plasma Sources Sci. Technol.* **2013**, *22*, 025009. [[CrossRef](#)]
24. Roth, J.R.; Sherman, D.M.; Wilkinson, S.P. Electrohydrodynamic flow control with a glow-discharge surface plasma. *AIAA J.* **2000**, *38*, 1166–1172. [[CrossRef](#)]
25. Post, M.L.; Corke, T.C. Separation control on high angle of attack airfoil using plasma actuators. *AIAA J.* **2004**, *42*, 2177–2184. [[CrossRef](#)]
26. Siliprandi, R.A.; Roman, H.E.; Barni, R.; Riccardi, C. Characterization of the streamer regime in dielectric barrier discharges. *J. Appl. Phys.* **2008**, *104*, 063309. [[CrossRef](#)]
27. Orlov, D.M.; Font, G.I.; Edelstein, D. Characterization of discharge modes of plasma actuators. *AIAA J.* **2008**, *46*, 3142–3148. [[CrossRef](#)]
28. Dedrick, J.; Boswell, R.W.; Audier, P.; Rabat, H.; Hong, D.; Charles, C. Plasma propagation of a 13.56 MHz asymmetric surface barrier discharge in atmospheric pressure air. *J. Phys. Appl. Phys.* **2011**, *44*, 205202. [[CrossRef](#)]
29. Biganzoli, I.; Barni, R.; Gurioli, A.; Pertile, R.; Riccardi, C. Experimental investigation of filamentary and non-filamentary regimes in a surface dielectric barrier plasma actuator. *J. Phys. Conf. Ser.* **2014**, *550*, 012038. [[CrossRef](#)]
30. Biganzoli, I.; Barni, R.; Riccardi, C. Temporal evolution of a surface dielectric barrier discharge for different groups of plasma microdischarges. *J. Phys. Appl. Phys.* **2012**, *46*, 025201. [[CrossRef](#)]
31. Raizer, Y.P.; Mokrov, M.S. Physical mechanisms of self-organization and formation of current patterns in gas discharges of the Townsend and glow types. *Phys. Plasmas* **2013**, *20*, 1091604. [[CrossRef](#)]
32. Koscielny-Bunde, E.; Bunde, A.; Havlin, S.; Roman, H.E.; Goldreich, Y.; Schellnhuber, H.-J. Indication of a universal persistence law governing atmospheric variability. *Phys. Rev. Lett.* **1998**, *81*, 729. [[CrossRef](#)]
33. Kantelhardt, J.W.; Roman, H.E.; Greiner, M. Discrete wavelet approach to multifractality. *Phys. Stat. Mech. Its Appl.* **1995**, *220*, 219–238. [[CrossRef](#)]

34. Barni, R.; Biganzoli, I.; Dell'Orto, E.C.; Riccardi, C. Effect of duty-cycles on the air plasma gas-phase of dielectric barrier discharges. *J. Appl. Phys.* **2015**, *118*, 143301. [[CrossRef](#)]
35. Unfer, T.; Boeuf, J.P. Modeling and comparison of sinusoidal and nanosecond pulsed surface dielectric barrier discharges for flow control. *Plasma Phys. Control. Fusion* **2010**, *52*, 124019. [[CrossRef](#)]
36. Likhanskii, A.V.; Shneider, M.N.; Macheret, S.O.; Miles, R.B. Modeling of dielectric barrier discharge plasma actuator in air. *J. Appl. Phys.* **2008**, *103*, 053305. [[CrossRef](#)]
37. Hoskinson, A.R.; Hershkowitz, N. Modelling of dielectric barrier discharge plasma actuators with thick electrodes. *J. Phys. Appl. Phys.* **2011**, *44*, 085202. [[CrossRef](#)]
38. Nishida, H.; Abe, T. Numerical analysis of plasma evolution on dielectric barrier discharge plasma actuator. *J. Appl. Phys.* **2011**, *110*, 013302. [[CrossRef](#)]
39. Barni, R.; Esena, P.; Riccardi, C. Chemical kinetics simulation for atmospheric pressure air plasmas in a streamer regime. *J. Appl. Phys.* **2005**, *97*, 073301. [[CrossRef](#)]
40. Shang, J.S.; Huang, P.G. Surface plasma actuators modeling for flow control. *Prog. Aerosp. Sci.* **2014**, *67*, 29–50. [[CrossRef](#)]
41. Shang, K.; Wang, M.; Peng, B.; Li, J.; Lu, N.; Wu, Y. Characterization of a novel volume-surface DBD reactor: Discharge characteristics, ozone production and benzene degradation. *J. Phys. Appl. Phys.* **2019**, *53*, 065201. [[CrossRef](#)]
42. Doležalová, E.; Prukner, V.; Kuzminova, A.; Simek, M. On the inactivation of *Bacillus subtilis* spores by surface streamer discharge in humid air caused by reactive species. *J. Phys. Appl. Phys.* **2020**, *53*, 245203. [[CrossRef](#)]
43. Wei, W.; He, S.; Yang, Z.; Wang, S.; Mei, G.; Gao, G.; Wu, G. Electromechanical efficiency improvement of the surface DBD by composite dielectric. *AIP Adv.* **2019**, *9*, 045127. [[CrossRef](#)]
44. Argüeso, M.; Robles, G.; Sanz, J. Implementation of a Rogowski coil for the measurement of partial discharges. *Rev. Sci. Instrum.* **2005**, *76*, 065107. [[CrossRef](#)]
45. Biganzoli, I.; Barni, R.; Riccardi, C. Note: On the use of Rogowski coils as current probes for atmospheric pressure dielectric barrier discharges. *Rev. Sci. Instrum.* **2013**, *84*, 016101. [[CrossRef](#)] [[PubMed](#)]
46. Laux, C.O.; Spence, T.G.; Kruger, C.H.; Zare, R.N. Optical diagnostics of atmospheric pressure air plasmas. *Plasma Sources Sci. Technol.* **2003**, *12*, 125. [[CrossRef](#)]
47. Hoder, T.; Brandenburg, R.; Basner, R.; Weltmann, K.-D.; Kozlov, K.V.; Wagner, H.-E. A comparative study of three different types of barrier discharges in air at atmospheric pressure by cross-correlation spectroscopy. *J. Phys. Appl. Phys.* **2010**, *43*, 124009. [[CrossRef](#)]
48. Barni, R.; Biganzoli, I.; Riccardi, C. Spatial and temporal evolution of microdischarges in Surface Dielectric Barrier Discharges for aeronautical applications plasmas. *J. Phys. Conf. Ser.* **2014**, *550*, 012036. [[CrossRef](#)]

A.2 High concentration propane depletion with photocatalysis

Reproduced from Piferi, C.; Riccardi, C. High Concentration Propane Depletion with Photocatalysis. *AIP Advances* 2021, 11 (12), 125008, <https://doi.org/10.1063/5.0073924>, with the permission of AIP Publishing.

High concentration propane depletion with photocatalysis

Cite as: AIP Advances 11, 125008 (2021); <https://doi.org/10.1063/5.0073924>

Submitted: 05 October 2021 • Accepted: 09 November 2021 • Published Online: 06 December 2021

 C. Piferi and  C. Riccardi



View Online



Export Citation



CrossMark



Call For Papers!

AIP Advances
SPECIAL TOPIC: Advances in
Low Dimensional and 2D Materials

AIP Advances 11, 125008 (2021); <https://doi.org/10.1063/5.0073924>

11, 125008

© 2021 Author(s).

High concentration propane depletion with photocatalysis

Cite as: AIP Advances 11, 125008 (2021); doi: 10.1063/5.0073924

Submitted: 5 October 2021 • Accepted: 9 November 2021 •

Published Online: 6 December 2021



C. Piferi and C. Riccardi^{a)}

AFFILIATIONS

Department of Physics, University of Milano-Bicocca, Piazza della Scienza 3, 20126 Milano, Italy

^{a)} Author to whom correspondence should be addressed: claudia.riccardi@unimib.it

ABSTRACT

Our work is aimed at studying the abatement of volatile organic compounds produced by photocatalysts working in different light spectra, investigating the best catalyst able to treat propane in air mixtures at high concentrations of the order of thousands of ppm. The experimental data were analyzed in order to extract the relevant parameters and to compare the catalytic activities of three different photocatalysts, TiO₂, WO₃, and their mixtures. In a reactor box of 1.5 l, photocatalysis processing with TiO₂ catalysts gave the best propane depletion of the order of 10% for initial propane concentrations of up to 5000 ppm after 22 min and UV-A lamps with an intensity of 0.4 mW/cm² while the TiO₂ and WO₃ catalysts produced an abatement of about 5% after 22 min using UV-C light at an intensity of 5 × 10² mW/cm².

© 2021 Author(s). All article content, except where otherwise noted, is licensed under a Creative Commons Attribution (CC BY) license (<http://creativecommons.org/licenses/by/4.0/>). <https://doi.org/10.1063/5.0073924>

I. INTRODUCTION

Several methods have been proposed for depletion of VOCs, including adsorption,¹ absorption,² thermal decomposition,³ catalytic oxidation,⁴ bio-filtration,⁵ and membrane separation.⁶

Photocatalytic oxidation (PCO) of VOCs is a very attractive and promising alternative technology for air purification.⁷

It has been demonstrated that organics can be oxidized to carbon dioxide, water, and simple mineral acids at low temperatures on metal oxides catalysts using, for example, the TiO₂ catalyst. Several parameters affect the VOC conversion processes: the specific surface area of the catalyst and the VOC concentration. However, the time conversion takes hours and is effective for low VOC concentrations of the order of tens of ppm. In addition, it is critical that the choice of the substrate should be degraded as well as its concentration and its significance in actual use and the type of irradiation source and its irradiance at the sample surface.

For VOC degradation at relatively higher concentrations of the order of hundreds and thousands of ppm, new studies have oriented to thermal plasmas, such as spark discharges^{8–10} and non-thermal plasma (NTP).^{11,12} While thermal plasmas are too expensive, non-thermal plasma (NTP) has recently attracted more attention as a convenient and clean alternative.

In the non-thermal plasma, chemical reaction charged species and radicals are produced under steady-state conditions. The primary electrons collide with background molecules producing

secondary electrons, photons, ions, and radicals.¹³ This process is highly non-selective and creates a chemical reactive environment able to treat materials as well as gases at room temperature.^{14–16} Previous studies on NTP demonstrated they are very effective in material applications by employing different gas precursors because of their ability to highly dissociate molecules in the gas phase, producing very reactive chemical groups at room temperature: materials are not damaged and can be easily functionalized.^{17–20} When generated at atmospheric pressure, plasma produces chemical species able to also dissociate VOC molecules at higher concentrations up to thousand ppm,^{21–24} but the processes are non-selective.

Despite the success of NTP in VOC dissociation, the production of by-products such as ozone, aerosol particles, and incompletely oxidized compounds requires further research, including chemical simulations, in order to understand the process phenomenology.^{25–27} A combination of NTP and catalysis was attempted in order to increase the depletion efficiency. The addition of a catalyst bed near the plasma zone seems to enhance the decomposition rate of pollutants, reducing the undesirable by-products due to the increase in retention time.²⁸

In fact, NTPs can contain a diverse mix of highly reactive species, and they are difficult to operate in such a way as to produce single products in high yield and at high selectivity.^{29,30} Integration of plasma and catalysts together promises to combine the advantages of the two to effect transformations that are currently difficult or impossible to achieve.^{31,32}

In our recent studies, we employed NTP surface discharges in which discharge is performed on the surface of the dielectric layer where also an electrode is located.^{33–35} In this plasma configuration, the catalysis can be integrated near the plasma source, directly near the electrodes.

In order to increase the abatement efficiency and to understand which mechanisms underlie the depletion processes, some more research would be focused on the kinetics of the reaction products from an experimental point of view.

A better insight into the underlying physical and chemical processes is crucial and can be obtained by experiments applying diagnostics, studying both the chemical processes occurring at the catalyst surface and the dependence of the catalysis processes on the VOC concentration.^{36,37}

Our work is aimed at studying the abatement produced by photocatalysts working in different light spectra, investigating the best catalyst able to treat propane in air mixtures at high concentrations. These studies represent the starting point for the next research in which the catalyst and NTP will be combined in a hybrid reactor system.

We designed an experimental reactor in order to study the VOC abatement by catalytic processes using TiO_2 , WO_3 , and their mixtures and UV-A, UV-C, and visible light. We study the reaction kinetics in different propane gas air mixtures, evaluating the propane abatement as a function of time. The experimental data were analyzed in order to extract the relevant parameters and to compare the three photocatalytic activities.

We worked at high propane concentrations between 1200 and 5000 ppm in view of further applications in which photocatalysis will be combined with plasma processing. In the literature, there are few experiments carried out by photocatalysis at these high concentrations. This work, therefore, intends to explore these conditions in order to broaden the effects of photocatalysis on this new application field.

II. EXPERIMENTAL SETUP

In our experiment, we used a vacuum cross chamber (20 cm length and 10 cm diameter) with a volume of about 1.5 l. The catalytic support is placed in a chamber, and the lamps are placed facing the catalytic support inside the chamber or outside the chamber in front of a quartz window. Three of the four openings are closed by vacuum gauges, and the last one is closed by a quartz window to let the emission light from the lamp activate the catalyst (Fig. 1).

The lamp characterization has been previously explained in our article.³⁸ The intensity emission of our lamps is reported in Table 1.

We employed two different catalysts, TiO_2 and WO_3 , in different mixtures deposited on plane rectangular tile surfaces. In this paper, we refer to the following three depositions:

- **A:** 34.5 mg/cm² of TiO_2 deposited over the 7.6 × 7.3 cm² tile,
- **B:** 40.9 mg/cm² of 50% TiO_2 + 50% WO_3 deposited over the 7.7 × 7.5 cm² tile, and
- **C:** 38.2 mg/cm² of WO_3 deposited over the 7.4 × 7.3 cm² tile.

The setup is shown in Fig. 2. The black bold lines represent the tube connections through the whole system. In the diagram, pure air represents a gas cylinder containing ~80% of N_2 and 20% of O_2 , meaning that the concentration of CO_2 , CO , hydrocarbons,

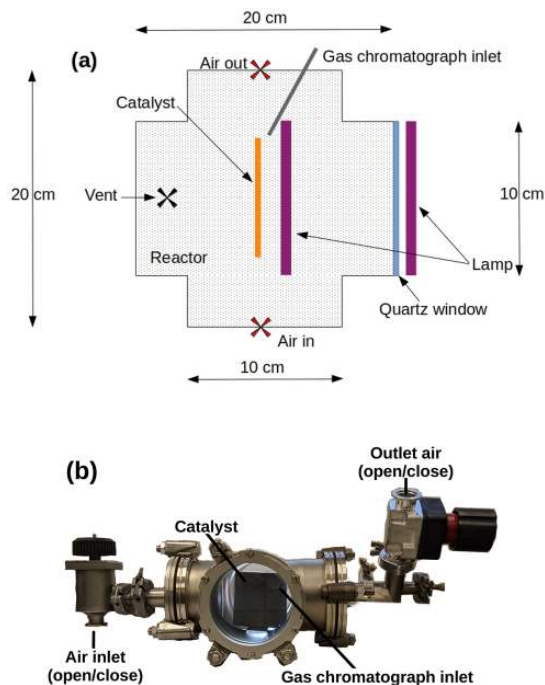


FIG. 1. Reactor setup: (a) scheme and (b) photo. The lamp can be placed either inside or outside the reactor box. The reactor is equipped with a quartz window to let the lamp light from the outside activate the catalyst, a vent to recirculate the air, a catalyst, a gas chromatograph inlet, and air inlet and outlet valves.

TABLE I. Intensity emission of our lamps at different distances.³⁸

Distance	0.5 cm	11 cm
	(lamp inside the box)	(lamp outside the box)
UV-A	30 mW/cm ²	0.4 mW/cm ²
UV-C	4 W/cm ²	35 mW/cm ²
Visible	0.5 W/cm ²	0.9 mW/cm ²

and other pollutants is negligible. The red crosses are the symbol of open-close valves. The VOC gas (propane) is placed in a cylinder, and its flow is regulated by flow meter 1, while the pure air cylinder flow is regulated by flow meter 2. We used two gas flow meters manufactured by the Bronkhorst factory.

For the gas chromatographic analysis, we used a Micro GC Agilent 3000 instrument.

III. MEASUREMENT RESULTS

A. Gas chromatograph calibration

The gas chromatograph (GC) output reports a signal composed of peaks of intensity proportional to the concentration of specific

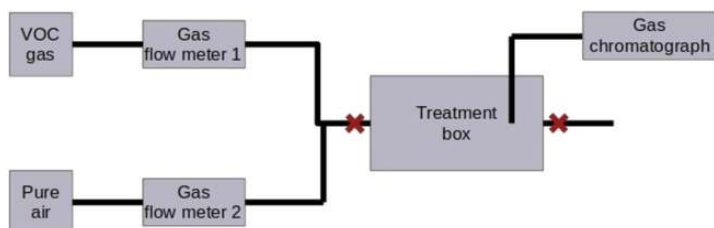


FIG. 2. Equipment setup. The VOC gas (propane) is placed in a cylinder, and its flow is regulated by flow meter 1, while the pure air cylinder flow is regulated by flow meter 2. The analyses are made using a Micro GC Agilent 3000 gas chromatograph.

species. The area of each peak is strongly dependent on the setting parameters during the sampling conditions. For a precise evaluation of concentration, it is necessary to perform a specific calibration first. Usually, the calibration is carried out using a cylinder containing

a known concentration of the desired gas (one point calibration). However, we decided for a multipoint calibration.

As discussed in Sec. II, we deliver propane by means of a flow meter system (Fig. 2). The propane flow relative to the total

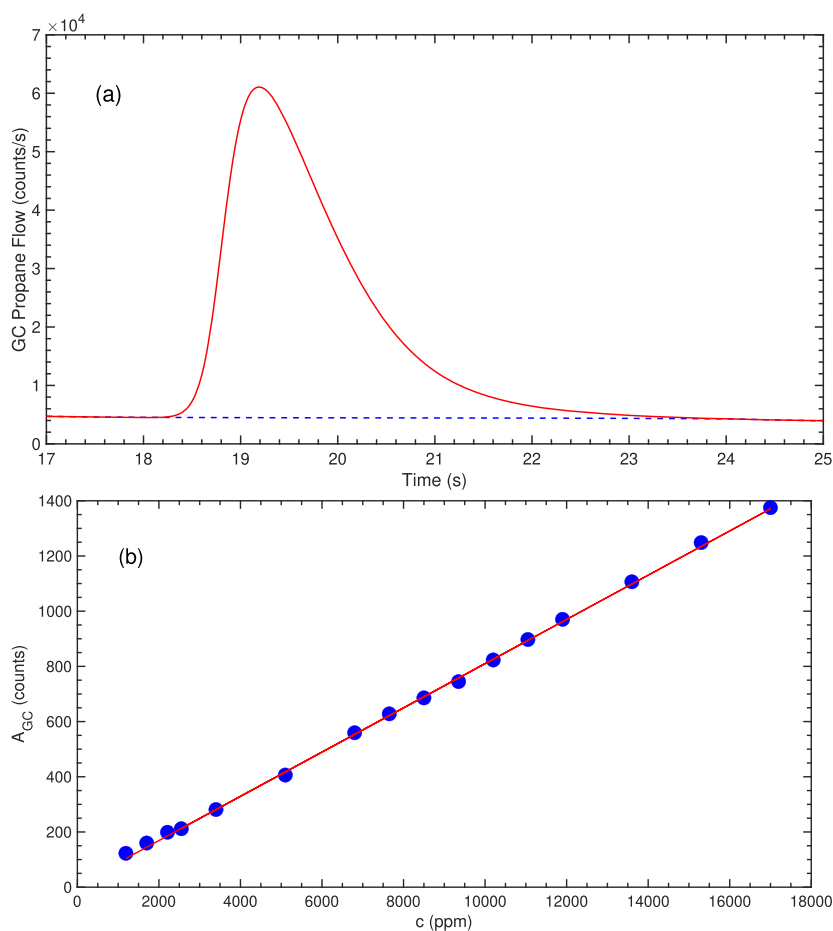


FIG. 3. (a) Example of propane chromatogram peak and (b) the calibration plot of propane reporting 16 couples of data (AreaGC and c) measured varying the propane inlet in the reactor box.

(air-pentane) input flow, denoted as c , typically expressed in ppm, is given by

$$c = \frac{\Phi_{C_3H_8}}{\Phi_{air} + \Phi_{C_3H_8}}, \quad (1)$$

where Φ_{air} is the pure air flow and $\Phi_{C_3H_8}$ is the propane flow, given in liters/sec. The values of air and propane flows are measured by the gas flow meters (Fig. 2). These two values determine the initial conditions of the experiment before the treatment. The relative propane flow, Eq. (1), can be used to determine the actual propane concentration (in ppm), present in the air-propane mix system, with the help of a GC connected to the reactor chamber, as indicated in Fig. 2.

A typical propane chromatogram trace is shown in Fig. 3(a), as a function of tracing time. The quantity of interest to us is the total count measured by the GC [red line in Fig. 3(a)], which is given by the integral of the excess count with respect to the reference line without the presence of propane [dashed line in Fig. 3(a)].

A set of 16 measurements of the GC area, A_{GC} , vs the corresponding relative propane flow c is displayed in Fig. 3(b). The results suggest a linear regression,

$$A_{GC} = \frac{801 c \text{ (ppm)} + 8.65}{10^4}, \quad (2)$$

where A_{GC} is expressed in counts and c in ppm. It is assumed now that for arbitrary flow conditions, we can determine A_{GC} ; we can then estimate the actual propane concentration by inverting Eq. (2), yielding

$$c \text{ (ppm)} = 10^4 \frac{A_{GC} - 8.65}{801}. \quad (3)$$

B. Experimental results

The experimental campaign consists in placing the catalyst and the lamp in the desired position; the inlet and outlet valves

are opened in order to ensure flow of the desired concentration of propane through the reactor for three minutes; then the valves are closed. A first chromatographic sampling is performed in order to measure the initial propane concentration. When switching on the lamp, the catalyst starts to act on the propane gas. We analyzed the gas concentrations repeating the sampling at different treatment times. In the reactor box, a vent is switched on during the chromatographic sampling in order to ensure the flow of the gases toward the chromatograph is uniform.

The experimental concentrations are plotted as a function of time in Figs. 4–8.

We fit the experimental curves by estimating the propane decomposition simply as

$$\rho(t) = \rho(0) \exp\left(-\frac{t}{\tau}\right), \quad (4)$$

where $\rho(0)$ is the initial concentration and τ represents the half time depletion. In terms of normalized concentration $c(t) = \rho(t)/\rho(0)$, the equation becomes

$$c(t) = \exp\left(-\frac{t}{\tau}\right). \quad (5)$$

We started our experiments using catalyst A. During this campaign, we used different UV-A, UV-C, and visible lamps,³⁸ varying the working conditions such as the propane concentrations and the catalyst–lamp distances.

With the UV-C and visible lamps, no propane depletion occurred, while about 7%–9% of propane dissociation was detected using the UV-A lamp, after 16 min of treatment (Fig. 4). These results are in agreement with the well-known photocatalytic activity of TiO₂ in the range of the UV-A spectrum.

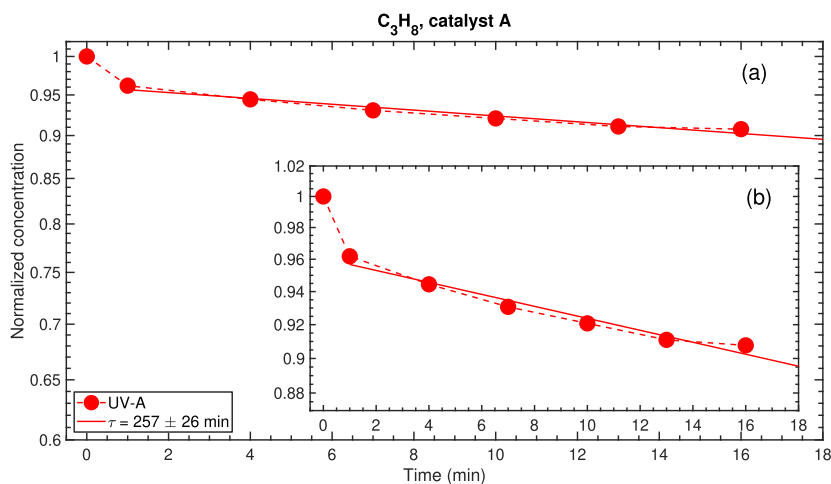


FIG. 4. Propane depletion using UV-A at an intensity of 30 mW/cm². About 10% of pentane was abated. Both graphs are in the y-log scale; (a) in the y range (0.6–1.02), while (b) in (0.88–1.02).

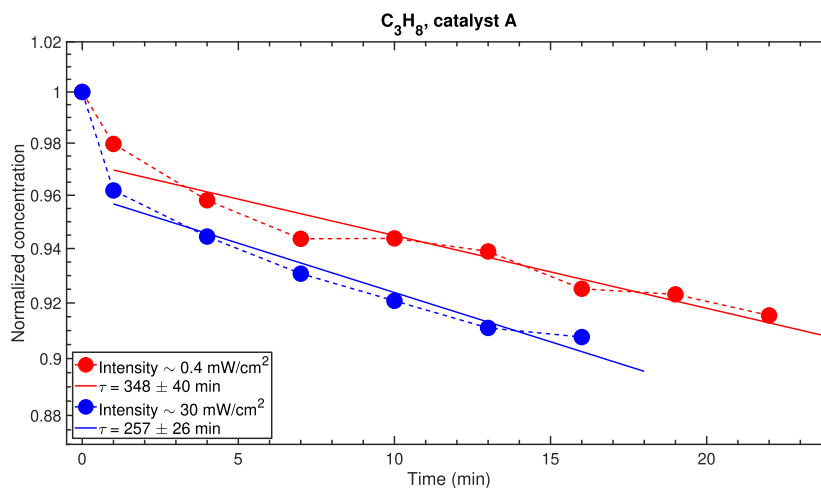


FIG. 5. Propane depletion using UV-A at different distances between lamp and catalyst, which means a different intensity of the lamp.

Tests with the UV-A lamp in different positions with respect to the catalyst and placement of the lamp outside and inside of the reactor box were also performed. The light intensity on the catalyst when the lamp is outside the box at a distance of 11 cm is about 0.4 mW/cm^2 , while that when located inside the box at a distance of 0.5 cm is of about 30 mW/cm^2 . As we can see in Fig. 5, propane depletions are similar for the two light intensities, and this means that a low intensity is sufficient to ignite the photocatalytic processes.

We performed measurements for different starting propane concentrations, and we found that the photocatalysis does not depend on the initial concentrations as depicted in Fig. 6. Contrary to what happens at low VOC concentrations, where the photocatalytic depletion strongly depends on the concentration itself,³⁹ at high initial concentrations, between 1200 and 5000 ppm, the dissociation occurs at similar time rates.

Then we compared the depletion of propane using three different catalysts A, B, and C, and different UV-A, UV-C, and

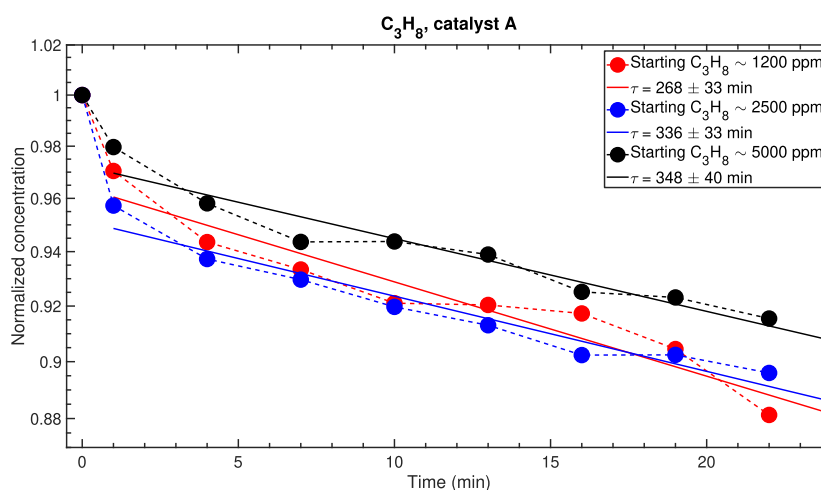


FIG. 6. Propane depletion using UV-A and different starting propane concentrations.

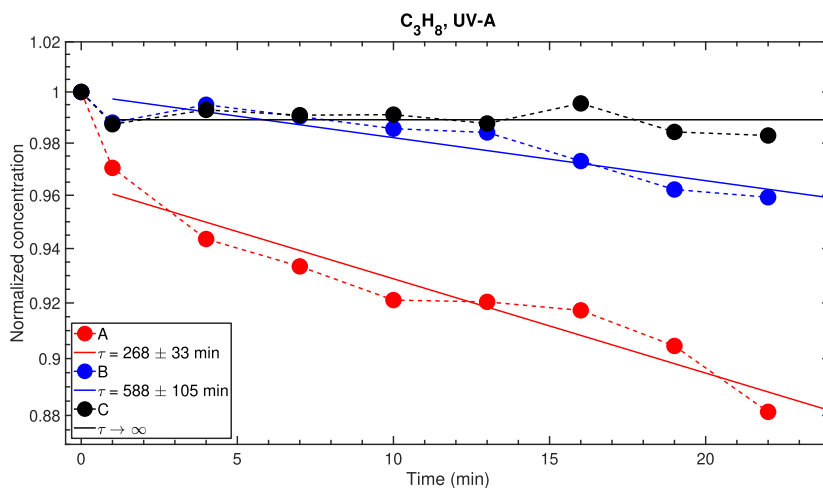


FIG. 7. Propane depletion using catalysts A, B, and C using UV-A lamp.

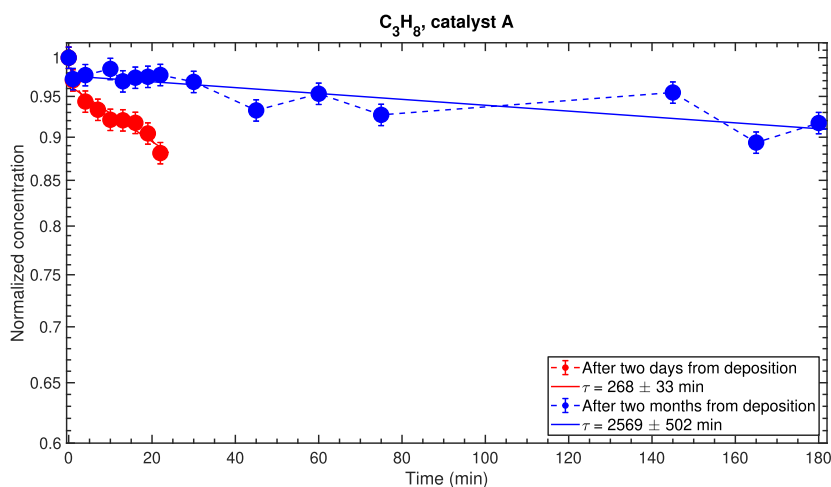


FIG. 8. Propane depletion using catalyst A and UV-A lamp for different times after catalyst deposition.

visible lamps, at a concentration of about 1200 ppm. Using the UV-A lamp with an intensity of 0.4 mW/cm^2 , a propane depletion of 12% occurred with catalyst A, while a dissociation of a few percentages with catalysts B and C was measured (Fig. 7). Using UV-C at an intensity of 4 W/cm^2 , a depletion of about 5% occurred after 22 min only for catalyst B. Although the VOC depletion is quite low, this result outlines the photocatalytic activity of the

mixture of WO_3 and TiO_2 already reported in the literature with UV-C light.^{40,41}

To evaluate the aging of the catalytic support due to exposure to air, we measured the abatement using catalyst A deposited on the tile support for two months. In this experiment, a lower depletion trend was observed, as reported in Fig. 8. This result permits to estimate the lifetime of our catalytic support.

IV. CONCLUSIONS

In this paper, we demonstrated the ability of TiO₂ catalysts to abate high propane concentrations using a relatively low intensity UV-A lamp of about 0.4 mW/cm².

We performed an experimental reactor in order to study the propane abatement at high concentrations by catalytic processes using TiO₂, WO₃, and their mixtures deposited on a tile, whose surface is about 55 cm², and using UV-A, UV-C, and visible lights. The highest abatement has been obtained using the TiO₂ catalyst and UV-A light. The abatement rate for the initial propane concentration between 1200 and 5000 ppm is of the order of 10% after 22 min, and the time scale of depletion is of the order of hours. We found that the TiO₂ photocatalytic activity does not depend on the initial concentration, contrary to what happens at low VOC concentrations, as reported in the literature.³⁹

The TiO₂ catalyst suffers from aging effects since after two months, its depletion action is greatly reduced. A relatively lower abatement is detected by the UV-C lamp when the TiO₂ and WO₃ mixture of about 5% is used in 22 min. Null abatement was measured when using visible lamps for all the catalysts and when using WO₃.

This analysis demonstrates the efficacy of the photocatalysis for high VOC concentrations and also represents a starting point for further studies on the hybrid plasma-catalysis, where the TiO₂ catalyst will be deposited in the vicinity of the plasma electrodes.

ACKNOWLEDGMENTS

We are grateful to Fondazione di Comunità Milano-Fondo Solidale Professor Ignazio Renato Bellobono (Grant No. 2020-CONT-0206) for funding our research. We also gratefully acknowledge the technical support of Alessandro Mietner and Alessandro Baù in device development and experiment execution.

AUTHOR DECLARATIONS

Conflict of Interest

The authors declare no conflict of interest.

DATA AVAILABILITY

The data that support the findings of this study are available from the corresponding author upon reasonable request.

REFERENCES

- I. A. Aguayo-Villarreal, M. A. Montes-Morán, V. Hernández-Montoya, A. Bonilla-Petriciolet, A. Concheso, C. K. Rojas-Mayorga, and J. González, "Importance of iron oxides on the carbons surface vs the specific surface for VOC's adsorption," *Ecol. Eng.* **106**, 400–408 (2017).
- W. Wang, X. Ma, S. Grimes, H. Cai, and M. Zhang, "Study on the adsorbability, regeneration characteristics and thermal stability of ionic liquids for VOCs removal," *Chem. Eng. J.* **328**, 353–359 (2017).
- E. Donley and D. Lewandowski, "Optimized design and operating parameters for minimizing emissions during VOC thermal oxidation," *Metal Finishing: Guidebook-directory* (Elsevier, 1998).
- X. Chen, S. A. C. Carabineiro, S. S. T. Bastos, P. B. Tavares, J. J. M. Órfão, M. F. R. Pereira, and J. L. Figueiredo, "Catalytic oxidation of ethyl acetate on cerium-containing mixed oxides," *Appl. Catal., A* **472**, 101–112 (2014).
- A. Vergara-Fernández, S. Revah, P. Moreno-Casas, and F. Scott, "Biofiltration of volatile organic compounds using fungi and its conceptual and mathematical modeling," *Biotechnol. Adv.* **36**, 1079–1093 (2018).
- B. Belaissaoui, Y. Le Moulec, and E. Favre, "Energy efficiency of a hybrid membrane/condensation process for VOC (volatile organic compounds) recovery from air: A generic approach," *Energy* **95**, 291–302 (2016).
- M. Hussain, N. Russo, and G. Saracco, "Photocatalytic abatement of VOCs by novel optimized TiO₂ nanoparticles," *Chem. Eng. J.* **166**, 138–149 (2011).
- R. Barni, I. Biganzoli, D. Tasseti, and C. Riccardi, "Characterization of a plasma jet produced by spark discharges in argon air mixtures at atmospheric pressure," *Plasma Chem. Plasma Process.* **34**, 1415–1431 (2014).
- R. Barni, A. Quintini, M. Piselli, and C. Riccardi, "Hydrocarbon plasma reforming through intermittent spark discharges," *High Temp. Mater. Process.* **13**, 453 (2009).
- R. Barni, A. Quintini, M. Piselli, and C. Riccardi, "Experimental study of hydrogen plasma reforming by intermittent spark discharges," *J. Appl. Phys.* **103**, 063302 (2008).
- R. Barni, R. Benocci, N. Spinicchia, H. E. Roman, and C. Riccardi, "An experimental study of plasma cracking of methane using DBDs aimed at hydrogen production," *Plasma Chem. Plasma Process.* **39**, 241–258 (2019).
- R. Barni and C. Riccardi, "Gas-phase evolution of Ar/H₂O and Ar/CH₄ dielectric barrier discharge plasmas," *Eur. Phys. J. D: Atom. Mol. Opt. Phys.* **72**, 62 (2018).
- A. Bogaerts, X. Tu, J. C. Whitehead, G. Centi, L. Lefteris, O. Guaitella, F. Azzolina-Jury, H.-H. Kim, A. B. Murphy, W. F. Schneider, T. Nozaki, J. C. Hicks, A. Rousseau, F. Thévenet, A. Khacef, and M. Carreon, "The 2020 plasma catalysis roadmap," *J. Phys. D: Appl. Phys.* **53**, 443001 (2020).
- B. Marcandalli and C. Riccardi, "Plasma treatments of fibres and textiles," in *Plasma Technologies for Textiles: A Volume in Woodhead Publishing Series in Textiles* (Woodhead Publishing Limited, 2007), pp. 282–300.
- A. Raffaele-Addamo, C. Riccardi, E. Selli, R. Barni, M. Piselli, G. Poletti, F. Orsini, B. Marcandalli, M. R. Massafra, and L. Meda, "Characterization of plasma processing for polymers," *Surf. Coat. Technol.* **174–175**, 886–890 (2003).
- S. Zanini, E. Grimoldi, and C. Riccardi, "Development of controlled releasing surfaces by plasma deposited multilayers," *Mater. Chem. Phys.* **138**, 850–855 (2013).
- S. Zanini, P. Massini, M. Mietta, E. Grimoldi, and C. Riccardi, "Plasma treatments of pet meshes for fuel-water separation applications," *J. Colloid Interface Sci.* **322**, 566–571 (2008).
- S. Zanini, C. Riccardi, C. Canevali, M. Orlandi, L. Zoia, and E.-L. Tolppa, "Modifications of lignocellulosic fibers by Ar plasma treatments in comparison with biological treatments," *Surf. Coat. Technol.* **200**, 556–560 (2005).
- R. Barni, C. Riccardi, E. Selli, M. R. Massafra, B. Marcandalli, F. Orsini, G. Poletti, and L. Meda, "Wettability and dyeability modulation of poly(ethylene terephthalate) fibers through cold SF₆ plasma treatment," *Plasma Process. Polym.* **2**, 64–72 (2005).
- S. Zanini, R. Ziano, and C. Riccardi, "Stable poly(acrylic acid) films from acrylic acid/argon plasmas: Influence of the mixture composition and the reactor geometry on the thin films chemical structures," *Plasma Chem. Plasma Process.* **29**, 535–547 (2009).
- F. Thévenet, L. Sivachandiran, O. Guaitella, C. Barakat, and A. Rousseau, "Plasma-catalyst coupling for volatile organic compound removal and indoor air treatment: A review," *J. Phys. D: Appl. Phys.* **47**, 224011 (2014).
- A. A. Abdelaziz, T. Seto, M. Abdel-Salam, and Y. Otani, "Performance of a surface dielectric barrier discharge based reactor for destruction of naphthalene in an air stream," *J. Phys. D: Appl. Phys.* **45**, 115201 (2012).
- A. A. Assadi, A. Bouzaza, and D. Wolbert, "Comparative study between laboratory and large pilot scales for VOC's removal from gas streams in continuous flow surface discharge plasma," *Chem. Eng. Res. Des.* **106**, 308–314 (2016).
- J. H. Byeon, J. H. Park, Y. S. Jo, K. Y. Yoon, and J. Hwang, "Removal of gaseous toluene and submicron aerosol particles using a dielectric barrier discharge reactor," *J. Hazard. Mater.* **175**, 417–422 (2010).

- ²⁵R. Barni, E. Dell'Orto, and C. Riccardi, "Chemical kinetics of the plasma gas-hase in humid air non-thermal atmospheric pressure discharges," *Int. J. Plasma Environ. Sci. Technol.* **12**, 109–113 (2019).
- ²⁶R. Barni, P. Esena, and C. Riccardi, "Chemical kinetics simulation for atmospheric pressure air plasmas in a streamer regime," *J. Appl. Phys.* **97**, 073301 (2005).
- ²⁷P. Esena, S. Zanini, and C. Riccardi, "Plasma processing for surface optical modifications of pet films," *Vacuum* **82**, 232–235 (2007).
- ²⁸X. Feng, H. Liu, C. He, Z. Shen, and T. Wang, "Synergistic effects and mechanism of a non-thermal plasma catalysis system in volatile organic compound removal: A review," *Catal. Sci. Technol.* **8**, 936–954 (2018).
- ²⁹R. A. Siliprandi, H. E. Roman, R. Barni, and C. Riccardi, "Characterization of the streamer regime in dielectric barrier discharges," *J. Appl. Phys.* **104**, 063309 (2008).
- ³⁰I. Biganzoli, R. Barni, C. Riccardi, A. Gurioli, and R. Pertile, "Optical and electrical characterization of a surface dielectric barrier discharge plasma actuator," *Plasma Sources Sci. Technol.* **22**, 025009 (2013).
- ³¹Z. Bin, L. Zhang, Y. Yan, L. Meng, and Z. Yimin, "Enhancing toluene removal in a plasma photocatalytic system through a black TiO₂ photocatalyst," *Plasma Sci. Technol.* **21**, 115503 (2019).
- ³²A. A. Assadi, A. Bouzaza, I. Soutrel, P. Petit, K. Medimagh, and D. Wolbert, "A study of pollution removal in exhaust gases from animal quartering centers by combining photocatalysis with surface discharge plasma: From pilot to industrial scale," *Chem. Eng. Process* **111**, 1–6 (2017).
- ³³C. Piferi, R. Barni, H. E. Roman, and C. Riccardi, "Current filaments in asymmetric surface dielectric barrier discharge," *Appl. Sci.* **11**, 2079 (2021).
- ³⁴S. Zanini, E. Grimoldi, A. Citterio, and C. Riccardi, "Characterization of atmospheric pressure plasma treated pure cashmere and wool/cashmere textiles: Treatment in air/water vapor mixture," *Appl. Surf. Sci.* **349**, 235–240 (2015).
- ³⁵I. Biganzoli, R. Barni, and C. Riccardi, "Temporal evolution of a surface dielectric barrier discharge for different groups of plasma microdischarges," *J. Phys. D: Appl. Phys.* **46**, 025201 (2012).
- ³⁶Z. Shayegan, C.-S. Lee, and F. Haghghat, "TiO₂ photocatalyst for removal of volatile organic compounds in gas phase—A review," *Chem. Eng. J.* **334**, 2408–2439 (2018).
- ³⁷W.-C. Chung, D.-H. Mei, X. Tu, and M.-B. Chang, "Removal of VOCs from gas streams via plasma and catalysis," *Catal. Rev.* **61**, 270–331 (2019).
- ³⁸C. Piferi, A. Brescia, and C. Riccardi, "Intensity comparison between UV lamps and plasma emission for air purification studies," *AIP Adv.* **11**, 085209 (2021).
- ³⁹M. Minella and C. Minero, "Evaluation of gas/solid photocatalytic performance for the removal of VOCs at ppb and sub-ppb levels," *Chemosphere* **272**, 129636 (2021).
- ⁴⁰D. Hu, R. Li, M. Li, J. Pei, F. Guo, and S. Zhang, "Photocatalytic efficiencies of WO₃/TiO₂ nanoparticles for exhaust decomposition under UV and visible light irradiation," *Mater. Res. Express* **5**, 095029 (2018).
- ⁴¹V. O. Odhiambo, A. Ongarbayeva, O. Kéri, L. Simon, and I. M. Szilágyi, "Synthesis of TiO₂/WO₃ composite nanofibers by a water-based electrospinning process and their application in photocatalysis," *Nanomaterials* **10**, 882 (2020).

A.3 Intensity comparison between UV lamps and plasma emission for air purification studies

Reproduced from Piferi, C.; Brescia, A.; Riccardi, C. Intensity Comparison between UV Lamps and Plasma Emission for Air Purification Studies. *AIP Advances* 2021, 11 (8), 085209, <https://doi.org/10.1063/5.0057033>, with the permission of AIP Publishing.

Intensity comparison between UV lamps and plasma emission for air purification studies

Cite as: AIP Advances 11, 085209 (2021); <https://doi.org/10.1063/5.0057033>
Submitted: 18 May 2021 . Accepted: 24 July 2021 . Published Online: 06 August 2021

 C. Piferi,  A. Brescia, and  C. Riccardi



ARTICLES YOU MAY BE INTERESTED IN

[Fluctuations of the plasma potential in atmospheric pressure micro-plasma jets](#)

AIP Advances 11, 085128 (2021); <https://doi.org/10.1063/5.0049322>

[Role of density gradients on miscible Rayleigh–Taylor fingers in porous media](#)

AIP Advances 11, 085201 (2021); <https://doi.org/10.1063/5.0054224>

[Unsteady flow of igniter combustion–gas heating base bleed propellant by convection](#)

AIP Advances 11, 085208 (2021); <https://doi.org/10.1063/5.0050517>



Call For Papers!

AIP Advances

SPECIAL TOPIC: Advances in Low Dimensional and 2D Materials

AIP Advances 11, 085209 (2021); <https://doi.org/10.1063/5.0057033>

11, 085209

© 2021 Author(s).

Intensity comparison between UV lamps and plasma emission for air purification studies

Cite as: AIP Advances 11, 085209 (2021); doi: 10.1063/5.0057033

Submitted: 18 May 2021 • Accepted: 24 July 2021 •

Published Online: 6 August 2021



C. Piferi,  A. Brescia,  and C. Riccardi^{a)} 

AFFILIATIONS

Department of Physics, University of Milano-Bicocca, Piazza della Scienza 3, 20126 Milano, Italy

^{a)} Author to whom correspondence should be addressed: claudia.riccardi@unimib.it

ABSTRACT

We compared spectra and intensity light of different sources, such as a UV-A lamp, a UV-C lamp, and a visible bulb, and atmospheric nonthermal plasma emission. Spectroscopic measurements were performed with an optical emission spectrometer and radiometric measurements with a radiometer to which UV-A, UV-C, and visible probes were coupled to measure the light intensity per unit surface. For each light source, we measured the emission spectrum and light intensity using different probes and also varying the relative distance. The nonthermal atmospheric plasma was generated by means of a surface barrier dielectric discharge varying the relevant parameters. This work allowed us to create the experimental setup suitable for further studies on volatile organic compound abatement by plasma-catalysis processing and compared it to the photocatalysis techniques based on UV and visible lamps.

© 2021 Author(s). All article content, except where otherwise noted, is licensed under a Creative Commons Attribution (CC BY) license (<http://creativecommons.org/licenses/by/4.0/>). <https://doi.org/10.1063/5.0057033>

I. INTRODUCTION

Nonthermal plasmas are generated in nonthermodynamical equilibrium. They are weakly ionized, containing a few electrons and ions and several atomic and molecular species at high excitation levels. These plasmas are characterized to be composed of high reactive species at ambient temperature and are largely employed for various applications.¹⁻⁴

Nonthermal plasmas can be, for instance, employed for creating a chemical reactive environment in which several processing steps can be performed to treat materials for modifying surface properties⁵⁻¹⁰ as well as to treat harmful substances to decompose them.¹¹⁻¹⁶

The needs for efficient processes for the abatement of harmful substances, including Volatile Organic Compounds (VOCs) emitted in industrial processes, are really strategic to save our environment.

Some competitive processing aimed to reduce VOC concentrations concerns UV photocatalysis.¹⁷⁻²⁴ Photocatalysis is the activity occurring when a light source interacts with the surface of semiconductor materials, the so-called photocatalysts. During this process, there must be at least two simultaneous reactions occurring: oxidation from photogenerated holes and reduction from photogenerated electrons.

Photocatalysis can be successfully used in a real environment to decompose pollutants and enhance the quality of the atmospheric air. Usually for a material's environmental applications, metal oxides made of Ti, Zn, Mn, and Cu are suitable to induce the photocatalysis reactions. In this regard, the photocatalysis is more easily induced by UV light or/and visible light.

Nonthermal plasmas, in addition to generating reactive species, produce light. With regard to this, plasmas could be used as light sources instead of UV and visible lamps. It is therefore possible to also induce catalytic processes with plasma light, during plasma gas processing, in the presence of a catalyst. This process is very interesting in the application for the decomposition and the abatement of noxious substances, as demonstrated by the previous literature.²⁵⁻²⁷

We are, therefore, interested to use the plasma as a source of both molecular dissociation by charges and oxidating active species and photocatalysis reactions in the presence of a catalyst deposited in the vicinity of the plasma source.

In developing the plasma-catalytic system, we are first interested in studying and comparing the plasma catalytic activity with that induced by UV and visible light.

This work is aimed to create the experimental setup suitable for the study of VOC abatement by both plasma-catalysis and photocatalysis processes.

To this purpose, this paper presents the experimental setup and a study on the optical properties of plasma in comparison with those related to UV and visible lamps.

Here, we present a characterization of the spectra and the power per surface unit for different light sources, such as a UV-A lamp, a UV-C lamp, and a visible LED bulb, and plasma emission presenting the experimental setup. This study permits us to further use the nonthermal atmospheric plasma coupled with photocatalytic medium for the VOC depletion.

This paper is organized as follows: In Sec. II, we describe the experimental setup. In Sec. III, we present results of the experimental campaign, the light sources spectra, and the intensity per surface unit in different conditions. In Sec. IV, we present a final discussion of the results.

II. EXPERIMENTAL SETUP

In our experiment, we used a vacuum cross chamber ($20 \times 20 \text{ cm}^2$ in length and 10 cm in diameter). The plasma source and the catalytic support are placed in a chamber, while the lamps are placed in front of a quartz window facing the catalytic support outside the chamber. Three of the four openings are closed by vacuum gauges, and the last one is left opened for the first part of the experiment when we study the plasma emission light and the light emitted by the lamps. In the last part of the experiment, we close the last opening by a quartz window to study the light emission lamp abatement from a filter. The same chamber will be also used for the VOC depletion experiments placing the plasma and the catalytic plate inside and the lamp outside.

For the characterization of the light sources, we used optical emission spectroscopy and a radiometric system. As light sources, we used an UV-C lamp (UV Lawtronics centered at 253.7 nm), an UV-A lamp (UV Philips Lighting centered at 370 nm), and a visible LED bulb (GLS Osram at 4000 K). All the lamps are powered by 4 W. During the intensity light measurements, we placed the radiometric probe (or alternatively during the spectra analysis, the optical fiber) at the middle of a semi-closed box aligned with the light source, as shown in Fig. 1. To obscure the ambient light, we covered the device with a blanket. The radiometric probes were placed exactly where we will place the photocatalytic support.

For the characterization of the plasma emission, we placed the plasma source inside the chamber and the probe in front of it

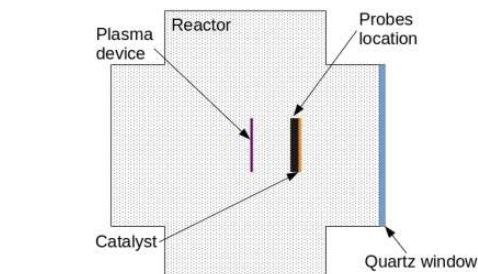
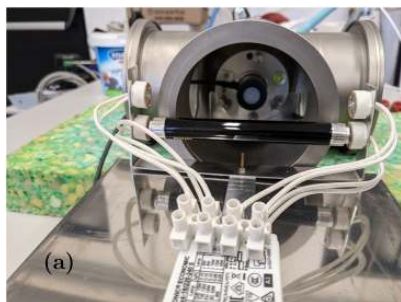


FIG. 2. Plasma device scheme setup.

(Fig. 2). We used an alumina Surface Dielectric Barrier Discharge (SDBD).^{2,28–31}

In our experiment, the SDBD is a $9 \times 5 \text{ cm}^2$ alumina dielectric surface, 1 mm thickness, with 9 metal fingers, 7 cm long, 1 mm large, and 4 mm apart made of an alloy of ruthenium, nickel, silver, and palladium. The plasma is lit up by a high voltage (HV) power supply working in a power range between 8 and 80 W and a frequency of the order of tens of kilohertz.^{30,31}

A. Optical emission spectroscopy device

The used spectrometer is Ocean Optic PS2000, which works in a range of wavelengths between 180 and 870 nm with a resolution of $\sim 0.3 \text{ nm}$.^{1,2} The fiber slit is $10 \mu\text{m}$.

B. Radiometric device

As a radiometric device, we used a HD 31 datalogger from DeltaOhm coupled with three radiometric probes that collect the irradiated power per surface unit ($\mu\text{W}/\text{cm}^2$) in the specified spectra range. The probe are LP47-RAD for visible spectra (400–1050 nm range), LP471-P-A for UV-A spectra (315–400 nm), and LP471-UVC for UV-C spectra (220–280 nm).

Each probe was employed to collect the intensity per surface unit in the specific spectrum range of the light sources.

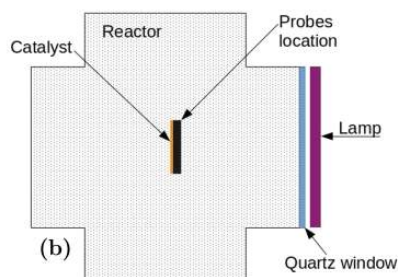


FIG. 1. (a) Lamp equipment setup and (b) scheme.

III. MEASUREMENT RESULTS

For every light source, we measured the optical emission spectra and the radiometric intensity by means of the probes.

A. Optical emission spectroscopy

We used optical emission spectroscopy to characterize the light source spectra (Fig. 3).

The UV-C lamp is characterized by the typical line spectrum of the low pressure Hg: the main peak is at 253.7 nm. The UV-A lamp has only a peak at 370 nm produced by the low pressure Hg vapors, while all the other lines are suppressed by the lamp glass. The visible bulb has a continuous spectrum in the visible range from about 450 to 700 nm. The SDBD plasma is generated at atmospheric pressure in air gas. The plasma emission is characterized by a line spectrum, mainly in the UV-A region, due to the principal, rotational, and vibrational emission of N_2 species. The observed N_2 lines are at 315.93, 337.13, 357.69, 380.49, and 405.94 nm.

We are interested in knowing the light source spectra not only to compare them but also to couple them with the specific catalytic substance for the catalysis processing. Different catalysts are, in fact, activated by different specific light frequencies. In Fig. 3, we can see that plasma emits in the frequency range of the UV-A lamp; in this frequency range, we could expect a synergic effect due to both the light sources in the presence of catalytic support and interactions of the plasma reactive species with the noxious substances. VOC depletion with catalysis activated in the UV-A spectrum region by plasma and UV-A lamp will be the object of future studies.

B. Lamps radiometric measurements

It was observed that the light sources require some time to achieve stable intensity. That time is about 5 min for the UV-A lamp, about 3 min for the UV-C lamp, and about 2 min for the visible bulb.

To set up our apparatus, for each light source, we collected the intensities at different distances between the source itself and the probe, as shown in Fig. 4.

We fitted the UV-A and UV-C data considering the emission source as a uniform limited cylinder ($L = 11$ cm), so its intensity is

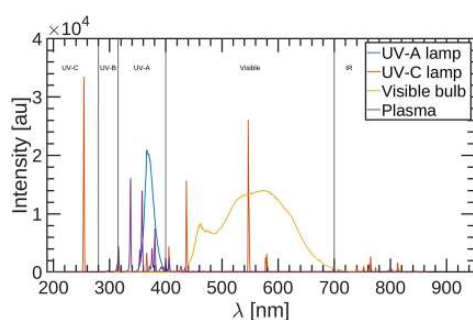


FIG. 3. Spectra emission (in arbitrary units) of the used lamps and plasma detected by the emission spectroscopy device.

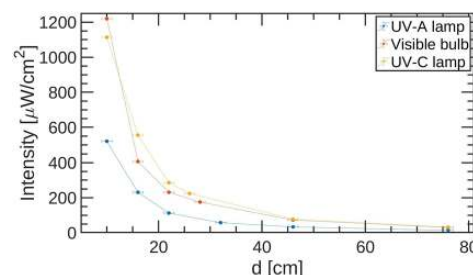


FIG. 4. Intensity ($\mu\text{W}/\text{cm}^2$) vs distance (cm) for the three light sources using the coupled probe.

given by

$$E(d) = 2 \frac{A}{d} \left[\text{atan} \left(\frac{L/2}{d} \right) \right] + B, \quad (1)$$

while for the visible bulb, it is a spherical symmetry, and the intensity is given by

$$E(d) = \frac{A}{d^2} + B, \quad (2)$$

where d is the lamp-probe distance.

In Eqs. (1) and (2), the additive parameter B is due to a functional approximation. The errors occurring in the distance measurements are predominant on the intensity ones; to get a better fit, we fitted the inverse function of Eqs. (1) and (2). The fitting curve and parameters are shown in Fig. 5, denoting good agreement between experiments and theory.

Concerning the intensity of the light sources in the other spectrum regions, by radiometric probes, we also found the following:

- Using the UV-A lamp, the visible component is about 0.08 times the UV-A component, while there is no UV-C component.
- Using the UV-C lamp, the visible component is about 0.14 times the UV-C component, while the UV-A component is about 0.02 times the UV-C one.
- Using the visible bulb, there are no UV-A and UV-C components.

We summarize these results in Table I.

Since we are interested in using the catalyst support inside the chamber while the lamps outside the chamber in front of a quartz window, we measured the intensity transmission factor due to the quartz window. The results are shown in Table II. As can be seen, the transmission factor is high and the same in UV-A and visible regions, while it is lower in UV-C light.

C. Plasma radiometric measurements

Using plasma, we measured the intensity per surface unit at different ignition powers at a fixed distance (about 3.5 cm) using both the UV-A and visible probes (Fig. 6). UV-C radiation is almost null in the plasma light.

Comparing the UV-A plasma emission with the UV-A lamp ones at 3.5 cm distance, we found that the latter is between 20

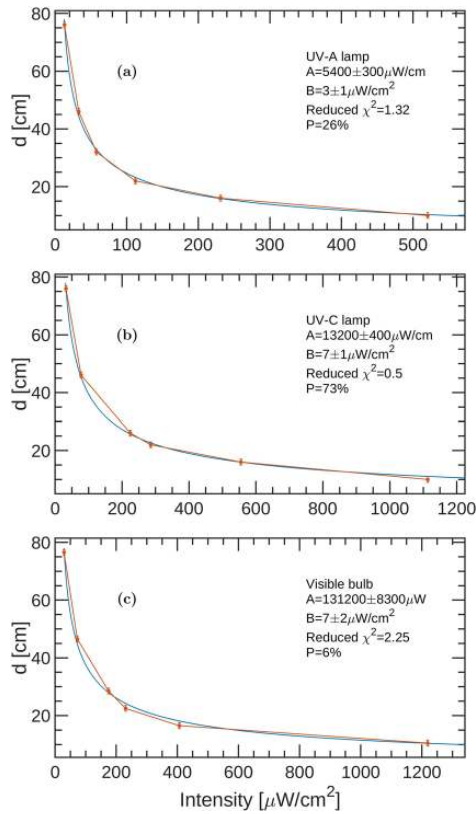


FIG. 5. Fit and experimental data of distance (cm) vs intensity ($\mu\text{W}/\text{cm}^2$) for (a) UV-A, (b) UV-C, and (c) visible light sources.

and 600 times brighter than plasma, depending on their distance from the radiometric probe. A higher intensity factor was found between the visible bulb and the visible component of the plasma.

These results force us to place the catalysts directly on the alumina dielectric surface of our SDBD source between the electrodes. In this way, the catalyst is directly induced by the plasma light, being located at a distance of the order of 1 mm.

TABLE I. Comparison of the intensity emission of the light sources in the different spectrum regions.

Probe \ Source	UV-A	UV-C	Visible
UV-A lamp	1	0	0.08
UV-C lamp	0.02	1	0.14
Visible bulb	0	0	1
Plasma	1	0	0.50

TABLE II. Transmission factor due to the quartz window filter.

Source	Transmission factor (%)
UV-A lamp	80
UV-C lamp	55
Visible bulb	80

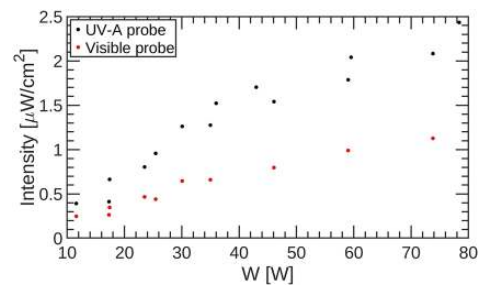


FIG. 6. Intensity ($\mu\text{W}/\text{cm}^2$) vs plasma ignition power (W) for the UV-A probe (black dots) and visible probe (red dots).

IV. DISCUSSION

We investigated the intensity of UV light lamps in comparison with the light emitted by a SDBD plasma at different powers. The intensity of each light source can be summarized in Table I. In this table, we compare the source intensities in the different spectrum regions with respect to the predominant emission spectrum. We demonstrated that the UV-A lamp emits in the UV-A region of the spectrum with also a minor contribution in the UV-C spectrum; the UV-C lamp emits in the UV-C region with a minor contribution in the UV-A spectrum; for the visible LED bulb, it is in the visible region; and for the plasma, the main emission is in the UV-A region.

We also verified that the emission of UV-A and UV-C lamps vs the distance follows Eq. (1), while the visible bulb emission vs the distance follows Eq. (2) and we found the fitting parameters for all our lamps.

Concerning the plasma emission, we found that the intensity is strictly dependent on the applied ignition power and it is much lower than the lamp intensity. This result suggested us to deposit the catalyst near the plasma light, that is, directly on the alumina surface on which plasma is ignited. Then, as the plasma emits both in the visible and in the UV regions, a catalyst can be chosen from among those activated by UV and visible light.

The next step will concern experiments including photocatalysts to study the abatement of various noxious substances. A comparison of photocatalysis processes by lamps and plasma processes with and without the photocatalysts will be object of future studies.^{28,29}

ACKNOWLEDGMENTS

We kindly acknowledge the Fondazione di Comunità Milano—Fondo Solidale Professor Ignazio Renato Bellobono

(Grant No. 2020-CONT-0206) for funding our research. We also gratefully acknowledge the technical support of Alessandro Mietner and Alessandro Baù in the device development and experiment execution.

DATA AVAILABILITY

The data that support the findings of this study are available from the corresponding author upon reasonable request.

REFERENCES

- ¹I. Biganzoli, R. Barni, and C. Riccardi, "Temporal evolution of a surface dielectric barrier discharge for different groups of plasma microdischarges," *J. Phys. D: Appl. Phys.* **46**, 025201 (2012).
- ²I. Biganzoli, R. Barni, C. Riccardi, A. Gurioli, and R. Pertile, "Optical and electrical characterization of a surface dielectric barrier discharge plasma actuator," *Plasma Sources Sci. Technol.* **22**, 025009 (2013).
- ³R. A. Siliprandi, H. E. Roman, R. Barni, and C. Riccardi, "Characterization of the streamer regime in dielectric barrier discharges," *J. Appl. Phys.* **104**, 063309 (2008).
- ⁴A. Raffaele-Addamo, C. Riccardi, E. Selli, R. Barni, M. Piselli, G. Poletti, F. Orsini, B. Marcandalli, M. R. Massafra, and L. Meda, "Characterization of plasma processing for polymers," *Surf. Coat. Technol.* **174–175**, 886–890 (2003).
- ⁵S. Zanini, A. Citterio, G. Leonardi, and C. Riccardi, "Characterization of atmospheric pressure plasma treated wool/cashmere textiles: Treatment in nitrogen," *Appl. Surf. Sci.* **427**, 90–96 (2018).
- ⁶S. Zanini, S. Freti, A. Citterio, and C. Riccardi, "Characterization of hydro- and oleo-repellent pure cashmere and wool/nylon textiles obtained by atmospheric pressure plasma pre-treatment and coating with a fluorocarbon resin," *Surf. Coat. Technol.* **292**, 155–160 (2016).
- ⁷S. Zanini, E. Grimoldi, A. Citterio, and C. Riccardi, "Characterization of atmospheric pressure plasma treated pure cashmere and wool/cashmere textiles: Treatment in air/water vapor mixture," *Appl. Surf. Sci.* **349**, 235–240 (2015).
- ⁸S. Zanini, C. Riccardi, C. Canevali, M. Orlandi, L. Zoia, and E.-L. Tolppa, "Modifications of lignocellulosic fibers by Ar plasma treatments in comparison with biological treatments," *Surf. Coat. Technol.* **200**, 556–560 (2005).
- ⁹R. A. Siliprandi, S. Zanini, E. Grimoldi, F. S. Fumagalli, R. Barni, and C. Riccardi, "Atmospheric pressure plasma discharge for polysiloxane thin films deposition and comparison with low pressure process," *Plasma Chem. Plasma Process.* **31**, 353–372 (2011).
- ¹⁰B. Marcandalli and C. Riccardi, "Plasma treatments of fibres and textiles" in *Plasma Technologies for Textiles*, edited by R. Shishoo (Woodhead Publishing Ltd., 2007), pp. 282–300.
- ¹¹R. Barni, E. Dell'Orto, and C. Riccardi, "Chemical kinetics of the plasma gas-phase in humid air non-thermal atmospheric pressure discharges," *Int. J. Plasma Environ. Sci. Technol.* **12**, 109–113 (2019).
- ¹²R. Barni, R. Benocci, N. Spinicchia, H. E. Roman, and C. Riccardi, "An experimental study of plasma cracking of methane using DBDs aimed at hydrogen production," *Plasma Chem. Plasma Process.* **39**, 241–258 (2019).
- ¹³S. Zanini, P. Massini, M. Mietta, E. Grimoldi, and C. Riccardi, "Plasma treatments of PET meshes for fuel–water separation applications," *J. Colloid Interface Sci.* **322**, 566–571 (2008).
- ¹⁴R. Barni, P. Esena, and C. Riccardi, "Chemical kinetics simulation for atmospheric pressure air plasmas in a streamer regime," *J. Appl. Phys.* **97**, 073301 (2005).
- ¹⁵R. Barni, I. Biganzoli, E. C. Dell'Orto, and C. Riccardi, "Effect of duty-cycles on the air plasma gas-phase of dielectric barrier discharges," *J. Appl. Phys.* **118**, 143301 (2015).
- ¹⁶R. Barni and C. Riccardi, "Gas-phase evolution of Ar/H₂O and Ar/CH₄ dielectric barrier discharge plasmas," *Eur. Phys. J. D* **72**, 62 (2018).
- ¹⁷A. L. Linsebigler, G. Lu, and J. T. Yates, Jr., "Photocatalysis on TiO₂ surfaces: Principles, mechanisms, and selected results," *Chem. Rev.* **95**, 735–758 (1995).
- ¹⁸P. Di Lazzaro, D. Murra, G. Felici, and S. Fu, "Spatial distribution of the light emitted by an excimer lamp used for ultraviolet-B photo-therapy: Experiment and modeling," *Rev. Sci. Instrum.* **75**, 1332–1336 (2004).
- ¹⁹D. L. Maurer and J. A. Koziel, "On-farm pilot-scale testing of black ultraviolet light and photocatalytic coating for mitigation of odor, odorous VOCs, and greenhouse gases," *Chemosphere* **221**, 778–784 (2019).
- ²⁰M. Stucchi, F. Galli, C. L. Bianchi, C. Pirola, D. C. Boffito, F. Biasioli, and V. Capucci, "Simultaneous photodegradation of VOC mixture by TiO₂ powders," *Chemosphere* **193**, 198–206 (2018).
- ²¹H. Zheng, J. Z. Ou, M. S. Strano, R. B. Kaner, A. Mitchell, and K. Kalantar-zadeh, "Nanostructured tungsten oxide—properties, synthesis, and applications," *Adv. Funct. Mater.* **21**, 2175–2196 (2011).
- ²²H. Xu, S. Ouyang, L. Liu, P. Reunchan, N. Umezawa, and J. Ye, "Recent advances in TiO₂-based photocatalysis," *J. Mater. Chem. A* **2**, 12642–12661 (2014).
- ²³X. Yang, J. A. Koziel, Y. Laor, W. Zhu, J. van Leeuwen, W. S. Jenks, S. J. Hoff, J. Zimmerman, S. Zhang, U. Ravid *et al.*, "VOC removal from manure gaseous emissions with UV photolysis and UV-TiO₂ photocatalysis," *Catalysts* **10**, 607 (2020).
- ²⁴I. R. Bellobono, F. Groppi, M. Sturini, A. Albini, and F. Morazzoni, "A kinetic approach to photomineralization of methane in air by membranes based on TiO₂/WO₃," *J. Chem. Chem. Eng.* **14**, 73–85 (2020).
- ²⁵J. Karuppiah, E. L. Reddy, P. Manoj Kumar Reddy, B. Ramaraju, R. Karvembu, and C. Subrahmanyam, "Abatement of mixture of volatile organic compounds (VOCs) in a catalytic non-thermal plasma reactor," *J. Hazard. Mater.* **237–238**, 283–289 (2012).
- ²⁶L. Sivachandiran, F. Thévenet, and A. Rousseau, "Isopropanol removal using Mn₂O₃ packed bed non-thermal plasma reactor: Comparison between continuous treatment and sequential sorption/regeneration," *Chem. Eng. J.* **270**, 327–335 (2015).
- ²⁷X. Zhu, X. Gao, X. Yu, C. Zheng, and X. Tu, "Catalyst screening for acetone removal in a single-stage plasma-catalysis system," *Catal. Today* **256**, 108–114 (2015).
- ²⁸I. Biganzoli, R. Barni, and C. Riccardi, "Note: On the use of Rogowski coils as current probes for atmospheric pressure dielectric barrier discharges," *Rev. Sci. Instrum.* **84**, 016101 (2013).
- ²⁹I. Biganzoli, R. Barni, A. Gurioli, R. Pertile, and C. Riccardi, "Experimental investigation of Lissajous figure shapes in planar and surface dielectric barrier discharges," *J. Phys.: Conf. Ser.* **550**, 012039 (2014).
- ³⁰P. Esena, S. Zanini, and C. Riccardi, "Plasma processing for surface optical modifications of pet films," *Vacuum* **82**, 232–235 (2007).
- ³¹C. Piferi, R. Barni, H. E. Roman, and C. Riccardi, "Current filaments in asymmetric surface dielectric barrier discharge," *Appl. Sci.* **11**, 2079 (2021).

A.4 Pentane Depletion by a Surface DBD and Catalysis Processing

Reproduced from Piferi, C.; Daghetta, M.; Schiavon, M.; Roman, H. E.; Riccardi, C. Pentane Depletion by a Surface DBD and Catalysis Processing. *Applied Sciences* 2022, 12 (9), 4253, <https://doi.org/10.3390/app12094253>.

Article

Pentane Depletion by a Surface DBD and Catalysis Processing

 Cecilia Piferi ¹, Matteo Daghetta ¹, Marco Schiavon ², Hector Eduardo Roman ¹ and Claudia Riccardi ^{1,*}

- ¹ Dipartimento di Fisica, University of Milano-Bicocca, Piazza della Scienza 3, 20126 Milano, Italy; c.piferi@campus.unimib.it (C.P.); matteo.daghetta@unimib.it (M.D.); hector.roman@unimib.it (H.E.R.)
- ² Department of Civil, Environmental and Mechanical Engineering, University of Trento, via Mesiano 77, 38123 Trento, Italy; marco.schiavon@unitn.it
- * Correspondence: claudia.riccardi@unimib.it

Abstract: We study pentane depletion using a hybrid plasma system based on a surface dielectric barrier discharge (SDBD), with and without a catalyst, and as a function of plasma power and alkane concentration. We evaluate pentane decomposition efficiency based on plasma power and quantify the role of the catalyst in the resulting depletion of intermediate products. Analyses of the temporal evolution of pentane and the intermediate decomposition products allow us to estimate the corresponding decomposition rates according to the plasma parameters. We find that depletion efficiency increases as a function of pentane concentration. Furthermore, it is shown that the catalytic processes are responsible for a significant increase in the depletion rates of the intermediate reaction products, thus contributing to the total abatement process of pentane.

Keywords: surface dielectric barrier discharge; atmospheric pressure; Non-Thermal Plasmas; streamer discharge; pentane and VOC abatement



Citation: Piferi, C.; Daghetta, M.; Schiavon, M.; Roman, H.E.; Riccardi, C. Pentane Depletion by a Surface DBD and Catalysis Processing. *Appl. Sci.* **2022**, *12*, 4253. <https://doi.org/10.3390/app12094253>

Academic Editor: Xinpei Lu

Received: 22 March 2022

Accepted: 21 April 2022

Published: 22 April 2022

Publisher's Note: MDPI stays neutral with regard to jurisdictional claims in published maps and institutional affiliations.



Copyright: © 2022 by the authors. Licensee MDPI, Basel, Switzerland. This article is an open access article distributed under the terms and conditions of the Creative Commons Attribution (CC BY) license (<https://creativecommons.org/licenses/by/4.0/>).

1. Introduction

One of the most important environmental issues at present is air pollution, which can be harmful to both the environment and to human health. Thanks to recent strict regulations, emissions of atmospheric pollutants have been reduced significantly during the last decades, especially in heavily industrialized countries. Despite all these efforts, the concentrations of pollutants within large urban zones remain too high, particularly in developing countries, and further improvement in atmospheric air quality is required. This can be accomplished by encouraging more specific studies [1].

A large and important group of pollutants is the volatile organic compounds (VOCs); due to their high volatility, these compounds rapidly evaporate, thus easily leaving the places where they are produced and diffusing into the atmosphere. It is now well-understood that they can cause a variety of deleterious effects to human health and the environment [2]. VOCs are mostly emitted during industrial processing in different types of mixtures with air, where the magnitude of fluxes ranges from 1000 m³/h to approximately 10,000 m³/h.

Different methods for VOC depletion are being tested on pilot plants, with some already being employed in industries, including: adsorption [3], absorption [4], thermal decomposition [5], catalytic oxidation [6], bio-filtration [7], and membrane separation [8]. Most of these technologies present several economic and efficiency limitations when treating effluents with low VOC concentrations, high airflow rate, and with compounds that have low solubility in water [9].

Plasma can serve as an alternative in the removal of VOCs from gas streams. Various equilibrium and non-equilibrium plasma reactors are being investigated, and their selective efficiency in VOC abatement has been reported in literature reviews [10,11]. Equilibrium plasmas are also thermal ones, since charges and neutrals are produced at high temperatures of the order of 10⁴ K. Thermal plasmas such as torches and arches are employed for different

purposes, including, for instance, in the gasification of coal [12] as well as in the waste gas decomposition of hard-to-convert components such as Perfluorocarbons PFCs [13].

These plasmas have the advantage of high and fast dissociation rates and rather good efficiency, but most of them are characterized by high energetic consumption, which is required to sustain the discharge itself, and high maintenance and equipment costs. They often employ noble gas carriers, liquids, or vapor water [14]. Although they can be used for the abatement of harmful toxic gases, they are economically unsustainable for the abatement of VOCs at low concentrations.

Non-equilibrium plasmas, often called Non-Thermal Plasmas (NTPs), can instead be sustained with lower energy than Thermal Plasmas. NTPs are very weakly ionized and are not in thermodynamic equilibrium because electrons absorb most of the electromagnetic energy, reaching temperatures of several eV, while ionic species and neutral kinetic energies remain at room temperature. For this reason, they are also called cold plasmas. NTPs are generated by using different types of devices such as the dielectric barrier discharge [10], gliding arc discharge [15], microwave plasma [16], and plasma jets [17,18].

Nowadays, they are employed in several environmental applications. For instance, some NTPs such as plasma jets and microwaves are intensively studied for reforming methane and carbon dioxide because of their high efficiency [16], while DBDs are often used for the removal of VOCs at low concentrations, and also for odor abatement in combination with catalysis [19].

Most of the NTP sources working at atmospheric pressure are called Cold Atmospheric Plasmas (CAPs). The abatement phenomena in CAPs are dominated by kinetic effects, where electrons are the primary source of molecular dissociation and radical formation. Then, the resulting chemical reactions between radicals promote their degradation and oxidation in the presence of oxygen species. Compared to the aforementioned thermal plasmas, they are characterized by lower dissociation rates, but not by lower efficiency [9].

As reported in the literature, one of the most employed cold plasma devices is the Dielectric Barrier Discharge, which has the advantage of requiring very low energy. DBDs are also used in combination with catalysis, an example of which is the dielectric packed bed discharge [18]. DBDs, as most of CAPs, have the drawback of processing only small gas volumes. In the DBD configuration, the gas is physically confined to pass between the two electrodes, the plasma state is mostly confined to a volume of a few mL, and gas air flows between a few mL/min and some L/min [9,17]. Only very recently, a system composed of DBDs, a mineral adsorber, and a bio-scrubber [11] has been investigated for gas flows of up to 1000 m³/min, yielding a good VOC abatement efficiency. The scale-up factors and operating costs need to be investigated in order to evaluate their real economic sustainability in view of the most interesting applications.

A possible way to overcome the difficulty of a redeeming technology on a large scale—that is, treating large gas volumes at low VOC concentrations—could be through the employment of a peculiar CAP: the surface DBD (SDBD) [20]. In SDBDs, the plasma is produced on a surface without being confined between two electrodes. In this new configuration, the gas can move on the surface and rapidly diffuse into larger volumes. Moreover, these devices have not been investigated in such a detail as the DBD and the packed DBD for their waste air remediation applications. Only recently have a few research papers been devoted to the application of SDBDs in VOC abatement [21,22].

Starting from our previous knowledge on DBD [18,23] and SDBD plasmas, this paper presents a study on the performance of a single SDBD module working at static conditions, aimed at evaluating the VOC abatement rates based on the relevant parameters, particularly including possible synergies with post-catalysis processing. More specifically, we employ an asymmetrical SDBD configuration [20] and investigate the chemical kinetics dissociation of a specific VOC in an air mixture while varying its concentrations and plasma energy. We choose pentane as a VOC and whose decomposition by-products are mainly acetylene and propane. The concentration of pentane and its by-products are measured according to time in order to analyze their decay law measured during the experiments. From these results,

we can draw some conclusions about performance efficiencies for different parameters as well as estimate the best possible operating conditions, such as by evaluating the opportunity of using a number of SDBD modules fed in an asymmetrical configuration for specific real applications.

Although NTPs have been largely studied in the last decades for their role in the depletion of VOCs in air, the literature on pentane abatement/conversion is still scarce. To the authors' knowledge, no experiments on the oxidation of pentane in air in low temperature atmospheric pressure plasmas have been reported in the literature. Thus, the present paper describes a novel application of NTP-catalysis and contributes to the enrichment of the available literature.

The paper is organized as follows. In Section 2, we present the experimental setup and briefly discuss the calibration of the gas chromatograph. Section 3 is devoted to the experimental results, and Section 4 presents a discussion of our results as compared to others from the literature. Finally, in Section 5, we conclude with our final remarks.

2. Experimental Setup

The configuration adopted in our experiments, the simplest version of the SDBD used in plasma aerodynamics applications, is called a plasma actuator. It consists of two conducting electrodes attached to the opposite sides of a flat dielectric panel, as seen in the asymmetrical arrangement sketched in Figure 1.

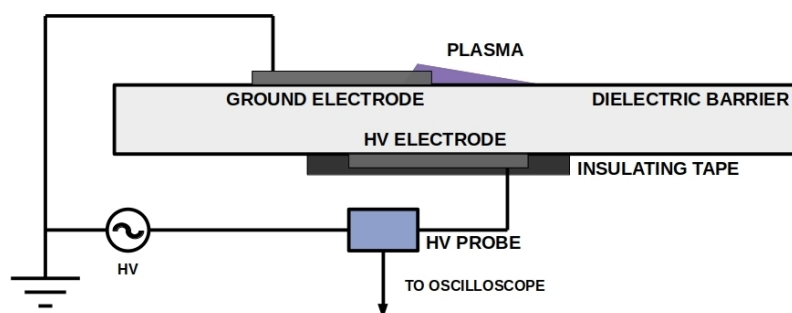


Figure 1. Plasma device scheme: The two electrodes, consisting of deposited copper (35 μm thick, 4 cm wide, and 12 cm long), are attached to a dielectric material and are laterally shifted from each other by about 0.5 cm (typical asymmetry in SDBD). The lower electrode, fed at a high voltage (HV), is covered with an insulating material, whereas the upper one, fed to the ground, is exposed to air. The HV probe measures the applied potential.

The lower electrode is covered with an insulating material, whereas the upper one remains fully exposed to the air. In this way, the plasma generation region is confined above the dielectric plate. For the dielectric barrier, we used a vetronite sheet, with the possibility to change its thickness (1.5–3.0 mm). More specifically, we used a 1.5 mm thick dielectric barrier in vetronite and a pair of 12 cm long conductive electrodes leaning on the two faces of the barrier.

Upon the application of a sufficiently high voltage (HV), the air portion in proximity to the device gets weakly ionized, thus creating a thin plasma layer above the insulating plate, as illustrated in Figure 1. The SDBD plasma actuator generates a non-thermal self-limiting plasma, in which the accumulation of charged particles on the dielectric surface opposes the applied electric field. Consequently, AC or pulsed high voltages are required to have a temporally prolonged discharge operation; otherwise, only a transient air ionization occurs at the voltage ignition.

In the present configuration, the exposed electrode is grounded, whereas the covered one is fed by a high-voltage power supply line. This consists of a DC-voltage supplier and

a signal generator feeding the primary windings of an HV transformer, whose secondary windings are connected to the electrode. We set the reference DC supply voltage (VDC) within the range of 7–14 V. The whole system behaves similarly to a resonant circuit, so the sinusoidal voltage frequency slightly depends on the DC-supply voltage. In this asymmetric configuration, due to the partial overlapping of the electrodes by about a centimeter, a so-called ionic wind is generated, which is a directional flow from the exposed electrode to the buried one.

The SDBD is located in the reactor, a parallelepiped with the size of $1.8 \times 20 \times 18 \text{ cm}^3$ made by Delrin and with a cover in Plexiglas (box used for the experiments that has not been attacked by the used VOC or its decomposition products), inside which VOC depletion takes place. The volume of the free space used for the air treatment is about 0.5 L. The experiments were performed in static conditions, as described below. The VOC used in this experiment is pentane (C_5H_{12}), employed at variable concentrations between 300 ppm and 1200 ppm.

The VOC contamination setup is shown in Figure 2. The black bold lines represent the tube connections through the whole system. In the diagram, “Pure air” represents a gas cylinder from Sapio S.R.L. containing 79% N_2 and 21% O_2 , which means that the concentration of CO_2 (0.5 ppm), CO (0.5 ppm), hydrocarbons (0.1 ppm), water (3 ppm), and other pollutants is negligible. The red crosses represent ball valves. The liquid pentane is placed in a bubbler bottle (denoted as Liquid VOC in Figure 2) and is allowed to circulate through the flow meter by the action of the air pressure. We used two gas flow meters and one liquid flow meter, all produced by the Bronkhorst factory. The controlled evaporator and mixer (CEM) allow the liquid coming from the liquid flow meter to evaporate and mix with a line of pure air that comes from gas flow meter 1, thus producing the first dilution of pentane. A second dilution is performed after the CEM through the addition of pure air coming from gas flow meter 2. This whole system allows for the control of the chamber pentane concentration before the experiments. Finally, for the gas chromatographic analysis, we used a Micro GC Agilent 3000 instrument with the column PoraPLOT U, which is a column specific for VOCs, and with a Thermal Conductivity Detector (TCD). The program used is as follows: inlet temperature at 70° , inject temperature at 100° , column temperature at 110° , inject time 50 ms, and run time 300 s. The gas chromatograph (GC) samples are of the order of 10^{-3} mL for each time. The GC inlet pipe is placed at about 5 cm after the plasma region.

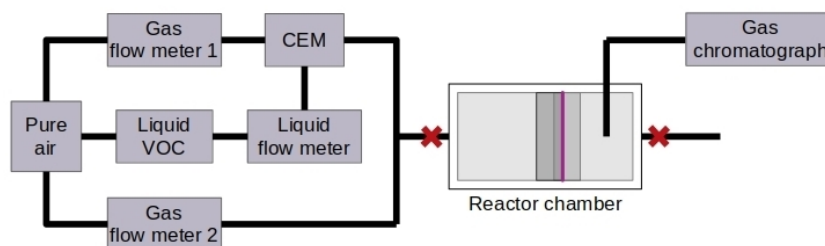


Figure 2. Liquid VOC contamination setup: The pure air cylinder supply for both the gas carriers and the bubbler device containing the VOC. A controlled evaporator and mixer (CEM) allow the liquid to evaporate and then mix with a line of pure air flow. The SDBD is located in the reactor, a parallelepiped with the size of $1.8 \times 20 \times 18 \text{ cm}^3$ made by Delrin and with a cover in Plexiglas, inside which VOC depletion takes place. The volume of the free space used for the air treatment is about 0.5 L. The gas chromatographic analysis was performed with a Micro GC Agilent 3000 instrument.

The experiments were performed with and without a catalyst. The catalyst consisted of a dispersion of TiO_2 in an aqueous solution of polyvinyl alcohol (PVA). It was deposited by means of a fine brush, as a strip of 4 cm in width and 12 cm in length, at a distance of 0.3 cm from the exposed copper electrode. After the evaporation of water at room

temperature, the deposition was repeated until a uniform distribution of the product was obtained. A total of 0.2 g of dried catalyst TiO_2 was deposited. In order to prepare the catalyst, 6 g of Ti(IV) oxide anatase 325 mesh (Sigma Aldrich) was carefully added to a solution, initially prepared with the use of 1 g of PVA (Kuraray Poval 10-98) and 100 mL of deionized water. After vigorous stirring, a fluid suspension was obtained, which was stored at room temperature until the deposition. In Figure 3, we show an SEM image of the catalyst where we can clearly identify sub-micrometre TiO_2 particles on the PVA matrix.

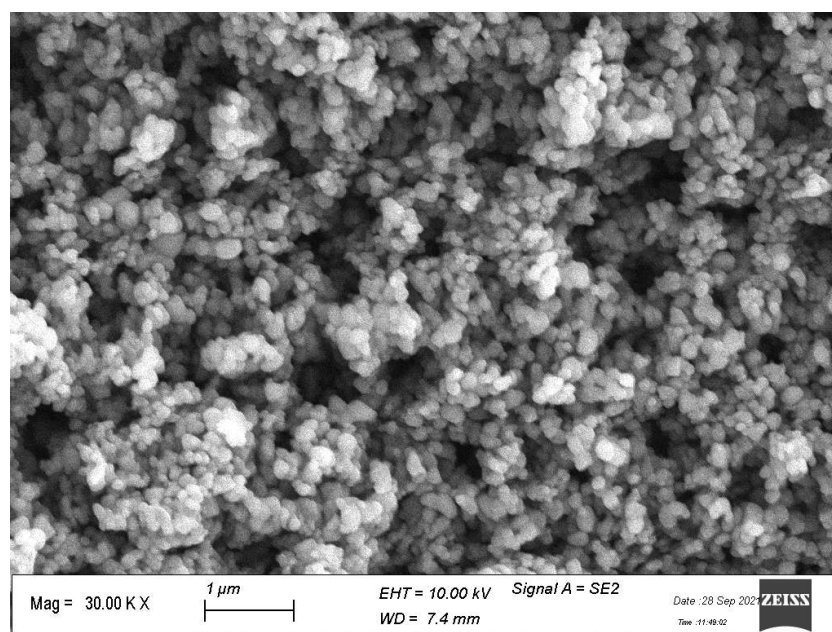


Figure 3. SEM image of a sample of TiO_2 and PVA deposition over vetronite at 30,000 \times magnification.

The electrical parameters involved in the discharge events were measured in the experiments. We used a Rogowski coil sensor to detect the current flowing in the system [24,25], and an HV probe to measure the associated applied high voltage.

The GC output reports a signal composed of peaks of intensity proportional to the concentration of specific species. The area of each peak is strongly dependent on the setting parameters during the sampling conditions. For a precise evaluation of concentration, we carried out a GC calibration with respect to pentane, considering the relative flow of pentane relative to the total air–pentane input flow. After calibration, we estimated the error in the pentane concentration to be around 10%. The errors were estimated as the standard deviation obtained from several measurements of the same starting concentration.

3. Experimental Results

To analyze the pentane depletion, we determined the resulting pentane concentrations based on the treatment time for various plasma conditions. The experimental campaign consisted of three steps: First, we opened the in-let and out-let valves in order to allow the pentane to flow through the reactor for two minutes. Second, the in-let and out-let valves were closed, after which the GC sampled the atmosphere in the reactor without plasma in order to measure the initial pentane concentration. Finally, in the third step, the plasma was turned on and kept working for a total time t , followed by a GC sampling of the treated gas. The treatment times t were taken in the range of 1–5 min. We repeated the process for each time t separately.

3.1. Gas Chromatograms

Several chromatogram measurements were repeated at different treatment times, plasma conditions, and pentane concentrations to improve the statistics of the results. The initial pentane concentrations chosen were $c = 300, 600, 1200$ ppm. The experiments were performed at two plasma power levels, i.e., 16.9 W and 44.2 W. We assigned c to be the nominal concentration that we add to the chamber, while ρ_5 represents the concentrations estimated by the GC sampling.

In Figure 4, we show a few examples of chromatograms. The initial pentane concentration was 1200 ppm, and the plasma was lit up at 44.2 W. We considered the two experimental conditions: depletion without a catalyst (Figure 4a) and depletion with a catalyst (Figure 4b).

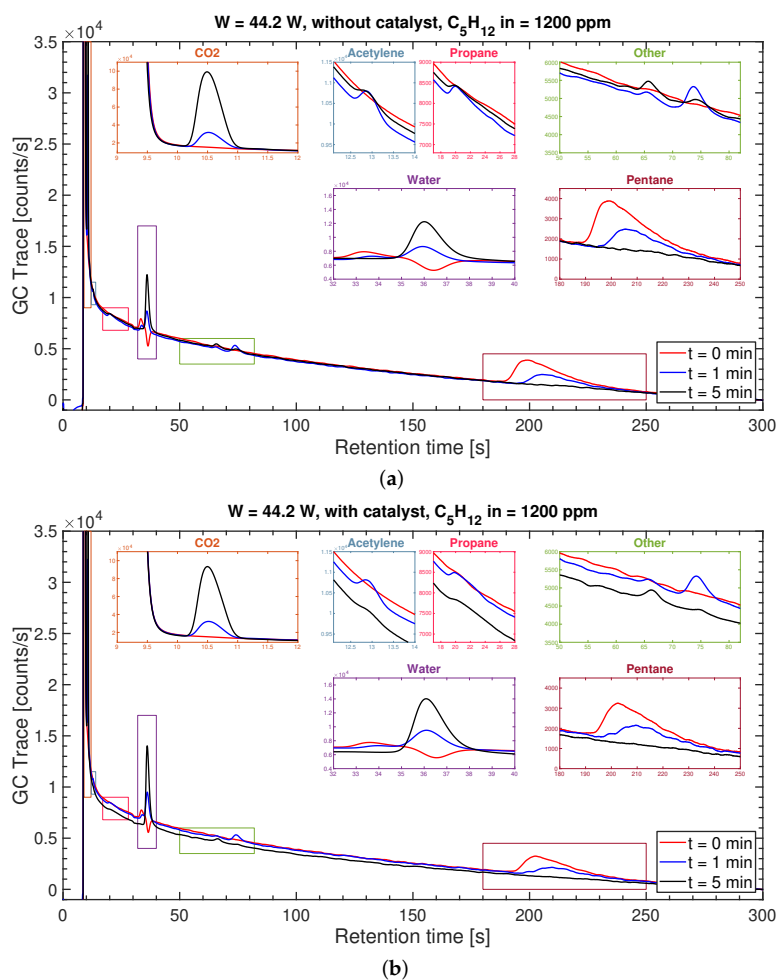


Figure 4. Gas chromatograms vs. retention time [s]. The shown traces correspond to pentane and intermediate products, for treatment times $t = 0, 1, 5$ min; the plasma lit up at 44.2 W, and initial pentane concentration was at 1200 ppm. (a) Without catalyst. (b) With catalyst. The duration of a gas chromatogram is 300 s. The insets show the traces for the intermediate reaction products (CO_2 , acetylene, propane, water, and other unidentified species) and pentane.

The chromatograms shown in Figure 4a suggest that before the plasma treatment, except for the water peak, only the pentane peak was essentially present. After the plasma was switched on, the pentane concentration decreased, while intermediate reaction products such as carbon dioxide (CO₂), acetylene (C₂H₂), propane (C₃H₈), and water (H₂O) increased. The vertical positions of the lines are relative ones as they depend on the GC measurement. Only the peaks emerging from the red, blue, and black lines are relevant. It was not possible to identify other species, and their traces are reported in the upper right boxes of Figure 4.

In Figure 4b, we report the results in the presence of the catalyst. In both experimental conditions, pentane was completely abated after less than 5 min. It is interesting to note that the concentrations of some residual intermediates increased after 1 min of plasma treatment, while after 5 min, they were converted into CO₂ and water. We will discuss these features in Section 3.3.

3.2. Pentane Decomposition

In what follows, we analyze pentane depletion according to treatment time t , for the different experimental conditions, i.e., plasma power, initial pentane concentration, and catalyst activity. We found that relative to t , pentane concentration strongly depends on the plasma power used and on the catalyst activity. In particular, without the catalyst and at 16.9 W plasma power, pentane was almost fully, but not completely, decomposed after 5 min. However, at 44.2 W plasma power, a full decomposition took about 2 min.

It should be emphasized, however, that the full decomposition of pentane does not mean that pentane is completely converted to CO₂. As we discuss in Section 3.3, the plasma also produces intermediate reaction products such as acetylene and propane. In the presence of the catalyst, pentane is fully decomposed at the lower plasma power (16.9 W) in $t = 5$ min. At the higher plasma power (44.2 W), the catalyst activity is able to shorten the depletion time such that the pentane is completely decomposed in about 1 min.

To understand the chemical dynamics, we plotted the experimentally measured pentane concentrations (having an error of about 10%), $\rho_5(t)$, in Figure 5 relative to treatment time t . The basic idea here is to represent the data in semi-log scale in order to see whether the data are consistent with an exponential decay [26], either a single one or a more complex decay. We therefore used the following basic function:

$$\rho_5(t) = \rho_5(0) e^{-t/\tau_5}, \quad (1)$$

where $\rho_5(0)$ is the initial pentane concentration before plasma treatment, τ_5 is a parameter representing the characteristic time scale for depletion, which is related to the decomposition mean lifetime, $t_{1/2}$, according to $t_{1/2} = \tau_5 \log(2)$. As a general feature, we found that τ_5 depends on the initial pentane concentration.

As one can see from Figure 5a, the experimental values for the lower power, $P = 16.9$ W, scatter significantly. In particular, a double-exponential decay scenario seems to emerge at the initial pentane concentrations 600 ppm and 300 ppm. At the higher power of $P = 44.2$ W, considered in Figure 5b, the reduced time scale for depletion seems to be consistent with a single exponential decay for $\rho_5(t)$.

At plasma power $P = 16.9$ W, the reaction rates increase with decreasing initial pentane concentration (Figure 5a). At the highest pentane concentration (1200 ppm), we see a single decaying exponential, yielding a decomposition time of $\tau_5 = 5.3$ min. At lower pentane concentrations, the decay becomes faster, and a second regime seems to take place after $t = 2$ min. At these low concentrations and long times t , we expect the plasma to produce radical species more effectively. By increasing the residence time of the contaminated air in the plasma region (i.e., by prolonging the treatment time t), the availability of plasma-generated radical species for the air contaminant (pentane, in our case) increases. The availability of radical species becomes even higher when dealing with reduced concentrations of the air contaminant. Additional decomposition effects due to the catalyst are not apparent for pentane, such that pentane depletion seems to be dominated by the plasma to

a large extent. Given the uncertainties implied by the measurements, the present suggestion for a double-exponential decay remains to be understood. Additional measurements, which are beyond the scope of our work, are therefore required in order to draw a more quantitative conclusion.

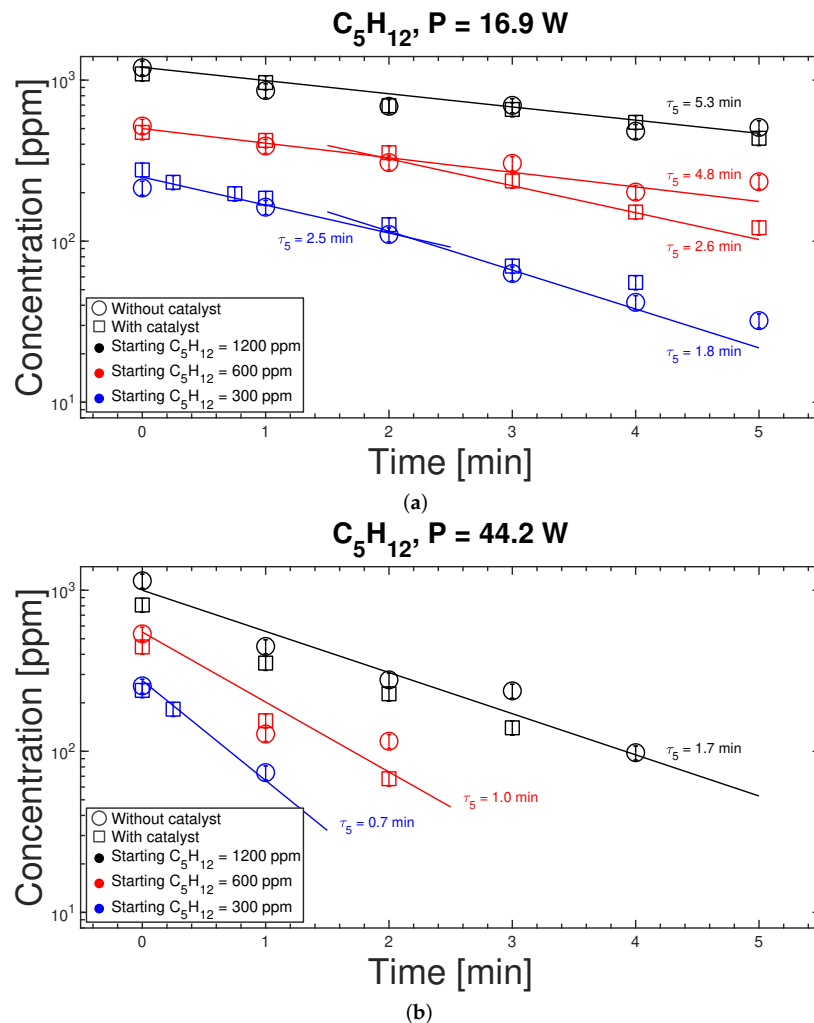


Figure 5. Depletion rate of pentane at different concentrations per plasma power: (a) $P = 16.9$ W, and (b) $P = 44.2$ W. The values for τ_5 (representing the slopes of the plotted straight lines) are summarized in Table 1 together with the estimated errors. The latter values were obtained by taking the highest and lowest slopes consistent with the data. The experimental uncertainties in the measured values, at about 10%, are roughly the size of the symbols shown.

At plasma power $P = 44.2$ W, much higher decomposition rates are found, and again, pentane depletion is plasma-dominated (Figure 5b). Now, we find single exponential decays for ρ_5 . The fact that we only have three experimental points in Figure 5b for the low initial pentane concentrations is a result of the fast depletion rate found. One should consider intermediate treatment times to have more data points. However, the observed trend is sufficient to conclude that depletion is happening at a much higher rate. The straight

line shown, with a slope given by $\tau_5 = 0.7$ min, is consistent with the available data. Notice that we only have one parameter in the model, i.e., τ_5 , and three times more data to fit it. Some deviations from the fit could be due to the presence of complex processes related to the generation of intermediate reaction products, as discussed below.

Quantitatively, pentane decomposition, denoted by D_5 , is evaluated as follows:

$$D_5(\%) = 100 \frac{[C_5H_{12}]_0 - [C_5H_{12}]_i}{[C_5H_{12}]_0}, \quad (2)$$

where $[C_5H_{12}]_0$ is the pentane concentration before treatment, and $[C_5H_{12}]_i$ is the pentane concentration after treatment time t . In Table 1, the pentane decomposition D_5 and the time scale for decomposition τ_5 are reported for $t = 5$ min in the absence and presence of the catalyst. As one can see for 44.2 W plasma power, pentane decomposition occurs in less than 2 min, and the depletion time scale τ_5 decreases with decreasing pentane concentrations, from 1.7 min (1200 ppm) to 0.7 min (300 ppm). Catalysis does not seem to compete with plasma at a high power level, and $D_5 > 95\%$. At the lower plasma power and for high pentane concentrations, neither the plasma nor the catalyst is able to completely abate pentane. At the lowest concentration, D_5 becomes larger than 95% in the presence of the catalyst. Indeed, the catalyst helps the depletion at low initial concentrations, while it does not greatly affect the depletion at higher concentrations. This can be explained by assuming that at high concentrations, the catalytic sites are saturated; therefore, the plasma controls the chemical kinetics.

Table 1. Pentane decomposition for the plasma treatment time $t = 5$ min, with and without a catalyst, for the two plasma powers and the three initial pentane concentrations considered in Figure 5. The associated pentane decomposition times, τ_5 , are reported. The estimated errors for τ_5 are obtained by taking the highest and lowest slopes of the straight lines, consistent with the data shown in Figure 5.

Power (W)	Starting C_5H_{12} (ppm)	Catalyst	D_5 (%)	τ_5 (min)
16.9	300	No	87	2.5 ± 0.3 for $t < 2$ min, 1.8 ± 0.1 for $t > 2$ min
		Yes	>95	2.5 ± 0.3 for $t < 2$ min, 1.8 ± 0.1 for $t > 2$ min
	600	No	55	4.8 ± 0.5
		Yes	75	4.8 ± 0.5 for $t < 2$ min, 2.6 ± 0.2 for $t > 2$ min
	1200	No	58	5.3 ± 0.8
		Yes	60	5.3 ± 0.8
44.2	300	No	>95	0.7 ± 0.1
		Yes	>95	0.7 ± 0.1
	600	No	>95	1.0 ± 0.1
		Yes	>95	1.0 ± 0.1
	1200	No	>95	1.7 ± 0.2
		Yes	60	1.7 ± 0.2

We also estimated the pentane decomposition efficiency after 1 min of plasma treatment, displayed in Figure 6. The efficiency is estimated as the ratio between the amount in grams of the decomposed pentane to the applied energy in kWh. The efficiency increases with the pentane concentration, and the catalyst does not seem to play any relevant role in pentane decomposition, even at low concentrations. The increase in efficiency with pentane concentration demonstrates that for these plasma parameters, plasma processing occurs in the gas phase. These results are comparable to the efficiencies found in the NTP devices [10,27].

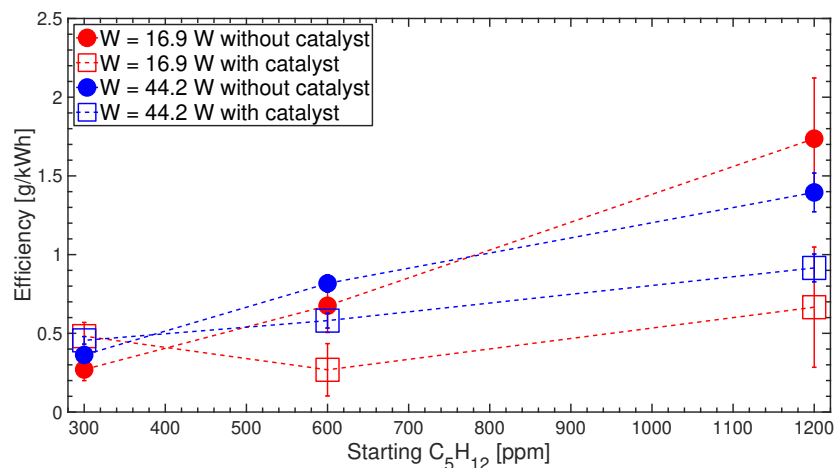


Figure 6. Pentane decomposition efficiency (g/kWh) after 1 min of plasma treatment according to the initial pentane concentration. The lines serve as visual guides. The error bars were obtained by calculating the error propagation in the estimation of the efficiency.

We also measured the ozone using the MQ131 ozone sensor coupled with Arduino Mega2560. We found that (in pure air, to avoid VOC sensor cross-sensitivity) for 16.9 W plasma power, the ozone was between 10 ppm and 20 ppm, while for 44.2 W, the ozone grew up to 400 ppm. The maximum efficiency of about 1.8 was obtained at the lower plasma power. At the higher plasma power, the fact that the efficiency was found to be smaller was probably due to the distribution of energy in the gas volume not being optimum at such higher power [28].

3.3. Intermediate Reaction Species

As shown in Figure 4, the plasma (acting for $t > 0$) shrinks the area of the pentane chromatogram peak, while other peaks appear. The water trace also changes as it depends on both the depletion processing, generated as by-products of VOC abatement species, and on the humidity transported by the chromatograph carrier gas (Helium). We could identify the acetylene and the propane peaks with the use of a calibration cylinder.

We were not able to identify the peaks classified as “Other” in Figure 4, which are suspected to be C₄ species, nor were we able to perform a CO₂ calibration. Thus, we will just concentrate on acetylene and propane here.

In order to fit the measured concentrations of the acetylene and propane species, denoted generically by x , we assume that the latter is regulated by a simple phenomenological differential equation consisting of a source term, proportional to $\rho_5(t)$, minus a loss term describing its extinction. The time evolution of the concentration $\rho_x(t)$ of species x is then given by the following equation:

$$\frac{d\rho_x(t)}{dt} = \frac{1}{\tau_{x5}}\rho_5(t) - \frac{1}{\tau_x}\rho_x(t), \quad (3)$$

where $\rho_5(t) = \rho_5(0) \exp(-t/\tau_5)$ (cf. Equation (1)), and x stands for acetylene or propane. Here, τ_{x5} represents the time scale for the generation of species x as a result of pentane decomposition, and τ_x is the time during the decomposition of the species x itself during the treatment. Thus, τ_{x5} and τ_x are the two parameters in the model.

The differential equation (Equation (3)) admits an exact solution, given by the equation below:

$$\frac{\rho_x(t)}{\rho_5(0)} = \frac{\tau_x \tau_5}{\tau_5 - \tau_x} \frac{1}{\tau_{x5}} \left(e^{-t/\tau_5} - e^{-t/\tau_x} \right). \quad (4)$$

In the case of an initial pentane concentration of $\rho_5(0) = 1200$ ppm, for the two plasma powers, with and without a catalyst, we obtain the $\tau_{x5,x}$ parameters by fitting the experimental data, as reported in Figure 7.

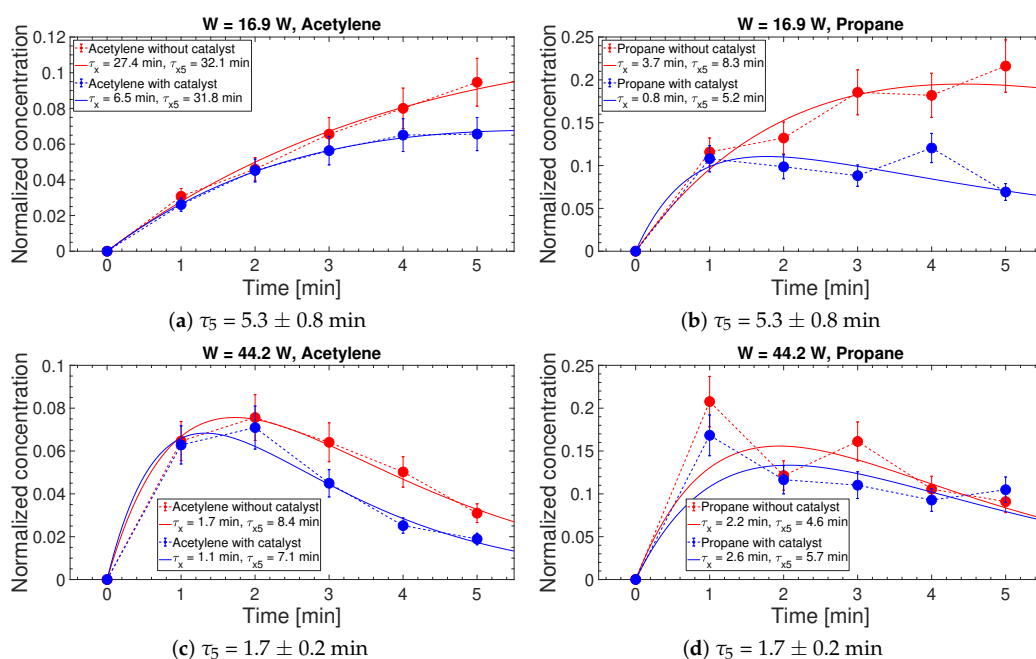


Figure 7. Normalized concentrations of intermediate products, acetylene, and propane, according to treatment time T (min), at 1200 ppm initial pentane concentration. (a,c) Acetylene at $P = 16.9$ W and $P = 44.2$ W, respectively. (b,d) Propane at $P = 16.9$ W and $P = 44.2$ W, respectively. The experimental uncertainties for the product concentrations were obtained by propagating the error due to the initial concentration of pentane yielding values equal to $\sqrt{2}$ 10%. The continuous lines are the results of the least-square fits obtained with Equation (4), while the dashed lines are just visual guides. The errors for τ_5 are from Table 1 (see also Figure 5). The errors associated with τ_x and τ_{x5} are those from the least-square fits and are reported in Table 2.

Table 2. Acetylene and propane characteristic times for different plasma treatments. The initial pentane concentration for this table corresponds to 1200 ppm. The errors for τ_x and τ_{x5} were obtained as discussed in Figure 7.

Specie	Power (W)	Catalyst	τ_5 (min)	τ_{x5} (min)	τ_x (min)
Acetylene	16.9	No	5.3 ± 0.8	32.1 ± 3.0	27.4 ± 8.0
		Yes	5.3 ± 0.8	31.8 ± 2.0	6.5 ± 1.0
	44.2	No	1.7 ± 0.2	8.4 ± 0.7	1.7 ± 0.2
		Yes	1.7 ± 0.2	7.1 ± 1.0	1.1 ± 0.1
Propane	16.9	No	5.3 ± 0.8	8.3 ± 2.0	3.7 ± 1.0
		Yes	5.3 ± 0.8	5.2 ± 2.0	0.8 ± 0.3
	44.2	No	1.7 ± 0.2	4.6 ± 1.0	2.2 ± 0.8
		Yes	1.7 ± 0.2	5.7 ± 2.0	2.6 ± 1.0

4. Discussion

A closer analysis of the results in terms of the time scales shown in Table 2 suggests that the catalyst is not directly involved in the decomposition of pentane. In fact, the time scales τ_5 are independent of the presence of the catalyst. At plasma power $P = 16.9$ W, $\tau_5 = (5.3 \pm 0.8)$ min, and at $P = 44.2$ W, $\tau_5 = (1.7 \pm 0.2)$ min, suggesting that the pentane decomposition is primarily due to the action of the plasma.

In contrast, the role of catalysts is very important for the depletion of the intermediate reaction products, as displayed by the associated time scales and denoted by τ_x , particularly at lower plasma power. For the latter, the catalytic depletion of intermediates is very efficient, as much as four times faster than that of plasma. Catalysis processing without plasma refers to an experiment where plasma is not switched on, and so only the catalyst (present on the surface of plasma module) is operating.

The reactions that the catalyst speeds up are the oxidation of acetylene and propane, which are previously formed by the partial decomposition of pentane, mainly by means of plasma action. At higher powers, the catalyst acts weakly on the depletion of acetylene, but not on propane. The time scale for the production of acetylene is weakly dependent on the catalyst, and at low power, it seems to diminish propane production.

These studies support the experimental evidence that catalysis concurs with the depletion of the intermediate reaction products in the plasma reactor, as also reported in the literature [29,30]. In the previous experiments reporting propane abatement, catalysis processing was used without a plasma, which showed very low efficiency. Therefore, the higher efficiency reported here is due to the synergetic effect of the plasma and the catalyst.

In fact, our previous study [31] demonstrated a much lower abatement efficiency for propane, performed by catalysis processing and using only UV-A light energy. In the case of TiO₂, we used light with a UV-A range of 340–400 nm and a peak at 370 nm to obtain an efficiency of less than 10% of the abatement after 22 min of application [31,32]. As previously reported in our studies, the UV-A power emitted by our SDBD was very low, from 20 to 600 times less bright in comparison with the typical UV-A lamps used for catalytic processing [33].

Other previous works suggested that introducing a catalyst into a plasma reactor could generate more highly energetic and reactive species, which favor plasma-induced reactions towards the deep oxidation of VOCs. In our case, the study of the kinematical evolution of depletion demonstrates that catalysts do not affect the pentane decomposition. We may conclude that the catalyst does not generate reactive species favoring the decomposition of the pentane, but it is the ability of the plasma state to primarily decompose pentane, thus generating the active intermediate species that could be removed by the catalyst. Catalytic processes are mainly responsible for removing the produced species, such as propane and acetylene, thus shifting the chemical kinetics towards full VOC depletion.

Hence, the combination of plasma with catalysis has a great potential to lower the activation temperature of the catalysts, enhance the removal of pollutants, and minimize the formation of undesired intermediate reaction products, all of which may contribute in different ways to the enhancement of the energy efficiency of the plasma process [27].

The results obtained in the present paper show that TiO₂ does not directly affect the removal/conversion of pentane, with the catalyst only having clear effects on the removal of excited species and by-products. The choice of the catalyst deserves further investigation in order to understand if different choices may influence the depletion of pentane. As an example, a recent study investigated the abatement of another alkane (n-undecane) and the related CO_x selectivity, achievable through the application of a packed-bed DBD reactor and using γ -Al₂O₃ spheres as packing material [34]. The removal efficiency of n-undecane and the CO_x selectivity increased from 40% to 80–92% and from 37% to 40–80%, respectively, when loading γ -Al₂O₃ with CeO₂ at different weight fractions.

In light of the numerous studies on cold atmospheric plasmas and their potentials for VOC abatement/conversion, such devices could be successfully employed in a broad spectrum of applications concerning VOC removal. The applications might be different

depending on the mode NTP devices used. Under static conditions, as in the present study, NTP devices show great potential in the decontamination of polluted environmental matrices such as contaminated air in confined volumes or contaminated soil [35].

NTP devices could also be applied to the treatment of contaminated air streams, thus under dynamic conditions. In this case, optimizing energy efficiency is a challenge that plasma technologies should face in the future, especially in applications regarding the treatment of high airflow rates. The use of catalysts, the combination with other removal technologies, or the study of peculiar configurations [36] may help to reduce the energy consumption in order to achieve the same targets.

The use of SDBD instead of volume DBDs also seems to be promising for energy optimization purposes. In a review paper, Vandenbroucke et al. [2] compared the results obtained by Oda et al. [37,38], who measured the abatement performance of trichloroethylene (TCE) by: (1) an SDBD reactor with a V_2O_5/TiO_2 catalyst, and (2) a volume DBD with a TiO_2 catalyst. At the same airflow rate (400 mL/min) and TCE concentration (1000 ppm), the first configuration allowed for the acquisition of the same removal efficiency for the second configuration (>95%) by using only 25–48% of the energy consumed by the latter. Other authors [39] carried out a comparison between an SDBD and a volume DBD reactor in terms of ozone generation. The authors found out that under the same operating conditions and specific energy density, the ozone generation obtained with the SDBD exceeds the amount of ozone generated by the volume DBD by a factor of 2.5–3.5. Similar results were obtained in a more recent study comparing the application of an SDBD and a volume DBD reactor to ethanol in air [40]. Under the same operating conditions and specific energy density, the authors obtained ethanol removal efficiencies of 80% and 60% when using the SDBD and the volume DBD reactor, respectively.

5. Conclusions

In this work, an SDBD reactor was employed for the decomposition of pentane, at different plasma discharge power levels (16.9 W and 44.2 W), gas concentrations in air, and plasma treatment time. It was found that pentane could be totally depleted in a few (about 5) minutes at 44.2 W, where the efficiency reaches the value of 1.3 g/kWh for the initial pentane concentration of 1200 ppm. The maximum efficiency of 1.8 g/kWh was found at 16.9 W, also for the initial pentane concentration of 1200 ppm. The efficiency increased with the pentane concentration, suggesting that plasma effects are volume-dependent because the reactions occurred in the gas phase. The fact that efficiency decreased with power suggests that plasma energy was either not well-distributed in the reactor or that the plasma produced a larger amount of by-products such as ozone, thus limiting other chemical reactions [28].

The analysis of the temporal evolution of pentane and the associated concentrations of the intermediate reaction products allowed us to quantitatively describe the kinetics of VOC depletion in the plasma hybrid system. In an SDBD–catalyst reactor, the plasma primarily acts to decompose pentane, while the catalyst mostly concerns the intermediate reaction products. During the first minutes of treatment in a single experiment, gas processing is dominated by plasma decomposition of pentane, followed by the generation of the intermediate products, which are progressively depleted by the catalytic processes acting on longer time scales.

Worthy of note is the fact that plasma dynamics depends on both the pentane concentration and applied power. It is faster at higher power and lower concentrations, where pentane is abated in less than 1 min. The typical time scale varies between 0.7 and 1.7 min for 300 ppm and 1200 ppm initial pentane concentrations, respectively. At extremely low powers, e.g., at 11 W, the pentane is not totally dissociated, and the time scale for abatement is longer, well above two minutes and roughly in the range of 2.5–5.3 min; this may be addressed by varying the concentrations between 300 ppm and 1200 ppm.

Different metal catalysts have been investigated in single-stage plasma-catalytic gas cleaning processes for the oxidation of VOCs. Transition metal oxide catalysts in combi-

nation with plasma have attracted growing interest for pollution abatement because of their comparable performance and low cost. In our previous work, we found that the TiO₂ and/or WO₃ catalysts alone are not able to efficiently remove propane [31], while here, we managed to increase the pentane depletion by using plasma together with a catalyst, thus yielding an efficient abatement of the intermediate reaction products.

Author Contributions: Conceptualization, C.R., C.P. and M.D.; methodology, C.R., C.P. and M.D.; software, C.P. and H.E.R.; validation, C.P.; formal analysis, C.P. and H.E.R.; investigation, C.P.; resources, C.R.; data curation, C.P.; writing—original draft preparation, C.R., C.P., H.E.R. and M.D.; writing—review and editing, C.R., C.P., H.E.R., M.D. and M.S.; visualization, C.P.; supervision, C.R.; project administration, C.R.; funding acquisition, C.R. All authors have read and agreed to the published version of the manuscript.

Funding: This research received no external funding.

Institutional Review Board Statement: Not applicable.

Informed Consent Statement: Not applicable.

Data Availability Statement: The data that support the findings of this study are available from the corresponding author upon reasonable request.

Acknowledgments: The authors gratefully acknowledge technical support from Alessandro Mietner and Alessandro Bau' in device development and experiment execution.

Conflicts of Interest: The authors declare no conflict of interest.

References

1. EEA. *Air Pollution*; European Environment Agency: Copenhagen, Denmark, 2017.
2. Vandembroucke, A.; Morent, R.; De Geyter, N.; Leys, C. Non-thermal plasmas for non-catalytic and catalytic VOC abatement. *J. Hazard. Mater.* **2011**, *195*, 30–54. [[CrossRef](#)] [[PubMed](#)]
3. Aguayo-Villarreal, I.; Montes-Morán, M.; Hernández-Montoya, V.; Bonilla-Petriciolet, A.; Concheso, A.; Rojas-Mayorga, C.; González, J. Importance of iron oxides on the carbons surface vs the specific surface for VOC's adsorption. *Ecol. Eng.* **2017**, *106*, 400–408. [[CrossRef](#)]
4. Wang, W.; Ma, X.; Grimes, S.; Cai, H.; Zhang, M. Study on the absorbability, regeneration characteristics and thermal stability of ionic liquids for VOCs removal. *Chem. Eng. J.* **2017**, *328*, 353–359. [[CrossRef](#)]
5. Donley, E.; Lewandowski, D. Optimized Design and Operating Parameters for Minimizing Emissions During VOC Thermal Oxidation. *Met. Finish. Guideb.-Dir.* **1998**, *96*, 52–58. [[CrossRef](#)]
6. Chen, X.; Carabineiro, S.; Bastos, S.; Tavares, P.; Órfão, J.; Pereira, M.; Figueiredo, J. Catalytic oxidation of ethyl acetate on cerium-containing mixed oxides. *Appl. Catal. A Gen.* **2014**, *472*, 101–112. [[CrossRef](#)]
7. Vergara-Fernández, A.; Revah, S.; Moreno-Casas, P.; Scott, F. Biofiltration of volatile organic compounds using fungi and its conceptual and mathematical modeling. *Biotechnol. Adv.* **2018**, *36*, 1079–1093. [[CrossRef](#)]
8. Belaissaoui, B.; Le Moullec, Y.; Favre, E. Energy efficiency of a hybrid membrane/condensation process for VOC (Volatile Organic Compounds) recovery from air: A generic approach. *Energy* **2016**, *95*, 291–302. [[CrossRef](#)]
9. Schiavon, M.; Torretta, V.; Casazza, A.; Ragazzi, M. Non-thermal plasma as an innovative option for the abatement of volatile organic compounds: A review. *Water Air Soil Pollut.* **2017**, *228*, 1–20. [[CrossRef](#)]
10. Li, S.; Dang, X.; Yu, X.; Abbas, G.; Zhang, Q.; Cao, L. The application of dielectric barrier discharge non-thermal plasma in VOCs abatement: A review. *Chem. Eng. J.* **2020**, *388*, 124275. [[CrossRef](#)]
11. Dobsław, C.; Glocker, B. Plasma Technology and Its Relevance in Waste Air and Waste Gas Treatment. *Sustainability* **2020**, *12*, 8981. [[CrossRef](#)]
12. Shin, D.; Hong, Y.; Lee, S.; Kim, Y.; Cho, C.; Ma, S.; Chun, S.; Lee, B.; Uhm, H. A pure steam microwave plasma torch: Gasification of powdered coal in the plasma. *Surf. Coat. Technol.* **2013**, *228*, S520–S523. [[CrossRef](#)]
13. Choi, S.; Hong, S.; Lee, H.; Watanabe, T. A comparative study of air and nitrogen thermal plasmas for PFCs decomposition. *Chem. Eng. J.* **2012**, *185*, 193–200. [[CrossRef](#)]
14. Suris, A. Investigation of high-temperature steam-air reagents for plasma waste treatment processes. *Theor. Found. Chem. Eng.* **2017**, *51*, 348–351. [[CrossRef](#)]
15. George, A.; Shen, B.; Craven, M.; Wang, Y.; Kang, D.; Wu, C.; Tu, X. A Review of Non-Thermal Plasma Technology: A novel solution for CO₂ conversion and utilization. *Renew. Sustain. Energy Rev.* **2021**, *135*, 109702. [[CrossRef](#)]
16. Pietanza, L.; Colonna, G.; Capitelli, M. Kinetics versus thermodynamics on CO₂ dissociation in high temperature microwave discharges. *Plasma Sources Sci. Technol.* **2020**, *29*, 035022. [[CrossRef](#)]

17. Dobsław, D.; Ortlinghaus, O.; Dobsław, C. A combined process of non-thermal plasma and a low-cost mineral adsorber for VOC removal and odor abatement in emissions of organic waste treatment plants. *J. Environ. Chem. Eng.* **2018**, *6*, 2281–2289. [[CrossRef](#)]
18. Barni, R.; Benocci, R.; Spinicchia, N.; Roman, H.; Riccardi, C. An experimental study of plasma cracking of methane using DBDs aimed at hydrogen production. *Plasma Chem. Plasma Process.* **2019**, *39*, 241–258. [[CrossRef](#)]
19. Long, H.; Shang, S.; Tao, X.; Yin, Y.; Dai, X. CO₂ reforming of CH₄ by combination of cold plasma jet and Ni/ γ -Al₂O₃ catalyst. *Int. J. Hydrogen Energy* **2008**, *33*, 5510–5515. [[CrossRef](#)]
20. Piferi, C.; Barni, R.; Roman, H.; Riccardi, C. Current Filaments in Asymmetric Surface Dielectric Barrier Discharge. *Appl. Sci.* **2021**, *11*, 2079. [[CrossRef](#)]
21. Abdelaziz, A.; Seto, T.; Abdel-Salam, M.; Otani, Y. Performance of a surface dielectric barrier discharge based reactor for destruction of naphthalene in an air stream. *J. Phys. D Appl. Phys.* **2012**, *45*, 115201. [[CrossRef](#)]
22. Assadi, A.; Bouzaza, A.; Wolbert, D. Comparative study between laboratory and large pilot scales for VOC's removal from gas streams in continuous flow surface discharge plasma. *Chem. Eng. Res. Des.* **2016**, *106*, 308–314. [[CrossRef](#)]
23. Silliprandi, R.; Roman, H.; Barni, R.; Riccardi, C. Characterization of the streamer regime in dielectric barrier discharges. *J. Appl. Phys.* **2008**, *104*, 063309. [[CrossRef](#)]
24. Biganzoli, I.; Barni, R.; Riccardi, C. Note: On the use of Rogowski coils as current probes for atmospheric pressure dielectric barrier discharges. *Rev. Sci. Instrum.* **2013**, *84*, 016101. [[CrossRef](#)] [[PubMed](#)]
25. Biganzoli, I.; Barni, R.; Gurioli, A.; Pertile, R.; Riccardi, C. Experimental investigation of Lissajous figure shapes in planar and surface dielectric barrier discharges. *J. Phys. Conf. Ser.* **2014**, *550*, 012039. [[CrossRef](#)]
26. Kim, H. Nonthermal plasma processing for air-pollution control: A historical review, current issues, and future prospects. *Plasma Process. Polym.* **2004**, *1*, 91–110. [[CrossRef](#)]
27. Chung, W.; Mei, D.; Tu, X.; Chang, M. Removal of VOCs from gas streams via plasma and catalysis. *Catal. Rev.* **2019**, *61*, 270–331. [[CrossRef](#)]
28. Nguyen, H.; Park, M.; Kim, S.; Kim, H.; Baik, L.; Jo, Y. Effective dielectric barrier discharge reactor operation for decomposition of volatile organic compounds. *J. Clean. Prod.* **2018**, *198*, 1232–1238. [[CrossRef](#)]
29. Shayegan, Z.; Lee, C.; Haghghat, F. TiO₂ photocatalyst for removal of volatile organic compounds in gas phase—A review. *Chem. Eng. J.* **2018**, *334*, 2408–2439. [[CrossRef](#)]
30. Feng, X.; Liu, H.; He, C.; Shen, Z.; Wang, T. Synergistic effects and mechanism of a non-thermal plasma catalysis system in volatile organic compound removal: A review. *Catal. Sci. Technol.* **2018**, *8*, 936–954. [[CrossRef](#)]
31. Piferi, C.; Riccardi, C. High concentration propane depletion with photocatalysis. *AIP Adv.* **2021**, *11*, 125008. [[CrossRef](#)]
32. Bin, Z.; Zhang, L.; Yan, Y.; Meng, L.; Yimin, Z. Enhancing toluene removal in a plasma photocatalytic system through a black TiO₂ photocatalyst. *Plasma Sci. Technol.* **2019**, *21*, 115503.
33. Piferi, C.; Brescia, A.; Riccardi, C. Intensity comparison between UV lamps and plasma emission for air purification studies. *AIP Adv.* **2021**, *11*, 085209. [[CrossRef](#)]
34. Xia, T.; Yao, S.; Wu, Z.; Li, G.; Li, J. High ratio of Ce³⁺/(Ce³⁺+Ce⁴⁺) enhanced the plasma catalytic degradation of n-undecane on CeO₂/ γ -Al₂O₃. *J. Hazard. Mater.* **2022**, *424*, 127700. [[CrossRef](#)] [[PubMed](#)]
35. Aggelopoulos, C.; Svarnas, P.; Klapa, M.; Tsakiroglou, C. Dielectric barrier discharge plasma used as a means for the remediation of soils contaminated by non-aqueous phase liquids. *Chem. Eng. J.* **2015**, *270*, 428–436. [[CrossRef](#)]
36. Martini, L.; Collier, G.; Schiavon, M.; Cernuto, A.; Ragazzi, M.; Dilecce, G.; Tosi, P. Non-thermal plasma in waste composting facilities: From a laboratory-scale experiment to a scaled-up economic model. *J. Clean. Prod.* **2019**, *230*, 230–240. [[CrossRef](#)]
37. Oda, T.; Takahashi, T.; Kohzuma, S. Decomposition of Dilute Trichloroethylene by Using Nonthermal Plasma Processing. *IEEE Trans. Ind. Appl.* **2001**, *37*, 965–970. [[CrossRef](#)]
38. Oda, T.; Takahashi, T.; Yamaji, K. Nonthermal plasma processing for dilute VOCs decomposition. *IEEE Trans. Ind. Appl.* **2002**, *38*, 873–878. [[CrossRef](#)]
39. Nassour, K.; Brahami, M.; Nemmich, S.; Hammadi, N.; Zouzou, N.; Tilmatine, A. Comparative experimental study between surface and volume DBD ozone generator. *Ozone Sci. Eng.* **2016**, *38*, 70–76. [[CrossRef](#)]
40. Nobrega, P.; Blin-Simian, N.; Bournonville, B.; Jorand, F.; Lacour, B.; Pasquiers, S.; Rohani, V.; Cauneau, F.; Fulcheri, L. Comparison between performances of surface and volume nanosecond pulsed dielectric barrier discharges for the treatment of volatile organic compounds. In Proceedings of the 23rd International Symposium on Plasma Chemistry-ISPC 23, Montréal, QC, Canada, 30 July 2017.

A.5 A study on propane depletion by surface dielectric barrier discharges

Reproduced from Piferi, C.; Riccardi, C. A Study on Propane Depletion by Surface Dielectric Barrier Discharges. *Cleaner Engineering and Technology* 2022, 8, 100486, <https://doi.org/10.1016/j.clet.2022.100486>.



Contents lists available at ScienceDirect

Cleaner Engineering and Technology

journal homepage: www.sciencedirect.com/journal/cleaner-engineering-and-technology



A study on propane depletion by surface dielectric barrier discharges

Cecilia Piferi, Claudia Riccardi*

Dipartimento di Fisica, Università degli Studi di Milano-Bicocca, Piazza della Scienza 3, 20126, Milano, Italy

ARTICLE INFO

Keywords:

Surface dielectric barrier discharge
Atmospheric pressure
Non thermal plasma
Streamer discharge
VOC Abatement

ABSTRACT

A study of volatile organic compounds (VOCs) depletion using a plasma system based on a surface dielectric barrier discharge SDBD has been carried out. The analysis of the temporal evolution of VOCs permitted to estimate the corresponding dissociation rates as a function of the relevant parameters and to demonstrate the ability of SDBD in the abatement of large VOC concentrations up to 9,300 ppm. The depletion rate increases as a function of plasma power and concentration for propane, pentane and acetone. The efficiency evaluated as quantity of propane per unit of energy takes values between 2 and 7.5 g/kWh. A comparison between propane, pentane and acetone, exploits that propane efficiency is higher than of those pentane and acetone. On the basis of this study SDBD is a promising plasma source for VOCs abatement at high concentrations.

1. Introduction

Air pollution can be harmful to both the environment and the human health. As a result of a systematic application of strict regulations, the emissions of atmospheric pollutants have been reduced significantly during the last decades, especially in heavily industrialized countries. Despite these efforts, the concentrations of pollutants within large urban zones remain too high.

A large and important group of pollutants such as volatile organic compounds (VOCs) are produced in the environment and diffusing out into the atmosphere. Further improvement in the atmospheric air quality is still an issue requiring specific studies (EEA, 2017). Pollutants can cause a variety of deleterious effects depending on their chemical structure and concentration (Vandenbroucke et al., 2011). Some of these compounds have an impact on human health that goes from impairing the respiratory system to premature death caused by their toxicity or carcinogenic effects (EEA, 2017).

Several methods have been proposed for VOCs depletion, including adsorption (Aguayo-Villarreal et al., 2017), absorption (Wang et al., 2017), thermal decomposition (Donley and Lewandowski, 1998), catalytic oxidation (Chen et al., 2014), bio-filtration (Vergara-Fernández et al., 2018), membrane separation (Belaissouli et al., 2016).

Among the various alternative methods still under test, plasma technology (Bogaerts et al., 2020) is considered one of the most promising in various environmental application. Plasmas are generated by ionizing neutral gases with electrical power, it contains charges, electrons which are the prime source of ionization, ions and a variety of

neutral molecules and radicals exploiting a high chemical reactivity.

Plasma processing are highly non-selective, creating a chemical reactive environment able to treat materials (Zanini et al., 2016), as well as gases (Li et al., 2020).

Between plasma technologies we can identify plasmas produced in thermal equilibrium (Thermal Plasmas, TP) (Choi et al., 2012), and in non-thermal equilibrium conditions (Non-Thermal Plasmas NTP) (Feng et al., 2018). Thermal plasmas thanks to their high energy content have been intensively studied for waste composting, fermentation residue, perfluoro carbons abatements (Dobslaw and Glocker, 2020).

NTP plasmas have recently been employed for their lower energy consumption, in various applications for the treatment of materials (Zanini et al., 2018), for the dissociation and abatement of organic molecules (Dobslaw et al., 2018), for the production of hydrogen-rich mixtures (Barni et al., 2019), and CO₂ conversion (George et al., 2021). Among the various configurations in which NTP can be produced those most efficient in the literature are based on the dielectric barrier discharges, DBD (Byeon et al., 2010).

DBDs are studied for the abatement of many organic compounds as can be found in the recent literature review (Chung et al., 2019). In some case DBD plasmas employ also catalysts in order to improve the abatement efficiency (Thévenet et al., 2014).

In DBDs, plasma is performed between two electrodes allowing the generation of uniform charge filaments within the discharge gap (Barni et al., 2005), preventing the development of destructive arc discharges (Siliprandi et al., 2008). The width of the discharge gap, of the order of a few millimeters, determines the required discharge energy, such that

* Corresponding author.

E-mail address: claudia.riccardi@unimib.it (C. Riccardi).

<https://doi.org/10.1016/j.clet.2022.100486>

Received 22 November 2021; Received in revised form 16 March 2022; Accepted 2 April 2022

Available online 13 April 2022

2666-7908/© 2022 The Authors. Published by Elsevier Ltd. This is an open access article under the CC BY-NC-ND license (<http://creativecommons.org/licenses/by-nc-nd/4.0/>).

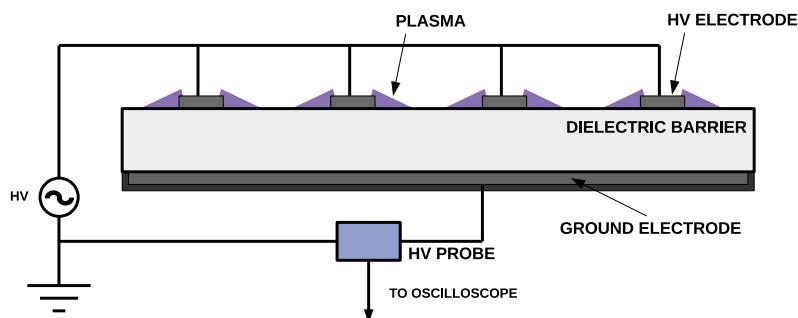


Fig. 1. Plasma device scheme: a plane and a different shape (fingers or honeycomb) electrode are attached to a dielectric material. The lower electrode, fed at the ground is covered with an insulating material, whereas the upper one, fed to high voltage (HV), is exposed to air. The HV probe measures the applied potential.

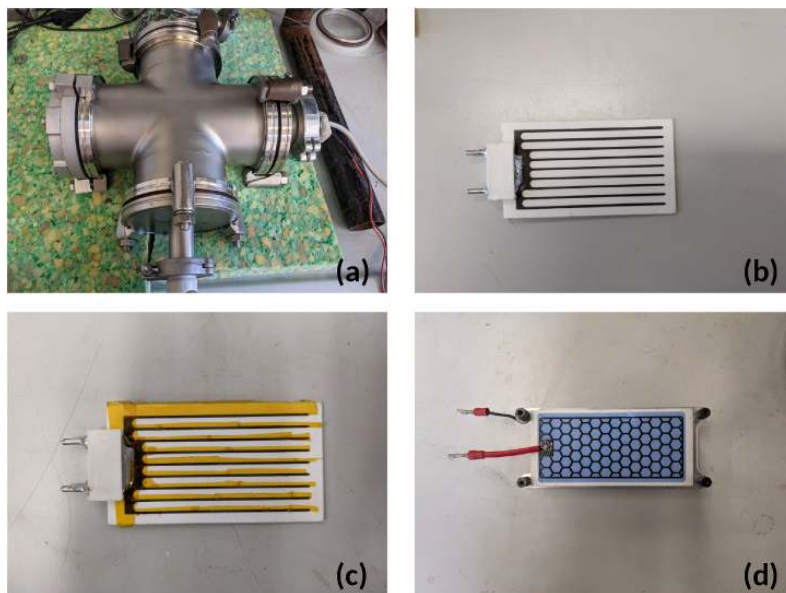


Fig. 2. Experimental setup. (a) Reactor. Plasma device configuration (b) bidirectional fingers electrode, (c) monodirectional fingers electrode, (d) honeycomb electrode. The bi and monodirectional breadboard are made by $9 \times 5 \text{ cm}^2$ alumina dielectric surface, 1 mm thickness, with 9 metal fingers, 7 cm long, 1 mm large, and 4 mm apart made of an alloy of ruthenium, nickel, silver, and palladium. The isolation of the monodirectional electrode are made using kapton. The honeycomb breadboard is made by $9 \times 4 \text{ cm}^2$ alumina dielectric surface, 1 mm thickness, with aluminum esagonal exposed electrode with a diameter of the circumscribed circumference of 7 mm.

smaller gaps require less power discharge (Brandenburg, 2017). Thin gaps are associated to small VOC treatment volumes, limiting the abatement of large amounts as required in most applications. A special version of the DBD is the Surface Dielectric Barrier Discharge (SDBD). The SDBD has the advantage of being able to handle larger volumes of gas. SDBD constitute a hopeful alternative in which a discharge is performed on the surface of a dielectric layer (Nguyen et al., 2020). The absence of a discharge gap allows to work at lower energies, and to treat larger amounts of VOC in comparison with conventional DBD.

The surface plasma dielectric discharge SDBD are very promising as recently been demonstrated for VOCs abatement (Abdelaziz et al., 2012). While many studies have been carried out using DBDs (Bogaerts et al., 2020), few experiments have been performed employing SDBDs for VOC abatement. These sources have much lower energy consumption and the advantage of generating plasma on a free surface, facilitating the passage of larger gas fluxes to be treated (Piferi et al., 2021a). In this new configuration abatement of VOCs such as naphthalene, trimethylamine and isovaleric acid have been recently experimented at efficiencies comparable to those obtained by DBD reactors (Assadi et al., 2016). Propane depletion with SDBD has been studied already at very low concentrations of the order of 100 ppm in Hill et al. (2008).

Our work is focused on SDBDs, with the aim of studying the abatement efficiencies of some specific VOCs at low and high concentrations never before investigated: propane, pentane and acetone up to 9,300 ppm. This study permits to better understand the kinetics of abatement evaluating the depletion times and efficiencies and to demonstrate the ability of this source to abate large VOCs concentrations in view of applications in the industry. A comparison of the latter with the literature experiments demonstrate that these discharges are very promising. The results will also allow to deep the knowledge on the abatement processes in view of a possible scale-up of the system.

The paper is organized as follows. In Section 2, the experimental setup is presented. Section 3 is devoted to the experimental results, and Section 4 to conclusions.

2. Experimental setup

The configuration adopted in our experiments was suggested by a modification of the simplest version of SDBD used in plasma aerodynamics experiments (Biganzoli et al., 2014). It consists of two conducting electrodes attached at the opposite sides of a flat dielectric panel, sketched in Fig. 1.

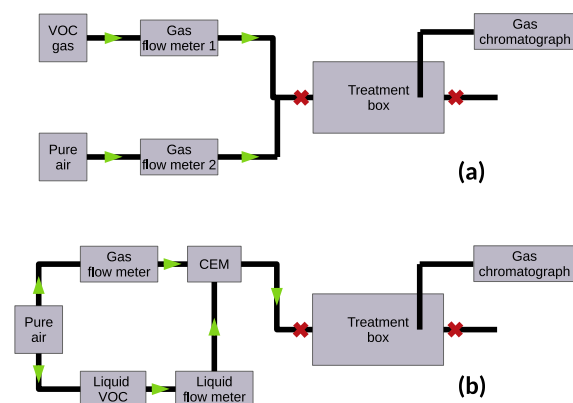


Fig. 3. (a) Gas VOC contamination setup: The VOC gas is in a cylinder and its flow is regulated by the flow meter 1, the pure air cylinder flow is regulated by the meter 2. (b) Liquid VOC contamination setup: The pure air cylinder supply for both the gas carriers and the bubbler device containing the VOC. A controlled evaporator and mixer (CEM) let the liquid to evaporate and mixes it with a line of pure air flow.

A metallic plasma box of about 1.5 l volume (Fig. 2a) and three different SDBD plasma configurations for the HV electrode are used:

- bidirectional fingers electrode (Fig. 2b);
- monodirectional fingers electrode (Fig. 2c);
- honeycomb electrode (Fig. 2d).

The ground electrode is a metallic plain plate. The plasma is lit up by a high voltage (HV) power supply working in a power range between 8 and 30 W (Biganzoli et al., 2013) and a frequency of the order of 10 kHz. The applied HV is between 5 and 10 kVpp (Piferi et al., 2021b).

The VOCs used in experiments are Propane (C_3H_8), Pentane (C_5H_{12}) and Acetone (C_3H_6O). The VOC contamination setup is different for gas and liquid VOC. The contamination setup is shown in Fig. 3. The black bold lines represent the tube connections through the whole system and the green arrows indicates the direction of the flow. In the diagram, pure air represents a gas cylinder containing approximately 80% of N_2 and 20% of O_2 , meaning that the concentration of CO_2 , CO, hydrocarbons and other pollutants is negligible. The red crosses are the symbol of open-close valves. If the VOC is a gas (Fig. 3a), the VOC is in a cylinder and its flow is regulated by the flow meter 1, while the pure air cylinder flow is regulated by the flow meter 2. If the VOC is liquid (Fig. 3b), the VOC is placed in a bubbler bottle (denoted as Liquid VOC in Fig. 3b) and let it circulate through the flow meter by the action of the air pressure. The controlled evaporator and mixer (CEM) let the liquid, coming from the liquid flow meter, to evaporate, and mix it with a line of pure air, coming from the gas flow meter, making the VOC dilution. In both cases, as a flow meter gas and liquid flow meter produced by Bronkhorst factory are used. For the gas chromatographic analyses a Micro GC Agilent 3000 instrument are employed. The gas chromatograph inlet pipe is placed inside the treatment box.

In literature an acceleration of the reaction kinetics by physico-chemical interactions with the photo-catalytic surface may be observed. The catalyst used in this experiments is TiO_2 , 34.5 mg/cm² of TiO_2 over 7.6 × 7.3 cm² tile (Piferi and Riccardi, 2021) has been deposited.

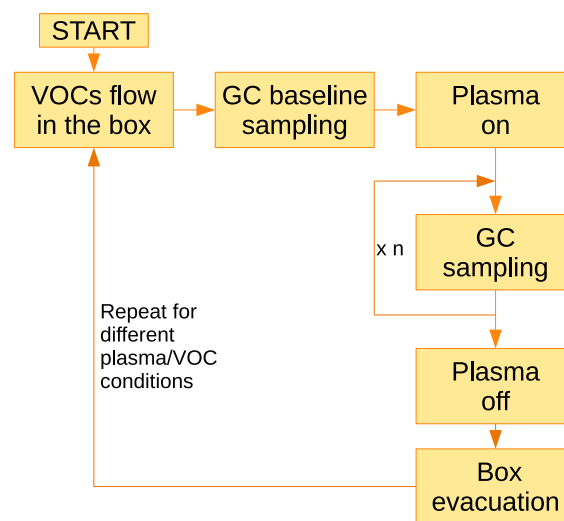


Fig. 4. Flow chart of the experimental process.

3. Experimental results

Plasma abatement of VOCs occurs by a series of oxidations, radical damages and electron impact reactions; the reaction path of VOC is very complex.

To analyze the depletion, VOC concentrations are determined as a function of the treatment time in static conditions for various plasma setups. The experimental campaign consists of three steps: first, the in-let and out-let valves are opened in order to allow the chosen VOC to flow through the reactor for at least 3 min. Second, the in-let and out-let valves are closed, then the GC samples the atmosphere in the reactor without plasma in order to measure the initial VOC concentration. In the third step, the plasma is turned on for the desired time, followed by a GC sampling of the treated gas. This step is repeated for the desired number of times at different times t . The flow chart of the experimental process is shown in Fig. 4.

To better understand the chemical dynamics of the VOC decomposition, the experimentally measured VOC concentration is normalized to the starting concentration as a function of treatment time and referring to the formula (Nguyen et al., 2018) in Eq. (1) a comparison of measurements has been performed:

$$\rho(t) = \rho(0) \exp\left(-\frac{t}{\tau}\right), \quad (1)$$

where $\rho(0)$ is the initial concentration and τ represents the characteristic time scale for dissociation, which is related to the decomposition mean lifetime, $t_{1/2}$, according to $t_{1/2} = \tau \log(2)$. In terms of normalized concentration $c(t) = \rho(t)/\rho(0)$, the Eq. (1) becomes

$$c(t) = \exp\left(-\frac{t}{\tau}\right). \quad (2)$$

Eq. (2) is used for fitting our experimental results.

3.1. Propane

The propane gas chromatograph calibration has been previously performed (Piferi and Riccardi, 2021). The propane concentration is

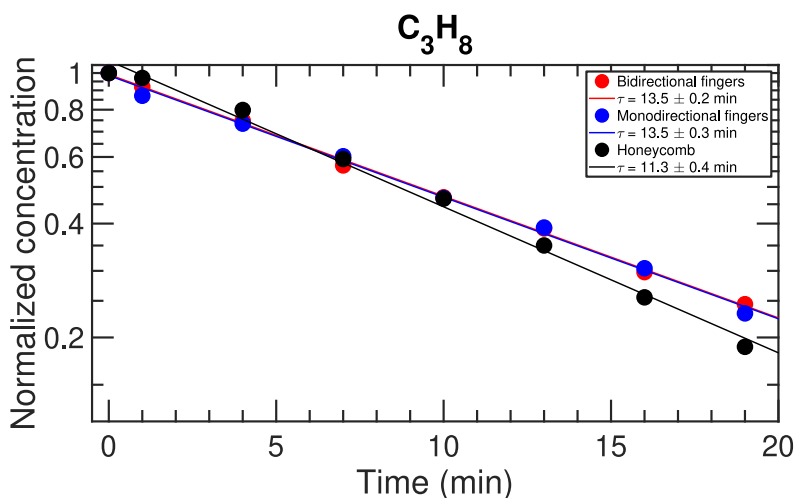


Fig. 5. Propane decomposition using different electrodes, starting concentration at about 5,000 ppm and plasma power at 14 W.

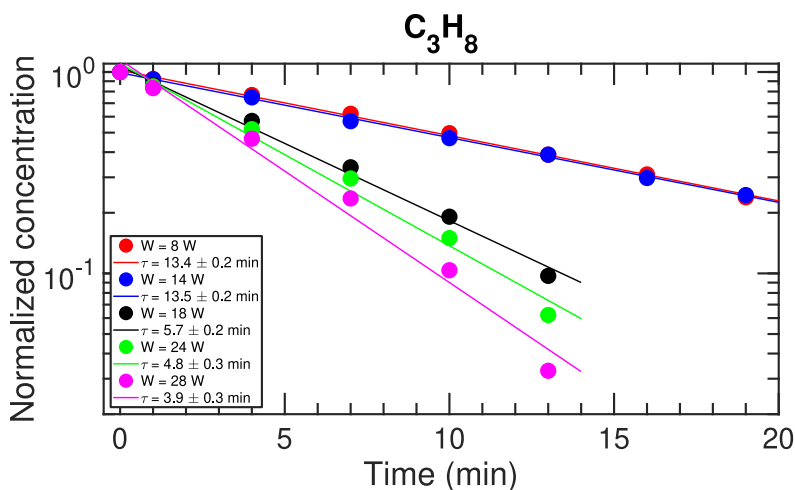


Fig. 6. Propane decomposition using bidirectional electrodes, starting concentration at about 5,000 ppm and different plasma power.

derived by Eq. (3)

$$\rho \text{ (ppm)} = 10^{\frac{A_{GC} - 8.65}{801}} \tag{3}$$

where A_{GC} is the gas chromatograph area and ρ the converted concentration in ppm.

The decomposition is measured in different conditions: different electrode configurations (Fig. 2), starting concentrations (of about 9,300, 5,000, 2,500, 1,200 ppm) and plasma powers (8, 14, 17.6, 24, 28 W).

For the different electrode configurations (Fig. 5) we worked at 5,000 ppm of starting propane concentration and 14 W plasma power. τ is almost the same for the bidirectional and the monodirectional fingers ($\tau = 13.5$ min), and it is a bit lower ($\tau = 11.3$ min) for the honeycomb one. While in the monodirectional and bidirectional geometrical conditions the gas flow is parallel to the surface, in the honeycomb geometrical configuration gas flow is perpendicular, favoring 1. a mixing of the gas species in the entire volume, 2. avoiding the adsorption of

the molecular species from the surface. This last occurrence favors the production of reactive oxygen at the DBD surface, necessary to oxidize the propane.

Increasing the plasma power (Fig. 6) above the threshold of 14 W the depletion rate increases. The number of reactive species able to promote the oxidation of the organic molecules increases with the energy supplied to the system.

In Fig. 7 is reported the efficiency after 10 min versus the applied plasma power. The efficiency is estimated as the ratio between the amount of decomposed propane in grams to the applied energy in kWh. The efficiency increases with power up to 18 W, then saturates at a value around 7.5 g/kWh. In comparison with respect to DBD abatement, these efficiency values are in the same range (Du et al., 2019).

An interesting depletion trend is found varying the propane starting concentration. For the different starting conditions reported in Fig. 8, τ is quite similar for the highest concentrations, that is 15 min for the initial propane concentration of 9,300 ppm and 13.5 min for 5,000 ppm. τ drastically decreases for lower starting concentrations and for

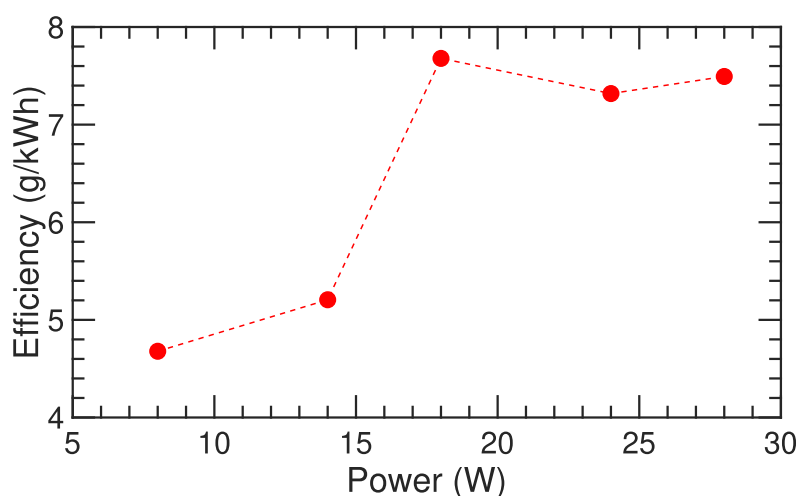


Fig. 7. Propane decomposition efficiency [g/kWh] after 10 min of plasma treatment as a function of the plasma power at starting concentration at about 5,000 ppm.

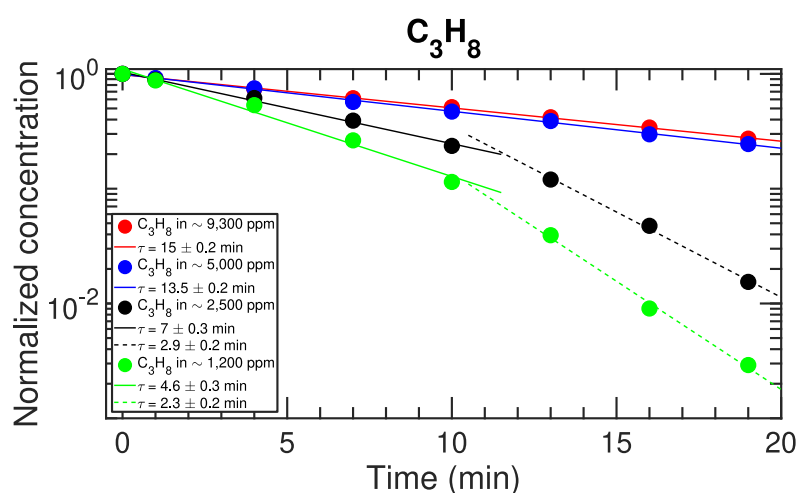


Fig. 8. Propane decomposition using bidirectional electrodes, different starting concentration and plasma power at 14 W.

concentrations lower than 2,500 ppm the depletion curves are also exploiting two different linear slopes. It turns to be out that plasma quickly dissociates propane at low concentrations.

Looking at the curves of Fig. 8, for concentrations below 250 ppm obtained during the plasma abatement, the depletion becomes faster and occurring in a time scale of the order of 2–3 min. At low VOC concentrations of the order of hundred of ppm, the faster depletion rates is ascribed to the larger availability of reactive species plasma produced per number of VOC molecules.

While the depletion is faster at low concentration, the efficiency increases with concentration. An explanation is that at high concentration collisions increase and the probability that propane molecules meet the plasma surface, where oxygen radicals are produced, is higher.

The efficiency of the plasma system after 10 min for the different starting concentration has been calculated. As can be seen in the Fig. 9 the SDBD processing is more efficient at high propane concentrations, for instance at 9,300 ppm a maximum efficiency of 5.5 g/kWh is obtained.

Measurement overlooking the TiO₂ catalyst (Bin et al., 2019) tile to the plasma at a distance at about 6 mm (Fig. 10) have been carried out. What we found is that the main decomposition is done by the plasma, and that the catalyst processing at high propane concentration is negligible (Shayegan et al., 2018).

3.2. Comparison between propane, pentane and acetone

Pentane (Fig. 11) and acetone (Fig. 12) at initial concentration of about 1,200 ppm gave similar depletion trends as a function of the plasma power: the depletion time τ decreases with power. Different depletion rates are found for the three different VOCs. The depletion rate for propane is faster than the pentane and acetone ones. The depletion rate of pentane is faster than the acetone ones. A comparison between the three VOCs is reported in Table 1.

The result is consistent with the magnitude of the binding energies of the molecules of each VOC in the oxidation processes (Chung et al., 2019).

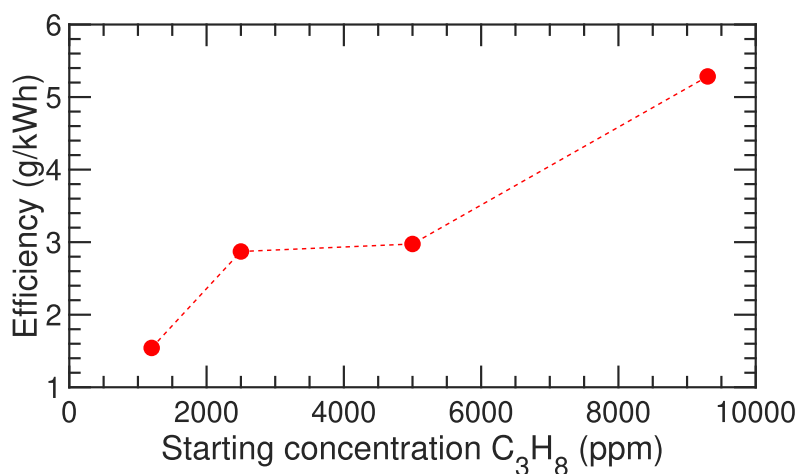


Fig. 9. Propane decomposition efficiency (g/kWh) after 10 min of plasma treatment as a function of the starting propane concentration.

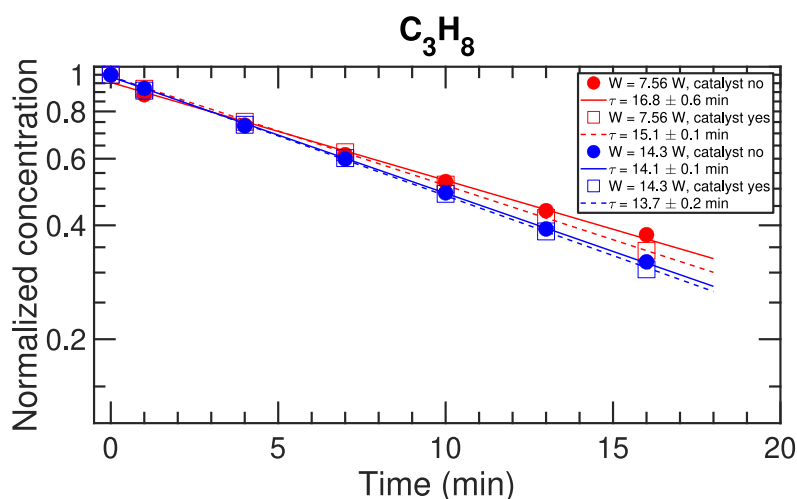


Fig. 10. Propane decomposition using bidirectional electrodes, starting concentration at about 5,000 ppm, different plasma power and catalyst.

4. Conclusions

A study of VOCs depletion using surface dielectric barrier discharges has been carried out. The advantage of the SDBD is to handle larger volumes with reduced power consumption than of the DBD ones. The analysis of the temporal evolution of propane provided in a wide range of VOC concentrations, between about 1,000 and 10,000 ppm, permitted to evaluate depletion time rates decreasing as a function of plasma power and concentration. The efficiency evaluated as quantity of propane per unit of energy takes values between 2 and 7.5 g/kWh and depends strongly on the propane concentration: is higher at the maximum concentration of 9,300 ppm. The plasma source works at competitive efficiency levels, similar to the DBD ones. A comparison between propane, pentane and acetone exploits larger depletion efficiency for propane. The abatement of acetone having highest chemical binding energies occurs slower and at lowest efficiency. In comparison with the DBDs processing SDBDs behaves at competitive efficiencies and are a promising source for VOC dissociation mainly at high concentrations. SDBD plasma could be used in synergy with other abatement

techniques, as a preliminary abatement stage, in order to reduce the VOC concentrations in the industrial gas steam. The simple geometry permits to compose SDBD modules in series to build an abatement reactor, as already recently proposed (Assadi et al., 2017).

Author contributions

Conceptualization, C.R. and C.P.; methodology, C.R. and C.P.; software, C.P.; validation, C.P.; formal analysis, C.P.; investigation, C.P.; resources, C.R.; data curation, C.P.; writing—original draft preparation, C.R. and C.P.; writing—review and editing, C.R. and C.P.; visualization, C.P.; supervision, C.R.; project administration, C.R.; funding acquisition, C.R. All authors have read and agreed to the published version of the manuscript.

Declaration of competing interest

The authors declare that they have no known competing financial interests or personal relationships that could have appeared to influence

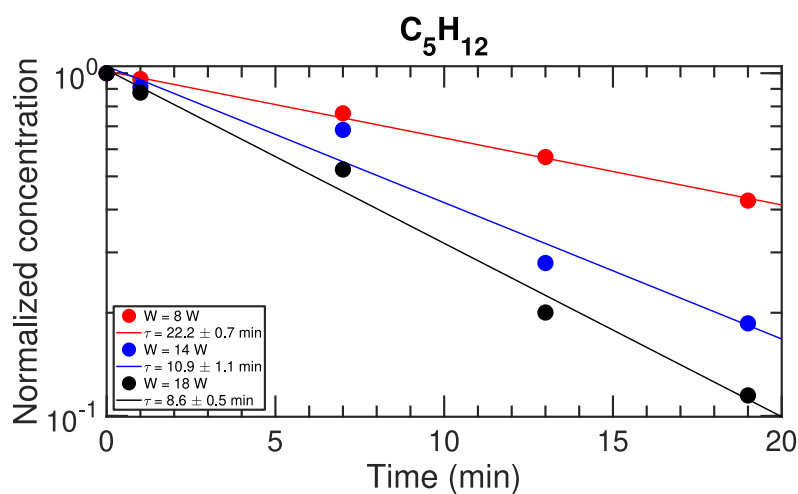


Fig. 11. Pentane decomposition using bidirectional electrodes and different plasma power.

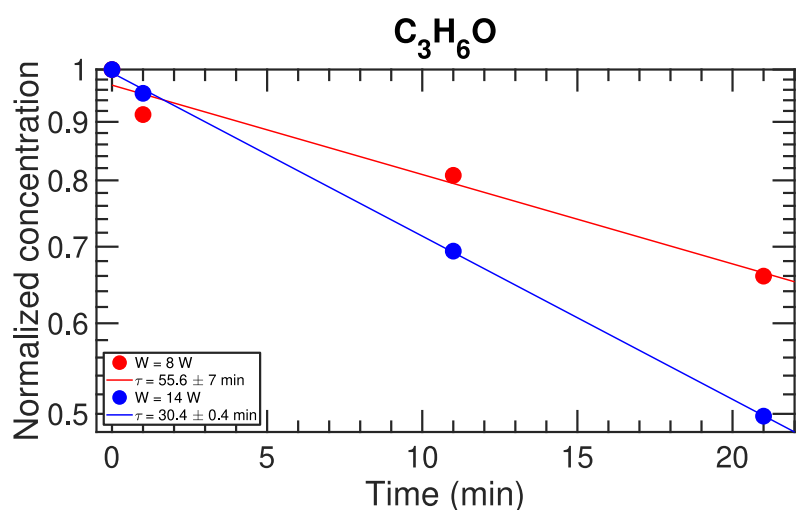


Fig. 12. Acetone decomposition using bidirectional electrodes and different plasma power.

Table 1

Comparison of the depletion time of the three studied VOC at plasma power of 14 W and starting concentration at about 1,200 ppm.

VOC	τ
Propane	4.6 ± 0.3 for $t < 10$ min, 2.3 ± 0.2 for $t > 10$ min
Pentane	10.9 ± 1.1
Acetone	30.4 ± 0.4

the work reported in this paper.

Acknowledgments

The author gratefully acknowledge the technical support of Alessandro Mietner and Alessandro Baù in the device development and experiment execution.

References

- Abdelaziz, A.A., Seto, T., Abdel-Salam, M., Otani, Y., 2012. Performance of a surface dielectric barrier discharge based reactor for destruction of naphthalene in an air stream. *J. Phys. Appl. Phys.* 45, 115201.
- Aguiayo-Villarreal, I., Montes-Morán, M., Hernández-Montoya, V., Bonilla-Petriciolet, A., Concheso, A., Rojas-Mayorga, C., González, J., 2017. Importance of iron oxides on the carbons surface vs the specific surface for VOC's adsorption. *Ecol. Eng.* 106, 400–408.
- Assadi, A.A., Bouzaza, A., Soutrel, I., Petit, P., Medimagh, K., Wolbert, D., 2017. A study of pollution removal in exhaust gases from animal quartering centers by combining photocatalysis with surface discharge plasma: from pilot to industrial scale. *Chem. Eng. Process: Process Intensif.* 111, 1–6.
- Assadi, A.A., Bouzaza, A., Wolbert, D., 2016. Comparative study between laboratory and large pilot scales for VOC's removal from gas streams in continuous flow surface discharge plasma. *Chem. Eng. Res. Des.* 106, 308–314.
- Barni, R., Benocci, R., Spinicchia, N., Roman, H.E., Riccardi, C., 2019. An experimental study of plasma cracking of methane using DBDs aimed at hydrogen production. *Plasma Chem. Plasma Process.* 39, 241–258.
- Barni, R., Esena, P., Riccardi, C., 2005. Chemical kinetics simulation for atmospheric pressure air plasmas in a streamer regime. *J. Appl. Phys.* 97, 073301.

- Belaïssouï, B., Le Moullec, Y., Favre, E., 2016. Energy efficiency of a hybrid membrane/condensation process for VOC (Volatile Organic Compounds) recovery from air: a generic approach. *Energy* 95, 291–302.
- Biganzoli, I., Barni, R., Gurioli, A., Pertile, R., Riccardi, C., 2014. Experimental investigation of Lissajous figure shapes in planar and surface dielectric barrier discharges. In: *Journal of Physics: Conference Series*. IOP Publishing., 012039
- Biganzoli, I., Barni, R., Riccardi, C., 2013. Note: on the use of Rogowski coils as current probes for atmospheric pressure dielectric barrier discharges. *Rev. Sci. Instrum.* 84, 016101.
- Bin, Z., Zhang, L., Yan, Y., Meng, L., Yimin, Z., 2019. Enhancing toluene removal in a plasma photocatalytic system through a black TiO₂ photocatalyst. *Plasma Sci. Technol.* 21, 115503.
- Bogaerts, A., Tu, X., Whitehead, J.C., Centi, G., Lefferts, L., Guaitella, O., Azzolina-Jury, F., Kim, H.H., Murphy, A.B., Schneider, W.F., et al., 2020. The 2020 plasma catalysis roadmap. *J. Phys. Appl. Phys.* 53, 443001.
- Brandenburg, R., 2017. Dielectric barrier discharges: progress on plasma sources and on the understanding of regimes and single filaments. *Plasma Sources Sci. Technol.* 26, 053001.
- Byeon, J.H., Park, J.H., Jo, Y.S., Yoon, K.Y., Hwang, J., 2010. Removal of gaseous toluene and submicron aerosol particles using a dielectric barrier discharge reactor. *J. Hazard Mater.* 175, 417–422.
- Chen, X., Carabineiro, S., Bastos, S., Tavares, P.B., Órfão, J., Pereira, M., Figueiredo, J.L., 2014. Catalytic oxidation of ethyl acetate on cerium-containing mixed oxides. *Appl. Catal. Gen.* 472, 101–112.
- Choi, S., Hong, S.H., Lee, H.S., Watanabe, T., 2012. A comparative study of air and nitrogen thermal plasmas for PFCs decomposition. *Chem. Eng. J.* 185, 193–200.
- Chung, W.C., Mei, D.H., Tu, X., Chang, M.B., 2019. Removal of VOCs from gas streams via plasma and catalysis. *Catal. Rev.* 61, 270–331.
- Dobslaw, C., Glocker, B., 2020. Plasma technology and its relevance in waste air and waste gas treatment. *Sustainability* 12, 8981.
- Dobslaw, D., Ortlinghaus, O., Dobslaw, C., 2018. A combined process of non-thermal plasma and a low-cost mineral adsorber for VOC removal and odor abatement in emissions of organic waste treatment plants. *J. Environ. Chem. Eng.* 6, 2281–2289.
- Donley, E., Lewandowski, D., 1998. Optimized Design and Operating Parameters for Minimizing Emissions during VOC Thermal Oxidation. *Metal Finishing. Guidebook-directory* 96.
- Du, C., Gong, X., Lin, Y., 2019. Decomposition of volatile organic compounds using corona discharge plasma technology. *J. Air Waste Manag. Assoc.* 69, 879–899.
- EEA, 2017. *Air Pollution. European Environment Agency*. URL: <https://www.eea.europa.eu/themes/air/intro>.
- Feng, X., Liu, H., He, C., Shen, Z., Wang, T., 2018. Synergistic effects and mechanism of a non-thermal plasma catalysis system in volatile organic compound removal: a review. *Catal. Sci. Technol.* 8, 936–954.
- George, A., Shen, B., Craven, M., Wang, Y., Kang, D., Wu, C., Tu, X., 2021. A Review of Non-Thermal Plasma Technology: a novel solution for CO₂ conversion and utilization. *Renew. Sustain. Energy Rev.* 135, 109702.
- Hill, S.L., Kim, H.H., Futamura, S., Whitehead, J.C., 2008. The destruction of atmospheric pressure propane and propene using a surface discharge plasma reactor. *J. Phys. Chem.* 112, 3953–3958.
- Li, S., Dang, X., Yu, X., Abbas, G., Zhang, Q., Cao, L., 2020. The application of dielectric barrier discharge non-thermal plasma in VOCs abatement: a review. *Chem. Eng. J.* 388, 124275.
- Nguyen, H.P., Park, M.J., Kim, S.B., Kim, H.J., Baik, L.J., Jo, Y.M., 2018. Effective dielectric barrier discharge reactor operation for decomposition of volatile organic compounds. *J. Clean. Prod.* 198, 1232–1238.
- Nguyen, H.P., Santos, C.A., Lee, T.J., Park, Y.K., Jo, Y.M., 2020. Decomposition of VOCs using serial surface dielectric barrier discharge reactors. *Environ. Technol.* 1–10.
- Piferi, C., Barni, R., Roman, H.E., Riccardi, C., 2021a. Current filaments in asymmetric surface dielectric barrier discharge. *Appl. Sci.* 11, 2079.
- Piferi, C., Brescia, A., Riccardi, C., 2021b. Intensity comparison between UV lamps and plasma emission for air purification studies. *AIP Adv.* 11, 085209.
- Piferi, C., Riccardi, C., 2021. High concentration propane depletion with photocatalysis. *AIP Adv.* 11, 125008.
- Shayegan, Z., Lee, C.S., Haghghat, F., 2018. TiO₂ photocatalyst for removal of volatile organic compounds in gas phase—A review. *Chem. Eng. J.* 334, 2408–2439.
- Siliprandi, R., Roman, H., Barni, R., Riccardi, C., 2008. Characterization of the streamer regime in dielectric barrier discharges. *J. Appl. Phys.* 104, 063309.
- Thévenet, F., Sivachandiran, L., Guaitella, O., Barakat, C., Rousseau, A., 2014. Plasma-catalyst coupling for volatile organic compound removal and indoor air treatment: a review. *J. Phys. Appl. Phys.* 47, 224011.
- Vandenbroucke, A.M., Morent, R., De Geyter, N., Leys, C., 2011. Non-thermal plasmas for non-catalytic and catalytic VOC abatement. *J. Hazard Mater.* 195, 30–54.
- Vergara-Fernández, A., Revah, S., Moreno-Casas, P., Scott, F., 2018. Biofiltration of volatile organic compounds using fungi and its conceptual and mathematical modeling. *Biotechnol. Adv.* 36, 1079–1093.
- Wang, W., Ma, X., Grimes, S., Cai, H., Zhang, M., 2017. Study on the absorbability, regeneration characteristics and thermal stability of ionic liquids for VOCs removal. *Chem. Eng. J.* 328, 353–359.
- Zanini, S., Citterio, A., Leonardi, G., Riccardi, C., 2018. Characterization of atmospheric pressure plasma treated wool/cashmere textiles: treatment in nitrogen. *Appl. Surf. Sci.* 427, 90–96.
- Zanini, S., Freti, S., Citterio, A., Riccardi, C., 2016. Characterization of hydro-and oleo-repellent pure cashmere and wool/nylon textiles obtained by atmospheric pressure plasma pre-treatment and coating with a fluorocarbon resin. *Surf. Coating Technol.* 292, 155–160.

A.6 Hydrophilicity and Hydrophobicity Control of Plasma-Treated Surfaces via Fractal Parameters

Reproduced from Piferi, C.; Bazaka, K.; D'Aversa, D. L.; Girolamo, R. D.; Rosa, C. D.; Roman, H. E.; Riccardi, C.; Levchenko, I. Hydrophilicity and Hydrophobicity Control of Plasma-Treated Surfaces via Fractal Parameters. *Advanced Materials Interfaces* 2021, 2100724, <https://doi.org/10.1002/admi.202100724>.



RESEARCH ARTICLE

**ADVANCED
MATERIALS
INTERFACES**
www.advmatinterfaces.de

Hydrophilicity and Hydrophobicity Control of Plasma-Treated Surfaces via Fractal Parameters

Cecilia Piferi, Kateryna Bazaka, Debora L. D'Aversa, Rocco Di Girolamo, Claudio De Rosa, H. Eduardo Roman, Claudia Riccardi,* and Igor Levchenko

It is still problematic to define a direct relationship between specific properties of a nanostructured surface (e.g., wettability) and its morphology. Not surprisingly, scientists continue to explore en masse the cut-and-try method. In this work, new insights are presented into the correlation of functional properties of the complex nanocomposites with their morphological characteristics. Using polyethylene-terephthalate (PET) as a model material due to its importance and wide use in experiments, super-hydrophilic nanocomposites amenable to be used in a variety of industrial applications are first developed, by exposing PET samples to oxygen plasma under controlled conditions. The morphology of the surfaces is confirmed using AFM and SEM techniques, and wettability in air and its oleophobic properties in water using contact angle and roll-off measurements. Next, different analytical tools such as Minkowski connectivity (Euler-Poincaré characteristic), Hough distributions and 2D FFT are applied to study ordering, connectivity, and fractal characteristics of the samples. It is concluded that fractal dimension, along with ordering and connectivity, are among the major characteristics of the nanocomposite that determine many important physical and chemical properties of the functional nanomaterials, and the fractal dimension could be a target morphological feature to inform the design of fabrication technology.

1. Introduction

Complex nanomaterials and nanocomposites based on hierarchical surface structures are currently under extensive investigation. This is because such materials can be applied in a very broad range of contexts,^[1–3] from sensors,^[4–6] photocatalysts,^[7] bio-electronic interface devices,^[8] water repelling and self-cleaning materials,^[9] various nanoelectronics devices^[10,11] to even space technology applications such as photon-active diamond films for space propulsion^[12,13] and nanostructured emitters for plasma propulsion systems^[14,15] that are critical for miniaturized space assets.^[16,17] It is not uncommon for the nanocomposites of this type to feature very complex surface, internal and interfacial structures that may in some instances form a fractal-like morphology.^[18,19] Our understanding of the physical and chemical processes that lead to the development of such morphologies during material fabrication remains somewhat limited, hindering our ability to tailor the morphologies to suit desired applications.^[20] In part, this is because the fabrication of such complex hierarchical structures relies on the use of sophisticated processes and complex environments such as, e.g., low-temperature plasma^[1] and in particular, the highly-reactive oxygen plasma.^[21] Here, by carefully balancing the fluxes of highly energetic ions and electrons, it is possible to introduce desired physical and/or chemical changes without affecting material bulk.^[22–26] Importantly, these changes may be induced across several length scales, opening up new applications as antibacterial coatings,^[27,28] in energy and environmental devices,^[29–31] as textiles, etc.,^[32,33] and enabling the creation of intricate nano-structured surfaces that mimic those created by Nature to meet its needs.^[34] Creation of such surfaces remains a technological challenge, even in plasmas where a large number of competitive processes make careful control of the many different parameters challenging. Furthermore, at larger length scales the study of the interplay between micro- and macro-meter properties are still one of the most important issues both in applied as well as in basic sciences.^[35,36]

Because of its strong potential and versatility, plasma-enabled synthesis, assembly and modification of materials at the nanoscale constitute one of the fastest growing fields both in

C. Piferi, D. L. D'Aversa, H. E. Roman, C. Riccardi
Department of Physics
University of Milano-Bicocca
Piazza della Scienza 3, Milano 20126, Italy
E-mail: claudia.riccardi@unimib.it

K. Bazaka
School of Engineering
The Australian National University
Canberra, ACT 2601, Australia

K. Bazaka, I. Levchenko
Plasma Sources and Application Centre NIE
Nanyang Technological University
Singapore 637616, Singapore

K. Bazaka
School of Mechanical, Medical and Process Engineering
Faculty of Engineering
Queensland University of Technology Brisbane
Queensland 4000, Australia

R. Di Girolamo, C. De Rosa
Department of Chemical Sciences
University of Napoli Feder Sant'Angelo
Via Cintia, Napoli 80126, Italy

The ORCID identification number(s) for the author(s) of this article can be found under <https://doi.org/10.1002/admi.202100724>.

DOI: 10.1002/admi.202100724

basic materials science research as well as in technology and engineering applications. The resulting nanostructured surfaces can be specifically designed to possess new characteristic properties not achievable with more traditional methods, such as extreme hydrophilic properties.^[37] Despite having very small dimensions, the newly created surface nanostructures introduce desirable variations in macroscopic functional properties without altering the intrinsic bulk properties of the material. These nanostructures often take form of nanorods, nanowires, and nanotubes, with chemical vapor deposition (CVD) and its more advanced variations, e.g., Plasma Assisted Supersonic Jet Deposition (PA-SJD), frequently used to produce such thin nanostructured films.^[38–40]

- The primary aim of our study is to gain a deeper insight into the interplay of several surface morphology descriptors such as ordering, connectivity, self-affinity and fractality of the plasma treated surfaces to discover how these characteristics influence the ultimate wettability and thus contribute to the development of another powerful tool for the future progress in the fabrication of PET-based and other functional nanomaterial-based devices.

We used polyethylene-terephthalate (PET) as a model material and oxygen plasma as a treatment environment due to their importance and wide use in both fundamental studies and industrial applications. PET is one of the most common thermoplastic polymer resins of the polyester family. It is mainly used in containers for liquids and foods, thermo-forming for manufacturing, fibers for clothing, and in combination with glass fiber for engineering resins. In its natural state, PET is a colorless, semi-crystalline resin, and a good insulating material with very low ionic conductivity.

The PET samples were treated with a radiofrequency (RF) air plasma under different operating conditions, with the aim of permanently increasing their hydrophilicity. Indeed, the chemical structure of polyesters results in the presence of a low surface free energy and poor wettability, mainly due to its lack of polar groups such as $-\text{COOH}$ and $-\text{OH}$. These polar groups may be introduced on the polymer surface by cold plasma treatments employing either oxygenated or inert gases. Their introduction, however, is always accompanied by etching and

by surface cross-linking, that may affect the durability of the plasma-imparted surface modifications. The changes in surface chemical composition and topography, as well as aging phenomena, of plasma-treated specimens were examined under different conditions. These investigations yield valuable information on the processes undergone by the treated polymer surfaces, in particular the interplay between surface morphology of treated PET surfaces and the associated wettability properties, such as contact angle of hydrophilic films in air, and oleophobic properties in water.

The paper is organized as follows. In Section 2 we describe the experimental setup. In Section 3 we describe the results of the plasma treatment and characterize their morphological properties, presenting the quantitative analysis of the atomic force microscopy (AFM) and scanning electron microscopy (SEM) images as a function of duration of plasma treatment. In Section 4 we discuss the results on wettability determined by contact and roll-off angle measurements. In Section 5 we present the detailed analysis of the morphological characteristics of the produced samples to elate their fractal dimensions, connectivity and ordering with the physical parameters. Finally, in Section 6 we present our concluding remarks.

2. Experimental Setup

The vacuum chamber was designed by the Plasma Prometeo Center of the University of Milano Bicocca and commissioned to a MORI MECCANICA mechanical workshop (Parma Italy). The system consists of a cylinder and two closures, equipped with vacuum feed-throughs for RF power supply, vacuum sensors, gas dispenser, opening for pumping systems, and inspection window made of quartz. The capacitive antenna was designed and built by the mechanical workshop at the University of Milano Bicocca. It is made up of two parallel aluminum plates of diameter 190 mm. The distance between the plates can be varied between 3 and 20 cm, and in our experiment it was fixed at 8 cm. The oxygen gas was uniformly distributed in the reactor by the upper shower-head electrode with pinholes of 2 mm diameter (Figure 1c). This electrode was connected to a 13.56 MHz RF power supplier (Advanced Energy RFX-600)

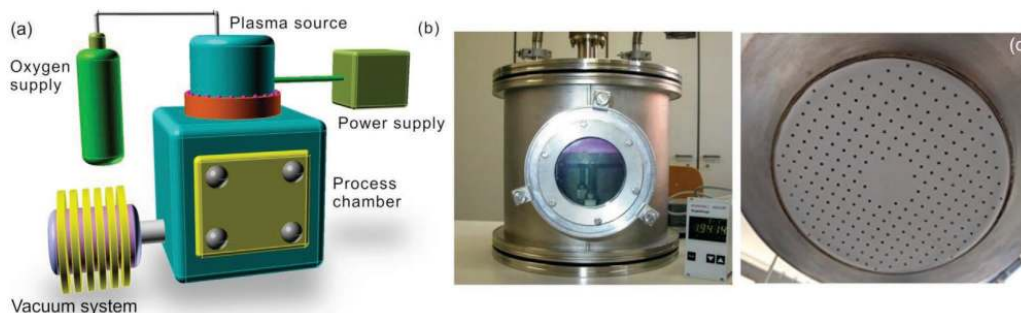


Figure 1. a) General schematics of the experimental setup, b) photograph of the process chamber with ignited plasma and of the upper aluminum plate (upper electrode) with about c) 250 holes of 2 mm diameter spaced at a distance of 10 mm. Discharge was ignited by the capacitively coupled planar electrodes at 13.56 MHz RF power. The lower electrode was grounded and used as a sample holder.

which provided an RF voltage to the grounded chamber. The second plate, where the samples are mounted, was connected to ground. The maximum working power is 500 W.

At one cap, the chamber was connected to the pumping system, which allowed to evacuate the reactor up to a residual pressure lower than 10^{-6} mbar. After evacuation, the vacuum chamber was filled with oxygen and pressure was kept constant inside the reactor (at a level ranging between 0.05 and 10 mbar, monitored by a Pirani gauge), acting on a leakage valve mounted on the cap opposite to that connected to the pumps. Under such operating conditions, the pumping system sustained a flow rate of about 25 sccm, corresponding to a residence time in the plasma of about 0.2 s with a flow velocity of about 50 cm s^{-1} at a pressure of 0.1 mbar. The total gas flow into the chamber is regulated by micrometric needle valves and their partial pressures are monitored using three capacitance pressure gauges and a full range vacuum gauge, which couples a Pirani and a cold cathode system. Before every discharge operation the reactor was evacuated to 10^{-6} mbar. During the plasma treatment, the chamber was evacuated only by means of the rotary pump, protected with a liquid nitrogen trap.

We used two different PET samples: PET film (36 m in height) and PET tissue (31 m in diameter, 165 wire per cm in density, 30 m of mesh opening and 24% of empty surface). The thermo-fixed PET fabric used in this work was washed for 10 min at 40 °C with a water solution containing 0.5 wt% of an anionic detergent, thoroughly rinsed up to total removal of this latter and dried. Treated and untreated specimens ($6.0 \times 6.0 \text{ cm}$) were usually stored at $(20 \pm 2) \text{ }^\circ\text{C}$ and $(65 \pm 2)\%$ relative humidity (conditioned atmosphere). The samples (6 cm^2 in area and 36 m in height) are attached to the ground electrode with two little pieces of adhesive tape.

The working conditions are: 4.5 sccm O_2 flow, 0.09 mbar pressure, 150 W power and 13.56 MHz radiofrequency. We considered different treatment times (we use T to denote the treatment time, not to be confused with temperature): $T = (0, 2, 5, 10, 15, 20, \text{ and } 30) \text{ min}$. For the analysis of morphological properties we used AFM Solver P47-PRO (NT-MDT, Moscow, Russia), and for the wettability properties we measured the contact angle using the DataPhysics OCA 20 (Dataphysics) instrument (Figure S1, Supporting Information).

The choice of the feedstock gas was dictated by the capability of producing reactive species in the plasma phase that could act as precursors of the hydrophilic groups to be implanted on the polymer surface. Oxygenated gases were thus preferred to inert gases. The prevailing actions of inert gases are expected to be etching and cross-linking of polymer surfaces, besides creating radical species able to combine with atmospheric oxygen, thus indirectly introducing polar groups on the polymer surface.^[41] In particular, oxygen plasma was employed in the present work, as it was proved to be efficient in inducing a permanent hydrophilic modification to the PET fibers. The species prevailing in such plasma under different plasma treatment conditions were identified through a plasma diagnostics and simulation of the gas phase composition. The efficacy of oxygen plasma treatment in inducing more or less stable wettability of PET fibers was investigated by varying the radiofrequency power of the reactor, WRF, the pressure, the time of treatment, T , the position of the treated sample downstream from the emitting

antenna and the sample holder polarization. The results of such investigation provide the best plasma stability configuration, in the chosen reactor geometry, which corresponds to the values: 4.5 sccm O_2 flow, 0.09 mbar pressure, and RF of 150 W transmitted power.

Excellent durability of wettability properties was achieved by using a relatively higher RF power (up to 300 W) providing a basis for achieving good hydrophilicity immediately after the plasma treatment, although this did not assure enough stability of the treated surface. According to our plasma diagnostics studies, surface etching or cross-linking phenomena should efficiently compete with the implantation of hydrophilic groups, especially when operating at higher pressures (up to 1 mbar). Indeed, etching and cross-linking have relevant roles in stabilizing plasma-induced modifications of treated polymer surfaces.^[39] We found that the closer the samples were to the treatment antenna, the longer they maintained their high hydrophilicity. Moreover, PET samples, positioned on the grounded electrode, were treated at 8 cm away from the upper electrode.

Previous studies on the effect of the negative polarization of the fabric specimen during plasma treatment, and the resulting increase of positive ion flux on its surface, point to a large weight loss during the treatment (etching) and to thermal effects due to the higher temperature in the vicinity of the upper electrode (up to 70 °C). In contrast, a positive polarization of the sample holder did not produce any increase of PET wettability, with respect to samples that were treated without polarization, indicating that negatively charged species (mainly negative species O^- and electrons) play minor roles in etching and the grafting of polar groups on the polymer surface.

3. Morphological Properties

3.1. AFM and SEM Measurements

AFM and SEM measurements were made to reveal and study the μm -scale and nanoscale morphologies of the untreated and plasma-treated samples. Figures 2 and 3 show the planar images of AFM and SEM characterizations, along with the 3D reconstruction of the surfaces.

The field emission scanning electron microscope (FE-SEM, FEI Nova NanoSEM450) was used to study the morphology of the synthesized nanostructures, as well as the surfaces of the non-treated and treated PET (Figure 3). Before SEM analysis, the samples were coated with a thin (5–7 nm) layer of gold-palladium alloy to ensure electrical conductance, and then the images were acquired at an accelerating voltage of 5 kV by collecting secondary electrons (SE) with Everhart-Thornley detector (ETD) or through-the-lens detector (TLD).

A Solver P47-PRO NT-MDT AFM was used to analyze surface morphology by AFM technology in semi-contact (tapping) mode in air, using High Accuracy Non-Contact (HANC) silicon tips of Etalon NT-MDT and NSG01 series, typical spring constant $(5.8 \pm 1.2) \text{ N m}^{-1}$ and resonance frequency of $(200 \pm 20) \text{ kHz}$. The tip curvature radius was less than 10 nm. Square images were collected at a typical frequency of 1.5 Hz, with a resolution of 256 pixels per line. The scanned areas were $10 \times 10 \text{ }\mu\text{m}$ for each sample, and the surface roughness

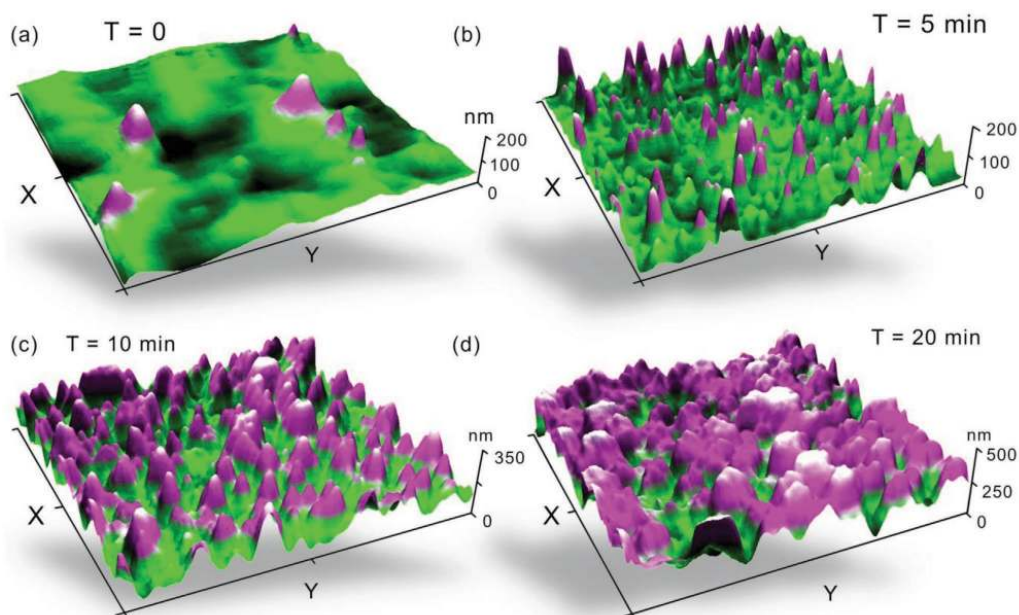
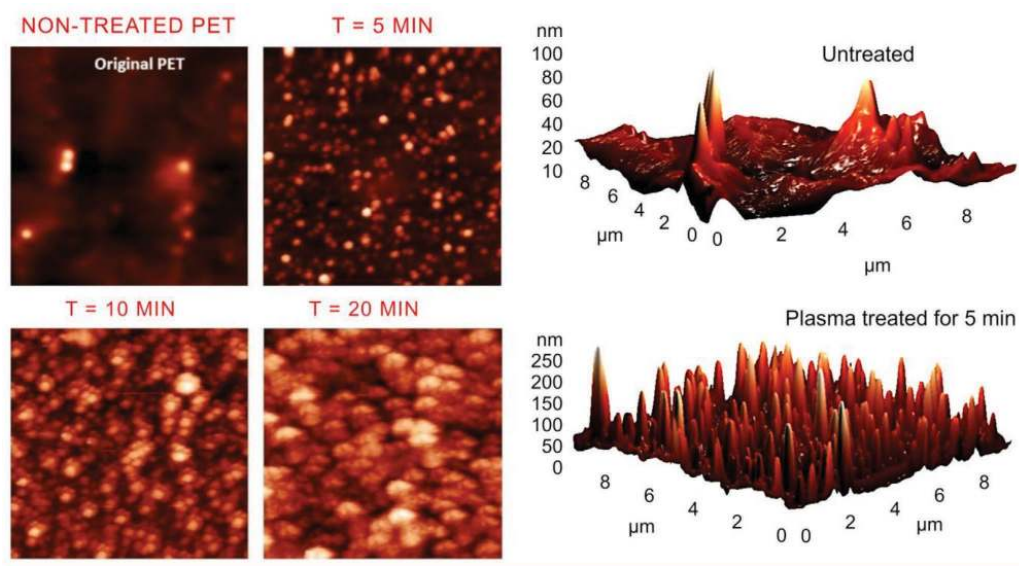


Figure 2. Evolution of nanometer-scale topography of PET surfaces with treatment time. Top panel: planar AFM images for non-treated PET and treated for 5, 10, and 20 min, and typical 3D images for untreated and plasma-treated surfaces. The data is given in the form of a (256×256) pixel matrix from which we obtain the heights and different moments in arbitrary units. Then, we scale the values using the standard deviation $\sigma(T)$. Bottom panel: 3D representation of AFM data for a) the untreated surface ($T = 0$) and b–d) surfaces treated with plasma for 5, 10, and 20 min. Note the difference in height profile for samples (maximum peaks height of $\approx 200, 200, 350, 500$ nm), respectively.

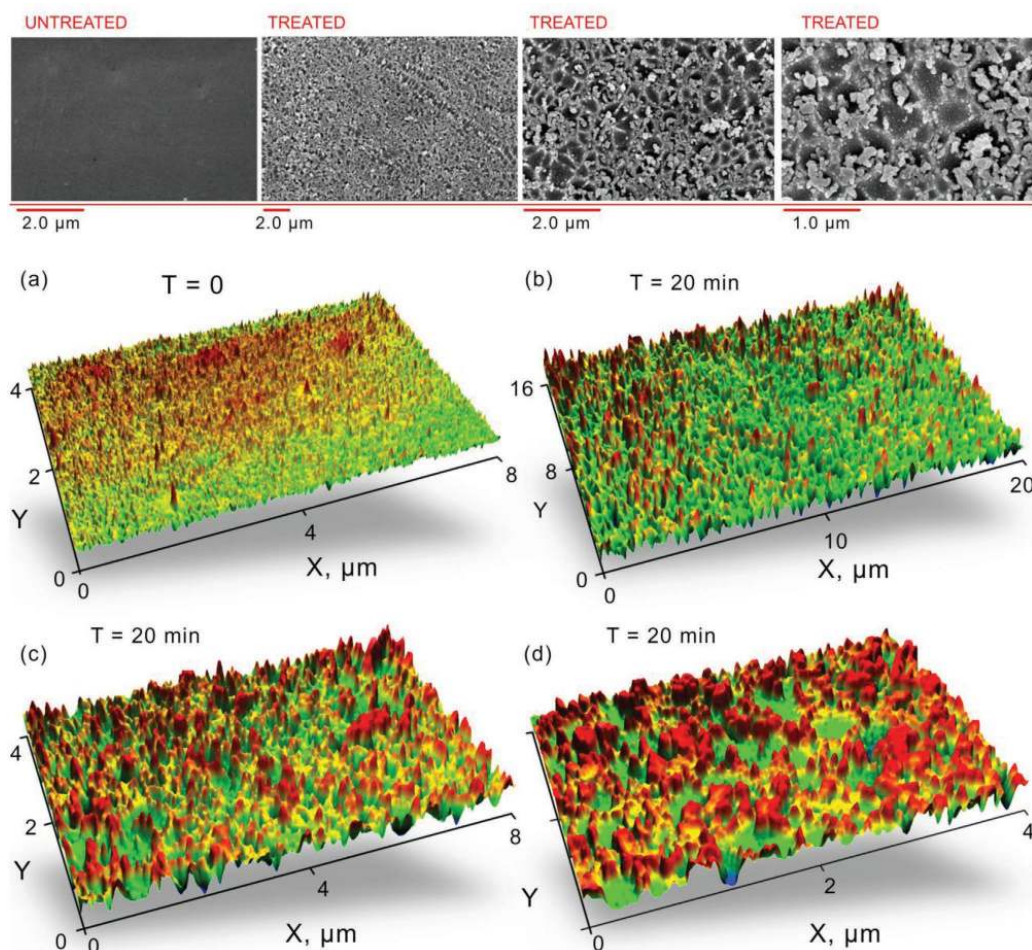


Figure 3. Micrometer-scale topography of the treated and untreated samples. Top panel: SEM images for the non-treated PET (left) and treated for 20 min at different scales. Bottom panel: 3D representation of SEM data for a) the untreated surface ($T=0$) and b–d) plasma-treated for 5, 10, and 20 min. Very complex, developed surfaces can be noticed in the processed samples. Along with the sole-standing peaks, contacting structures also present, thus forming the fractal-like topography (see quantitative assessments of the fractality, connectivity and other parameters in Figures 6, 7, and 8 below).

increased with the treatment time T , as one can see from the 3D images shown in Figure 2, upper panel. AFM analysis performed on PET samples treated under the same conditions showed reproducible data with the same dependence of the nanostructure density on plasma exposure times. Moreover, Figures S4 and S5 (Supporting Information) show AFM images obtained on larger areas of $10 \times 10 \text{ m}$ $30 \times 30 \text{ m}$ of the same samples exposed to plasma for various lengths of time. The presence of the grains affected the height scale which is higher than that of the figure (c) related. These images confirm that exposure of surfaces to the effects of plasma for longer lead to progressively more significant changes in the sample morphology.

SEM microscopy was also used to study the samples surface morphology at the micrometer scale. Thanks to these imaging it was possible to obtain a better understanding of the morphological modification process induced by the interaction of the polymer surface with the cold oxygen plasma. Here, we report the analysis on the most exemplary samples focusing our attention on the non-treated and 20 min treated samples. The SEM scans, shown in Figure 3, confirm the increase in roughness toward the nanoscale observed with the AFM measurements. The original (non-treated) film is very smooth, unlike the 20 min treated sample, displaying micro- and nano-meter structures clearly seen in Figure 3a–d. In particular, the planar images in Figure 3 show the presence of both nano- and micro-metric

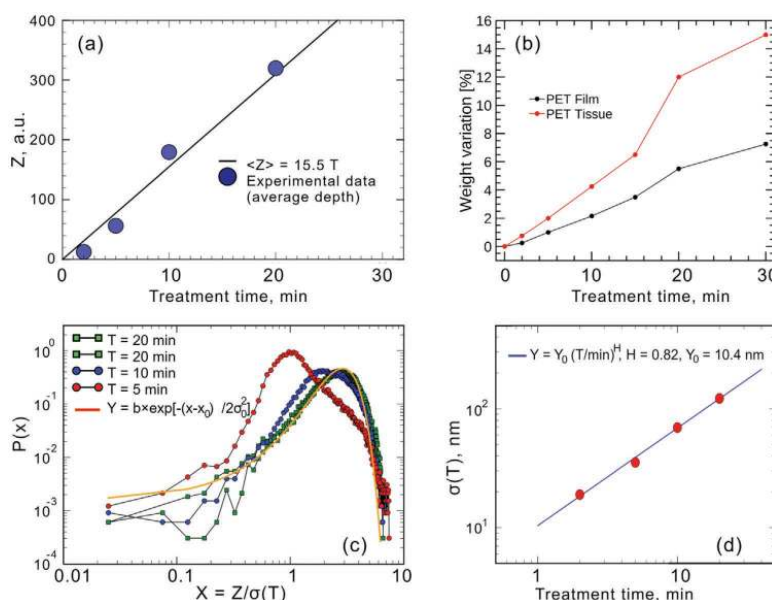


Figure 4. a) Mean etched depths $\langle z \rangle$ versus treatment time T . Shown is a linear fit: $\langle z \rangle = bT$, with $b = 15.5 \text{ min}^{-1}$. b) Weight variation of the treated samples as a function of treatment time T . The relative missing mass variation of treated surfaces ($T > 0$) with respect to the untreated one ($T = 0$) is calculated as $\Delta W(T) = [W(0) - W(T)]/W(0)$, where $W(T)$ is the weight of the treated film and $W(0)$ the one of the untreated sample. The treated surfaces are carefully cleaned (washed) to remove the etched material before the measurement is performed. The weight W is measured with an accuracy of 0.1 mg. c) Probability distribution functions of normalized heights, $x = z/\sigma(T)$, for the three times. For $T = 20 \text{ min}$ two distributions obtained from two different PET samples are displayed. The continuous yellow line represents a normal distribution fit to the empirical data with parameters. d) Standard deviations of etched film heights from the 2D AFM images. The continuous line represents a fit with a power law dependence indicated in the inset. The exponent is denoted as the Hurst exponent.

structures. Here, it is possible to see how the plasma etching creates craters and troughs, but also new micro- and nanostructures. The latter are due to the clustering of polymer chains, deposited on the surface and having lower molecular weight than the original PET sample, which were previously broken during the interaction with the oxygen plasma.

To check the reproducibility of our results, we have made additional experiments to produce and characterize PET samples to demonstrate the good reproducibility of our technique, and added the relevant information to the Supporting Information. Several PET substrates were plasma treated in plasma oxygen under similar conditions (RF power, substrate distance from the upper plate, oxygen flux, residual pressure, time exposures). Figures S6 and S7 (Supporting Information) show the AFM analysis of a series of PET samples treated with plasma for different times of 0, 5, 10, 15, 20, and 30 min, with similar plasma working parameters to the previous samples. These results demonstrated essentially the same trend as described above.

We can estimate the roughness of the resulting thin etched films by determining the standard deviations of the surface heights, $\sigma(T)$. We found that $\sigma(T)$ increases with the treatment time until about (15–20) min, and saturates afterward. There is another aspect related to these images, and that is the property of “self-similarity”, or scale invariance.^[42] This means that the structure looks the “same” (statistically speaking) when studied

at different length scales. Quantitatively, scale invariance is represented by a power-law behavior of the quantity of interest (in our case surface rigidity) as a function of length scales. Scale invariance can be also defined in the temporal domain, as we will discuss below. Therefore, according to the AFM results in Figure 2, we expect a type of power law behavior of spatial surface fluctuations (roughness) as a function of treatment time T . Figure 2a–c shows the 3D representation of AFM data for the untreated surface ($T = 0$) and plasma-treated for 5, 10, and 20 min.

To calculate $\sigma(T)$, we consider 2D images as illustrated in Figure 2. Each image consists of a 256×256 pixels matrix, in which the light intensity is proportional to local height z . Thus the spatial resolution is about 40 nm. The results for $\sigma(T)$ shown in Figure 4a indeed suggest a power-law behavior of height fluctuations as a function of treatment time, $\sigma(T) = \alpha T^H$, where H is denoted as the Hurst exponent.^[40] We find a relatively strong persistence with an exponent $H = 0.82$. This indicates a sort of self-similar fluctuations which can be interpreted in terms of an effective fractal dimension, $d_F = 3 - H = 2.2$, of the etched surface.^[40]

Another important macroscopic property of the sample is its total weight. We found that the weight of a treated sample is lower than the original one, and the variation can become as large as 7% for PET films, and 15% for PET tissues (Figure 4b). The percentage of missing mass of the treated samples is due

to the etching process produced by the cold oxygen plasma, which increases as a function of treatment time. The plasma treatment breaks polymer chains, removing part of them probably belonging to the amorphous phase of the polymer.^[43]

We have calculated the probability distribution function $P(x)$ of the scaled heights $x = z/\sigma(T)$, for different treatment times. The results are shown in Figure 4c, suggesting that the distribution depends on T , as displayed by the changes in shape in going from $T = 5$ min to longer $T = 10$ min. A truly scale invariant regime is characterized by a single distribution though. Thus, we need to look at longer times, i.e., for $T > 10$ min the probability distribution function $P(x)$ tends to achieve a single shape, in this case a normal distribution. This suggests that fluctuations are equally distributed in space. A more accurate analysis of surface fluctuations can be performed using wavelet transforms as already done in the context of plasma devices.^[44] Such an analysis goes beyond the scope of the present work and will be discussed elsewhere. Finally, we report calculations of the mean etched depths $\langle z \rangle$ as a function of treatment time T . These results will be used in Section 4.2 regarding the estimation of the roll-off angles for oleophobic surfaces under water.

This study suggests, therefore, that the competition between plasma breaking and removal of polymer chains, followed by a clustering and deposition of the ablated polymer chains, gives rise to the morphological characteristics discussed above. The behavior of macroscopic quantities of treated surfaces reveals different competitive processes. The oxygen plasma etches the polymer surface breaking polymer chains, while removing material with a resulting consistent loss of mass. At the early stages of treatment (short treatment times), small structures (of about 100 nm in size) are created representing the incipient new features in the treated surface morphology. These structures grow as a function of the treatment time, probably due to a cluster deposition of the etched polymer fragments on the surface itself. The competition between fragmentation/etching and deposition seems to be balanced around 20 min of treatment, as suggested by the saturation of surface roughness and the achievement of a stable probability distribution function of height fluctuations. The latter is found to be consistent with a normal distribution.

4. Wettability

Wettability is a macroscopic property of a material, representing its ability to maintain a liquid in contact with its surface. We investigate two different aspects of wettability of the treated PET surfaces: Its hydrophilic properties in air, and its oleophobic characteristics in water. We use a DataPhysics OCA 20 optical device for measuring contact angles, both in air and in water, and roll-off angle measurements for determining surface oleophobic properties in water. The contact angle is the angle between the liquid-vapor interface of a droplet and the solid surface. Hydrophobic surfaces have large contact angles ($>90^\circ$), while hydrophilic ones have small angles ($<90^\circ$). The roll-off angle is the inclination angle of the sample surface just before the droplet starts to slide off. An oleophobic surface has small roll-off angles, while an oleophilic one displays large roll-off angles. The analysis device

consists of a tiltable sample holder, a syringe, a lamp, a camera and a software for the images acquisition. To study hydrophilic properties in air, we measured the contact angle of a deionized water droplet over the sample. Regarding oleophobic properties in water, we determine the roll-off angle of a droplet, constituted by a nonpolar substance such as α -bromo naphthalene, placed over the sample and fully immersed in water.

The measurement procedures were as follows (please find the detailed description in the Supporting Information). By means of a graduated syringe and a dosing system equipped with micrometers, a known quantity of liquid was deposited onto the surface. The image of the drop in the shape of a spherical cap that forms when liquid comes into contact with the surface is enlarged with a microscope and imaged by a camera. Control knobs allow to adjust the positions of the sample, syringe, and camera. The image is then processed by instrument software. The quality of the image is optimized by adjusting the zoom, focus and intensity of the light source. In this particular study, drops of deionized water with a volume of 3 μ L were used and all the angles obtained were determined by averaging 5 or 6 values evaluated at different points for each sample.

To study oleophobicity under water, the roll-off angles of drops of an apolar substance were measured. For this test, 10 μ L drops of α -bromine naphthalene were used. The angles were then measured using the Data-Physics OCA 20 optical device. For this analysis, however, a tilting plate (equipped with a goniometer) was used on which a small glass case was placed. This is filled with water and the treated samples are immersed in it, fixed on a metal support a drop of 10 μ L of α -bromine naphthalene is deposited onto the surface of samples.

In the following, we present results for PET films and for PET tissues, the latter are made of mono-filaments of PET building an ordered net-like structure.

4.1. Contact Angles

We find that the contact angle decreases when the treatment time increases and therefore there is an increase in hydrophilic properties (Figure 5a).

According to Young equation, the contact angle θ_c between a fluid (L) and a solid (S) interface, in the presence of a surrounding gas phase (G), obeys:

$$\cos \theta_c = \frac{\gamma_{SG} - \gamma_{SL}}{\gamma_{LG}} = \frac{1 - \gamma_{SL} / \gamma_{SG}}{\gamma_{LG} / \gamma_{SG}} \quad (1)$$

where γ_{ij} is the interfacial energy (surface tension) between phases i and j . Considering that the surface tensions with the gas phase do not change during the plasma treatment, we can define the constant A as follows:

$$A = \frac{\gamma_{SG}}{\gamma_{LG}} \quad (2)$$

which is independent of treatment time T . The interfacial energy γ_{SL} will depend on T due to changes in the morphology of the treated surface. We are interested in a fractal regime in which the nanostructure obeys the kind of (self-affine) scaling

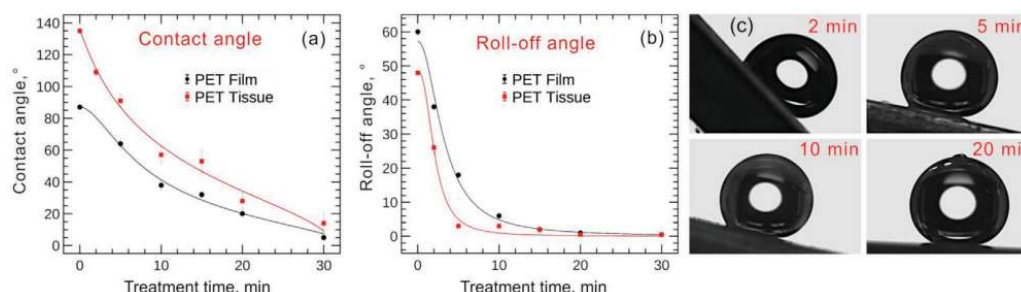


Figure 5. a) Contact angle of a water droplet over the treated surfaces as a function of treatment time T , min. The values of parameters are: for PET film $-H = 0.82$ (Figure 4d), $d_f = 3-H = 2.18$, and the three fit values are $A = 1.05$, $B = 0.95$ and $T_0 = 6.18$ min; for tissue using $A(1-B) = \cos(135^\circ)$, $d_f = 3-H$, the three fit values are $A = 1.34$, $T_0 = 7.88$ min, and $H = 0.46$, from which one can find $B = 1.53$ and $d_f = 2.54$. b) Roll-off angle versus treatment time T , min. From (a) we take the same values of d_f , and the resulting two fit parameters are: for Film $A = 0.84$ and $T_0 = 3.65$ min; for tissue $A = 0.75$ and $T_0 = 2.25$ min. c) Photos of the roll-off of an α -bromo naphthalene droplets in water over treated surfaces.

as obtained in the experiments (Figure 4d). We denote the ratio $R(T) = \gamma_{SL}/\gamma_{SG}$ and assume the behaviour:

$$R(T) = \frac{B}{1 + (\sigma(T)/\sigma_0)^{d_f}} \quad (3)$$

where $B = \gamma_{SL}/\gamma_{SG}$ is evaluated at $T = 0$. The interfacial energies ratio $R(T)$ decreases as the surface roughness of the treated film increases, as found experimentally. Therefore, we have $R(0) = B$ and for $R(T) = B/S_{eff}(T)$ for $T > T_0$, where $S_{eff}(T) = \sigma(T)^{d_f}$ is the effective surface that the fluid sees at the interface with the substrate, and T_0 is a characteristic time for the treatment process. In other words, larger roughness implies a larger effective surface at the fluid-solid interface. Equation (3) describes a purely geometric effect due to the fractal geometry at the nanoscale. Combining (1), (2), (3) we find:

$$\cos \theta_c = A(1 - R(T)) = A \left(1 - \frac{B}{1 + (T/T_0)^{d_f}} \right) \quad (4)$$

where we have used $\sigma(T)/\sigma_0 = (T/T_0)^{d_f}$, according to the results in Figure 4d. We actually have three fitting parameters in Equation (4), i.e., A , B and T_0 , since $H = 0.82$ and $d_f = 3 - H = 2.18$ are given. The results shown in Figure 5a suggest that Equation (4) describes the experimental findings very accurately. The behavior described by Equation (4), that is increasing hydrophilicity with increasing surface roughness, resembles a type of Wenzel regime, rather than a Cassie-Baxter one (see, e.g., refs. [45,46]).

To be noted is that, in the case of the PET tissues (Figure 5a), the fit is performed using the condition: $A(1 - B) = -0.707$ for $T = 0$, corresponding to an angle $\theta_c = 135^\circ$. In this case, since we do not have morphological information about the treated tissues, H is taken as a new parameter, while $d_f = 3 - H$. Altogether, there are three unknown parameters A , T_0 and H , yielding a fit also in very good agreement with the experiments.

To understand the behavior of the contact angle in our model, we relate it to the Cassie-Baxter expression for the contact angle between a liquid drop and a solid surface made of

two components (see Supporting Information). To this end, Equation (4) can be expressed in the form:

$$\cos \theta_c = A \left(1 - \frac{B}{1 + (\sigma(T)/\sigma_0)^{d_f}} \right) \quad (5)$$

Considering the low roughness limit, i.e., $\sigma(T) \ll \sigma(0)$, which corresponds to $T \ll T_0$ in Equation (4), the latter can be expressed as,

$$\cos \theta_c \approx A(1 - B) + AB(\sigma(T)/\sigma_0)^{d_f} \quad (6)$$

which coincides with the Fractal-Wenzel (see SI) result when: $A(1 - B) = \cos \Theta_1$ and $AB = a \cos \Theta_1$. Indeed, we find (see Figure 5a), $A \approx 1.05$ and $B \approx 0.95$, so that $A B \approx 1$, $\Theta_1 \approx 87^\circ$ and $a \approx 19$.

We conclude that the Fractal-Wenzel equation describes a hydrophilic homogeneous fractal regime in the limit of low roughness, i.e., for short treatment times T (small length scales). We can therefore regard our result Equations (4 and 5) as a suitable generalization of the Fractal-Wenzel equation for self-affine surfaces on larger length scales, which become accessible for longer plasma treatments.

The detailed discussion can be found in the Supporting Information. Moreover, the interested readers could also find some more details in the relevant references.^[34,35,36,47-49]

4.2. Roll-Off Angles

Results for the roll-off angles are reported in Figure 5b, and pictures of α -bromo naphthalene droplets rolling off the treated surfaces are displayed in Figure 5c. We find a rapid decrease of the angle as a function of treatment time T . For times $T > 15$ min, we find a super-oleophobic behavior under water, as the roll-off angle gets close to zero, as shown in Figure 5b.

The estimation of the roll-off angle for α -bromo naphthalene droplets in our problem is closely related to the phenomenology described above for the contact angle. In both cases we are dealing with a Wenzel type of regime, in the sense that roughness increases both the hydrophilicity of the surface in

air, and its oleophobicity in water. We find that a suitable fit for the roll-off angle θ_R obeys the relation:

$$\sin \theta_R = \frac{A}{1 + (T/T_0)^{d_f}} \quad (7)$$

where A and T_0 are the fitting parameters. As one can see, the roll-off angle decreases with the treatment time T , suggesting that the surface gets more oleophobic as its roughness increases. The idea behind Equation (7) is that the mean surface depth $\langle z \rangle \approx T$ (see Figure 4a) determines the length scale here (instead of surface fluctuations, i.e., the standard deviation in Equation (4), for the contact angle), while the exponent d_f reminds us of the fractal self-affine scaling of the surface.

5. Fractal Characteristics

Thus far, our experimental studies have confirmed that plasma treatment could be extremely efficient for significant modification of the PET surface characteristics. However, the key factors that ensure super-hydrophilicity and super-hydrophobicity in other cases^[50] are still not well understood. The well-developed surface morphology is the main factor that provided unusual properties, but to sophisticatedly control them, we need to deeper understand these drivers.

In our previous publications we attempted to relate some simple, physically clear integrative characteristics of complex nanomaterials to their practically applicable physical and chemical properties such as wetting, sensing,^[4] antibacterial activity,^[51] photocatalytic efficiency^[52] and others.^[3] The degree of spatial ordering in the nanostructured materials and the connectivity were considered as the characteristics that could possibly explain many important properties of a complex nanomaterial.^[53] While ordering and in part connectivity of isolated nanostructures within the nanocomposite material indeed determine many properties of the nanomaterial, they still cannot be considered as a self-consistent set of the fingerprints that could comprehensively describe the whole set of the properties of nanocomposites and metamaterials.

Here we have made a suggestion that along with spatial ordering and connectivity, the fractal properties of the nanocomposite may be the main ruling key for controlling the properties of nanomaterials. To support this suggestion, we have conducted an in-depth analysis of the surface morphology using the advanced characterization theoretical technologies, to relate the surface morphology descriptors to the experimentally studied wettability properties. In particular, we have conducted the following analyses:

- First, we have made a detailed comparison of the evolution of height distributions at micrometer- and nanometer-scale levels;
- Second, we assessed the ordering of the samples at the nano- and micro-scale levels using the Hough and 2D fast Fourier transforms (FFT) distributions;
- Next, we assessed the Minkowski connectivity of the samples at the nano- and micro-scale levels using the Hough and 2D FFT distributions;
- Finally, we have calculated the fractal dimensions for the samples, both integral and the different-level.

Figure 6 shows the comparison of the evolution of height distributions at micrometer- and nanometer-scale levels. The comparison has demonstrated that at the μ -scale, the mean height does not change significantly (increases from 0.33 to 0.56), but the distribution becomes wider; this means that the surface features smaller and larger than the mean-height peaks appear during plasma etching. At the nanoscale, the distributions move significantly to the right and significantly wide; thus, a large number of higher features is created at the nanoscale during plasma etching. Different behaviors at nano- and μ -scales results in the formation of a very complex fractalized surface topography.

Next, we have analyzed and compared the samples at nano- and micro-scales using Hough distributions (Figure 7a,b, top panel). This analysis revealed the same interesting features, namely that at the micro-scale (analysis using SEM data) the ordering parameters depend on the size of scan area on the sample, and specifically, larger scan shows better ordering (Figure 7a). This evidences that the surface is not perfectly self-affine and hence, the fractal parameters (in particular, fractal dimension) should have a complex character. On the other hand, the samples for nano-scale (Figure 7b) shows improvement in the regularity with the treatment duration. In our previous works we have analyzed the influence of ordering to the surface characteristics^[4,46] but here we try to relate the two important characteristics, namely fractality and ordering.

To quantitatively assess the morphological and geometrical characteristics of facile nanoscale systems formed by irregularly distributed nanosized features, so called statistical measures could be used. Among other approaches and criteria, Minkowski functionals were tested and proved to be efficient tools.^[18] In particular, Minkowski functionals were used to investigate the surface processes that lead to the formation of the specific parameters of materials, and to relate the structural characteristic of a material to the properties of the whole system. To mention, Minkowski functionals were used as an analytical tool to examine structural characteristics of different nanomaterial-based systems, such as, e.g., the strength of a metamaterial formed by multiple elemental sub-structures,^[54] and to assess the percolation threshold of plasma-treated materials.^[55] In nanofabrication, Minkowski functional technique were used to examine very complex patterns of nanostructures such as facial patterns of nanostructures including grapheme flakes, nanotips and nanocones.^[56]

The technique of utilizing Minkowski functionals for the examination of nano-textured surfaces was tested on various material systems including, e.g., ultra-thin aluminum oxide membranes,^[57] plasma-made polymer films,^[58] superhydrophobic carbon nanomaterials for the photocatalysis applications,^[59] and graphene flake arrays. One of the Minkowski functionals, the Minkowski connectivity (Euler-Poincaré characteristic) is particularly important for nanofabrication, due to its capability to reveal the degree of connectivity (number of connections between the nanostructures in the pattern) in large irregular arrays of nanostructures. This technique calculates the ratio of disconnected and connected points in the pattern of nanostructures.

The mean panel of Figure 7 shows the Minkowski connectivity graphs for nanoscale and microscale samples. At the micrometer-scale (Figure 7c), the wider scan (20 μ m) returns

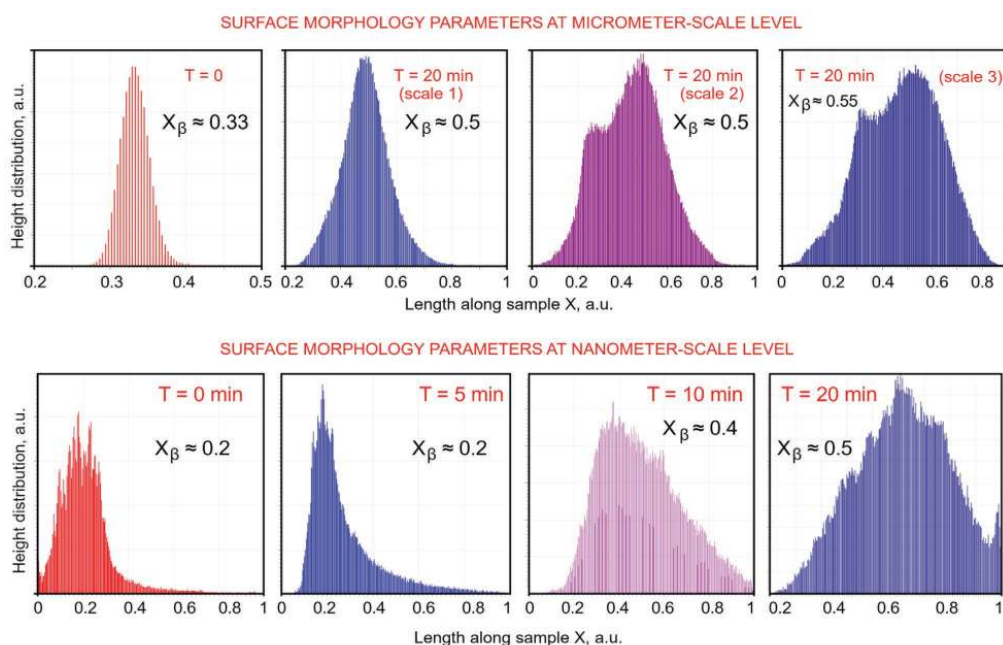


Figure 6. Comparison of height distributions at micrometer-scale and nanometer-scale levels. At $\mu\text{-scale}$, the mean height does not change significantly (increases from 0.33 to 0.56), but the distribution becomes wider; this means that the surface features smaller and larger than the mean-height peaks appear during plasma etching. At the nanoscale, the distribution significantly moves to the right and significantly widens; thus, a large number of higher features is created at the nanoscale during plasma etching. Different behaviors at nano- and $\mu\text{-scales}$ results in the formation of very complex fractalized surface topography.

the highest connectivity and highest ordering. At the nanoscale (Figure 7d), the sample treated with oxygen plasma for 5 min. demonstrates the highest connectivity but lower ordering, as evidenced by Hough distributions (Figure 7a,b). Importantly, the changes in the connectivity for untreated ($T = 0$) and treated (5, 10, 20) samples are quite significant, with the 5-min treated sample featuring three-fold increase in the connectivity as compared to the untreated material. The difference in connectivities for micro-scale are also significant, reaching 100%.

Figure 7e shows the numbers of relative connectivities for both nano- and micro-scales, i.e., the normalized maximum values of the connectivity numbers for all samples. At the nanoscale (black points), the connectivity abruptly jumps for 5 min of plasma treatment and then decreases with the treatment time. This may be explained using the two-stage mechanism similar to that described for the plasma-grown carbon nanofibers.^[60] At the first stage of plasma treatment, the connectivity increases due to temperature rise and development of interconnections between the isolated nanostructures.^[61,62] At the second stage, the connectivity decreases due to plasma etching and sputtering. Bottom panel shows the 2D Fast Fourier Transforms for nano and μm scales. For nanoscale, the difference is not quite strong (it is also not quite strong for Hough distributions), but quite strong for μm scales (left).

Figure 8 presents the fractal dimensions for all samples, along with the images of several well-known fractal objects to see where our plasma-treated samples are in the world of fractals (Figure 8a). It should be noted that the exact assessment of the fractal dimension of a realistic (irregular) object is not possible, so three methods (partitioning, cube counting and triangulation) were used here which returned the results with the scatter of about 10%. As it is seen from the image, the plasma-treated samples correspond to well-developed fractal objects such as Apollonian sphere and 3D Von Koch.^[55] Increase of the fractal dimension for the larger scans can be interpreted as an argument for even higher fractal dimension for the whole object. Figure 8c shows the dependence of fractal dimension on the time of plasma treatment.

Thus, the nanoscale samples demonstrate the highest fractal dimension for $T = 5$ min sample, yet these values are close for other untreated samples; untreated sample demonstrate lowest fractal dimension. Interestingly, the $T = 5$ min sample features lowest ordering among treated samples. On the other hand, the untreated sample with the lowest fractal dimension shows the lowest ordering.

- At the nanoscale, the relation of fractal dimension / ordering is opposite for treated and untreated samples; this means that plasma treatment changes the morphology fundamentally, i.e., it changes fractality independently of ordering.

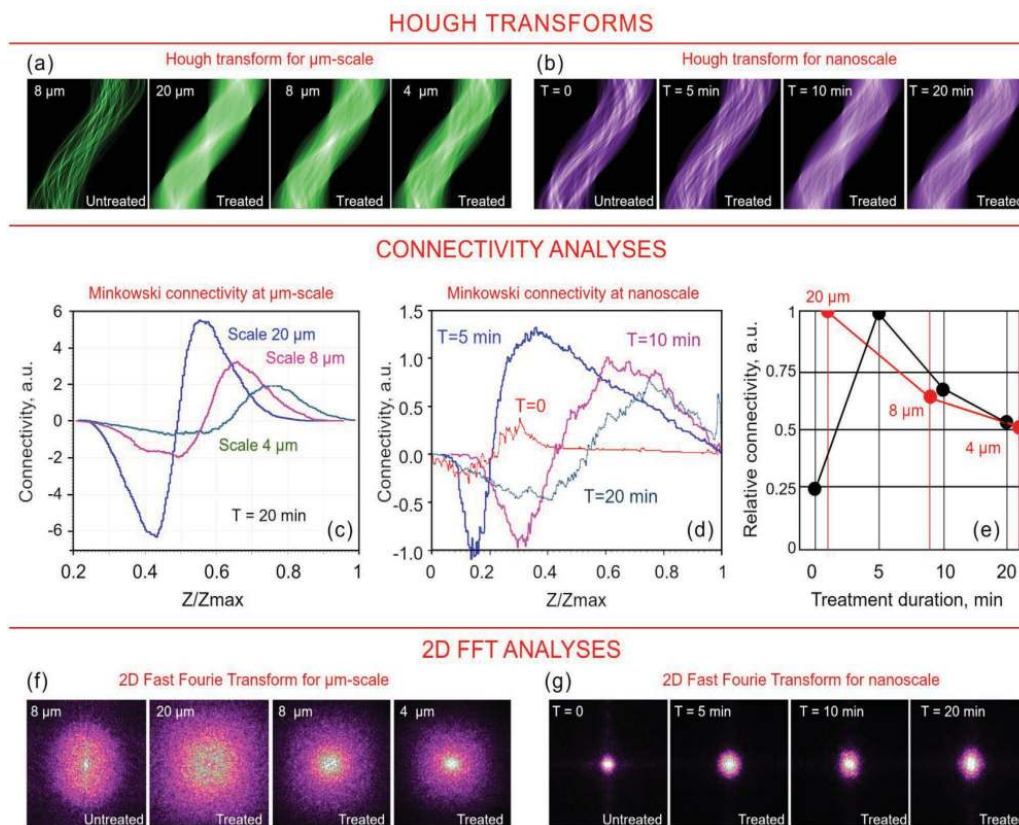


Figure 7. Top panel (a,b): Hough distributions for nano- and micro-scales. Center panel (c,d,e): Minkowski connectivity for nanoscale and microscale samples. Importantly, 5 min – treated sample demonstrates the highest connectivity but lower ordering, as evidenced by Hough distributions. At the micrometer-scale, the wider scan (20 μm) returns the highest connectivity and highest ordering. Also note quite significant change in the connectivity for untreated ($T = 0$) and treated (5, 10, 20) samples. Bottom panel (f,g): 2D fast Fourier transforms for nano and μm scales. For nanoscale, the difference is not quite strong (it is also not quite strong for Hough distributions), but quite strong for μm scales (left).

The situation is opposite at the micro-scale (Figure 8b). The larger-scanned (20 μm) sample shows the highest ordering and highest fractal dimension – this means, the self-affinity is limited inside smaller areas but fractal dimension is still high for larger scans.

Where we are with these numbers of fractal dimensions? Figure 8 illustrates the graphical representation of fractal dimensions for all samples, along with the images of some known fractal objects. As one can see, the plasma-treated samples correspond to well-developed fractal objects such as Apollonian sphere and 3D Von Koch. It should be noted that the exact assessment of realistic (irregular) objects is not possible, so three methods were used which return the results with the scatter of about 10%.

- Increase of the fractal dimension for the larger scans (increase from 2.35 for nanoscale to 2.6 for 20 μm) can be interpreted as an argument for even higher fractal dimension for the whole object

The results of fractal dimension assessment are listed in Table S1 (Supporting Information).

Besides, Figures S2 and S3 (Supporting Information) show the attempts to assess the fractal dimensions for several cross-sections parallel to the top surfaces of the samples. While we do not have exact data on the morphology of cross-sections and thus this assessment was made by processing the ASM and SEM images, it still can be used to detect the overall trend. As one can see from these images, the change is not too pronounced and as expected, the highest numbers of fractal dimension are reached inside the nanostructures, i.e., between the top surface and solid wafer at the bottom.

In general, the relation between the fractal dimension and regularity (ordering) is not apparent, since highly fractalized surfaces could be highly organized, but could be quite stochastic (see examples in the literature^[64,65]). In our case we expect self-organization under the plasma treatment^[66,67] and

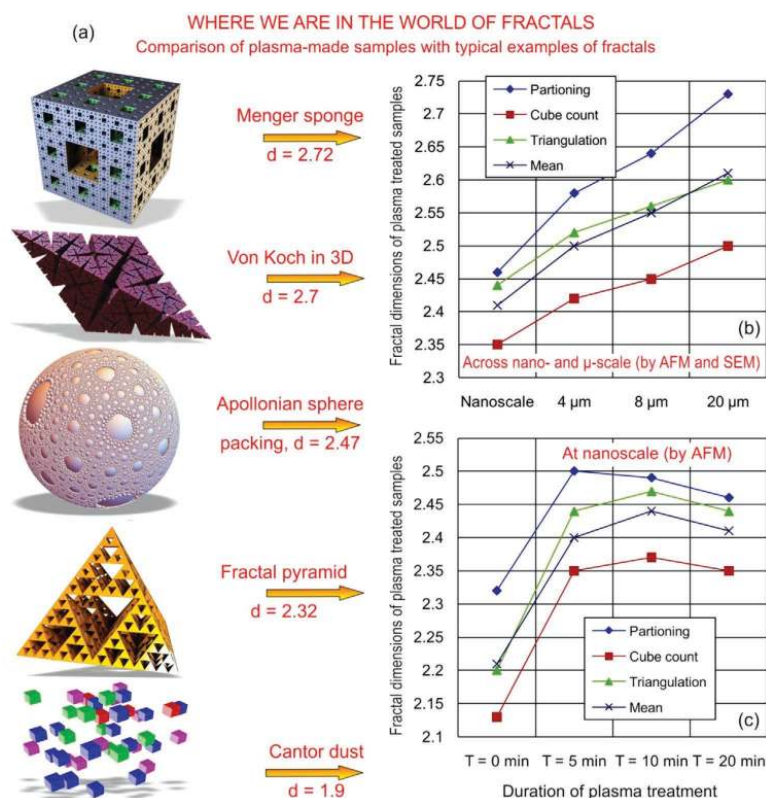


Figure 8. a) Graphical representation of several known fractal objects and b) fractal dimensions for all samples across the nano- and micro-scales. Three methods were used (partitioning, cube counting and triangulation). c) The dependence of fractal dimension on the time of plasma treatment. The plasma-treated samples correspond to well-developed fractal objects such as Apollonian sphere and 3D Von Koch. Increase of the fractal dimension for the larger scans can be interpreted as an argument for even higher fractal dimension for the whole object. The images of Menger sponge and Von Koch objects are reprinted under conditions of Creative Commons licenses. The image of Apollonian sphere: Reproduced under the terms of the CC-BY 3.0 license.^[63] Copyright 2020, The Authors, published by IOP Publishing.

hence, the surface could be quite ordered; on the other hand, we definitely see a quite high fractality.

6. Summary and Conclusions

In summary, we find that i) the nanostructured morphology and wettability properties of PET surfaces treated with a cold oxygen plasma strongly depend on the treatment time T ; ii) very high degree of hydrophilicity could be reached; and iii) the wettability properties could be related to the ordering, connectivity and fractal dimensions of the surface textures. Moreover, the fractal dimension could be the most important descriptor to predict and hence control the surface properties. In more detail:

- The surface roughness increases up to $T = 20$ min, and saturates afterward. The AFM images of the treated surfaces clearly

display the formation of a complex nanostructure architecture, which appears to have partially scale-invariant properties;

- A noticeable decrease in the contact angle of the water droplets in air is observed, changing from 90° for non-treated PET film down to 0° for $T = 30$ min, suggesting a super-hydrophilic behavior;
- A considerable decrease in the roll-off angle of a nonpolar substance droplet (α -bromo naphthalene) in water is found, which eventually goes to zero for $T = 30$ min, suggesting a super-oleophobic behavior under water;
- The extended analysis has revealed that morphological descriptors such as ordering, connectivity and fractal dimensions of the nanocomposites are closely related to the physical surfaces such as wettability. Since we have demonstrated in our previous works that the morphological descriptors could relate to some other properties of nanomaterials, we can conclude their general importance for the prediction of physical activity of complex hierarchical nanocomposites.

Thus, the macroscopic properties of cold oxygen plasma treated PET surfaces, such as wettability in air and oil repellency under water, can be modified considerably as a function of treatment time. This yields surfaces which can be both extremely hydrophilic in air and oleophobic in water, as a result of the complex hierarchical nanostructured surface which is created by the oxygen plasma processes. These structures are very similar to the naturally developed microscopic surfaces having well-tailored properties.^[68] The super hydrophilic properties thus obtained are very stable, more than those obtained by deposition of hydrophilic polymer by plasma.^[69,70]

A simple theoretical model for the treated surface-air interface energy is developed, based on a self-affine scaling behavior, in very good agreement with the experimental findings. We conclude that PET treated surfaces (both films and tissues) display characteristic wetting properties typical of a Wenzel regime, rather than a Cassie-Baxter one.

A new deeper insight into the correlation of physical properties of the complex hierarchical nanocomposites allows to conclude that the fractal dimension is one of the major characteristics of the nanocomposite that determines many important physical and chemical properties of the functional nanomaterials, and hence, consolidated proactive efforts are needed to better investigate the internal physical mechanisms behind the influence of fractality to the behavior of complex surfaces.

Then the present cold oxygen plasma technique appears to be very promising and versatile for future applications in the field of surface engineering at the nanoscale, such as oil-water separation, handling of hydrocarbons, filtration, self-cleaning and anti-fouling surfaces, most of which play an important role in actual industrial processes.

Supporting Information

Supporting Information is available from the Wiley Online Library or from the author.

Acknowledgements

This work was supported in part by the following funds and organizations: Università degli Studi di Milano-Bicocca; The Australian National University; K.B. acknowledges support from the Australian Research Council; C.R., C.P. and D.L.D. acknowledge Alessandro Mietner for the technical support.

Conflict of Interest

The authors declare no conflict of interest.

Data Availability Statement

The data that support the findings of this study are available in the supplementary material of this article.

Keywords

fractal parameters, oxygen plasma treatment, super-hydrophobicity, wettability

Received: May 3, 2021

Revised: June 25, 2021

Published online:

- [1] I. Levchenko, K. Bazaka, M. Keidar, S. Xu, J. Fang, *Adv. Mater.* **2018**, *30*, 1702226.
- [2] O. Baranov, I. Levchenko, J. M. Bell, J. W. M. Lim, S. Huang, L. Xu, B. Wang, D. U. B. Aussems, S. Xu, K. Bazaka, *Mater. Horiz.* **2018**, *5*, 765.
- [3] S. Alancherry, M. V. Jacob, K. Prasad, J. Joseph, O. Bazaka, R. Neupane, O. K. Varghese, O. Baranov, S. Xu, I. Levchenko, K. Bazaka, *Carbon* **2020**, *159*, 668.
- [4] S. Alancherry, K. Bazaka, I. Levchenko, A. Al-Jumaili, B. Kandel, A. Alex, F. C. R. Hernandez, O. K. Varghese, M. V. Jacob, *ACS Appl. Mater. Interfaces* **2020**, <https://doi.org/10.1021/acsami.0c04353>.
- [5] Z. Fusco, M. Rahmani, T. Tran-Phu, C. Ricci, A. Kiy, P. Kluth, E. D. Gaspera, N. Motta, D. Neshev, A. Tricoli, *Adv. Mater.* **2020**, *32*, 2002471.
- [6] Z. Wang, T. Liu, L. Jiang, M. Asif, X. Qiu, Y. Yu, F. Xiao, H. Liu, *ACS Appl. Mater. Interfaces* **2019**, *11*, 32310.
- [7] Y. R. Mimérand, K. Li, C. Zhou, X. Jin, X. Hu, Y. Chen, J. Guo, *ACS Appl. Mater. Interfaces* **2020**, *12*, 38, 43138.
- [8] H. Li, H. Liu, M. Sun, Y. Huang, L. Xu, *Adv. Mater.* **2021**, *33*, 2004425.
- [9] M. Konar, B. Roy, T. Govindaraju, *Adv. Mater. Interfaces* **2000**, *7*, 2020.
- [10] F. Shahzad, A. Iqbal, H. Kim, C. M. Koo, *Adv. Mater.* **2020**, *32*, 2002159.
- [11] Z. Chen, A. Narita, K. Müllen, *Adv. Mater.* **2020**, *32*, 2001893.
- [12] I. Levchenko, K. Bazaka, S. Mazouffre, S. Xu, *Nat. Photonics* **2018**, *12*, 649.
- [13] I. Levchenko, S. Xu, Y. L. Wu, K. Bazaka, *Nat. Astron.* **2020**, *4*, 1012.
- [14] I. Levchenko, S. Xu, G. Teel, D. Mariotti, M. L. R. Walker, M. Keidar, *Nat. Commun.* **2018**, *9*, 879.
- [15] I. Levchenko, K. Bazaka, T. Belmonte, M. Keidar, S. Xu, *Adv. Mater.* **2018**, *30*, 1802201.
- [16] I. Levchenko, M. Keidar, J. Cantrell, Y. L. Wu, H. Kuninaka, K. Bazaka, S. Xu, *Nature* **2018**, *56*, 185.
- [17] I. Levchenko, S. Xu, S. Mazouffre, D. Lev, D. Pedrini, D. Goebel, L. Garrigues, F. Taccogna, K. Bazaka, *Phys. Plasmas* **2020**, *27*, 020601.
- [18] H. Reinhardt, M. Kroll, S. L. Karstens, S. Schlabach, N. A. Hampf, U. Tallarek, *Adv. Mater. Interfaces* **2020**, *8*, 253.
- [19] S. Chowdhury, A. Roy, I. Bodemann, S. K. Banerjee, *ACS Appl. Mater. Interfaces* **2020**, *12*, 15885.
- [20] O. Baranov, I. Levchenko, S. Xu, J. W. M. Lim, U. Cvelbar, K. Bazaka, *2D Mater.* **2018**, *5*, 044002.
- [21] K. Bazaka, O. Baranov, U. Cvelbar, B. Podgornik, Y. Wang, S. Huang, L. Xu, J. W. M. Lim, I. Levchenko, S. Xu, *Nanoscale* **2018**, *10*, 17494.
- [22] S. Zanini, A. Citterio, G. Leonardi, C. Riccardi, *Appl. Surf. Sci.* **2018**, *427*, 90.
- [23] R. A. Siliprandi, S. Zanini, E. Grimoldi, F. S. Fumagalli, R. Barni, C. Riccardi, *Plasma Chem. Plasma Process.* **2011**, *31*, 353.
- [24] S. Zanini, E. Grimoldi, C. Riccardi, *Mater. Chem. Phys.* **2013**, *138*, 850.
- [25] I. Adamovich, S. Baalrud, A. Bogaerts, P. Bruggeman, M. Cappelli, V. Colombo, U. Czarnetzki, U. Ebert, J. Eden, P. Favia, D. B. Graves, S. Hamaguchi, G. Hieftje, M. Hori, I. D. Kaganovich, U. Kortshagen, M. J. Kushner, N. J. Mason, S. Mazouffre, S. Mededovic






- Thagard, H.-R. Metelmann, A. Mizuno, E. Moreau, A. B. Murphy, B. A. Niemira, G. S. Oehrlein, Z. Lj Petrovic, L. C. Pitchford, Y.-K. Pu, S. Rauf, O. Sakai, S. Samukawa, S. Starikovskaia, J. Tennyson, K. Terashima, M. M. Turner, M. C. M. van de Sanden, A. Vardelle, *J. Phys. D: Appl. Phys.* **2017**, *50*, 323001.
- [26] S. Zanini, M. Lehocky, J. Lopez-Garcia, C. Riccardi, *Thin Solid Films* **2019**, *677*, 55.
- [27] S. Zanini, A. Polissi, E. A. Maccagni, E. C. Dell'Orto, C. Liberatore, C. Riccardi, *J. Colloid Interface Sci.* **2015**, *451*, 78.
- [28] S. Zanini, L. Zoia, R. D. Pergola, C. Riccardi, *Surf. Coat. Technol.* **2018**, *334*, 173.
- [29] R. Barni, C. Riccardi, E. Selli, M. R. Massafra, B. Marcandalli, F. Orsini, G. Poletti, L. Meda, *Plasma Processes Polym.* **2005**, *2*, 64.
- [30] S. Zanini, L. Zoia, E. C. Dell'Orto, A. Natalello, A. M. Villa, R. D. Pergola, C. Riccardi, *Mater. Des.* **2016**, *108*, 791.
- [31] S. Asadollahi, M. Farzaneh, L. Stafford, *Coatings* **2019**, *9*, 679.
- [32] S. Zanini, P. Massini, M. Mietta, E. Grimoldi, C. Riccardi, *J. Colloid Interface Sci.* **2008**, *322*, 566.
- [33] E. Grimoldi, S. Zanini, R. Siliprandi, C. Riccardi, *Eur. Phys. J. D* **2009**, *54*, 165.
- [34] A. Tripathy, P. Sen, B. Su, W. H. Briscoe, *Adv. Colloid Interface Sci.* **2017**, *248*, 85.
- [35] D. P. Linklater, V. A. Baulin, X. L. Guével, J.-B. Fleury, E. Hanssen, T. H. P. Nguyen, S. Juodkazis, G. Bryant, R. J. Crawford, P. Stoodley, E. P. Ivanova, *Adv. Mater.* **2020**, *32*, 2005679.
- [36] D. P. Linklater, V. A. Baulin, S. Juodkazis, R. J. Crawford, P. Stoodley, E. P. Ivanova, *Nat. Rev. Microbiol.* **2021**, *19*, 8.
- [37] Y. Lv, X. Xi, L. Dai, S. Tong, Z. Chen, *Adv. Mater. Interfaces* **2021**, *8*, 2002030.
- [38] I. Biganzoli, F. Fumagalli, F. Di Fonzo, R. Barni, C. Riccardi, *J. Modern Phys.* **2012**, *3*, 1626.
- [39] E. C. Dell'Orto, S. Caldirola, A. Sassella, V. Morandi, C. Riccardi, *Appl. Surf. Sci.* **2017**, *425*, 407.
- [40] C. Carra, E. C. Dell'Orto, V. Morandi, C. Riccardi, *Coatings* **2020**, *10*, 788.
- [41] S. Zanini, R. Barni, R. D. Pergola, C. Riccardi, *J. Phys. D: Appl. Phys.* **2014**, *47*, 325202.
- [42] J. Feder, in *Fractals*, Springer Science & Business Media, Boston **1988**
- [43] B. Demirel, A. Yaras, H. Elcicek, *BAÜ Fen Bil. Enst. Dergisi Cilt.* **2011**, *13*, 26.
- [44] R. A. Siliprandi, H. E. Roman, R. Barni, C. Riccardi, *J. Appl. Phys.* **2008**, *104*, 063309.
- [45] G. Nagayama, D. Zhang, *Soft Matter* **2020**, *16*, 3514.
- [46] D. Murakami, H. Jinnai, A. Takahara, *Langmuir* **2014**, *30*, 2061.
- [47] M. N. MacGregor-Ramiasa, K. Vasilev, *Adv. Mater. Interfaces* **2017**, *4*, 1700381.
- [48] S. Cheeseman, S. Owen, V. K. Truong, D. Meyer, S. H. Ng, J. Vongsvivut, D. Linklater, M. J. Tobin, M. Werner, V. A. Baulin, P. Luque, *ACS Omega* **2018**, *3*, 6039.
- [49] A. Giacomello, S. Meloni, M. Chinappi, C. M. Casciola, *Langmuir* **2012**, *28*, 10764.
- [50] Z. Li, M. Cao, P. Li, Y. Zhao, H. Bai, Y. Wu, L. Jiang, *Matter* **2019**, *1*, 661.
- [51] O. Bazaka, K. Bazaka, V. K. Truong, I. Levchenko, M. V. Jacob, Y. Estrin, R. Lapovok, B. Chichkov, E. Fadeeva, P. Kingshott, R. J. Crawford, E. P. Ivanova, *Appl. Surf. Sci.* **2020**, *521*, 146375.
- [52] Q. Xiang, X. Ma, D. Zhang, H. Zhou, Y. Liao, H. Zhang, S. Xu, I. Levchenko, K. Bazaka, *J. Colloid Interface Sci.* **2019**, *556*, 376.
- [53] I. Levchenko, S. Xu, O. Baranov, O. Bazaka, E. P. Ivanova, K. Bazaka, *Molecules* **2021**, *26*, 4091.
- [54] R. Monetti, J. Bauer, I. Sidorenko, E. Rummery, M. Matsuura, *Proc. SPIE* **2009**, *7262*, 2620N.
- [55] M. A. Rodríguez-Valverde, P. J. Ramón-Torregrosa, M. A. Cabrerizo-Vilchez, in *Microscopy: Science, Technology, Applications and Education*, Vol. 3, (Eds: A. Méndez-Vilas, J. Díaz), Formatex Research Center, Badajoz, Spain **2010**, pp. 1978–1983
- [56] U. Cvelbar, *J. Phys. D: Appl. Phys.* **2011**, *44*, 4980.
- [57] R. Previdi, I. Levchenko, M. Arnold, M. Gali, K. Bazaka, S. Xu, K. K. Ostrikov, K. Bray, D. Jin, J. Fang, *J. Mater. Chem. A* **2019**, *7*, 9565.
- [58] K. Bazaka, M. V. Jacob, K. Ostrikov, *Chem. Rev.* **2016**, *116*, 163.
- [59] S. P. Suresh, G. S. Lekshmi, S. D. Kirupha, M. Ariraman, O. Bazaka, I. Levchenko, K. Bazaka, M. Mandhakini, *Carbon* **2019**, *147*, 323.
- [60] Z. L. Tsakadze, I. Levchenko, K. Ostrikov, S. Xu, *Carbon* **2007**, *45*, 2022.
- [61] I. Levchenko, K. Ostrikov, D. Mariotti, *Carbon* **2008**, *47*, 313.
- [62] I. Levchenko, K. Ostrikov, D. Mariotti, V. Švrček, *Carbon* **2009**, *47*, 2379.
- [63] M. Fennen, D. Giulini, *Class. Quantum Grav.* **2020**, *37*, 065007.
- [64] M. F. Barnsley, *Fractals Everywhere*, 2nd ed., Morgan Kaufmann, Burlington **2000**.
- [65] V. V. Mitić, L. M. Kocić, S. Tidrow, H.-J. Fecht, in *Nanotechnology for Energy Sustainability* (Ed: B. Raj), Vol. 32, Wiley-VCH, Verlag **2017**, Ch. 32.
- [66] I. Levchenko, S. Y. Huang, K. Ostrikov, S. Xu, *Nanotechnology* **2009**, *21*, 025605.
- [67] K. K. Ostrikov, I. Levchenko, S. Xu, *Pure Appl. Chem.* **2008**, *80*, 1909.
- [68] N. Zhang, C. Huang, J. Li, L. Kang, H. Zheng, Y. He, Z. Wang, X. Zhou, J. Zhang, *J. Bionic Eng.* **2020**, *17*, 436.
- [69] U. G. K. Wegst, H. Bai, E. Saiz, A. P. Tomsia, R. O. Ritchie, *Nat. Mater.* **2015**, *14*, 23.
- [70] R. Tamilselvi, G. S. Lekshmi, N. Padmanathan, V. Selvaraj, O. Bazaka, I. Levchenko, K. Bazaka, M. Mandhakini, *Renew. Energy* **2021**, <https://doi.org/10.1016/j.renene.2021.07.088>.

A.7 Controlled Deposition of Nanostructured Hierarchical TiO₂ Thin Films by Low Pressure Supersonic Plasma Jets

Reproduced from Piferi, C.; Carra, C.; Bazaka, K.; Roman, H. E.; Dell'Orto, E. C.; Morandi, V.; Levchenko, I.; Riccardi, C. Controlled Deposition of Nanostructured Hierarchical TiO₂ Thin Films by Low Pressure Supersonic Plasma Jets. *Nanomaterials* 2022, 12 (3), 533, <https://doi.org/10.3390/nano12030533>.

Article

Controlled Deposition of Nanostructured Hierarchical TiO₂ Thin Films by Low Pressure Supersonic Plasma Jets

Cecilia Piferi ¹, Chiara Carra ¹, Kateryna Bazaka ², Hector Eduardo Roman ¹, Elisa Camilla Dell'Orto ¹, Vittorio Morandi ³, Igor Levchenko ⁴ and Claudia Riccardi ^{1,*}

¹ Department of Physics, University of Milano-Bicocca, Piazza della Scienza 3, 20126 Milan, Italy; c.piferi@campus.unimib.it (C.P.); c.carra@campus.unimib.it (C.C.); eduardo.roman@mib.infn.it (H.E.R.); elisa.dellorto@unimib.it (E.C.D.)

² School of Engineering, College of Engineering and Computer Science, The Australian National University, Canberra 2600, Australia; katia.bazaka@anu.edu.au

³ CNR-IMM Sede di Bologna, Via Gobetti 101, 40129 Bologna, Italy; morandi@bo.imm.cnr.it

⁴ Plasma Sources and Applications Centre, NIE, Nanyang Technological University, Singapore 637616, Singapore; levchenko.igor@nie.edu.sg

* Correspondence: claudia.riccardi@unimib.it

Abstract: Plasma-assisted supersonic jet deposition (PA-SJD) is a precise technique for the fabrication of thin films with a desired nanostructured morphology. In this work, we used quadrupole mass spectrometry of the neutral species in the jet and the extensive characterization of TiO₂ films to improve our understanding of the relationship between jet chemistry and film properties. To do this, an organo-metallic precursor (titanium tetra-isopropoxide or TTIP) was first dissociated using a reactive argon-oxygen plasma in a vacuum chamber and then delivered into a second, lower pressure chamber through a nozzle. The pressure difference between the two chambers generated a supersonic jet carrying nanoparticles of TiO₂ in the second chamber, and these were deposited onto the surface of a substrate located few centimeters away from the nozzle. The nucleation/aggregation of the jet nanoparticles could be accurately tuned by a suitable choice of control parameters in order to produce the required structures. We demonstrate that high-quality films of up to several μm in thickness and covering a surface area of few cm² can be effectively produced using this PA-SJD technique.

Keywords: plasma; supersonic jet; deposition; nanostructures; TiO₂ film



Citation: Piferi, C.; Carra, C.; Bazaka, K.; Roman, H.E.; Dell'Orto, E.C.; Morandi, V.; Levchenko, I.; Riccardi, C. Controlled Deposition of Nanostructured Hierarchical TiO₂ Thin Films by Low Pressure Supersonic Plasma Jets. *Nanomaterials* **2022**, *12*, 533. <https://doi.org/10.3390/nano12030533>

Academic Editors: Carles Corbella, Sabine Portal and Christophe Petit

Received: 24 November 2021

Accepted: 1 February 2022

Published: 3 February 2022

Publisher's Note: MDPI stays neutral with regard to jurisdictional claims in published maps and institutional affiliations.



Copyright: © 2022 by the authors. Licensee MDPI, Basel, Switzerland. This article is an open access article distributed under the terms and conditions of the Creative Commons Attribution (CC BY) license (<https://creativecommons.org/licenses/by/4.0/>).

1. Introduction

The demand for new materials with specific features at nano/micro-scales has been considerably increasing in recent times. This is a consequence of the superior and/or unusual properties that arise from the unique combination of chemistry and complex structure across multiple length scales. Nanoparticles (NPs) are often the building blocks of choice for the synthesis and assembly of advanced nanomaterials with high chemical reactivity and mechanical strength, as well as new optical and electrical properties. This is because of their wide range of available chemistries, different shapes of varying sizes, large surface-to-bulk ratios, and quantum-confinement effects at small length scales. Metallic and metal oxide nanoparticles and their thin films play particularly important roles in the advancement [1,2] of sensors [3–5], photocatalysts [6,7], bio-electronic-based devices [8,9], super-hydrophobic and self-cleaning materials [10,11], and various nanoelectronic devices [12,13]. In addition, light-sensitive diamond films have found applications in space technology [14], while other types of nanostructured aggregates are promising for the achievement of propulsion systems based on plasma technologies [15,16]. Both space applications are envisaged as critical for the advancement of affordable and miniaturized space assets [17].

The quality, possible properties, and morphology of metal-oxide nanoparticles and their assemblies are defined to a large extent by the opportunities and limitations of the

processes used for their synthesis and assembly, of which there are many [18–20]. For the synthesis of ordered structures with engineered pore architecture, methods that rely on templating agents are frequently used, with soft templates offering the advantage of lower costs, simpler preparation, and greater versatility. For instance, mesoporous materials composed of TiO₂ microparticles have been produced by combining material precursors and block polymer micelles [21]. The template-free fabrication of ordered TiO₂ nanostructured materials is also being actively investigated in an effort to devise a method that would enable a greater level of tunability of all material characteristics in a controlled and predictable manner. Indeed, techniques aimed at the production of thin films, such as physical vapor deposition (PVD) [22], plasma-enhanced chemical vapor deposition (PECVD) [23,24], and reactive pulsed laser deposition (PLD) [25,26] have had much success in realizing this objective. Another relevant technique is atomic layer deposition (ALD), which is nowadays one of the most versatile and controllable techniques for thin film deposition [27,28]. The more recent development of plasma-assisted supersonic jet deposition (PA-SJD) [29–32] may offer a greater level of both flexibility and control. This can be obtained by segmenting the synthesis of the new material from the input gas into two separate steps, thus allowing for a greater control of, first, the chemistry involved by fine-tuning the properties of the reactive cold plasma environment, and second, the nucleation and assembly of nanoparticles carried by the supersonic jet and impacting the substrate [30,33]. In addition to the enhanced control and versatility of the deposition technique, large deposition areas and high deposition rates may be realized, the latter obtained by using high density plasmas of volatile and stable precursors for oxides, semiconductors, or metals. Importantly, when using supersonic jet deposition, new types of sintering processes may emerge during deposition at or close to room temperature [34]. These features, coupled with the strong adsorption and electrical surface properties of thus-fabricated hierarchical nano-assemblies, make this process suitable for many technological applications [35–41].

This paper presents an exploration of the relationship between the characteristics of the supersonic jet and the hierarchical nano/micro-structural properties of the resulting thin films in detail. The plasma and deposition chambers used in PA-SJD play different roles in the process. The former is used to create nanoparticles of a uniform size. The latter determines the morphology of the deposited thin films depending on the plasma control parameters, i.e., by varying the size of the nozzle connecting both chambers and the kinetic energy of the nanoparticles transported by the supersonic jet. In this way, it is possible to obtain films with a wide range of structures, from tree-like structures with different openings to more compact ones resembling cauliflower fractal-like configurations, from the very same nanoparticle building blocks, the nature of which remains virtually unaltered due to their negligible interactions in the jet.

Along with the high deposition rate, the proposed technique has the advantage of being able to control both the morphology and the stoichiometry of the films with high accuracy due to the specifics of the plasma-based process. Although the process is carried out at low pressures, the deposition rates are quite high due to the benefits of the plasma environment.

Our technique ensures results similar to those obtainable with Pulsed Laser Deposition (PLD), but it has several advantages over PLD and similar techniques, namely:

- (1) The process occurs at a low pressure that is still higher than pressures used in PLD, and deposition at a room temperature promotes a higher level of scalability. All low-pressure systems have inherent challenges regarding integration and scale-up, but they also feature definitive advantages. To overcome the scalability problem, several approaches are currently being explored, including designing a plasma source of larger volume to increase the surface area of films, using deposition systems that employ supersonic multi-jet systems, using systems with moving stages, and using other systems that could be adapted to the industrial scale.

- (2) The stoichiometric control of film composition with a high degree of reliability independently on the deposition process by injecting a metallic organic precursor into a mixture with inert gases and oxygen is also an advantage. Compared to sputtering or PLD based on the ablation of a material, 'direct' plasmochemistry enables variance in a wider spectrum the composition of the metallic oxide film and the deposition of layers of different chemical compositions, thus realizing, for instance, the additive manufacturing of multi-metal-based materials.
- (3) The direct control of the morphology of the deposited structures, by means of the compression ratio R acting on the pressure in the deposition chamber without therefore acting on the density of the precursor, allows researchers to create films with variable porosity and morphology, without the need to vary the nanoparticle size, in a well-controlled way (a fine morphology tuning).

These advantages are demonstrated in part in the paper. The question of changing the properties of the particles produced in the first chamber requires further investigation that is beyond the scope of the present work.

2. Experimental Setup

2.1. Plasma-Assisted Supersonic Jet Equipment

The PA-SJD [42,43] technique consists of a two-step process confined within two stainless steel vacuum chambers of cylindrical shape that are connected via a small nozzle of varying aperture size. The plasma chamber used in this study had a length $L_p = 95$ mm and radius $R_p = 62.5$ mm, and the respective metrics of the deposition chamber were $L_D = 200$ mm and $R_D = 160$ mm (see Figure 1). At the bottom of the former, a circular conduit of typically 100 mm in diameter (which could be varied by adjusting a gate valve) connected the vessel to the main pumping system, which consisted of a turbo molecular and a rotary pump. In this study, the effective pumping speed was about 130 l/s for the pressures of 8 Pa in the plasma chamber and 0.03 Pa in the deposition chamber. The lowest pressure reached in the deposition chamber was about 10^{-5} Pa when no gas was injected. The deposition chamber was provided with a 0.1 mm diameter circular orifice connecting it to the quadrupole mass spectrometer for sampling the gas of interest. The turbo molecular and rotary pumps ensured sufficient purity conditions in the chamber required by the spectrometry diagnostics by keeping the instrument pressure below 10^{-4} Pa.

The inlets for the gas and the precursor were located on one side of the plasma chamber that was opposite to the deposition chamber, as shown in Figure 1. Argon and oxygen were injected using two separate mass-flow controllers. The corresponding gas mixture could be considered to be found in a well-mixed state because the gas diffusion speed, 1.26 m/s, exceeded the gas flow speed, 0.04 m/s. The gas expansion by the sonic nozzle generated a focused and supersonic jet enabling the deposition at high growth rates [44]. As a result of the substantial volume increase, the temperature, pressure, and density of the transported material decreased following the isentropic law, in which the gas particles are accelerated and the Mach number (the ratio between the velocity of a particle and the local sound speed) takes values larger than 1.

Part of the NP thermal energy was transformed into a well-oriented beam of matter that started forming a supersonic jet. The expansion ended at the Mach disk, a position along the flow trajectory where a normal shock occurred. At the Mach disk, the values of the temperature, pressure, and density of the gas reached the background values and became subsonic (Mach number drops below one). The properties of the supersonic beam largely depended on the size and shape of the nozzle, in addition to the thermodynamic properties of the gas [45,46]. The geometry of the supersonic jet is represented in Figure 1c.

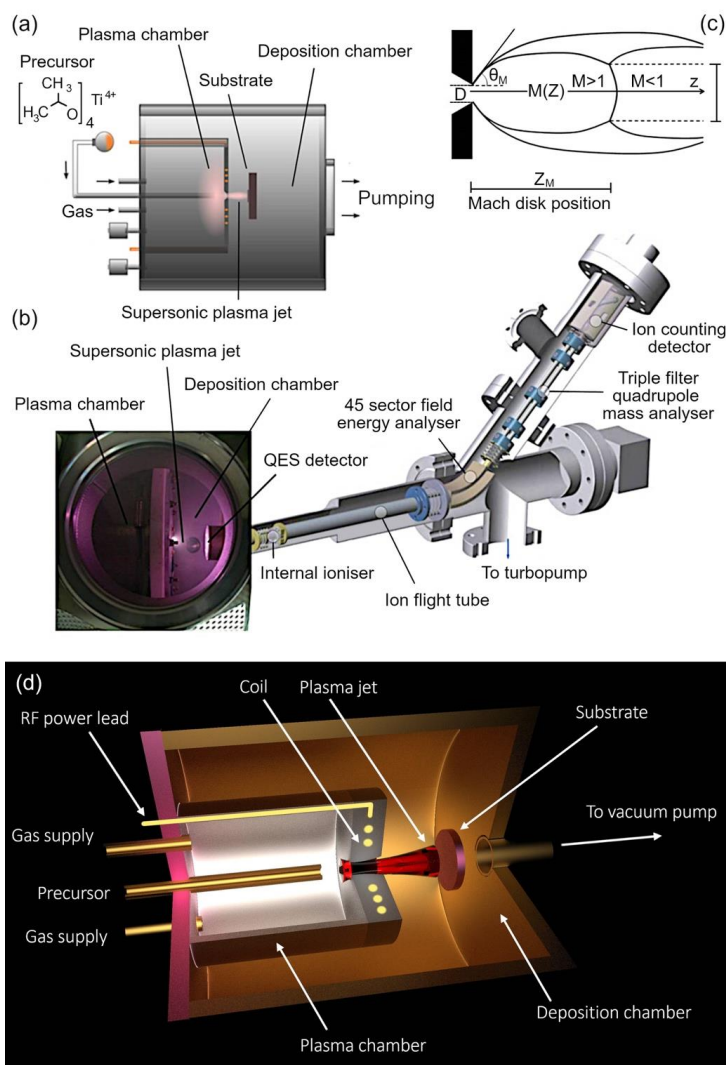


Figure 1. (a) Schematic representation of the experimental device. The whole vacuum vessel comprised two well-separated chambers. The positions of the RF coil antenna, nozzle, pumping system, the gas and precursor injections, and substrate holder are shown. (b) Photo of the PA-SJD: (left part) Plasma chamber, deposition chamber, and substrate holder right to the plasma jet; (right part) photo of the QMS detector used for the analysis of the plasma jet inside the deposition chamber. The QMS replaced the substrate holder during the mass measurements. (c) Scheme of the gas expansion in the chamber. The different Mach numbers, M , corresponding to the supersonic and subsonic regimes are indicated together with the position of the Mach disk at z_M separating them. The jet was free to expand along both the axial and the radial directions before it reached the Mach disk, where the transition to the subsonic condition took place. The position of the sampling holder could be changed along the z -axis in a continuous fashion. (d) 3D rendering of the device.

The supersonic regime occurred for distances $z < z_M$, where z_M represents the position of the Mach disk from the nozzle and is given by,

$$z_M = 0.67 D \sqrt{R} \quad (1)$$

where D is the diameter of the circular orifice at the nozzle and $R = p_p/p_D$ is the ratio between the pressures at the plasma and deposition chambers, respectively. In our experiments, we used a diameter $D = 6.9$ mm, and we used Equation (1) to find that R fell in the range of $2 < R < 40$ for z_M changing between 6.5 and 29 mm, depending on the background pressure we set in the deposition chamber. The particle density in the jet, $n(z)$ at position z , could be estimated from the empirical relation [47]:

$$n(z) = n_0 [1.44 (z/D)^2 - 0.65 (z/D) + 0.87]^{-1/\gamma} \quad (2)$$

where n_0 is the gas density inside the plasma chamber and γ is the adiabatic index of the gas.

RF plasma sources are usually employed to dissociate the precursors, and in the case of inductively coupled plasma (ICP) sources, they can provide uniform and high charge densities along with low ion energies that can be accurately controlled in most cases [43]. Here, the plasma was generated by a 13.56 MHz radiofrequency power generator (Huttinger PFG 1600 RF, Schwaig bei Nuremberg, Germany) connected by a tunable matching box. By feeding the RF antenna with a 450 W input power, an inductively coupled discharge and a stable dense plasma could be generated [44,47]. The plasma was analyzed by optical emission spectroscopy, Langmuir probes, and I–V measurements. The electron temperatures were about 1 eV, and the plasma densities were between 10^{11} and 10^{13} cm⁻³ depending on the reactor parameters.

We let the titanium precursor enter the plasma chamber after the argon/oxygen ratio had been adjusted so that it yielded an inductively sustained plasma discharge at the input power of 450 W. We used titanium (IV) tetra-isopropoxide Ti(OCH(CH₃)₂)₄ (atomic mass $M = 284$ amu). At 20 °C, the precursor was a liquid. Once it was heated, it reached its vapor phase. As a rule, we used a power transformer for this purpose. The gas temperature could be varied to produce different precursor flows from 0.25 to 0.8 g/h, as calculated by the resulting precursor consumption during deposition process, and was monitored using a thermocouple located above the precursor tank. By heating the TTIP precursor between 40 and 50 °C, a steady state precursor flow could be created in the plasma chamber.

We employed the quadrupole mass spectrometer (QMS) Hiden EQP-1000 Analyzer (Warrington, UK) in order to detect neutrals, radicals, and ion species [42]. The QMS could be positioned along the jet center line (the z -axis), so we are able to sample chemical species at different positions, as well as provide in situ real-time sampling.

2.2. Thin Films Characterization

The deposition was performed varying the distance between 5 and 30 mm inside the deposition chamber. Slabs of oxidized single crystal silicon were employed. The substrates were firstly cleaned using pure ethanol. An aluminum mask on the substrate defined the contour of the deposition area of 7×7 mm². The deposited films were annealed at 500 °C for about 20 min to remove any remaining organic impurities. The thickness of the PA-SJD films was evaluated with a Dektak 8 Stylus Profilometer from Veeco (Plainview, NY, USA). The applied stylus tracking force was 15 mg, and its nominal vertical resolution was 1 Å. To characterize the surface morphology, the sample surface was scanned with a P47-PRO NT-MDT AFM (Moscow, Russia) working in semi-contact mode using a silicon tip. The resonance frequency was 245 kHz, and the constant applied force was 12 N/m. The tip had a curvature radius of less than 10 nm. The resolution employed in each scan was fixed at 256×256 points [45,47]. To collect secondary electrons, the in-lens ZEISS 1530 SEM detector (Oberkochen, Germany), equipped with a Schottky emitter and operating at 10 keV, was used for the microscopic analysis of the deposited thin films' morphology. In previous works, this task also involved TEM imaging, and we will refer to some of those analyses performed in our previous papers [32,33]. We analyzed the chemical composition of the annealed thin film by means of RAMAN spectroscopy using a Labram (Dilor—JobinYvon,

HORIBA, Kyoto, Japan) device, X-ray diffraction (XRD) spectroscopy (Rigaku SmartLab, Rigaku Corporation, Tokyo, Japan), and Fourier Transform infrared spectroscopy (FTIR) (Nicolet iS10, Thermo Fisher Scientific, Waltham, Massachusetts, USA).

3. Results and Discussion

3.1. Plasma-Assisted Supersonic Jet Characterization

We set up a pressure of 10 Pa in the first chamber to ignite the plasma using a 2:3 mixture of Ar and O₂, respectively. The reason for this is that argon allowed us to stabilize the plasma and oxygen ensured the dissociation of the precursor. Above 175 W of input power, the discharge coupling changed from capacitive to inductive, which was of interest to us. Thus, most of experiments were performed at 450 W power.

By moving the QMS along the jet axis, we were able to detect a signal (measured in counts per seconds) proportional to the density of species. For each measured mass, the acquired data were renormalized to fit the density ratio expected from Equation (2). The statistical errors were within 1%. As can be seen in Figure 2, the isentropic expansion law, as given by Equation (2), yielded results in good agreement with our experimental data for distances z smaller than the Mach disk value.

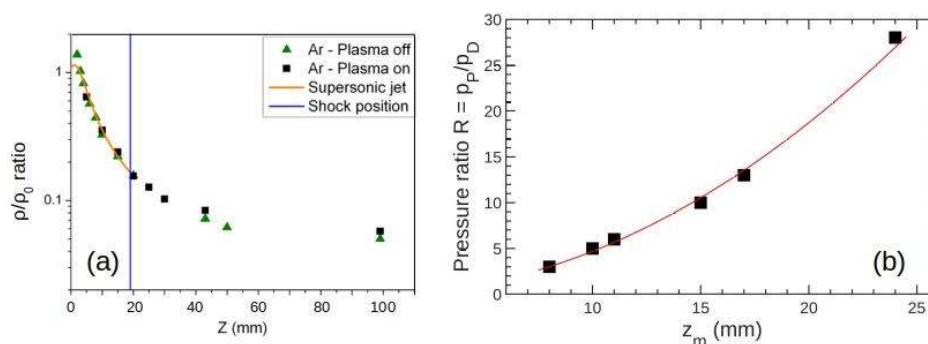


Figure 2. (a) Normalized argon number density, ρ/ρ_0 , as a function of position z (mm), measured in the deposition chamber for a pressure of 8 Pa in the plasma chamber, yielding $R = 28$. The Mach disk positions z_M (Equation (1)) are indicated by the blue vertical bar. (b) R vs. z_M . The red continuous line is a parabolic fit, $R \sim z_M^2$ from Equation (1) that is in good agreement with the experimental data.

In Figure 2b, we report z_M for different pressure ratios, $3 < R < 28$, all used in the same plasma chamber pressure, $p_p = 8$ Pa. The different R values were obtained by varying the pressure p_D in the deposition chamber up to 4 Pa. The Mach disk position z_M increased when increasing R , according to Equation (1). When the precursor was introduced inside the plasma, their reactive species (such as oxygen, the electrons, and the heating produced by chemical oxidations) promoted the formation of several organic and organo-metallic chemical groups.

In Figure 3a and Table 1, the main precursor species, together with their masses in amu, are reported. Larger molecule clusters in the plasma and deposition chambers could be considered negligible. The TTIP dissociation products could be easily identified, of which the most abundant heavy molecules were TiO_xH_y seeds that provided the mass peaks at 81 and 99 amu.

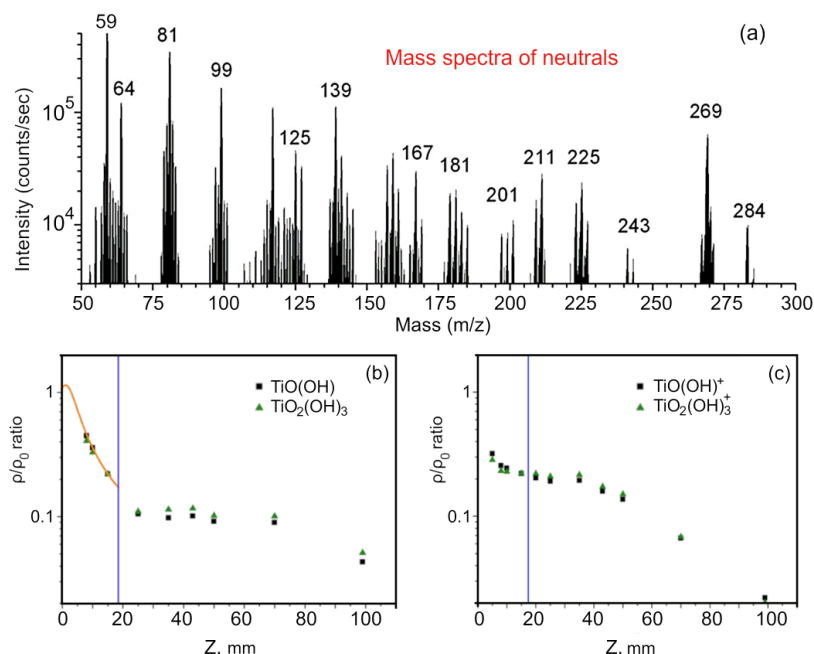


Figure 3. Generated species in the jet for 8 Pa of pressure in the plasma chamber. (a) Mass spectra (for masses between 50 and 300 amu) of precursor species in the discharge at 5 mm from the nozzle. (b) Normalized number density, ρ/ρ_0 , vs. z (mm) of the two main TiO_x species for $R = 13$ along the jet. (c) Normalized number density, ρ/ρ_0 , vs. z (mm) for ion species produced by plasma flowing along the jet at $R = 13$. The Mach disk positions z_M are indicated by blue vertical bars.

Table 1. Main species of the TTIP dissociation measured during experiments and corresponding mass M (amu).

M	Species	M	Species
15	CH ₃	139	TiO ₂ (OCH(CH ₃) ₂)
43	CH(CH ₃) ₂	167	Ti(OCH(CH ₃) ₂) ₂ H
59	OCH(CH ₃) ₂	181	TiO(OCH(CH ₃) ₂) ₂ -H
64	TiO	211	Ti(OCH(CH ₃) ₂) ₃ H-CH ₃
81	TiO ₂ H	225	Ti(OCH(CH ₃) ₂) ₃
99	TiO ₃ H ₃	243	Ti(OCH(CH ₃) ₂) ₄ -CH(CH ₃) ₂
125	TiO(OCH(CH ₃) ₂)	269	Ti(OCH(CH ₃) ₂) ₄ -CH ₃

Neutrals scans were performed during the plasma generation. The QMS counts along the z axis are reported in Figure 3b,c, which shows the peak area of some gas species calculated from mass spectra acquired at different positions for $R = 13$. In particular, densities of neutral TiO₂H and TiO₃H₃ seeds are reported along the jet axis in Figure 3b. The precursor seeds followed the theoretical isentropic expansion law, but, in contrast to the light gas carriers, their behavior was different after the Mach disk location: the measured signal did not decrease. The peak area for the products of the precursor dissociation was constant after the Mach disk location. This phenomenon may have been due to the longer mean free path related to their heavier masses. Due to their inertia, the TiO_x seeds did not expand further after the Mach disk location. In particular, different accelerations due to inertia promoted particle separation and the retention of heavier species along its centerline. This phenomenon, due to an inertial effect that maintained the heavier species near the jet

centerline, was particularly interesting because it allowed us to perform thin film deposition far away from the nozzle, where the jet was no longer supersonic. Similar results were found at a different pressure ratio. Figure 3c reports a similar trend for the ionized TiO_x seeds along the plasma jet, although their density decreased faster after 50 mm from the nozzle, probably due to neutral recombination [48].

3.2. TiO_2 Thin Film Characterization

PA-SJD was able to produce the depositions under the same experimental conditions. However, even if the precursor temperature was the same in different experiments, the TTIP mass flow could have changed inside the plasma chamber. The deposition rate could decrease after a set of successive depositions because the residual precursor could choke the chopper tube of the injector. However, repeatability was ensured when, after one or two hours of operation, the precursor injection system was refilled and cleaned up.

The film chemistry was controlled by tuning the plasma parameters such as plasma power and gas mixture. The determination of the optimal stoichiometry of TiO_2 films by varying the concentration of oxygen, argon, and precursor mixture was the subject of a preliminary study. Here, we considered the effects of heating the organic precursor mixture in the plasma chamber at different temperatures. Above 60°C , high precursor fluxes could be obtained, but the precursor was not effectively dissociated, and we detected the presence of organic residues even after annealing. At lower temperatures between 40 and 50°C , however, the precursor was efficiently dissociated and titanium oxide seeds, mainly Ti-like light species, were transported by the supersonic jet towards the substrate and yielded TiO_2 quasi-stoichiometric films, as shown below by the film analysis.

The chemical composition of the produced film was analyzed by means of FTIR spectroscopy. Figure 4 reports the FTIR spectrum of the titanium precursor.

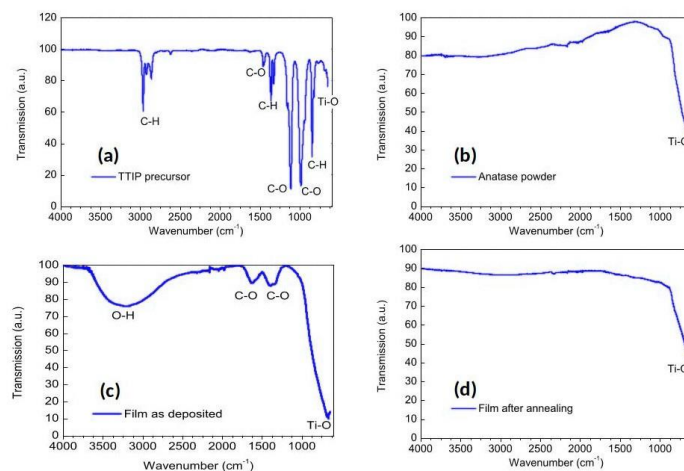


Figure 4. FTIR spectrum of: (a) TTIP precursor, (b) anatase powder, and (c) the as-deposited film, (d) annealed film. The spectrum of as-prepared film does not feature C–H stretching, indicating that the plasma efficiently dissociated and oxidized the precursor. The spectrum of annealing film (d) is similar to that of pure anatase (b).

The spectra shown in Figure 4a reveal the presence of several chemical bonds of the TTIP precursor ($\text{Ti}(\text{OCH}(\text{CH}_3)_2)_4$). Ti–O stretching can be identified around 635 cm^{-1} (in literature the value is 626 cm^{-1}). The peaks at 2864 , 2960 , and 2924 cm^{-1} represent C–H stretching bonds. In addition, traces of CH_3 bending are found at 1366 , 1318 , and 844 cm^{-1} . To be noted is that C–O stretching can be identified at 1114 and 982 cm^{-1} , and C–O vibrations are represented by the peak at 1450 cm^{-1} .

A typical spectrum measured on the deposited film is reported in Figure 4b. The spectrum is completely changed with respect to the TTIP one reported in Figure 4a. In particular, we could not detect C–H stretching, indicating that the plasma efficiently dissociated and oxidized the precursor. The two further broad peaks at 1637 and 1380 cm^{-1} are related to C–O-conjugated vibrations typical of transition metals. The last detected peak is the one corresponding to Ti–O stretching, shifted to 700 cm^{-1} because of the attachment of organic molecules. Then, we could observe O–H stretching vibrations between 3000 and 3500 cm^{-1} . We can conclude that CH chemical groups were missing in the as-deposited film, while some organics (C–O and O–H) were still present.

Figure 4c reports the analysis of a powder of pure anatase TiO_2 . In this case, we detected only one peak near 650 cm^{-1} that corresponded to Ti–O stretching. In Figure 4d, a spectrum similar to Figure 4c was obtained for the annealed film at 500 °C. Here, the spectrum reveals an only peak near 650 cm^{-1} related to Ti–O stretching. This analysis shows that the annealing was able to promote the purity of TiO_2 films, removing organic residuals. Additionally, annealing is essential to vary the crystallinity of deposited films, as we show later with Raman spectroscopy.

Figure 5a shows a typical result of a Raman spectroscopy experiment performed on the as-deposited and the annealed films. The Raman spectrum of the as-deposited film clearly suggests that we were dealing with an amorphous material. The Raman spectrum, following annealing at 500 °C for 20 min, shows a peak at 143 cm^{-1} and three mid-intensity peaks at 399, 519, and 639 cm^{-1} that are the signatures of the complete transformation of the film into anatase TiO_2 [49].

XRD analyses were conducted on annealed film samples to promote the formation and coalescence of crystalline domains. In the top box of Figure 5a, the diffraction spectrum measured on a deposit from TTIP under optimized conditions after annealing is shown. A comparison with the literature data, collected in a dedicated database available online [50], showed that the film was made of titanium dioxide in the form of allotropic anatase. We can therefore conclude by saying that heat treatment promoted the transition of our deposit into the allotropic anatase form. In fact, there were peaks due to scattering at angles of 25°, 38°, 38°, and 48° corresponding to reflection from some of the crystalline planes of anatase. Conversely, no angle corresponding to the crystalline phases of rutile or brookite appeared in the XRD spectrum. The absence of prominent shifts in the intensity and position of diffraction angles was also significant because it ensured that: (1) there was no residual stress in the film remaining during film growth, (2) there were no significant stoichiometry defects (for example, a sub-stoichiometry in oxygen would induce structural changes in the size of the crystalline cell), and (3) the presence of elements (both substitutional and interstitial) with different atomic radius from Ti and O was negligible so Ti and O occupied the positions of equilibrium of the anatase form. Finally, by applying the Debye–Scherrer formula [51] to the peaks shown in the box of Figure 5a, the size of the crystalline grains in the deposited film could be estimated. Using a form factor of 0.8 and an FWHM width of 0.31, the grain size could be estimated in the order of 25 nm.

We used a mechanical profilometer to determine the thicknesses and deposition rates of the samples. The growth rate was measured using the average height of the film divided by the film deposition time. Different growth rates were observed for depositions performed at different positions along the jet axis, which followed the gas expansion law, as shown in Figure 5b. The deposition rate was reported as a function of distance from the nozzle z for a given constant TTIP precursor flux. The theoretical gas density variation along the expansion, deduced from Equation (2), was applied to the experimental data. The comparison showed that the growth rate of TiO_2 thin films was related to the abundance of TiO_x seeds, as expected for an isentropic expansion. Specifically, the deposition rate can be varied, from few tens nm/min to more than 300 nm/min, depending on the substrate position from the nozzle. The deposition rates can widely vary between some tens of nm/min up to tens of $\mu\text{m}/\text{min}$ as a function of the precursor flows controlled by the heating temperature, allowing one to use the technology for different purposes [33,36].

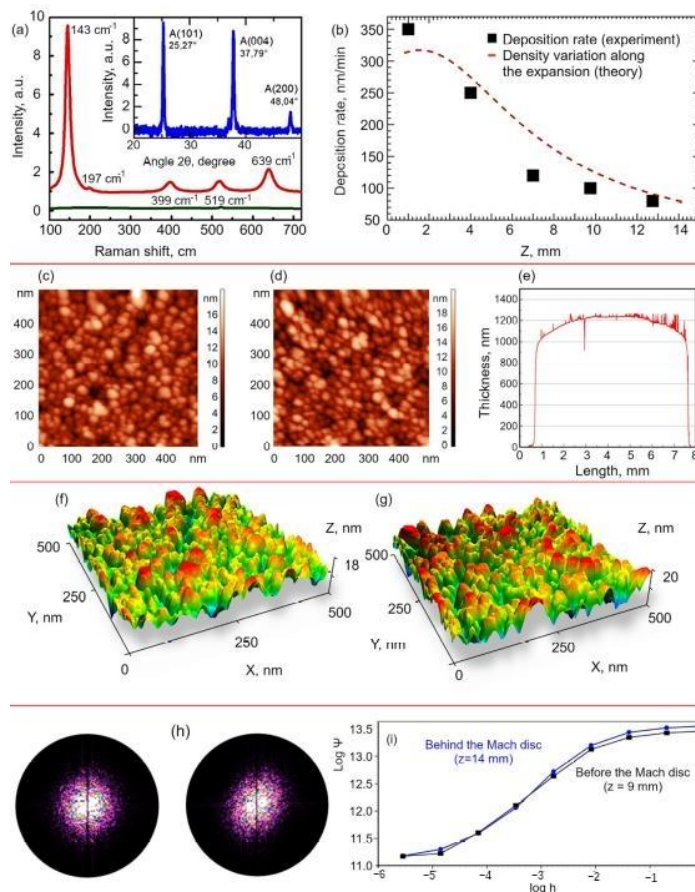


Figure 5. (a) Raman spectra (red line) following annealing processing at 500 °C. Characteristic peaks of anatase are labeled with the letter A. Raman spectrum before annealing (green line) shows that the as-deposited film spectrum is amorphous. In the inset, the XRD spectrum is shown (blue lines) (b) Experimental deposition rate (nm/min) (squares) compared to the density variation expected from Equation (2) (dashed line). (c,d) AFM images obtained using by scanning an area of 500 nm × 500 nm at distances of $z = 9$ nm and $z = 14$ nm. (e) Film thickness profile of the sample located at $z = 14$ nm. The precursor flux was 0.8 g/h and $R = 10$ for both samples. (f,g) Three-dimensional reconstruction of the nanostructures. (h) Power spectra density for the samples deposited at $z = 9$ nm (left) and $z = 14$ nm (right); the first sample demonstrated higher symmetry. (i) Distribution of fractal dimensions for the two samples. The sample deposited behind the Mach disk demonstrated slightly higher fractality, i.e., more developed nanostructured surface.

By annealing at 500 °C for 20 min, the film thickness decreased by less than 10% compared to the as-deposited film. In Table 2, the thicknesses of the as-deposited and the annealed films are listed as a function of the precursor heating temperature and time deposition. At higher annealing temperatures, the thickness greatly decreased by up to 50%.

AFM images, obtained at two different distances from the nozzle before the Mach disk ($z = 9$ nm and $z = 14$ nm), are reported in Figure 5c,d on the scale of hundred nanometers. Grain clusters at the film surfaces attained similar sizes of about tens of nanometers. The

two film depositions were performed with the same precursor flow and $R = 10$ so that we could speculate that collisional processes were negligible in the supersonic jet and mostly occurred in the plasma chamber, and nanoclusters mainly assembled in the plasma phase. This shows that before the Mach cone, the collisional rate was very low, thus allowing us to control the grain size of nanoparticles by tuning the pressure in the plasma chamber. A similar result was reported in literature when aerosol nanoparticles were supersonically accelerated [34]; it was found that the grain sizes embedded in the thin films were similar to those of primary aerosol nanoparticles, i.e., nanoparticles were conserving their sizes during the acceleration. The general observation deduced by experiments and simulations involving supersonic aerosol jets of similar energies as those here, (0.1–1) eV, is that sizes for primary nanoparticles and crystal grains in film are conserved.

Table 2. Film thickness versus temperature T ($^{\circ}\text{C}$) of precursor (precursor flows) for the as deposited and annealed films.

Precursor T ($^{\circ}\text{C}$)	Thickness as-Deposited (nm)	Thickness after Annealing (nm)		Deposition Time (min)
		at 500 $^{\circ}\text{C}$	at 1000 $^{\circ}\text{C}$	
40.5	350	330	-	
46.5	1200	1100	700	
51.5	3000	2900	1500	15
56.1	20,000	19,500	15,000	
51	5800	5700	1800	30

By exploiting the fact that particle speed in the jet abruptly decreased at the Mach disk location and grew slower at larger distances from it, it was possible to intercept the moving species at those large distances from the nozzle by just moving the position of the deposition substrate. Furthermore, since the jet had a transversal profile near the Mach disk that ensured quite flat deposition profiles, the resulting TiO_2 -deposited films displayed a rather good spatial uniformity in the transversal direction of up to 7 mm in comparison to the deposition performed at $z = 14$ mm. In Figure 5e, the deposition rate was about 62 nm/min. A specific discussion on the film thickness uniformity was described in a previous paper [30].

Figure 5h,i illustrates the results of a fractal analysis of the fabricated nanostructures. The power spectra density shown in Figure 5h are for the samples deposited at $z = 9$ mm (left, before the Mach disc) and $z = 14$ mm (right, behind the Mach disc). The first sample demonstrated higher symmetry. Figure 5i shows the distribution of fractal dimensions Ψ for the two samples as a function of height h . The sample deposited behind the Mach disk demonstrated a slightly higher fractality, i.e., more developed nanostructured surface.

While the grain size could be controlled with either the plasma pressure or by locating the substrate at distances far away from the Mach disk, the resulting morphology could still be affected by the R parameter. In particular, R determines the morphology of the incipient tree-like structure of a thin film. Before analyzing the role of R , we discuss the structural assembly of a thin TiO_2 film. SEM images of a typical annealed thin film are reported in Figure 6a,b for $R = 10$ and fixed TTIP flow at 0.8 g/h at $z = 10$ mm. In Figure 6a, the cross-section of the film shows nanoclusters mostly packed along the vertical growth on 100 nm. The top view of Figure 6b suggests a relatively smooth surface where the tips of rods emerged and were grouped to form structures composed of a few assembled nanoclusters.

The properties of the thus-produced thin films are reproducible. Similar nano-assembled structures, composed of few nanoclusters and having rod-like and weakly disordered elongated-grape shapes, can be fabricated when varying R . Thicker films develop different hierarchical structures as a function of the R parameter. For $R = 13$, an annealed film obtained at longer deposition times (in this case, after 40 min) and located at the same position ($z = 10$ mm) showed an elongated compact structure, as reported in Figure 6c,d. The vertical growth corresponded to compact films with a relatively low porosity of about 3 μm thickness. A previous study [30] showed that these films displayed

a high porosity in percentage of voids of between 35% and 45%. The surface of the film (see Figure 6d) showed emerging, well-packed, tree-like structures. After decreasing R , the tree-like nanostructures opened up, showing a more complex type of assembly. In Figure 6e,f, the cross-section of the annealed film, deposited at $R = 10$, shows an increase in the transversal direction, that is, the tree-like hierarchical assembly fanned out. The size of nanoclusters was of the order of 10 nm, and their tree structure could be better visualized by a TEM analysis [36]. The latter showed the formation of a zig-zag-like structure composed of single, mostly crystalline, domains of 10 nm in size.

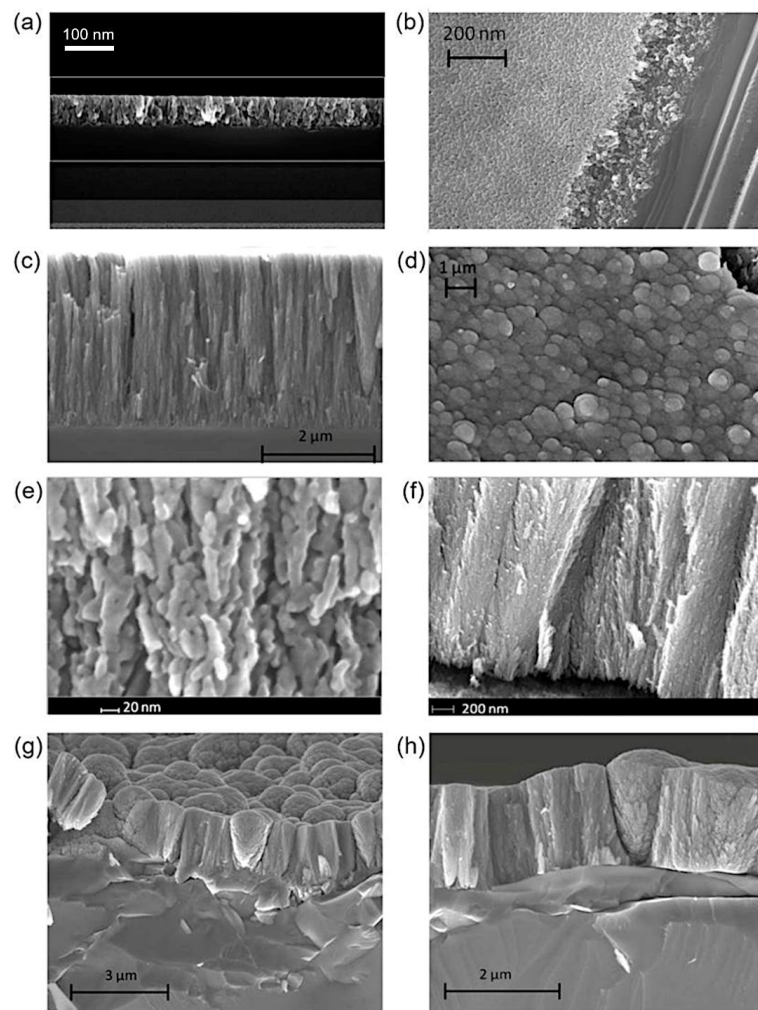


Figure 6. SEM analyses of annealed samples. (a,b) Cross-section and top view SEM images of a film deposited for 10 min located at $z = 10$ mm. (c,d) SEM images of a film deposited for 40 min located at $z = 10$ mm. Cross-section and top view. (e,f) SEM images of a film deposited for 30 min located at $z = 10$ mm. In (a–f), $R = 10$. (g,h) SEM images of a film deposited for 30 min located at $z = 10$ mm for and $R = 6$ (cross-sections at different magnifications). The precursor flow was 0.8 g/h.

Films of TiO₂ with this hierarchical structural morphology are characterized by a large surface area and have been fabricated as photocathode for photovoltaic applications [36]. In fact, it has been demonstrated that high-surface-area nanostructures enhance sunlight and dye absorption in specifically designed solar cells, known as dye-sensitized solar cells, and ordered nanostructured networks offer a more direct charge transport pathway that improves the same electron mobility. Similar brush-like structures, which are mostly vertically oriented on films, have been fabricated with PLD. In this case, they are well-separated from each other and become more open as height increases. The enhanced surface area of the emerging structures does not seem to result into an overall larger surface area due to the presence of large voids developing in between neighboring structures and to the larger spacing among the growing branches [52].

At lower values, $R = 6$, the structures in our study also developed conical shapes, as shown in Figure 6g,h. Conical and squared shapes alternated in the film, exploiting the available free space for growth. We can imagine that tree trunks were formed from the first rod elements and that they grew while leaning against each other to merge into larger structures. In Figure 6g,h, it is also possible to appreciate the presence of leaves attached to the structures. From above, the surface looks like a coniferous forest similar to a cauliflower. We can argue that the effect of the ballistic deposition depended on the energy and shape of the supersonic jet of seed nanoclusters, which was turned regulated by the parameter R .

At high R , the jet was well-oriented and the fast clusters attached themselves to the surface on top of previously deposited clusters. At low R , the jet was less energetic and less oriented and the clusters had transversal velocity that allowed them to laterally attach to the vertical structures, thus forming branches and leaves. In previous experiments, with supersonic aerosol jets [34], a decrease in deposition energy promoted less densification and no hierarchical grain growth, though with similar film mass densities of ~60% of bulk (i.e., about 40% of void densities) than ours. By means of PLD [52], porosity has been controlled by tuning the pressure in a vacuum chamber to between 20 and 500 mTorr. In [35], nanoporous films were grown by varying the background gas pressure in order to control the nature of the species on the film, their kinetic energy, and their aggregation dynamics.

Finally, we briefly discuss the effects of the annealing process on the morphology of films. In Figure 7a,b, the SEM images of an as-deposited film and its annealed form at 500 °C show that the appearance at the nanoscale of the structures remained unaltered and that the thickness of the annealed film was slightly decreased by about a 2% with respect to the as-deposited film. On the contrary, when the film was annealed at the higher temperature of 1000 °C, as can be seen in Figure 7c, its nanostructure completely changed into a rutile one and its thickness decreased by about a 30%.

3.3. TiO₂ Films on Wider Areas

In order to deposit films over wider areas, tests were performed by gradually vertically moving the substrate by few millimeters (generally 5 mm) at a time step of 2–4 min. The nozzle's ending orifice was replaced by a larger slit whose height and width (20 and 8 mm, respectively) were set to provide a conductance similar to the one of the circular orifices. A small slab made of glass coated by a fluorine-doped tin oxide was used as the substrate, which was fixed to a movable vertical bar.

The deposition was repeated by moving the substrate back and forth a few times (depending on the expected film thickness). The mean distance of the substrate from the nozzle was 7 mm. Figure 8a shows the result for an 80 × 5 mm² thin film, which was exposed to the seeded jet for few minutes at 41 °C with a small precursor flow. The profilometer scans refer to different sample lines along the sample minor axis of 5 mm. The whole area was successfully covered with a nearly uniform TiO₂ nanostructured deposition with an average height of 350 nm. At the higher precursor temperature of 50 °C, it was possible to boost the deposition rate and obtain a film with a thickness of the order of few μm.

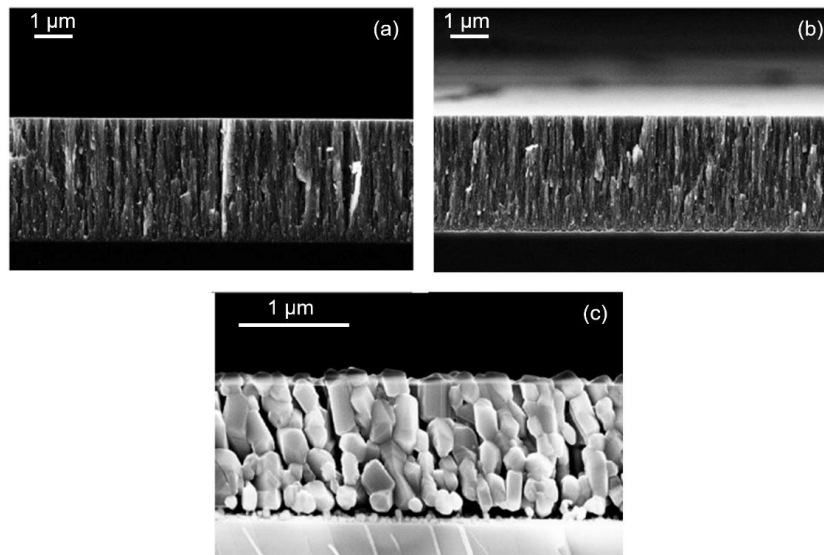


Figure 7. SEM images for a film deposited on a substrate at $z = 8.4$ mm, a precursor temperature of 51 °C, a deposition time of 30 min, and $R = 6$ (last sample reported in Table 2). (a) As-deposited film (thickness of 5800 nm); (b) annealed film at 500 °C for 20 min; (c) annealed film at 1000 °C for 60 min.

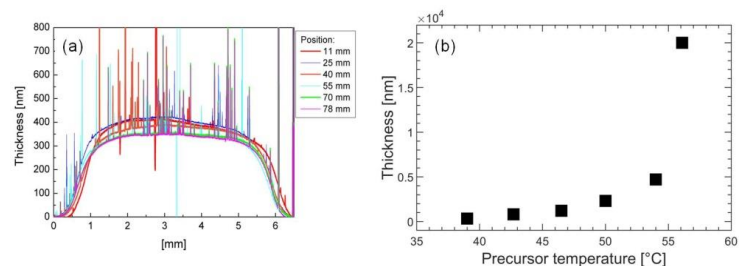


Figure 8. (a) Profilometer scans performed at different x positions ($0 < x < 5$ mm) on an area of 5×80 mm² of TiO₂ thin film. The considered y positions ($0 < y < 80$ mm) are shown in the inset. The thin film was deposited at a low deposition rate at 6 mm from the nozzle slit while vertically moving the substrate back and forth by 5 mm every 2 min. (b) Thickness of the thin films vs. TTIP temperature obtained at $z = 9$ mm.

By increasing the precursor temperature, larger precursor fluxes could be injected in the plasma chamber. The relation between temperature and precursor flux appeared linear, and it could be studied by looking at the dissociation products by QMS. In Figure 8b, the trend of the thickness is plotted as a function of temperature at a fixed position from the nozzle, $z = 9$ mm. We found that the growth rate was almost linearly dependent on the precursor temperature in the range from 40 to 50 °C.

Along these lines, another important feature concerns the role of the precursor flux. In the above discussion, we highlighted that the grain size in the Mach cone was conserved. The grain size could instead sensitively depend on the applied precursor density in the plasma chamber. As the precursor flux increased, the metal oxide aggregation phenomena increased due to the higher collision rates inside the plasma chambers. One can conclude that in the Mach cone, the dimension of the TiO₂ seeds was conserved, while the grain size could be modified by changing the precursor flux injected in the plasma chamber. Thus,

by increasing the precursor flux, two effects were produced: an increase in the grain size in the plasma chamber and an increase in the concentration of clusters inside the jet. Both yielded an increase in film deposition rates.

4. Conclusions

In PA-SJD, clusters of molecules and nanoparticles are formed in inductively coupled plasma, then transported in the expanding jet, and deposited on a substrate. In the former, the employed argon–oxygen plasma produces a reactive environment where an organo–metallic precursor can become well-dissociated and oxidized. Depending on the jet parameters, different nanostructure sizes and deposition rates can be achieved. We considered TiO₂ nanoparticles as seeds of thin films, whose structure and morphology were analyzed and characterized.

The titanium nanoparticles present in the jet were identified using QMS measurements. By sampling neutral gas species along the supersonic jet, we studied their profiles. Many molecules of partly dissociated precursors could be observed. The study of the supersonic jet axis profiles for gas carrier and the TiO_x seeds showed that titanium nanoparticles followed an isentropic expansion, like that of the light gas carrier, until the Mach disk location. After the Mach cone, titanium nanoparticles maintained their density over long distances due to an inertial effect that kept the heavier species near the jet centerline.

Nanostructured TiO₂ thin films deposited by PA-SJD could be grown at different deposition rates depending on the precursor mass flow and the distance of the deposited film from the nozzle. A thermal annealing performed at 500 °C could successfully remove any organic impurities while also setting the crystalline structure of the TiO₂ to anatase, which is the most interesting for most applications.

The growth rate ranged from few nm/min to few hundreds nm/min and scales with the isentropic density relation along the supersonic jet. Depositions were also performed over wide areas of the order of cm² using a movable substrate and changing the dimension of the supersonic nozzle. The morphology of the thin films was characterized by SEM imaging. The SEM images of some selected samples confirmed a vertical nanostructure with grain diameters of about 15 nm. Experiments also confirmed that the precursor density used inside the reactor chamber determined the grain size of the thin film building blocks. Depending on the selected supersonic jet parameters, different hierarchically complex nanostructures can be deposited in a controlled fashion, thus yielding structures with a predetermined desired morphology.

Despite the above-mentioned advantages of the technology based on supersonic plasma jets, scaling up towards industrial applications may represent a problem. Though any low-pressure system has inherent challenges regarding integration and scale-up, solutions based on plasma sources of larger volume to increase the processed surface area, along with deposition systems employing supersonic multi-jet systems and systems with moving stages, could be adapted to the industrial scale in order to keep the definite advantages of the plasma treatment such as control over the deposition, additional possibilities in morphology, and material structure control via energetic particles in plasma.

Author Contributions: Conceptualization, I.L. and C.R.; Data curation, C.C. and V.M.; Formal analysis, H.E.R.; Funding acquisition, C.R.; Investigation, V.M.; Methodology, E.C.D.; Project administration, C.R.; Supervision, I.L. and C.R.; Writing—original draft, C.P., K.B., H.E.R., I.L. and C.R.; Writing—review & editing, C.P., K.B., H.E.R., I.L. and C.R. All authors have read and agreed to the published version of the manuscript.

Funding: This research received no external funding.

Institutional Review Board Statement: Not applicable.

Informed Consent Statement: Not applicable.

Acknowledgments: We kindly acknowledge Stefano Caldirola for help during the experiments and for the collaborative working atmosphere during the completion of his Ph.D. thesis. We gratefully

acknowledge the technical support of Alessandro Mietner and Moreno Piselli in device development and experiment execution. We also acknowledge Politecnico di Milano for SEM images.

Conflicts of Interest: The authors declare no conflict of interest.

References

1. Levchenko, I.; Bazaka, K.; Keidar, M.; Xu, S.; Fang, J. Hierarchical Multicomponent Inorganic Metamaterials: Intrinsically Driven Self-Assembly at the Nanoscale. *Adv. Mater.* **2018**, *30*, 1702226. [[CrossRef](#)] [[PubMed](#)]
2. Baranov, O.; Levchenko, I.; Bell, J.M.; Lim, J.W.M.; Huang, S.; Xu, L.; Wang, B.; Aussems, D.U.B.; Xu, S.; Bazaka, K. From Nanometre to Millimetre: A Range of Capabilities for Plasma-Enabled Surface Functionalization and Nanostructuring. *Mater. Horiz.* **2018**, *5*, 765–798. [[CrossRef](#)]
3. Alancherry, S.; Jacob, M.V.; Prasad, K.; Joseph, J.; Bazaka, O.; Neupane, R.; Varghese, O.K.; Baranov, O.; Xu, S.; Levchenko, I.; et al. Tuning and Fine Morphology Control of Natural Resource-Derived Vertical Graphene. *Carbon* **2020**, *159*, 668–685. [[CrossRef](#)]
4. Alancherry, S.; Bazaka, K.; Levchenko, I.; Al-jumaili, A.; Kandel, B.; Alex, A.; Robles Hernandez, F.C.; Varghese, O.K.; Jacob, M.V. Fabrication of Nano-Onion-Structured Graphene Films from *Citrus Sinensis* Extract and Their Wetting and Sensing Characteristics. *ACS Appl. Mater. Interfaces* **2020**, *12*, 29594–29604. [[CrossRef](#)] [[PubMed](#)]
5. Fusco, Z.; Rahmani, M.; Tran-Phu, T.; Ricci, C.; Kiy, A.; Kluth, P.; Della Gaspera, E.; Motta, N.; Neshev, D.; Tricoli, A. Photonic Fractal Metamaterials: A Metal–Semiconductor Platform with Enhanced Volatile-Compound Sensing Performance. *Adv. Mater.* **2020**, *32*, 2002471. [[CrossRef](#)] [[PubMed](#)]
6. Abela, S.; Farrugia, C.; Xuereb, R.; Lia, F.; Zammit, E.; Rizzo, A.; Refalo, P.; Grech, M. Photocatalytic Activity of Titanium Dioxide Nanotubes Following Long-Term Aging. *Nanomaterials* **2021**, *11*, 2823. [[CrossRef](#)]
7. Ajibade, P.A.; Oluwalana, A.E. Enhanced Photocatalytic Degradation of Ternary Dyes by Copper Sulfide Nanoparticles. *Nanomaterials* **2021**, *11*, 2000. [[CrossRef](#)] [[PubMed](#)]
8. Li, H.; Liu, H.; Sun, M.; Huang, Y.; Xu, L. 3D Interfacing between Soft Electronic Tools and Complex Biological Tissues. *Adv. Mater.* **2021**, *33*, 2004425. [[CrossRef](#)] [[PubMed](#)]
9. Mavridi-Printezi, A.; Guernelli, M.; Menichetti, A.; Montalti, M. Bio-Applications of Multifunctional Melanin Nanoparticles: From Nanomedicine to Nanocosmetics. *Nanomaterials* **2020**, *10*, 2276. [[CrossRef](#)]
10. Konar, M.; Roy, B.; Govindaraju, T. Molecular Architectonics-Guided Fabrication of Superhydrophobic and Self-Cleaning Materials. *Adv. Mater. Interfaces* **2020**, *7*, 2000246. [[CrossRef](#)]
11. Piferi, C.; Bazaka, K.; D’Aversa, D.L.; Girolamo, R.D.; Rosa, C.D.; Roman, H.E.; Riccardi, C.; Levchenko, I. Hydrophilicity and Hydrophobicity Control of Plasma-Treated Surfaces via Fractal Parameters. *Adv. Mater. Interfaces* **2021**, *8*, 2100724. [[CrossRef](#)]
12. Shahzad, F.; Iqbal, A.; Kim, H.; Koo, C.M. 2D Transition Metal Carbides (MXenes): Applications as an Electrically Conducting Material. *Adv. Mater.* **2020**, *32*, 2002159. [[CrossRef](#)]
13. Chen, Z.; Narita, A.; Müllen, K. Graphene Nanoribbons: On-Surface Synthesis and Integration into Electronic Devices. *Adv. Mater.* **2020**, *32*, 2001893. [[CrossRef](#)] [[PubMed](#)]
14. Levchenko, I.; Bazaka, K.; Mazouffre, S.; Xu, S. Prospects and Physical Mechanisms for Photonic Space Propulsion. *Nat. Photonics* **2018**, *12*, 649–657. [[CrossRef](#)]
15. Levchenko, I.; Bazaka, K. Iodine Powers Low-Cost Engines for Satellites. *Nature* **2021**, *599*, 373–374. [[CrossRef](#)]
16. Levchenko, I.; Bazaka, K.; Belmonte, T.; Keidar, M.; Xu, S. Advanced Materials for Next-Generation Spacecraft. *Adv. Mater.* **2018**, *30*, 1802201. [[CrossRef](#)]
17. Levchenko, I.; Keidar, M.; Cantrell, J.; Wu, Y.-L.; Kuninaka, H.; Bazaka, K.; Xu, S. Explore Space Using Swarms of Tiny Satellites. *Nature* **2018**, *562*, 185–187. [[CrossRef](#)]
18. Adamovich, I.; Baalrud, S.D.; Bogaerts, A.; Bruggeman, P.J.; Cappelli, M.; Colombo, V.; Czarnetzki, U.; Ebert, U.; Eden, J.G.; Favia, P.; et al. The 2017 Plasma Roadmap: Low Temperature Plasma Science and Technology. *J. Phys. Appl. Phys.* **2017**, *50*, 323001. [[CrossRef](#)]
19. Grätzel, M. Sol-Gel Processed TiO₂ Films for Photovoltaic Applications. *J. Sol-Gel Sci. Technol.* **2001**, *22*, 7–13. [[CrossRef](#)]
20. Kandasamy, A.; Ramasamy, T.; Samrin, A.; Narayanasamy, P.; Mohan, R.; Bazaka, O.; Levchenko, I.; Bazaka, K.; Mohandas, M. Hierarchical Doped Gelatin-Derived Carbon Aerogels: Three Levels of Porosity for Advanced Supercapacitors. *Nanomaterials* **2020**, *10*, 1178. [[CrossRef](#)]
21. van den Bergh, W.; Williams, E.R.; Vest, N.A.; Chiang, P.-H.; Stefik, M. Mesoporous TiO₂ Microparticles with Tailored Surfaces, Pores, Walls, and Particle Dimensions Using Persistent Micelle Templates. *Langmuir* **2021**, *37*, 12874–12886. [[CrossRef](#)] [[PubMed](#)]
22. Wang, Z.; Liu, T.; Jiang, L.; Asif, M.; Qiu, X.; Yu, Y.; Xiao, F.; Liu, H. Assembling Metal–Organic Frameworks into the Fractal Scale for Sweat Sensing. *ACS Appl. Mater. Interfaces* **2019**, *11*, 32310–32319. [[CrossRef](#)] [[PubMed](#)]
23. De Rancourt de Mimérand, Y.; Li, K.; Zhou, C.; Jin, X.; Hu, X.; Chen, Y.; Guo, J. Functional Supported ZnO/Bi₂MoO₆ Heterojunction Photocatalysts with 3D-Printed Fractal Polymer Substrates and Produced by Innovative Plasma-Based Immobilization Methods. *ACS Appl. Mater. Interfaces* **2020**, *12*, 43138–43151. [[CrossRef](#)] [[PubMed](#)]
24. Zanini, S.; Grimoldi, E.; Riccardi, C. Development of Controlled Releasing Surfaces by Plasma Deposited Multilayers. *Mater. Chem. Phys.* **2013**, *138*, 850–855. [[CrossRef](#)]

25. Susanto, I.; Tsai, C.-Y.; Ho, Y.-T.; Tsai, P.-Y.; Yu, I.-S. Temperature Effect of van Der Waals Epitaxial GaN Films on Pulse-Laser Deposited 2D MoS₂ Layer. *Nanomaterials* **2021**, *11*, 1406. [CrossRef]
26. Romanov, R.; Fominski, V.; Demin, M.; Fominski, D.; Rubinkovskaya, O.; Novikov, S.; Volkov, V.; Doroshina, N. Application of Pulsed Laser Deposition in the Preparation of a Promising MoS_x/WSe₂/C(B) Photocathode for Photo-Assisted Electrochemical Hydrogen Evolution. *Nanomaterials* **2021**, *11*, 1461. [CrossRef]
27. Kavre Piltaver, I.; Peter, R.; Šarić, I.; Salamon, K.; Jelovica Badovinac, I.; Koshmak, K.; Nannarone, S.; Delač Marion, I.; Petravić, M. Controlling the Grain Size of Polycrystalline TiO₂ Films Grown by Atomic Layer Deposition. *Appl. Surf. Sci.* **2017**, *419*, 564–572. [CrossRef]
28. Jelovica Badovinac, I.; Peter, R.; Omerzu, A.; Salamon, K.; Šarić, I.; Samaržija, A.; Perčić, M.; Kavre Piltaver, I.; Ambrožič, G.; Petravić, M. Grain Size Effect on Photocatalytic Activity of TiO₂ Thin Films Grown by Atomic Layer Deposition. *Thin Solid Films* **2020**, *709*, 138215. [CrossRef]
29. Schmitt, I.L.I.; Halpern, B.L. Method for Microwave Plasma Assisted Supersonic Gas Jet Deposition of Thin Films. 1994. Available online: <https://www.freepatentsonline.com/5356672.html> (accessed on 21 October 2021).
30. Dell'Orto, E.C.; Caldirola, S.; Sassella, A.; Morandi, V.; Riccardi, C. Growth and Properties of Nanostructured Titanium Dioxide Deposited by Supersonic Plasma Jet Deposition. *Appl. Surf. Sci.* **2017**, *425*, 407–415. [CrossRef]
31. Bottani, E.; Di, F.F.; Fumagalli, F.S.; Piselli, M.; Riccardi, C. Method and Apparatus for Deposition of Thin Nanostructured Layers with Controlled Morphology and Nanostructure 2009. Available online: <https://patents.google.com/patent/ITMI20092107A1/en> (accessed on 21 May 2021).
32. Dell'Orto, E.C.; Caldirola, S.; Roman, H.E.; Riccardi, C. Nanostructured TiO₂ Film Deposition by Supersonic Plasma Jet Source for Energetic Application. In Proceedings of the 2nd International Congress on Energy Efficiency and Energy Related Materials (ENEFM2014), Fethiye, Turkey, 16–19 October 2014; Oral, A.Y., Bahsi Oral, Z.B., Ozer, M., Eds.; Springer International Publishing: Cham, Switzerland, 2015; pp. 349–355.
33. Carra, C.; Dell'Orto, E.; Morandi, V.; Riccardi, C. ZnO Nanostructured Thin Films via Supersonic Plasma Jet Deposition. *Coatings* **2020**, *10*, 788. [CrossRef]
34. Huang, C.; Nichols, W.T.; O'Brien, D.T.; Becker, M.F.; Kovar, D.; Keto, J.W. Supersonic Jet Deposition of Silver Nanoparticle Aerosols: Correlations of Impact Conditions and Film Morphologies. *J. Appl. Phys.* **2007**, *101*, 064902. [CrossRef]
35. Maffini, A.; Pazzaglia, A.; Dellasega, D.; Russo, V.; Passoni, M. Growth Dynamics of Pulsed Laser Deposited Nanofoams. *Phys. Rev. Mater.* **2019**, *3*, 083404. [CrossRef]
36. Trifiletti, V.; Ruffo, R.; Turrini, C.; Tasseti, D.; Brescia, R.; Fonzo, F.D.; Riccardi, C.; Abbotto, A. Dye-Sensitized Solar Cells Containing Plasma Jet Deposited Hierarchically Nanostructured TiO₂ Thin Photoanodes. *J. Mater. Chem. A* **2013**, *1*, 11665–11673. [CrossRef]
37. Stock, F.; Diebold, L.; Antoni, F.; Chowde Gowda, C.; Muller, D.; Haffner, T.; Pfeiffer, P.; Roques, S.; Mathiot, D. Silicon and Silicon-Germanium Nanoparticles Obtained by Pulsed Laser Deposition. *Appl. Surf. Sci.* **2019**, *466*, 375–380. [CrossRef]
38. Fehse, M.; Trócoli, R.; Hernández, E.; Ventosa, E.; Sepúlveda, A.; Morata, A.; Tarancón, A. An Innovative Multi-Layer Pulsed Laser Deposition Approach for LiMn₂O₄ Thin Film Cathodes. *Thin Solid Films* **2018**, *648*, 108–112. [CrossRef]
39. Novotný, M.; Vondráček, M.; Marešová, E.; Fitl, P.; Bulíř, J.; Pokorný, P.; Havlová, Š.; Abdellaoui, N.; Pereira, A.; Hubík, P.; et al. Optical and Structural Properties of ZnO:Eu Thin Films Grown by Pulsed Laser Deposition. *Appl. Surf. Sci.* **2019**, *476*, 271–275. [CrossRef]
40. Hashimoto, Y.; Ueda, M.; Kohiga, Y.; Imura, K.; Hontsu, S. Application of Fluoridated Hydroxyapatite Thin Film Coatings Using KrF Pulsed Laser Deposition. *Dent. Mater. J.* **2018**, *37*, 408–413. [CrossRef] [PubMed]
41. Caldirola, S.; Barni, R.; Roman, H.E.; Riccardi, C. Mass Spectrometry Measurements of a Low Pressure Expanding Plasma Jet. *J. Vac. Sci. Technol. A* **2015**, *33*, 061306. [CrossRef]
42. Biganzoli, I.; Fumagalli, F.; Fonzo, F.D.; Barni, R.; Riccardi, C. A Supersonic Plasma Jet Source for Controlled and Efficient Thin Film Deposition. *J. Mod. Phys.* **2012**, *3*, 1626–1638. [CrossRef]
43. Caldirola, S.; Roman, H.E.; Riccardi, C. Ion Dynamics in a Supersonic Jet: Experiments and Simulations. *Phys. Rev. E* **2016**, *93*, 033202. [CrossRef]
44. Barni, R.; Zanini, S.; Riccardi, C. Diagnostics of Reactive RF Plasmas. *Vacuum* **2007**, *82*, 217–219. [CrossRef]
45. Zanini, S.; Riccardi, C.; Orlandi, M.; Grimoldi, E. Characterisation of SiO_xCyHz Thin Films Deposited by Low-Temperature PECVD. *Vacuum* **2007**, *82*, 290–293. [CrossRef]
46. Abouali, O.; Saadabadi, S.; Emdad, H. Numerical Investigation of the Flow Field and Cut-off Characteristics of Supersonic/Hypersonic Impactors. *J. Aerosol Sci.* **2011**, *42*, 65–77. [CrossRef]
47. Grimoldi, E.; Zanini, S.; Siliprandi, R.A.; Riccardi, C. AFM and Contact Angle Investigation of Growth and Structure of Pp-HMDSO Thin Films. *Eur. Phys. J. D* **2009**, *54*, 165–172. [CrossRef]
48. Caldirola, S.; Barni, R.; Riccardi, C. Characterization of a Low Pressure Supersonic Plasma Jet. *J. Phys. Conf. Ser.* **2014**, *550*, 012042. [CrossRef]
49. Kim, Y.J.; Lee, M.H.; Kim, H.J.; Lim, G.; Choi, Y.S.; Park, N.-G.; Kim, K.; Lee, W.I. Formation of Highly Efficient Dye-Sensitized Solar Cells by Hierarchical Pore Generation with Nanoporous TiO₂ Spheres. *Adv. Mater.* **2009**, *21*, 3668–3673. [CrossRef]
50. MINCRYST-Crystallographic Database for Minerals. Available online: <http://database.iem.ac.ru/mincryst/> (accessed on 21 October 2021).

51. Lin, J.; Lin, Y.; Liu, P.; Meziani, M.J.; Allard, L.F.; Sun, Y.-P. Hot-Fluid Annealing for Crystalline Titanium Dioxide Nanoparticles in Stable Suspension. *J. Am. Chem. Soc.* **2002**, *124*, 11514–11518. [[CrossRef](#)]
52. Garvey, T.R.; Farnum, B.H.; Lopez, R. Pulsed Laser Deposited Porous Nano-Carpets of Indium Tin Oxide and Their Use as Charge Collectors in Core–Shell Structures for Dye Sensitized Solar Cells. *Nanoscale* **2015**, *7*, 2400–2408. [[CrossRef](#)]

Acknowledgments

All the results in this thesis would not be the same without all the people I worked with.

First, I thank my supervisor professor Claudia Riccardi for the trust she had in me, for all her helps and reassurances during these three years.

All the following lists are in alphabetical order. I would like to thank all the plasma group for their continuous support in technical and interpretational issues: prof. Ruggero Barni, Alessandro Baù, Marco Cavedon, Matteo Daghetta, prof. Emilio Martines, Alessandro Mietner, Eduardo Roman and Leonardo Zampieri. I also thank Arianna Brescia for her help in the characterization of the lamps. I am grateful to professor Ignazio Renato Bellobono and Fondazione di Comunità Milano–Fondo Solidale for funding part of this research. I would like to thank Alessio Malacrida, Priscilla Pasutto and prof. Alessandra Polissi for their work for the preparation of the bacteria and post-treatment investigations. I also acknowledge the SEM technicians Paolo Gentile and Fabrizio Vergani for their endurance in answering to all of our requests for SEM images, and Federico Cesura for the AFM imaging.

I really thank Luca Broggi for his uninterrupted support, even if I don't acknowledge him in previous works. Thanks to mamma, papà, Vittoria, Francesco, Agnese, and all my family for making me the person I am.